UNIVERSITAT POLITÈCNICA
DE CATALUNYA
BARCELONATECH

Optimal operation and design of modular multilevel converter for HVDC applications

Daniel Westerman Spier

ADVERTIMENT La consulta d'aquesta tesi queda condicionada a l'acceptació de les següents condicions d'ús: La difusió d'aquesta tesi per mitjà del repositori institucional UPCommons (http://upcommons.upc.edu/tesis) i el repositori cooperatiu TDX (http://www.tdx.cat/) ha estat autoritzada pels titulars dels drets de propietat intel·lectual **únicament per a usos privats** emmarcats en activitats d'investigació i docència. No s'autoritza la seva reproducció amb finalitats de lucre ni la seva difusió i posada a disposició des d'un lloc aliè al servei UPCommons o TDX. No s'autoritza la presentació del seu contingut en una finestra o marc aliè a UPCommons (*framing*). Aquesta reserva de drets afecta tant al resum de presentació de la tesi com als seus continguts. En la utilització o cita de parts de la tesi és obligat indicar el nom de la persona autora.

ADVERTENCIA La consulta de esta tesis queda condicionada a la aceptación de las siguientes condiciones de uso: La difusión de esta tesis por medio del repositorio institucional UPCommons (http://upcommons.upc.edu/tesis) y el repositorio cooperativo TDR (http://www.tdx.cat/?locale-attribute=es) ha sido autorizada por los titulares de los derechos de propiedad intelectual **únicamente para usos privados enmarcados** en actividades de investigación y docencia. No se autoriza su reproducción con finalidades de lucro ni su difusión y puesta a disposición desde un sitio ajeno al servicio UPCommons No se autoriza la presentación de su contenido en una ventana o marco ajeno a UPCommons (*framing)*. Esta reserva de derechos afecta tanto al resumen de presentación de la tesis como a sus contenidos. En la utilización o cita de partes de la tesis es obligado indicar el nombre de la persona autora.

WARNING On having consulted this thesis you're accepting the following use conditions: Spreading this thesis by the institutional repository UPCommons (http://upcommons.upc.edu/tesis) and the cooperative repository TDX (http://www.tdx.cat/?locale- attribute=en) has been authorized by the titular of the intellectual property rights **only for private uses** placed in investigation and teaching activities. Reproduction with lucrative aims is not authorized neither its spreading nor availability from a site foreign to the UPCommons service. Introducing its content in a window or frame foreign to the UPCommons service is not authorized (framing). These rights affect to the presentation summary of the thesis as well as to its contents. In the using or citation of parts of the thesis it's obliged to indicate the name of the author.

UNIVERSITAT POLITÈCNICA DE CATALUNYA

DEPARTAMENT D'ENGINYERIA ELÈCTRICA

Departament d'Enginyeria Elèctrica
UNIVERSITAT POLITÈCNICA DE CATALUNYA

CITCEA - Centre d'Innovació Tecnològica
en Convertidors Estàtics i Accionaments

Doctoral Thesis

Optimal Operation and Design of Modular Multilevel Converter for HVDC applications

Daniel Westerman Spier

Thesis advisors:
Prof. Dr. Oriol Gomis-Bellmunt (UPC, Spain)
Dr. Eduardo Prieto-Araujo (UPC, Spain)

Examination Commitee:
Dr. Salvador Ceballos (Tecnalia Research and Innovation, Spain)
Dr. Rodrigo Teixeira Pinto (Siemens Energy, Germany)
Dr. Elisabetta Tedeschi (Norwegian University of Science and Technology, Norway)

Barcelona, May 2022

Universitat Politècnica de Catalunya
Departament d'Enginyeria Elèctrica
Centre d'Innovació Tecnològica en Convertidors Estàtics i Accionaments
Av. Diagonal, 647, H building, 2nd floor
08028, Barcelona
Cinergia Power Solutions, S. L.
Carrer Can Baletes. 7 Nau A (Pol. El Cros)
08310, Argentona
Barcelona, Spain

First printing, May 2022

The research leading to this thesis has been supported by the InnoDC (Innovative Tools for Offshore Wind & Direct Current grids) funded by European Union's Horizon 2020 research innovation programme under the Marie Sklodowska-Curie grant agreement No 765585. This work reflects only the author's view. The Research Executive Agency and European Commission are not responsible for any use that may be made of the information it contains.

"Mistakes are, after all,
the foundations of truth,
and if a man does not know
what a thing is, it is at least
an increase in knowledge
if he knows what it is not."

Carl Jung

Acknowledgements

First of all I would like to thank God for all the things I have accomplished and for always being by my side. Minha eterna gratidão e amor a minha falecida mãe, Maria Aparecida, que mesmo em seu leito de morte me pediu que me mantivesse focado em minha carreira. Ao meu pai, Amilton, por seu apoio, amor incondicional, não tenho palavras para lhe agradecer o suficiente. A Tia Mé, Vó Lola, por seu amor, ajuda e precupação com o bem estar da nossa família. Vó Natalina, tio Beto, tia Doris, por sempre estarem comigo e me ajudar a seguir em frente nos momentos difíceis. Ao meu melhor amigo, Marcel, pelas conversas profundas e momentos de reflexão, além de todas as nossas risadas.

Now, back to English. I also have a warm thanks to my supervisors from UPC, prof. Oriol Gomis-Bellmunt and Dr. Eduardo Prieto-Araujo for all their patience, time, knowledge and friendship. By accepting me in this project, they have changed my life for better. And without them, this work would not be possible. For all my colleagues in Cinergia, especially to Miquel Teixidó, Joaquim López-Mestre and Marta Valls, I would like to thank you all for not giving up on me when they had to go through complicate bureaucratic matters in order to get my visa approved.

For all my InnoDC colleagues, specially, Saman, Jovana and Luis, for our moments together, laughs shared and la Fira nights. For the CITCEA colleagues, Dr. Marc, Dr. Enric, Carlos, Jaume, Jie, Vahid, Daniele and Josep (sorry if I forgot somebody). For my previous supervisors from Argentina prof. Germán and prof. Guillermo for the great talks and orientations since undergraduate times until now. I cannot forget to thank Dr. Rafael Peña Alzola for his encouragement words during hard times.

感谢我亲爱的妻子王小苑这些年来对我的理解和厚爱。我还要感谢我的岳母和岳父在我整个旅程中的信任和支持。

Summary

Modular Multilevel Converters (MMCs) are a type of Voltage Source Converter (VSC) which have become the preferred topology choice for High Voltage Direct Current (HVDC) applications. Compared to its HVDC converter predecessors, the Line Commutated Converter (LCC), the MMC can control active and reactive power independently, requires smaller filter reactors and have blackstart capabilities. Regarding classical two- and three-level VSCs, MMCs have improved efficiency, easier scalability to higher voltage levels and better alternate current (AC) output voltage harmonic content. However, they need more complex regulation strategy due to its increased number of degrees of freedom (DOFs). Nevertheless, when these DOFs are fully exploited, the MMC can provide better responses than classical converters, especially during unbalanced network conditions.

First, an in-depth steady-state mathematical analysis of the converter is performed to identify all its DOFs. Based on the DOFs and the currents imposed by them, the equations for the power transfer between the DC/AC networks and internally, between the upper and lower arms and among the phase-legs, are obtained. The resultant expressions indicate potential interactions between distinct DOFs. By taking advantage of those interactions, it is possible to improve existing circulating current reference calculation methods. Thus, enhancing the MMC response under balanced and unbalanced AC network conditions.

The performance of the MMC can be further improved when optimization algorithms are used to calculate its references, in which this thesis proposed two different methods. In the initial proposal, an optimization-based current reference calculation in the natural *abc* reference frame is presented. It considers the Transmission System Operator (TSO) requirements during AC network voltage sags in the form of active/reactive current set-points to provide Fault Ride Through (FRT) capability and the converter limitations. However, due its highly nonlinear characteristics it presents a high computation burden not allowing it to be solved in real-time applications. To cope with this issue, a second method is introduced whereby modifications are performed in the previous optimization formulation and linearization techniques are employed. The resultant linearized optimization-based reference calculation is then integrated with an energy-based control for MMCs and different case studies are analyzed to validate its performance compared to classical approaches.

Lastly, an optimization-based methodology to design the submodule (SM) capacitors is proposed. The algorithm considers all the DOFs of the MMC in order to size the SM capacitor. Finally, the suggested method is compared with classical approaches for different operating points, and it is further exploited by considering AC network voltage sag conditions.

Resum

Els convertidors multinivells modulars (MMC) són un tipus de convertidor de font de tensió (VSC) que s'han convertit en l'opció de topologia preferida per a les aplicacions de corrent continu d'alta tensió (HVDC). En comparació amb els seus predecessors convertidors HVDC, com ara el convertidor de commutació de línia (LCC), l'MMC pot controlar la potència activa i reactiva de manera independent, requereix filtre més petits i té capacitats d'arrencar la xarxa (black-start). Pel que fa als VSC clàssics de dos i tres nivells, l'MMC té una millor eficiència, una escalabilitat més fàcil a nivells de tensió més alts i un millor contingut harmònic de voltatge de corrent altern (CA). Tanmateix, necessiten una estratègia de regulació mès complexa a causa del seu major nombre de graus de llibertat (DOF). No obstant això, quan aquests DOFs exploten completament, l'MMC pot proporcionar millors respostes que els convertidors clàssics, especialment en condicions de xarxa desequilibrades.

En primer lloc, es realitza una anàlisi matemàtica de l'estat estacionari en profunditat del convertidor per identificar tots els seus DOF. A partir dels DOF i dels corrents imposats per aquests, s'obtenen les equacions de la transferència de potència entre les xarxes DC/AC i la transferència de potència interna, entre els braços superior i inferior i entre les diferents fases. Les expressions resultants indiquen interaccions potencials entre entre els diferents DOF. Aprofitant aquestes interaccions, és possible millorar el mètode de càlcul de referència de corrent circulant existent. D'aquesta manera és possible incrementar el funcionament de l'MMC en condicions desequilibrades i amb errors.

El funcionament de l'MMC es pot millorar encara més quan s'utilitzen algorismes d'optimització per calcular les seves referències. A la proposta inicial, es presenta un càlcul de referència actual basat en l'optimització en el marc de referència natural *abc*. Considera els requisits de l'operador del sistema de transmissió (TSO) durant els sots de tensió de la xarxa de CA en forma de consignes de corrent actiu/reactiu per proporcionar la capacitat de transmissió de fallades (FRT) i les limitacions del convertidor. Tanmateix, a causa de les seves característiques altament no lineals, presenta una gran càrrega de càlcul que no permet resoldre'l en aplicacions en temps real. Per fer front a aquest problema, es realitzen modificacions en la seva formulació i s'utilitzen tècniques de linealització. A continuació, el càlcul de referència basat en l'optimització linealitzada resultant s'integra amb un control basat en energia pel MMC i s'analitzen

diferents casos pràctics per validar el seu rendiment en comparació amb els enfocaments clàssics.

Finalment, es proposa una metodologia basada en l'optimització per dissenyar els condensadors de submòduls (SM). L'algorisme considera tots els DOF de l'MMC per tal de dimensionar el condensador SM alhora que compleix els requisits del TSO i les limitacions de disseny del convertidor. El mètode suggerit es compara amb els enfocaments clàssics per a diferents punts de funcionament, i s'aprofita encara més tenint en compte les condicions de sots de tensió de la xarxa de CA.

Contents

5 Real-time optimization-based reference calculation integrated control for MMCs 106

List of Figures

List of Tables

Nomenclature

AC	Alternating Current
AAM	Average Arm Model
CCSC	Circulating Current Suppressing Control
CIGRÉ	Conseil International des Grands Réseaux Électriques
CITCEA	Centre d'Innovació Tecnològica en Convertidors Estàtics i Accionaments
C_{SM}	Submodule capacitance
DC	Direct Current
DOF	Degrees of freedom
ENTSO-E	European Network of Transmission System Operators for Electricity
FRT	Fault Ride Through
HVAC	High Voltage Alternating Current
HVDC	High Voltage Direct Current
IGBT	Insulated-Gate Bipolar Transistor
INELFE	Interconexión Eléctrica Francia-España
KCL	Kirchhoff Current Law
KVL	Kirchhoff Voltage Law
LLG	Line-to-Line-to-Ground Fault
LTI	Linear Time Invariant
LTV	Linear Time Variant
MMC	Modular Multilevel Converter
MPC	Model Predictive Control
NLC	Nearest Level Control
OF	Objective Function
OP	Operating Point
OSQP	Operator Splitting Solver for Quadratic Programs
PCC	Point of Common Coupling
PI	Proportional-Integral
PLL	Phase-Locked Loop

RES	Renewable Energy Sources
RMS	Root Mean Square
SLG	Single-Line-to-Ground Fault
SM	Submodule
SQP	Sequential Quadratic Programming
STATCOM	Static Synchronous Compensator
TSO	Transmission System Operator
UPC	Universitat Politècnica de Catalunya
VSC	Voltage Source Converter

Chapter 1

Introduction

1.1 Current context

In the United Nations (UN) Climate Change Conference (COP21) 2015, a global scale agreement to deal with the impacts caused by the climate change has been reached. The so called Paris Agreement was signed by 191 parties plus the European Union (EU) in 2016, and it aims to reduce the greenhouse gas emission to limit the global average temperature increase up to 1.5^oC prior to industrial times by the year 2050 [1]. To cope with the COP21 agreement, the manner in which electricity is generated and transmitted will have an even more important role than it does today. Whereby the energy produced by conventional thermal-power plants (fossil-fuels) should be reduced to minimal levels while the energy generated from renewable energy (RE) resources must be fully exploited, see Fig. 1.1 [2].

Although this transition is of utmost importance, several environmental, economical and technical issues arise. In the engineering perspective, especially for Europe, one of the main challenges is to integrate and transport the renewable energy generated, which is generally more available in remote areas such as offshore or near the sea, to the consumption regions. Thus, not only optimizing the existing grids is needed but also new grid investments are urged. Between the two energy transmission system methods available, High Voltage Alternate Current (HVAC) and High Voltage Direct Current (HVDC), relying on HVAC becomes economically unfeasible in comparison with HVDC for applications that the length AC line cables are greater than 100 km and for overhead transmission when the distances are longer than 400 km, as shown in Fig. 1.2 [3].

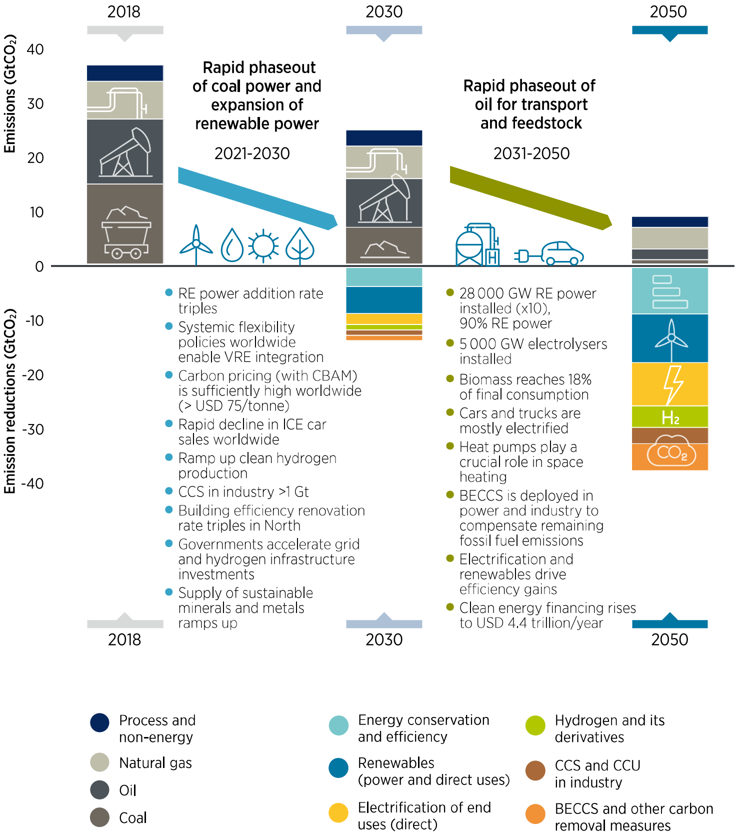

Fig. 1.1: Evolution of emissions with phaseouts of coal and oil, 2021-2050 [2]. Figure courtesy of IRENA.

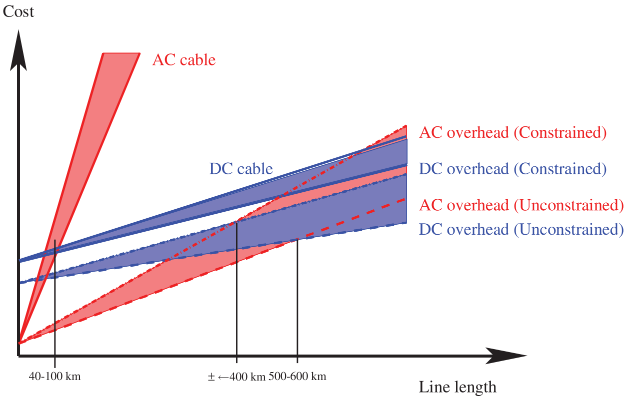

Fig. 1.2: Cost breakdown for AC and DC systems [3, 4].

1.2 HVDC technology

In HVDC transmission systems, the converters can either be Current Source Converter (CSC) or Voltage Source Converter (VSC). Their main characteristics, applications and differences are discussed next.

1.2.1 CSC-HVDC

CSC-HVDC, also known as Line Commutated Converter (LCC-HVDC), is a well-known and mature HVDC technology that was first used in the 1970s in the Gotland HVDC link (Sweden) [5, 6]. Such converters are based on thyristor switches; thus, they can be switched ON through Pulse Width Modulation (PWM), but are dependent on the zero-crossing point of the AC line current to be switched OFF. This type of converter holds the title of the longest HVDC line in the world, being commissioned for the Rio Madeira link (Brazil) in 2013 [7]. It also has high power capability making it well suited for bulky power transmission operations [8]. However, it presents stability issues if connected to weak grids, it is unable to regulate the active and reactive power separately and it can only be operated unidirectionally [9].

1.2.2 VSC-HVDC

In the past decades, the developments in the power electronics semiconductors have allowed the introduction of new technologies with higher current and voltage ratings, such as the Insulated-Gate Bipolar Transistor (IGBT) [10, 11]. IGBTs are self-commutated switches that share the controllability of the Metal-Oxide-Semiconductor Field-Effect Transistor (MOSFET) with similar power ratings of a Bipolar Junction Transistor (BJTs). VSCs are fully controllable converters as they are based on IGBTs. According to the modulation employed, the IGBTs can be turned ON and OFF to generate a synthesized AC waveform of an imposed frequency at the converter's output terminal. In contrast to LCCs, the VSC has reduced risk of commutation failure, blackstart capabilities, improved AC voltage harmonic content and they can regulate active and reactive power independently [12, 13]. The latter characteristics enable the reduction in volume and number of the AC filter reactors required in the converter station, minimizing its footprint [14].

1.2.3 VSC-HVDC projects

The first ever implementation of an experimental VSC-HVDC converter happened in 1997 in Hillesjön, Sweden. The experiment consisted of a two-level VSC 3 MW, ±10 kV overheadline link between Hillesjön and Grängesberg [15]. In 1999, Hitachi Energy commissioned the first commercial project in the island of Gotland, Sweden, where wind energy produced offshore was transmitted to its consumption area [16, 17]. It was a 50 MW, ±80 kV submarine cable line project which introduced the HVDC Light© technology, see Fig. 1.3. The converter employed in this project was based on a two-level VSC, where several IGBTs (switched at 2 kHz) were stacked in series to withstand the high blocking voltage levels.

Fig. 1.3: HVDC Light© station in Gotland: Photo courtesy of Hitachi Energy and Gunnar Britse [18].

In the year 2000, Hitachi Energy commissioned another VSC-HVDC project with higher power and voltage ratings. The Eagle Pass project is a 36 MW, 132 kV (AC), ±15.9 kV (DC) Back-to-Back link connecting the cities of Eagle Pass (USA) and Piedras Negras (Mexico), see Fig. 1.4 [19]. In order to achieve higher values and improved performance, a three-level Neutral Point Clamped (NPC) converter was used [20]. Although the previous two- and three-level technologies were successfully implemented, they present limited power and voltage levels and complex modulation (as all the IGBTs within each branch must be switched at the exact same time).

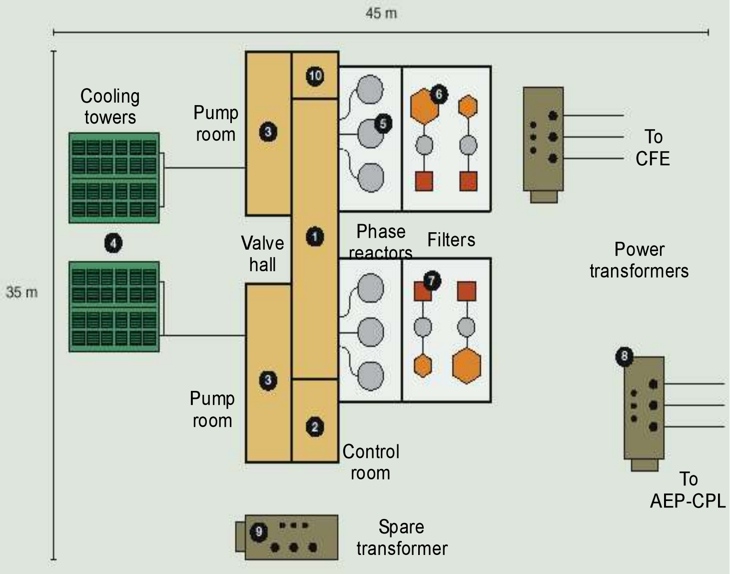

Fig. 1.4: Eagle Pass project layout: Photo courtesy of Hitachi Energy [20].

1.3 The Modular Multilevel Converter

The technological breakthrough that allowed VSCs to overcome the aforementioned drawbacks and to become the current preferred choice for HVDC applications happened in 2001 with the introduction of the modular multilevel converter (MMC) by Prof. Marquardt [21, 22]. Compared to classic two- and three-level converters the has improved efficiency, easier scalability to high voltage levels and inherent redundancy [22, 23]. The first project employing the MMC in an HVDC application was commissioned in 2010 by Siemens in the Trans Bay project, see Fig. 1.5. The 400 MW, ±200 kV (DC), 235 kV (AC) cable project interconnects the cities of San Francisco and Pittsburg.

Since then, important advances have been achieved to reduce the MMC's losses while raising its power and voltage capabilities. As shown in Fig. 1.6, the current generation of MMC converters are already as efficient as the classical HVDC converter technology.

As VSC-HVDC becomes more attractive, there is a higher trend in installing MMC-HVDC stations in comparison to other topologies [22, 23]. As it can be noted from Fig. 1.7, up to the year of 2017, the trend was more favourable for projects based on classical LCC-HVDC converters. However, at 2017, MMC-HVDC installations achieved the break-even

Fig. 1.5: Converter hall for Trans Bay link. Photo courtesy of NextEra Energy, Inc.

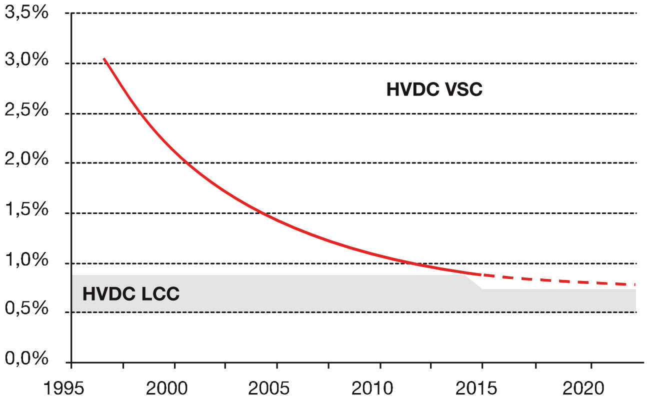

Fig. 1.6: Losses comparison between VSC- and LCC-HVDC [24].

point[1]. Finally, more than 80% of the projects planned for the following years from Hitachi Energy and Siemens will employ the MMC-HVDC converter [6, 8, 25, 26].

Currently in Europe, there are ten offshore wind power plants (OWPP-HVDC) connections using MMCs, whereas the largest ones from Hitachi Energy are DolWin1 (800 MW) [27] and DolWin2 (900 MW) [28] and from Siemens are SylWin1 (900 MW) [29] and BorWin3 (864 MW) [30].

---

[1] Note that after only 20 years since the first ever VSC-HVDC project have been commissioned, the trend of such technology already surpassed the classical LCC-HVDC converter (which was already 50 years in the market).

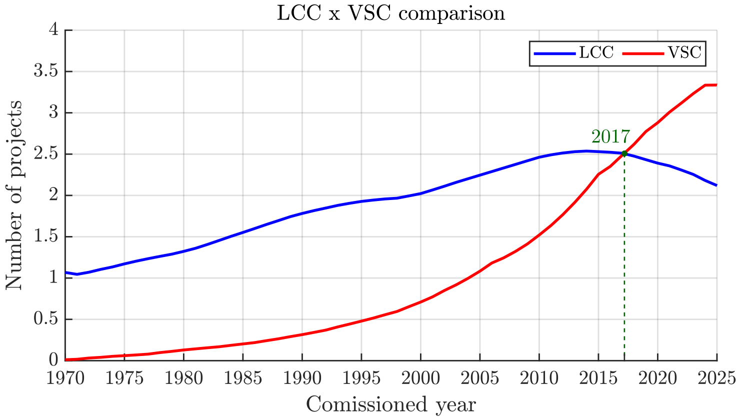

Fig. 1.7: Projects trend comparison between VSC- and LCC-HVDC [6, 8, 25, 26].

Onshore, the commissioned project with highest power capability is the one that interconnects France and Spain, named Interconexión Eléctrica Francia-España or Electricity Interconnection France-Spain (INELFE), as shown in Fig. 1.8. The interconnection consists of two 1000 MW converters, transferring energy through a ±320 kV link. In Fig. 1.9, the converter hall from the station is Spain is shown and the SM structure is highlighted.

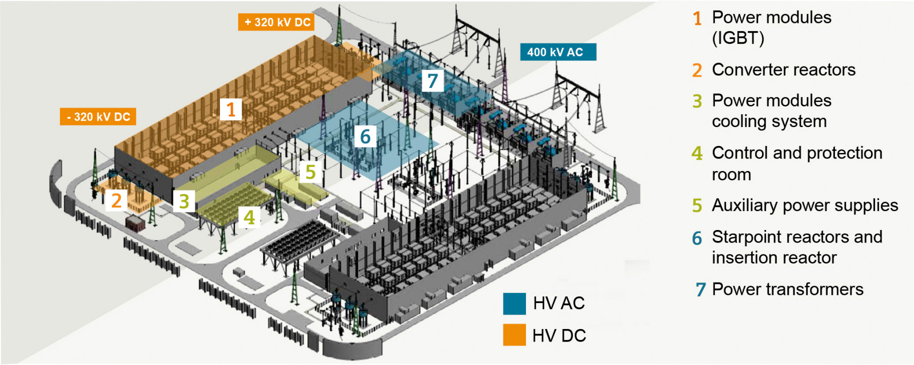

Fig. 1.8: Converter station layout. Courtesy of Siemens and [31].

1.3.1 Topology description

As one of the main components of an HVDC transmission system [4], the MMC is responsible for converting AC energy into DC or vice-verse. The overall scheme of the three-phase MMC is shown in Fig. 1.10. It consists

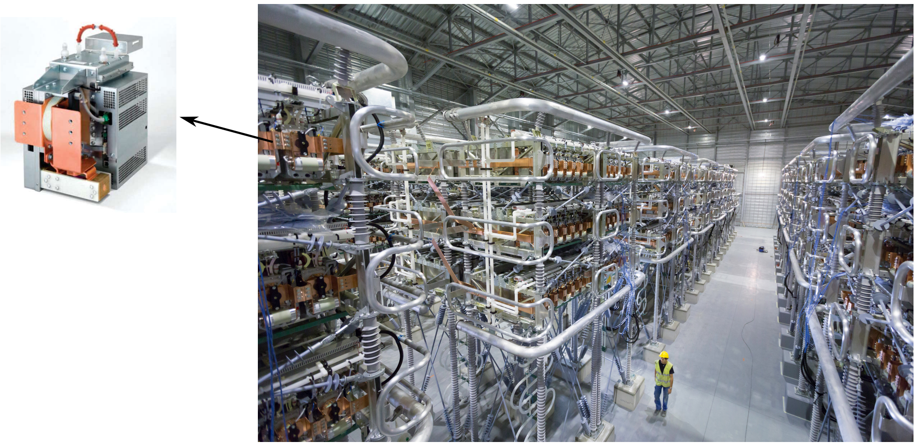

Fig. 1.9: Converter hall and half-bridge SM. Photo courtesy of Siemens and [31].

of three phase-legs, one per phase, and each of them has two stacks of N_a submodules (SMs) ($N_a + 1$ levels), known as the upper and lower arms [22]. Unlikely its predecessors that have several IGBTs connected in series in each arm, the MMCs are based on numerous series connected SMs which might be half-bridge, full-bridge or more complex structures depending on the application. Half-bridge SMs are the preferred choice, due to its robustness, when properly regulated can maintain the converter operating under AC network faults, volume and costs. However, under DC link fault scenarios, these SMs must be blocked as they are unable to synthesize negative voltages. In order to maintain the full controllability of the MMC during such conditions, full-bridge SMs should be employed [32].

1.3.2 Working principle

The energy conversion performed by the MMC is achieved by inserting or bypassing its SM capacitors in a controlled fashion. In Figs. 1.11 and 1.12, the three possible states for a half-bridge SM are displayed[2]. When the upper switch S_1 is turned ON and the lower switch S_2 is OFF (see Figs. 1.11a and 1.12a), the capacitor can either be charging (the current is entering the SM through the mid-point connection) or discharging (current is leaving the SM through the mid-point). To bypass the SM capacitor, S_1 is turned OFF while S_2 is turned ON (Figs. 1.11b and

---

[2] Note that a fourth state is possible. However, such state is not used as it would result in the SM capacitor to be short-circuited.

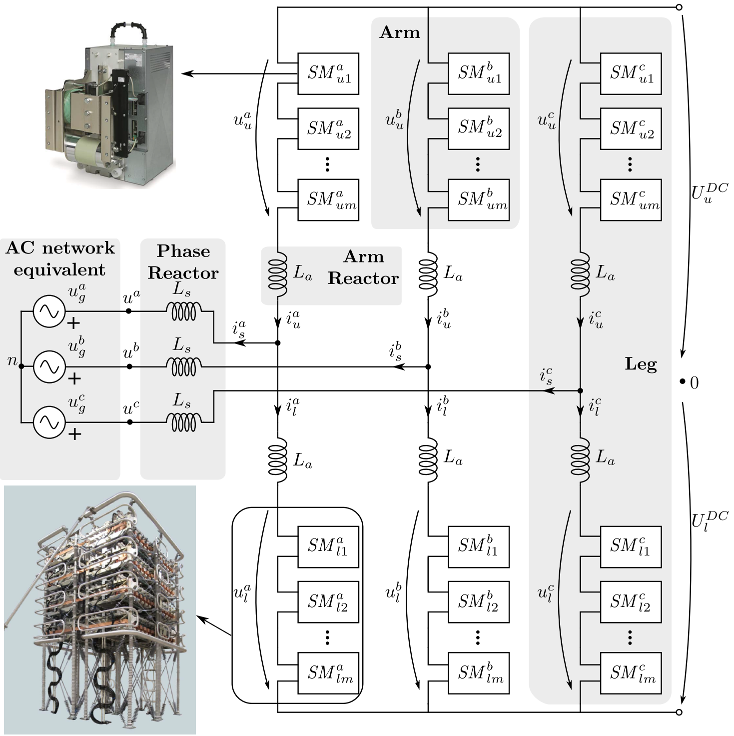

Fig. 1.10: Overall scheme of a three-phase MMC. The photos on the scheme are courtesy of Siemens.

1.12b). During this state the SM capacitor voltage remains constant with same value as its previous state. Under faulted conditions, the switches might be operated differently. During a DC link fault and still assuming half-bridge SM structure, for instance, both switches are blocked, as shown in Figs. 1.11c and 1.12c. Thus, the faulted current coming from the AC side of the converter will flow through the anti-parallel diodes (MMC operation is similar to a diode rectifier) until the DC protection is activated, clearing the fault. If full-bridge SMs are used, the MMC might be able to keep operational as these SMs can synthesize negative voltages providing fault ride through (FRT) capabilities.

As the SM capacitors in each arm are bypassed or inserted, DC voltage steps can be created which enables the converter to synthesize an AC voltage waveform in its AC side[3]. In Fig. 1.13, a simplified scheme

---

[3] The level of the DC voltage steps depends on the number of SMs installed in each arm. As an example, let's consider that the total DC voltage link is equal to 640 kV and that each arm has 400 SMs. Therefore, the voltage steps would be equal to 640/400 = 1.6 kV.

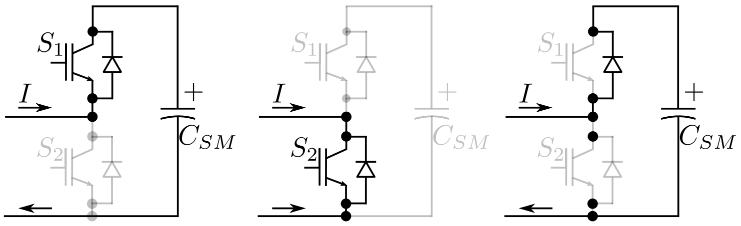

(a) S_1 ON, S_2 OFF (b) S_1 OFF, S_2 ON (c) S_1 OFF, S_2 OFF

Fig. 1.11: SM states considering positive current. Inserted, bypassed and blocked, respectively.

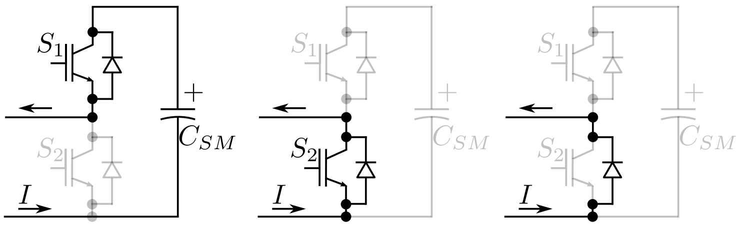

(a) S_1 ON, S_2 OFF (b) S_1 OFF, S_2 ON (c) S_1 OFF, S_2 OFF

Fig. 1.12: SM states considering negative current. Inserted, bypassed and blocked, respectively.

demonstrating how the converter generates AC voltages in its output terminals is depicted. It is assumed that at $t = 0$ s, all the SMs in the upper arm are inserted whereas the lower ones are bypassed. Consequently, the upper and lower arm voltages at this time instant are equal to the total DC link voltage and zero, respectively. Since the upper SMs start to be bypassed and the lower ones start to be inserted, the voltage in the upper arm decreases meanwhile the lower arm's voltage increases. Finally, the voltage at the AC output of the converter is equal to relation between the upper and lower arm voltages, $u_g = \frac{-u_u+u_l}{2}$.

Based on the aforementioned, it becomes clear why the MMC is an attractive option for current HVDC projects and its advantages in comparison to two- and three-level converters. The voltage ratings of the MMC can be easily scaled up or down based on the amount of SM installed in each arm. The SMs can be controlled independently, reducing the failure risk and eliminating the necessity of complex high-frequency modulations[4]. However, such benefits come with the cost of requiring more complex control strategies to maintain the SM capacitor energies balanced.

---

[4] Generally the SMs in the MMC are switched at 150 to 250 Hz, reducing the switching losses of the converter.

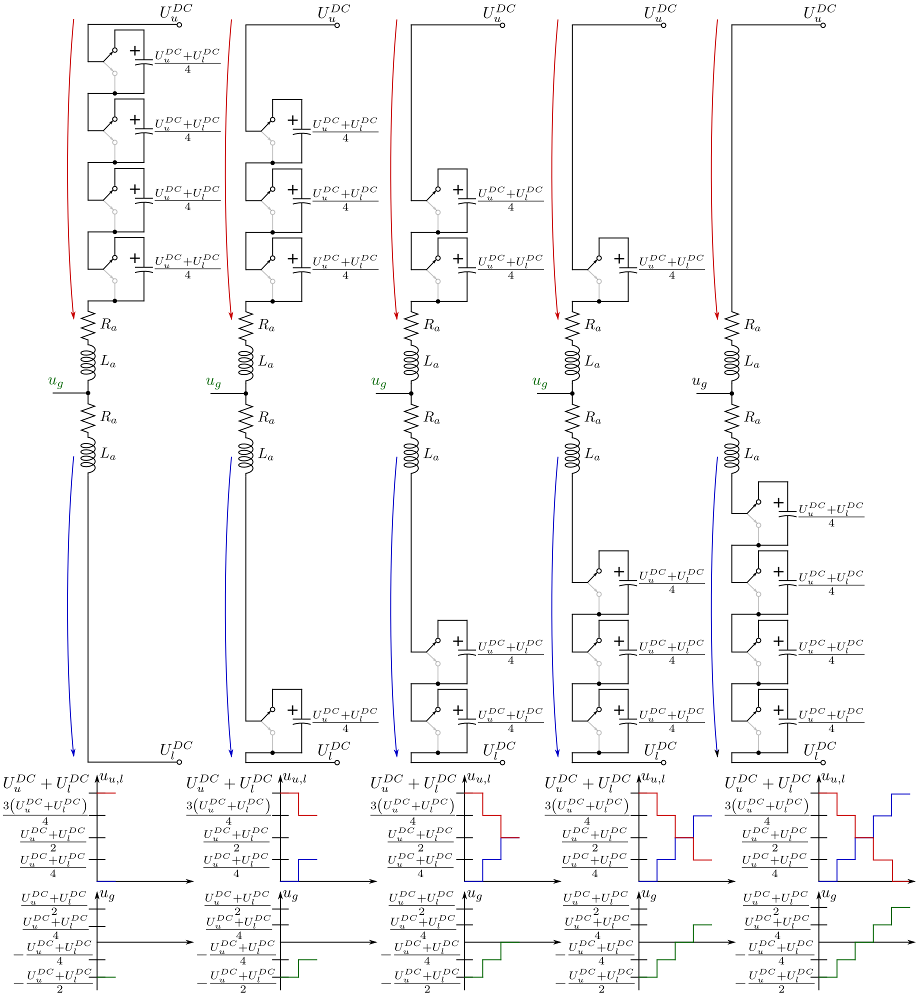

Fig. 1.13: Illustrative representation of the MMC's operation considering four SMs in each arm (five-levels).

1.4 Objective and scope

The focus of this work is on the operation, control and design of HVDC-MMCs assuming balanced and unbalanced operating conditions (e.g. AC/DC network faults, internal faults, etc.). Although there are several previous works available in the literature dealing with these topics, the existing research might not fully exploited all the degrees of freedom of the converter. Consequently, the operation and components' design of the MMC have not achieved their optimal state yet. The main research question that this thesis focuses on provide potential solutions for is:

How can we fully exploit the DOFs of the MMC to provide the best grid support under faulted scenarios while considering the converter's limitations?

Directly addressing such a very broad question can be quite challenging, as it requires an in-depth knowledge about the operation and control of the MMC. Firstly, it is necessary to identify all the DOFs of the converter and understand their roles in its operation. Then, it is needed to analyze if the DOFs' values obtained through steady-state models are optimal, providing the best grid support and within design limits. Finally, to adequate the MMC's control strategy to meet those goals either in normal or faulted scenarios, and not only under steady-state conditions but also during transients. Different studies were conducted seeking answers to the previous points, and they have been organized as presented in Fig. 1.14.

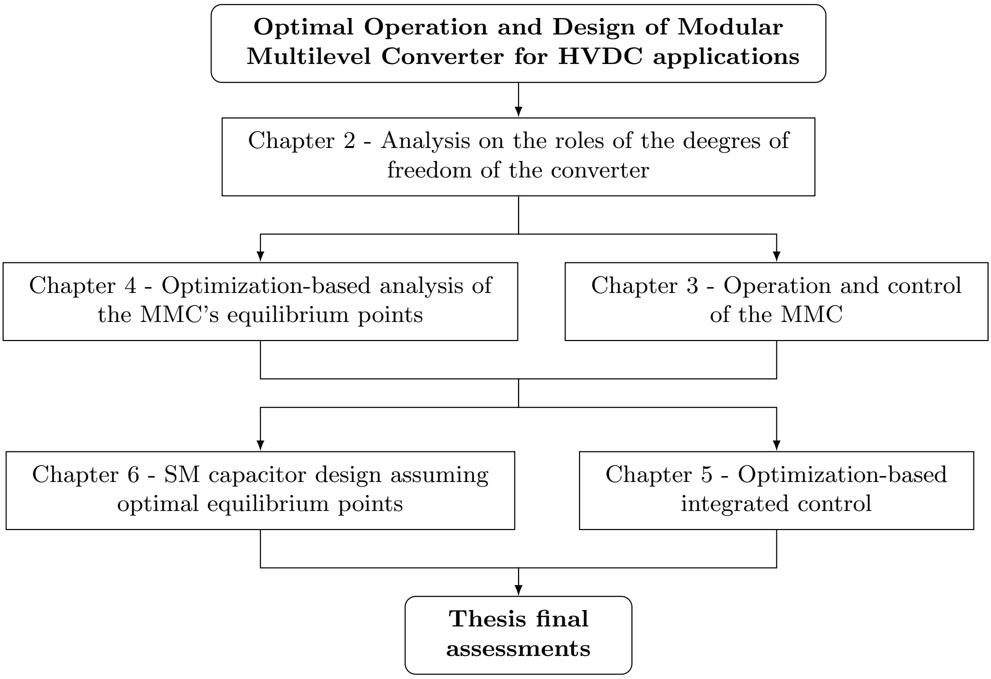

Fig. 1.14: Thesis organization layout.

Based on this figure, the objectives and scopes of the thesis are described next:

- **Analyze the degrees of freedom of the modular multilevel converter and their potential interactions to achieve in-**

ternal power balancing. An in-depth analysis of the degrees of freedom of the converter is performed. Firstly, the overall voltage equations of the MMC are displayed and pertinent transformations are employed to obtain the additive and differential models which ease the understanding of the MMC and to decouple its DC/AC sides. Based on the additive and differential voltage and current quantities, the vertical (between the upper and lower arms) and horizontal (among phase-legs) power transfer equations are derived where potential interactions between the differential and additive quantities are observed and discussed by means of simulation results.

- **Reference calculation method for an MMC's energy-based control to operate under AC and internal voltage sag conditions where their positive- and negative-sequence components are equal.** Based on the DOFs analysis performed in the previous chapter, a reference calculation technique which fully exploit all the MMC's DOFs to obtain the the AC circulating currents of the converter is proposed. The approach is an improvement of the work presented in [33]. In addition, another type of singular condition fault is identified, which occurs within the internal applied voltages of the converter. In order to validate the reference calculation proposal and compare it with previous methods, simulation results of a switched model of the converter are presented considering several different types of faults.

- **Design of an optimization algorithm to calculate the converter's currents during balanced and unbalanced conditions considering the TSO requirements and converter limitations.** The previous reference calculation exploited the DOFs based on additive and differential quantities. Although quantities in this reference frame provide an easy understanding of the MMC's power transfer principle, in scenarios where the converter needs to saturate, doing so in such reference frame can be challenging. As a potential solution to this problem, an optimization-based reference calculation algorithm is proposed to obtain the per-arm voltages and currents magnitudes of the converter during normal and fault operations in the *abc* reference frame. Under fault conditions, the converter must prioritize its quantities to meet the TSO requirements in the form of active and reactive power injected/absorbed per phase during the AC network voltage sags, for instance. Still, the methodology must ensure that the design limits of converter are respected, such as SM capacitor voltages, AC grid and arm currents and arm applied voltages(to avoid overmodulation and respect the SM structure employed). The proposed methodology is validated through simulation results comparing the results obtained from the optimization algorithm with an average model of the converter for different types of AC network faults and internal faults (SM failures).

- **Integration of the optimization-based reference calculation within an energy-based MMC control.** The former optimization algorithm is enhanced to consider the vertical and horizontal power sharing in its formulation and for its AC network current references to be based on the positive- and negative-sequence frame. The resultant optimization problem, however, is highly nonlinear requiring high computation burden to be solved in real-time. To cope with this issue, a linearization technique is applied to represent the nonlinear dynamics of the system as constant parameters, while a Linear Time-Invariant (LTI) system is used to formulate the optimization constraints. The linearized-optimization problem is integrated with the MMC controllers, evaluated under different AC and DC network conditions and compared with conventional control strategies.

- **Design the SM capacitors considering different operating conditions.** The final step of the present work is to modify the previous optimization algorithm (considering the internal power balancing) to design the SM capacitors. By doing so, the proposed sizing method is capable of minimizing the SM capacitor size while providing the optimal voltage and current values of the MMC for any operating point. The presented methodology is compared with classical and more recent approaches assuming normal network voltage conditions and different active/reactive power setpoints. Furthermore, the designing analysis is extended for different AC network fault conditions to ensure that the SM capacitor selected can meet with the TSO's requirements.

1.5 Thesis outline

In this section, the contents of each chapter of this thesis are detailed:

- **Chapter 2** introduces the overall MMC's structure, mathematical model which is used throughout the thesis, as well as an in-depth discussion on the roles that the converter's degrees of freedom play in its internal power balancing.

- **Chapter 3** presents an AC circulating current reference calculation that further exploits the converter's degrees of freedom to maintain the MMC's operation under AC network or internal voltage conditions whereby their positive- and negative-sequence components are equal.

- **Chapter 4** addresses an optimization-based reference calculation method for MMC's operating in normal and constrained situations (when the converter needs to prioritize its quantities as it has reached voltage or current limitations, e.g. during system faults).

- **Chapter 5** Improves the previous optimization-algorithm by considering the vertical and horizontal power transfer equations in its formulation. Furthermore, the computational burden of the methodology is reduced by linearizing its constraints. Finally, the linearized optimization is integrated with a control structure for the MMC operating under normal and constrained situations (where it has reached current and/or voltage limitations, as it may occur during system faults).

- **Chapter 6** proposes an optimization-based methodology to minimize the SM capacitor value of the MMC. The analysis is performed considering both the converter's current and voltage limitations and the TSO's FRT requirements.

- **Appendix A** lists the author's publications during the thesis, both related and non-related to the topics presented.

1.6 Works and activities performed during the thesis

The work and the pertinent activities performed by the author throughout the duration of this thesis are described in this section.

In the beginning of 2019, the author has moved from Cornélio Procópio, Paraná, Brazil to Barcelona, Spain, to start his doctoral activities related to the InnoDC project. In this context, the author has been hosted by an industrial partner, the company Cinergia Power Solutions and by the Universitat Politècnica de Catalunya (UPC) as the academic partner.

At the moment of the author's arrival, he was also engaged in other research projects related to DC-DC converters for photovoltaic applications. This was a cooperation between the *Grupo de Electrónica Aplicada (GEA)* from the *Universidad Nacional de Río Cuarto (UNRC*, Argentina and the *Laboratório de Eletrônica de Potência, Qualidade de Energia e Energias Renováveis (LEPQER)* from the *Universidade Tecnológica Federal do Paraná-CP (UTFPR-CP)*, Brazil. In order to finish these previous activities, during the weekends, the author was working on the DC-DC converter research, while during the week days his focus was to become familiarized with the working principle, mathematical and simulation models of the Modular Multilevel Converter. As a result of this combined work, the author was able to publish two papers, being one journal not included in the thesis [J4] and his first conference paper related to the activities regarding the InnoDC project [C1].

Based on the knowledge acquired from the previous conference paper, which introduced a phasor notation steady-state model of the MMC for balanced and unbalanced AC network conditions, two new topics started to be studied. The first one regarded the SM capacitor voltage ripple, which was published in a conference in October 2019 [C2], while the second one used the SM capacitor ripple as part of the formulation of an optimization algorithm to calculate the current references of the converter was proposed. This work was formulated to obtain the voltage and current references of the converter to meet the TSO's requirements while keeping the MMC's quantities within their design limitation during normal and fault scenarios. This resulted in the author's second journal paper [J1], the first one related to the project.

By the beginning of 2020, the author started studying in-depth the degrees of freedom of the converter, especially, their roles on the internal power balancing. However, by March of the same year, the COVID pandemic started in Spain and the activities had to be performed from home. Nevertheless, his analysis on the degrees of freedom provided better insights that allowed previous AC circulating current reference calculation approaches to be improved while the AC circulating current control was enhanced by adding another control loop in charge of regulating one degree of freedom that was missing in previous methods. This work was developed during his first secondment which was hosted by CITCEA-UPC and it generated two journal papers, one already published [J2] and another one that is currently under revision [S-J6]. In August of 2020, the author started collaborating with Imperial College and this work allowed the previous optimization algorithm to be improved and its computational burden to be reduced to be solved in real-time and integrated with an energy-based control for MMCs. As a consequence of this joint work, a journal paper was published [J3].

In the first semester of 2021, still under pandemic situation, the author was a lecturer in two undergraduate courses from UPC in the areas of micro grids and self-consumption systems. In May of the same year, the author remotely presented his [J1] paper in PowerTech Madrid. Still during the first semester, the author was able to start a collaboration between the CITCEA-UPC and the Key Laboratory of Smart Grid of Ministry of Education from the Tianjin University, China. As preliminary results of this ongoing collaboration, a journal paper proposing a new DC circuit breaker with DC fault current limiter integrated [J5] was published (which is not part of the thesis). On the second semester of 2021, the author was one of the lab lecturers for the Electrotechnics undergraduate course at UPC. In the meantime, the author has published his third conference paper in which the optimization algorithm was further enhanced to better comply with the TSO's regulations [C3]. Finally, the last work developed during the thesis in the submitted journal paper [S-J7], in which proposed an optimization-based methodology to improve the design of the submodule capacitor sizing.

Unfortunately, due to the several waves that the COVID pandemic had, the author's second placement which was supposed to take place in the *Laboratoire d' Electrotechnique et d' Electronique de Puissance (L2EP)* from *Université de Lille*, France, had to be performed remotely. However, the author has been working remotely with the colleagues from Lille, specially with the great support of Dr. Mohamed Moez Belhaouane and Prof. Xavier Guillaud, to validate one of the works developed in the thesis through experimental results. Furthermore, the author intends to go and to perform his duties with the L2EP group properly after the end of the PhD activities.

Chapter 2

Degrees of freedom of the Modular Multilevel Converter

This chapter is a revised version of the following work:
[**S-J6**] D. Westerman Spier, E. Prieto-Araujo, J. López-Mestre, H. Mehrjerdi and O. Gomis-Bellmunt, "On the roles and interactions of the MMC degrees of freedom in the internal energy balancing for three-wire three-phase connections", under review *IEEE Transactions on Power Delivery*

2.1 Introduction

Conventionally, the MMC's DOFs are described based on additive x_{sum} and differential x_{diff} quantities, allowing the DC- and AC-side related components of the converter to be conveniently analyzed separately [34–38]. Such quantities can be referenced in either abc, $\alpha\beta 0$ and $dq0$ reference frames, according to the control strategy employed. Still, the MMC's modelling must exploit all the differential and additive applied voltage DOFs, and the currents generated by those components, not only to ensure proper energy transfer between the AC/DC networks, but also to maintain the total energy stored in the SM capacitors balanced and within design limitations, during both normal and faulted operations [39]. The distribution of the internal energy of the converter can be performed in two manners. 1) Horizontally; whereby the DOFs enable the power-flow among the different phase-legs of the converter. 2) Vertically; energy is exchanged between the upper and lower arms in the same phase-leg.

Relevant previous works have been conducted addressing the roles of the different voltages that can be applied into the arms of the converter in order to achieve internal energy balance [33,37,40–42]. Regarding the horizontal balancing, several authors focus only in the DOFs regarding the DC additive voltage components in their formulation. The main difference among their methods relies on the reference frame chosen, abc [37,40] and $\alpha\beta 0$ [33]. Besides using the previous DOFs, authors in [41] improved the horizontal power balancing by employing the DOF related to the AC zero-sequence differential voltage. Further improvements in the operation of the MMC can be achieved by also enabling the DOFs to perform vertical energy balancing [42]. This can be done by analyzing each phase-leg of the converter or by studying each arm unit individually.

While the former cannot specify the DOFs used for the horizontal and vertical balance separately, the latter allows such feature. References [38, 43–45] analyze the energies in a phase-leg perspective, with the AC differential and DC additive voltage DOFs altogether. The main distinction among their approaches is that [38, 43] consider the DOFs' positive- and negative-sequence components intrinsically (as they analyze the converter in the natural *abc* reference frame) and [44, 45] only assume the positive-sequence components of the DOFs. By evaluating the arm units separately, the roles of the different DOFs can be better understood and the internal energy management can be enhanced. Authors in [33,46] perform the internal energy balancing analysis in the $\alpha\beta0$ reference frame. While [33] only assumes the DC additive DOF for the horizontal balance, [46] demonstrates that the AC differential positive and negative-sequence can be used in both vertical and horizontal power balances. The aforementioned methods did not consider the usage of the differential zero-sequence DOF to enhance the energy balancing. In [47], the horizontal balancing is similar than [33], whereas the converter operation is enhanced through the usage of the DC differential DOF along with the AC positive- and negative-sequence components of the additive voltage ones.

Although the previous works have presented different strategies of how to use the additive and differential DOFs in the internal energy balancing of the MMC, to the best of the authors, there are still DOFs that have not been considered yet. In addition, there are also interactions between the additive and differential DOFs that can lead to enhancements in the internal power sharing of the converter, which have not been analyzed up to date. The objective of this chapter is to demonstrate and analyze the working principle of the different DOFs of the MMC and the roles they play in order to achieve power transferring between the arm units and phase-legs of the converter. The main contributions of the chapter can be summarized as:

- Comprehensive individual analysis of all DOFs in the MMC.
- Extensive examination and derivation of the horizontal and vertical power balancing equations.

- Validation of the theoretical power transfer equations by means of simulation results.

2.2 MMC quantities description and modelling

The three-phase MMC complete circuit model is shown in Fig. 2.1. For analysis purposes, the phasorial notation $\underline{X}^k = X_r^k + jX_i^k = X^k\underline{/\theta^k}$ will be adopted, with $x(t) = X^k\mathrm{Re}(e^{j(\omega t+\theta^k)})$ and $k \in (a, b, c)$. The main quantities for each phase are: the AC grid voltages and currents $\underline{U}_g^k$, $\underline{I}_s^k$; the upper and lower arms' AC voltages and currents $\underline{U}_{u,l}^k$, $\underline{I}_{u,l}^k$; the upper and lower arms' DC voltages and currents $\underline{U}_{u,l}^{kDC}$, $\underline{I}_{u,l}^{kDC}$; the voltage between the neutral n point of the AC three-phase system and the 0 DC reference node $\underline{U}_{0n}$; the arm impedances R_a and L_a; and the grid equivalent resistance and inductance R_s and L_s. The voltage equations per phase can be written as

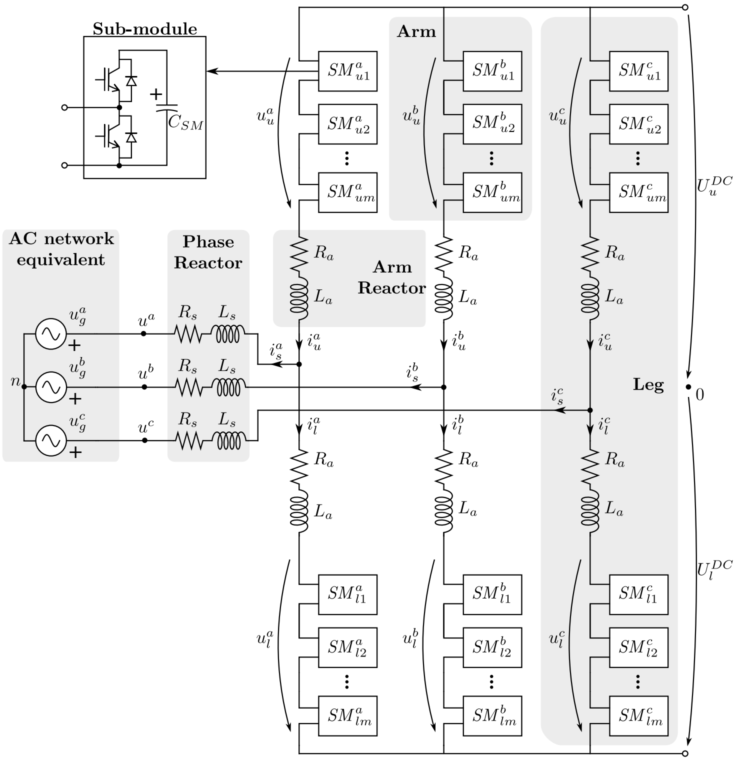

Fig. 2.1: Complete model of the MMC converter.

$$U_u^{DC} - \underline{U}_u^k - \underline{U}_g^k - \underline{U}_{0n} = R_a\underline{I}_u^k + L_a\frac{d\underline{I}_u^k}{dt} + R_s\underline{I}_s^k + L_s\frac{d\underline{I}_s^k}{dt} \tag{2.1}$$

$$-U_l^{DC} + \underline{U}_l^k - \underline{U}_g^k - \underline{U}_{0n} = -R_a\underline{I}_l^k - L_a\frac{d\underline{I}_l^k}{dt} + R_s\underline{I}_s^k + L_s\frac{d\underline{I}_s^k}{dt} \tag{2.2}$$

Before proceeding with the analysis, the following quantities and parameters are defined

$$\begin{cases} \underline{U}_{diff}^k \triangleq \frac{1}{2}(-\underline{U}_u^k + \underline{U}_l^k) \\ \underline{U}_{sum}^k \triangleq \underline{U}_u^k + \underline{U}_l^k \\ \underline{I}_s^k \triangleq \underline{I}_u^k - \underline{I}_l^k \\ \underline{I}_{sum}^k \triangleq \frac{1}{2}(\underline{I}_u^k + \underline{I}_l^k) \\ R_{eq} \triangleq R_s + \frac{R_a}{2} \\ L_{eq} \triangleq L_s + \frac{L_a}{2} \end{cases} \quad \begin{cases} \underline{U}_u^k = -\underline{U}_{diff}^k + \frac{1}{2}\underline{U}_{sum}^k \\ \underline{U}_l^k = \underline{U}_{diff}^k + \frac{1}{2}\underline{U}_{sum}^k \\ \underline{I}_u^k = \frac{1}{2}\underline{I}_s^k + \underline{I}_{sum}^k \\ \underline{I}_l^k = -\frac{1}{2}\underline{I}_s^k + \underline{I}_{sum}^k \end{cases} \tag{2.3}$$

with $k \in (a, b, c)$ and $\underline{U}_{diff}^k$, $\underline{U}_{sum}^k$ and $\underline{I}_{sum}^k$ as the differential and additive applied voltages and circulating currents of the converter, respectively. Adding and subtracting (2.1) and (2.2) while employing the transformation in (2.3) leads to

$$\frac{1}{2}(U_u^{DC} - U_l^{DC}) + \underline{U}_{diff}^k - \underline{U}_g^k - \underline{U}_{0n} = R_{eq}\underline{I}_s^k + L_{eq}\frac{d\underline{I}_s^k}{dt} \tag{2.4}$$

$$\underline{U}_{sum}^k - \underbrace{\left(U_u^{DC} + U_l^{DC}\right)}_{\triangleq U_t^{DC}} = -2R_a\underline{I}_{sum}^k - 2L_a\frac{d\underline{I}_{sum}^k}{dt} \tag{2.5}$$

2.3 Steady-State analysis

The steady-state analysis of the MMC is performed considering that the converter is connected to a generic AC and DC networks, which might be balanced or unbalanced [39]. The MMC arm quantities contain both AC and DC components that can be decoupled by applying superposition principle.

2.3.1 AC analysis

For the AC analysis, the voltage terms U_u^{DC} and U_l^{DC} from (2.4) and (2.5) are considered purely DC. Thus, the AC terms of the former equations can be written as

$$\underline{U}_{diff}^{k} - \underline{U}_{g}^{k} - \underline{U}_{0n} = \underline{Z}_{eq}\underline{I}_{s}^{k} \tag{2.6}$$

$$\underline{U}_{sum}^{k} = -2\underline{Z}_{a}\underline{I}_{sum}^{k} \tag{2.7}$$

where $\underline{Z}_{eq} = R_{eq} + j\omega L_{eq}$ and $\underline{Z}_{a} = R_{a} + j\omega L_{a}$. By applying Fortescue transformation (see (2.8)) to the former equations, the positive-, negative- and zero-sequence components of the differential and additive components of the converter can be analyzed individually as

$$\underline{\Theta}^{+-0} \triangleq \mathbf{F} \cdot \underline{\Theta}^{abc} = \frac{1}{3}\begin{bmatrix} 1 & \underline{p}^{2} & \underline{p} \\ 1 & \underline{p} & \underline{p}^{2} \\ 1 & 1 & 1 \end{bmatrix} \cdot \underline{\Theta}^{abc} \tag{2.8}$$

with $\underline{p} = e^{j\frac{-2\pi}{3}}$.

$$\underline{U}_{diff}^{+-0} - \underline{U}_{g}^{+-0} - \underline{U}_{0n}^{0} = \underline{Z}_{eq}\underline{I}_{s}^{+-0} \tag{2.9a}$$

$$\underline{I}_{s}^{+-0} = \underline{Z}_{eq}^{-1}\left(\underline{U}_{diff}^{+-0} - \underline{U}_{g}^{+-0} - \underline{U}_{0n}^{0}\right) \tag{2.9b}$$

Note that the zero-sequence of the grid current $\underline{I}_{s}^{0}$ is strictly zero due to the three-wire connection in the AC system. Thus, $\underline{U}_{g}^{0AC}$, $\underline{U}_{diff}^{0AC}$ and $\underline{U}_{0n}^{0AC}$ will not affect the power transfer to the grid. So, (2.9b) can be simplified as

$$\underline{I}_{s}^{+-} = \frac{1}{\underline{Z}_{eq}}\left(\underline{U}_{diff}^{+-} - \underline{U}_{g}^{+-}\right) \tag{2.10}$$

Therefore, only the positive- and negative- current components are responsible for the power sharing between the MMC and the AC grid. Although there is no zero-sequence current component, zero-sequence differential voltage can still be applied in the converter. As it will be discussed in Sections 2.4 and 2.5, this DOF can affect the internal power balance of the converter. The AC zero-sequence differential DOF can be mathematically described as

$$\underline{U}_{0n}^{0AC} = \underline{U}_{diff}^{0AC} - \underline{U}_{g}^{0AC} \tag{2.11}$$

note that, unlike the positive- and negative-sequence differential components, this DOF cannot be correlated with the AC network currents. To obtain this DOF, authors in [48] calculated it based on the maximum and minimum SM capacitor voltage levels, whereas [49] used an optimization-based calculation approach. Similarly to the procedures developed for the differential terms, (2.7) can be rewritten in terms of the symmetric components, leading to

$$\underline{I}_{sum}^{+-0} = \frac{1}{-2\underline{Z}_a}\underline{U}_{sum}^{+-0} \tag{2.12}$$

the roles of these components in the internal power transfer will be analyzed in details Section 2.4. Still, it is important to highlight that the zero-sequence component $\underline{I}_{sum}^{0AC}$ should be set to zero to avoid AC distortion in the DC network [39].

2.3.2 DC analysis

For the DC part of the MMC, the derivative terms in (2.4) and (2.5) are firstly set to zero. Then, an analogous analysis to the AC circuit can be performed. For the DC analysis, it is also interesting to separate the zero sequence current components from the remaining ones. This can be done employing Clarke transformation (see 2.13); thus, the DC steady-state forms of (2.4) are

$$\Theta^{\alpha\beta 0} \triangleq \mathbf{C} \cdot \Theta^{abc} = \frac{1}{3}\begin{bmatrix} 2 & -1 & -1 \\ 0 & -\sqrt{3} & \sqrt{3} \\ 1 & 1 & 1 \end{bmatrix} \cdot \Theta^{abc} \tag{2.13}$$

$$I_s^{\alpha\beta} = \frac{1}{R_{eq}} U_{diff}^{\alpha\beta} \tag{2.14a}$$

$$U_{0n}^{0DC} = U_{diff}^{0DC} - U_g^{0DC} \tag{2.14b}$$

As no zero-sequence current component is flowing through the AC network, the DC zero-sequence differential voltage cannot be calculated based on the current it generates. An attempt to calculate such DOF is presented in [47], where U_{diff}^{0DC} is correlated to the vertical power transfer of the converter and its circulating currents. The usage of this DOF in the internal power balancing is discussed in Section 2.4. Whereas the DC current component of the AC grid $I_s^{\alpha\beta}$ must be kept equal to zero in order to avoid DC currents circulating into AC transformer windings, leading to potential core saturation. Finally, the DC form of additive currents (2.5) can be described as

$$I_{sum}^{\alpha\beta} = -\frac{1}{2R_a} U_{sum}^{\alpha\beta} \tag{2.15}$$

and

$$I^0_{sum} = \frac{1}{2R_a}\left(U^{DC}_u + U^{DC}_l - U^0_{sum}\right) \tag{2.16}$$

The zero-sequence of the additive current is used to exchange power between the converter and the DC grid. While $I^{\alpha\beta}_{sum}$ can be defined as the DC components of the circulating currents.

2.4 Roles of the DOFs in the power transfer

This section presents an in-depth analysis and mathematical descriptions of the power transfers of the MMC. The main goal is to indicate which DOFs are used in the power distribution among the phase-legs and upper and lower arms of the converter. Firstly, the overall MMC scheme with all the additive and differential DOFs is presented. Later, the time-domain expressions for the applied voltage, AC network and circulating current components are mathematically defined. Based on these quantities, the analytical expression for the power transfer between the AC and DC sides of the converter is obtained. Following, the horizontal and vertical power equations are analyzed and potential interactions between the differential and additive quantities are identified.

2.4.1 Description of the DOFs

In Fig. 2.2, the voltages that can be applied into each arm of the converter are expanded to be represented as their respective AC and DC additive and differential DOFs. These voltages will lead to current circulation, which will play distinct roles in the power sharing of the converter. In total, the converter has 12 DOFs being 6 DC and 6 AC ones, in which only the AC and DC zero-sequence component of the differential voltage do not generate current flow. The AC and DC DOFs of the MMC can be obtained through the superposition principle [50], whereas it is assumed that the converter's arm applied voltages are equal to the summation the DOFs obtained in each equivalent circuit (DC and AC specifically).

As it can be noted from Fig. 2.2, there are 2 AC differential u^{abc}_{diff} and 2 AC additive u^{abc}_{sum} components which are related to the positive- and negative-sequences; 1 AC differential u^0_{diff} and 1 AC additive u^0_{sum} zero-sequence component; 2 DC additive U^{abc}_{sum} and 2 DC differential U^{abc}_{diff} voltages correlated with the $\alpha\beta$ components; and 1 DC additive U^0_{sum} and 1 DC differential U^0_{diff} zero-sequence component. In addition, the zero-sequence components are applied separately from the other components.

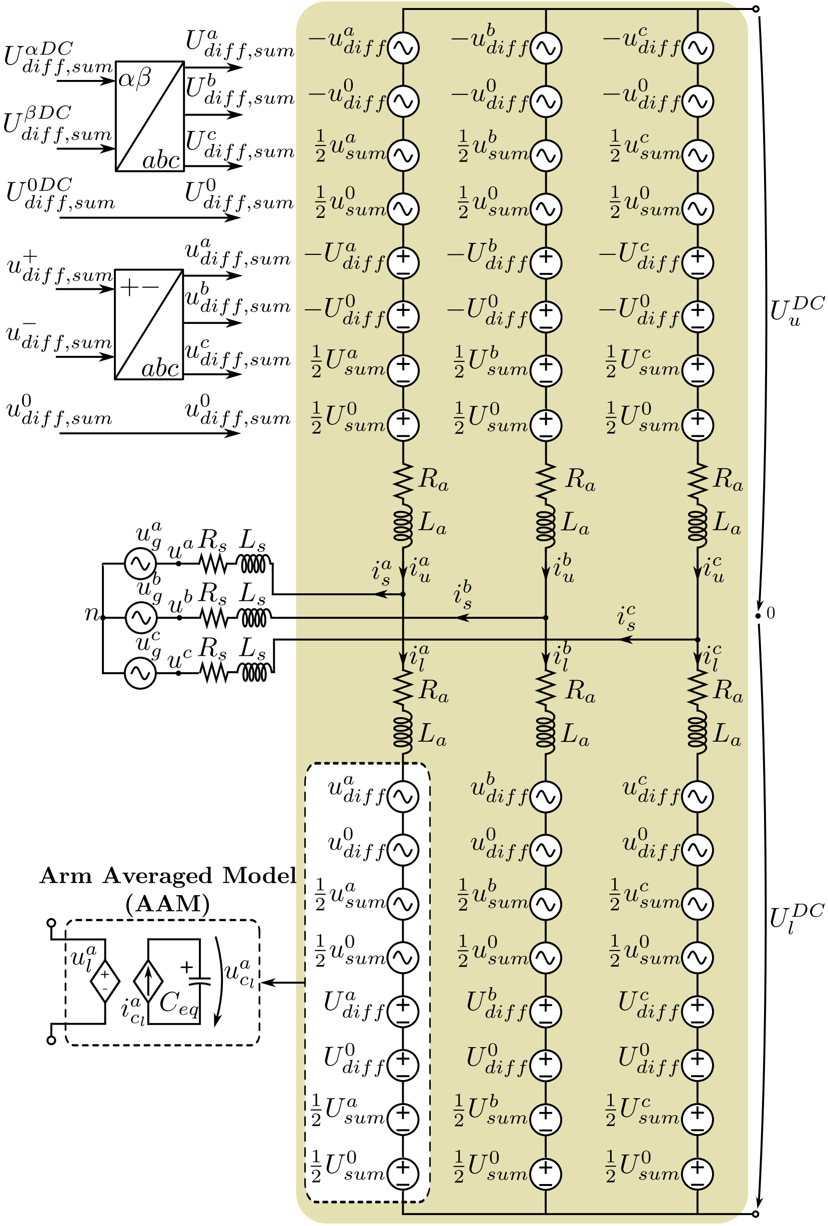

Fig. 2.2: Average model of the MMC with all its DOFs.

2.4.2 Definition of the MMC's additive and differential voltage and currents

The time-domain mathematical equations describing the differential and additive voltage components of the MMC are given as

$$\begin{aligned} u^k_{diff}(t) = U^{kDC}_{diff} + \sqrt{2}\Bigg[& U^+_{diff}\cos\left(\omega t + \theta^+_{diff} + \alpha^k\right) + \\ & U^-_{diff}\cos\left(\omega t + \theta^-_{diff} - \alpha^k\right) + U^0_{diff}\cos\left(\omega t + \theta^0_{diff}\right)\Bigg] \end{aligned} \tag{2.17}$$

$$\begin{aligned} u^k_{sum}(t) = U^{kDC}_{sum} + \sqrt{2}\Bigg[& U^+_{sum}\cos\left(\omega t + \theta^+_{sum} + \alpha^k\right) + \\ & U^-_{sum}\cos\left(\omega t + \theta^-_{sum} - \alpha^k\right) + U^0_{sum}\cos\left(\omega t + \theta^0_{sum}\right)\Bigg] \end{aligned} \tag{2.18}$$

where $\theta^{+,-,0}_{diff}$, $\theta^{+,-,0}_{sum}$ are the positive-, negative- and zero-sequence phase-angles of the differential and additive voltages, respectively. Assuming $\alpha^a = 0, \alpha^b = -\frac{2\pi}{3}, \alpha^c = \frac{2\pi}{3}$ for $k \in \{a, b, c\}$. Similarly, the additive and AC network currents are defined as follows

$$\begin{aligned} i^k_{sum}(t) = I^{kDC}_{sum} + \sqrt{2}\Bigg[& I^+_{sum}\cos\left(\omega t + \phi^+_{sum} + \alpha^k\right) + \\ & I^-_{sum}\cos\left(\omega t + \phi^-_{sum} - \alpha^k\right) + I^0_{sum}\cos\left(\omega t + \phi^0_{sum}\right)\Bigg] \end{aligned} \tag{2.19}$$

$$\begin{aligned} i^k_s(t) = & I^{kDC}_s + \sqrt{2}\Bigg[I^+_s\cos\left(\omega t + \phi^+_s + \alpha^k\right) + \\ & I^-_s\cos\left(\omega t + \phi^-_s - \alpha^k\right) + I^0_s\cos\left(\omega t + \phi^0_s\right)\Bigg] \end{aligned} \tag{2.20}$$

with $\phi^{+,-,0}_{sum}$, $\phi^{+,-,0}_s$ as the positive- and negative- and zero-sequence phase-angles of the additive and AC network currents, respectively.

2.4.3 AC/DC power transfer

The average power transferred from the DC-side to the AC-side of the MMC, or vice-verse, can be calculated as (assuming that the average energy in each of the arms in constant)

$$P^{DC}_t = P^{AC}_t + P_{losses} \tag{2.21a}$$

$$\sum_{k=a}^{c}\left(U_u^{kDC}I_u^{kDC}+U_l^{kDC}I_l^{kDC}\right)=\sum_{k=a}^{c}\mathrm{Re}\left\{\underline{U}_u^k\underline{I}_u^k+\underline{U}_l^k\underline{I}_l^k\right\}+ \qquad (2.21b)$$
$$+\left(R_a\sum_{k=a}^{c}\left(I_u^{k^2}+I_l^{k^2}+I_u^{kDC^2}+I_l^{kDC^2}\right)\right)$$

By replacing the upper and lower arms voltages and currents with their respective additive and differential quantities, the simplified AC/DC power transfer equation can be obtained as

$$U_{sum}^0 I_{sum}^0=\frac{9\left(U_{diff}^+I_s^+\cos\left(\theta_{diff}^+-\phi_s^+\right)+U_{diff}^-I_s^-\cos\left(\theta_{diff}^--\phi_s^-\right)\right)}{2}+$$
$$3R_a\left[\left(I_{sum}^{\alpha^2}+I_{sum}^{\beta^2}\right)+\frac{1}{2}\left(I_s^{+^2}+I_s^{-^2}\right)+2\left(I_{sum}^{+^2}+I_{sum}^{-^2}\right)\right] \qquad (2.22)$$

Based on (2.22), it is clear that the power transferred between the AC and DC networks is directly related to three DOFs: the zero-sequence DC additive voltage U_{sum}^0, the positive- and negative-sequence components of AC differential voltages $\underline{U}_{diff}^{+-}$; and indirectly dependent on four other DOFs: the AC additive voltages $\underline{U}_{sum}^{+-}$ (in the form of AC additive current $\underline{I}_{sum}^{+-}$) and DC additive voltage $U_{sum}^{\alpha\beta}$ (leading to the circulation of the currents $I_{sum}^{\alpha\beta}$). Note that currents induced by the AC and DC additive DOFs will influence the arm impedance losses. However, since the value for these DOFs will have a bigger impact in the vertical ($\underline{U}_{sum}^{+-}$) and horizontal ($U_{sum}^{\alpha\beta}$) power transfer (see Sections V-D and VI), it is recommended to set their magnitudes based on those power transferred set-points. Consequently, Fig. 2.2 can be reduced, by eliminating DOFs not employed in the AC/DC power transfer, as depicted in Fig. 2.3. Even though the AC additive and the DC differential quantities are also part of the circuit, as described in Section 2.3, such DOFs $\underline{U}_{sum}^0$ and $U_{diff}^{\alpha\beta}$ must be set to zero in order to avoid AC current circulating in the DC side ($\underline{I}_{sum}^0$) and DC current circulation in the AC side ($I_{diff}^{\alpha\beta}$). The zero-sequence current component in the AC side is strictly equal to zero due to the three-wire connection.

Following, the horizontal and vertical power balancing equations are presented. It is considered that the DOFs required for the power transferred between the AC and DC grids are kept activated and their values are set to maintain constant power transmission.

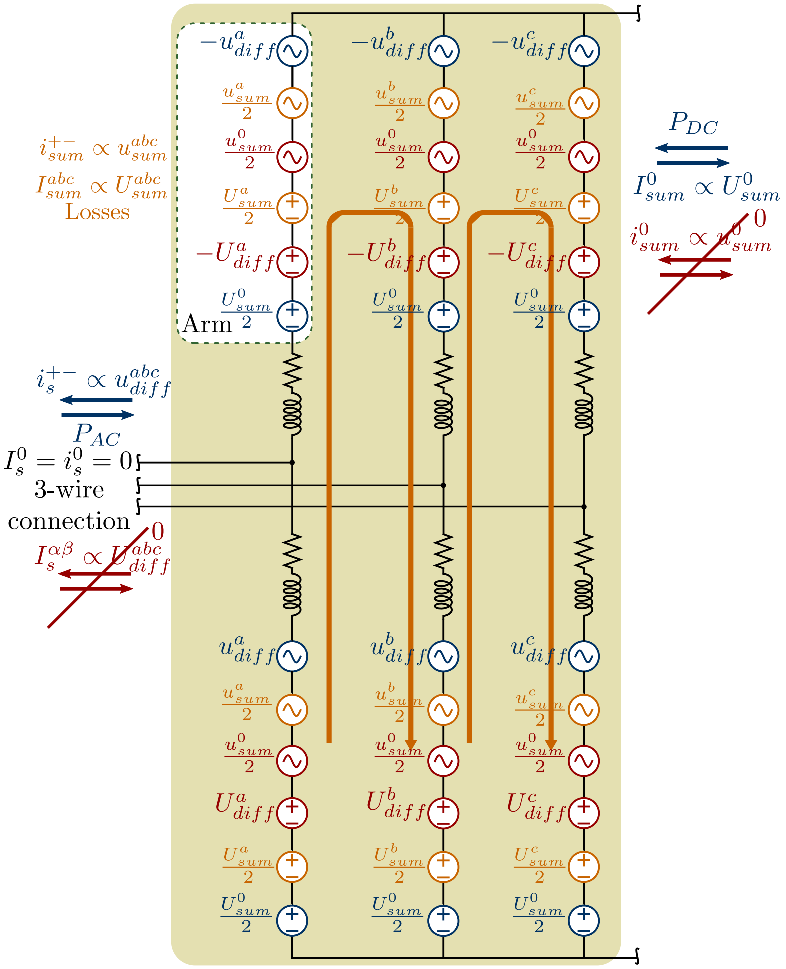

Fig. 2.3: DOFs required for proper AC/DC power transfer.

2.4.4 Horizontal Power balancing

During balanced AC grid conditions, each phase-leg of the MMC should transfer one third of the total power exchanged between the DC network and the AC system. However, during contingencies, they may transfer distinct power levels. Such deviations must be compensated to avoid sustained internal energy unbalances, which may lead to the undesired tripping of the converter. To understand which DOFs take part in the horizontal balancing of the converter, let's first define the average power transfer among the phase-legs of the converter as

$$P_{a\rightarrow b} = P_a - P_b = \mathrm{Re}\left\{ \left(\underline{U}_u^a \underline{I}_u^a + \underline{U}_l^a \underline{U}_l^a\right) - \left(\underline{U}_u^b \underline{I}_u^b + \underline{U}_l^b \underline{I}_l^b\right) \right\} + \tag{2.23a}$$

$$+ U_u^{aDC} I_u^{aDC} + U_l^{aDC} I_l^{aDC} - \left(U_u^{bDC} I_u^{bDC} + U_l^{bDC} I_l^{bDC}\right)$$

$$P_{a\rightarrow c} = P_a - P_c = \mathrm{Re}\left\{ \left(\underline{U}_u^a \underline{I}_u^a + \underline{U}_l^a \underline{U}_l^a\right) - \left(\underline{U}_u^c \underline{I}_u^c + \underline{U}_l^c \underline{I}_l^c\right) \right\} + \tag{2.23b}$$

$$+ U_u^{aDC} I_u^{aDC} + U_l^{aDC} I_l^{aDC} - \left(U_u^{cDC} I_u^{cDC} + U_l^{cDC} I_l^{cDC}\right)$$

$$P_{b\rightarrow c} = P_b - P_c = \mathrm{Re}\left\{ \left(\underline{U}_u^b \underline{I}_u^b + \underline{U}_l^b \underline{U}_l^b\right) - \left(\underline{U}_u^c \underline{I}_u^c + \underline{U}_l^c \underline{I}_l^c\right) \right\} + \tag{2.23c}$$

$$+ U_u^{bDC} I_u^{bDC} + U_l^{bDC} I_l^{bDC} - \left(U_u^{cDC} I_u^{cDC} + U_l^{cDC} I_l^{cDC}\right)$$

Now, the upper and lower arm's voltages and currents are substituted by their respective additive and differential quantities and the first and second order frequency terms are eliminated. By doing so, the average power transferred among the phase-legs of the converter are obtained as shown in (2.24). Observing the equations, Fig. 2.4 is obtained and the following can be noted:

$$P_{a\to b} = \begin{bmatrix} U_{diff}^{+} \\ U_{diff}^{-} \\ U_{diff}^{0} \\ U_{sum}^{+} \\ U_{sum}^{-} \end{bmatrix}^T \begin{bmatrix} 0 & -\sqrt{3}\cos(\theta_{diff}^{+} - \phi_s^{-} - \frac{\pi}{6}) & 0 & 0 \\ -\sqrt{3}\cos(\theta_{diff}^{-} - \phi_s^{-} + \frac{\pi}{6}) & 0 & 0 & 0 \\ -\sqrt{3}\cos(\theta_{diff}^{0} - \phi_s^{+} - \frac{\pi}{6}) & -\sqrt{3}\cos(\theta_{diff}^{0} - \phi_s^{-} + \frac{\pi}{6}) & 0 & 0 \\ 0 & 0 & 0 & \sqrt{3}\cos(\theta_{sum}^{+} - \phi_{sum}^{-} - \frac{\pi}{6}) \\ 0 & 0 & \sqrt{3}\cos(\theta_{sum}^{-} - \phi_{sum}^{+} + \frac{\pi}{6}) & 0 \end{bmatrix} \begin{bmatrix} I_s^{+} \\ I_s^{-} \\ I_{sum}^{+} \\ I_{sum}^{-} \end{bmatrix}$$
$$+ \frac{3I_{sum}^{0}U_{sum}^{\alpha}}{2} + \frac{3I_{sum}^{\alpha}U_{sum}^{0}}{2} - \frac{3I_{sum}^{\beta}U_{sum}^{\beta}}{4} + \frac{3I_{sum}^{\alpha}U_{sum}^{\alpha}}{4} + \frac{\sqrt{3}I_{sum}^{0}U_{sum}^{\beta}}{2} + \frac{\sqrt{3}I_{sum}^{\beta}U_{sum}^{0}}{2} - \frac{\sqrt{3}I_{sum}^{\beta}U_{sum}^{\alpha}}{2} - \frac{\sqrt{3}I_{sum}^{\alpha}U_{sum}^{\beta}}{2} \tag{2.24a}$$

$$P_{a\to c} = \begin{bmatrix} U_{diff}^{+} \\ U_{diff}^{-} \\ U_{diff}^{0} \\ U_{sum}^{+} \\ U_{sum}^{-} \end{bmatrix}^T \begin{bmatrix} 0 & -\sqrt{3}\cos(\theta_{diff}^{+} - \phi_s^{-} + \frac{\pi}{6}) & 0 & 0 \\ -\sqrt{3}\cos(\theta_{diff}^{-} - \phi_s^{-} - \frac{\pi}{6}) & 0 & 0 & 0 \\ -\sqrt{3}\cos(\theta_{diff}^{0} - \phi_s^{+} + \frac{\pi}{6}) & -\sqrt{3}\cos(\theta_{diff}^{0} - \phi_s^{-} - \frac{\pi}{6}) & 0 & 0 \\ 0 & 0 & 0 & \sqrt{3}\cos(\theta_{sum}^{+} - \phi_{sum}^{-} + \frac{\pi}{6}) \\ 0 & 0 & \sqrt{3}\cos(\theta_{sum}^{-} - \phi_{sum}^{+} - \frac{\pi}{6}) & 0 \end{bmatrix} \begin{bmatrix} I_s^{+} \\ I_s^{-} \\ I_{sum}^{+} \\ I_{sum}^{-} \end{bmatrix}$$
$$+ \frac{3I_{sum}^{0}U_{sum}^{\alpha}}{2} + \frac{3I_{sum}^{\alpha}U_{sum}^{0}}{2} - \frac{3I_{sum}^{\beta}U_{sum}^{\beta}}{4} + \frac{3I_{sum}^{\alpha}U_{sum}^{\alpha}}{4} - \frac{\sqrt{3}I_{sum}^{0}U_{sum}^{\beta}}{2} - \frac{\sqrt{3}I_{sum}^{\beta}U_{sum}^{0}}{2} + \frac{\sqrt{3}I_{sum}^{\beta}U_{sum}^{\alpha}}{2} + \frac{\sqrt{3}I_{sum}^{\alpha}U_{sum}^{\beta}}{2} \tag{2.24b}$$

$$P_{b\to c} = \begin{bmatrix} U_{diff}^{+} \\ U_{diff}^{-} \\ U_{diff}^{0} \\ U_{sum}^{+} \\ U_{sum}^{-} \end{bmatrix}^T \begin{bmatrix} 0 & -\sqrt{3}\sin(\theta_{diff}^{+} - \phi_s^{-}) & 0 & 0 \\ -\sqrt{3}\sin(\theta_{diff}^{-} - \phi_s^{-}) & 0 & 0 & 0 \\ -\sqrt{3}\sin(\theta_{diff}^{0} - \phi_s^{+}) & \sqrt{3}\sin(\theta_{diff}^{0} - \phi_s^{-}) & 0 & 0 \\ 0 & 0 & 0 & \sqrt{3}\sin(\theta_{sum}^{+} - \phi_{sum}^{-}) \\ 0 & 0 & -\sqrt{3}\sin(\theta_{sum}^{-} - \phi_{sum}^{+}) & 0 \end{bmatrix} \begin{bmatrix} I_s^{+} \\ I_s^{-} \\ I_{sum}^{+} \\ I_{sum}^{-} \end{bmatrix}$$
$$+ \frac{\sqrt{3}I_{sum}^{\beta}U_{sum}^{\alpha}}{2} - \sqrt{3}I_{sum}^{\beta}U_{sum}^{0} + \sqrt{3}I_{sum}^{0}U_{sum}^{\beta} + \frac{\sqrt{3}I_{sum}^{\alpha}U_{sum}^{\beta}}{2} \tag{2.24c}$$

- Although the AC positive- and negative-sequence components of the differential quantities are defined based on the amount of power transferred from the AC-side to the DC one, they can interfere with the power shared among the MMC's phase-legs.

- The DC zero-sequence additive DOF also contributes for the horizontal balancing.

- Two AC DOFs can be potentially used based on this power transfer, the AC additive voltages $\underline{U}_{sum}^{+-}$ and the zero-sequence AC differential voltage $\underline{U}_{diff}^{0}$.

- The positive-sequence DOFs interact with their respective negative-sequence currents, and vice-versa.

- Two DC DOFs, the DC additive voltages $U_{sum}^{\alpha\beta}$, can also be employed for the horizontal balancing. These DOFs will interact among themselves and with the DC zero-sequence additive components. Whereas the interactions with the former have higher contribution in the power sharing, as I_{sum}^{0} has the highest value (AC/DC network power transfer).

Finally, the selection of which DOFs should be employed for the vertical balancing must be done by the control designer. The authors suggest the usage of the AC zero-sequence differential DOF $\underline{U}_{diff}^{0}$ and the DC additive ones $U_{sum}^{\alpha\beta}$. Since the DOFs $\underline{U}_{diff}^{+-}$ not only would require the interaction between the positive- and negative-sequences, but along with U_{sum}^{0} are already used for the AC/DC network power transfer.

2.4.5 Vertical Power balancing

For the vertical power transfer equations, a similar procedure, as done for the horizontal case, is employed. The power transfer between the upper and lower arms of the MMC in each phase, can be described in the natural *abc* reference frame as (2.25) or in the additive and differential frame as shown in (2.26). Based on these equations, the DOFs used for the vertical power sharing are highlighted in Fig. 2.5.

$$P_{u\rightarrow l}^{k} = P_{u}^{k} - P_{l}^{k} = \mathrm{Re}\left\{ \underline{U}_{u}^{k}\underline{I}_{u}^{k} - \underline{U}_{l}^{k}\underline{I}_{l}^{k} \right\} + \left(U_{u}^{kDC} I_{u}^{kDC} - U_{l}^{kDC} I_{l}^{kDC} \right) \tag{2.25}$$

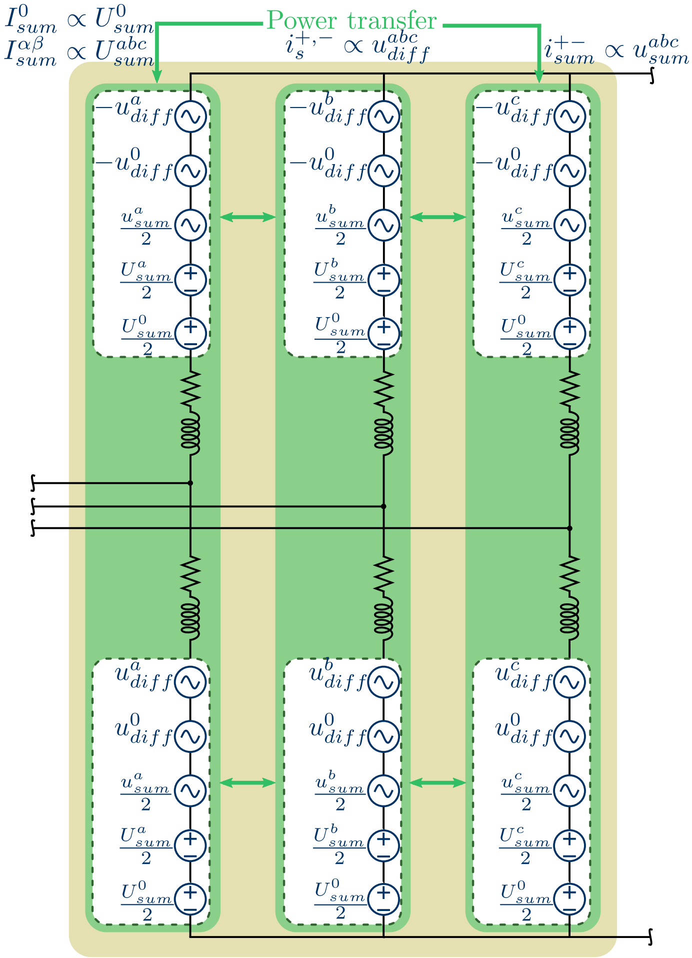

Fig. 2.4: DOFs required for transferring power among the phase-legs of the MMC.

$$P^k_{u\to l} = \begin{bmatrix} U^+_{diff} \\ U^-_{diff} \\ U^0_{diff} \\ I^+_s \\ I^-_s \end{bmatrix}^T \begin{bmatrix} -2\cos(\theta^+_{diff} - \phi^+_{sum}) & -2\cos(\theta^+_{diff} - \phi^-_{sum} - \alpha^k) & 0 & 0 \\ -2\cos(\theta^-_{diff} - \phi^+_{sum} + \alpha^k) & -2\cos(\theta^-_{diff} - \phi^-_{sum}) & 0 & 0 \\ -2\cos(\theta^0_{diff} - \phi^+_{sum}) & -2\cos(\theta^0_{diff} - \phi^-_{sum}) & 0 & 0 \\ 0 & 0 & \frac{\cos(\theta^+_{sum} - \phi^+_s)}{2} & \frac{\cos(\theta^-_{sum} - \phi^+_s + \alpha^k)}{2} \\ 0 & 0 & \frac{\cos(\theta^+_{sum} - \phi^-_s - \alpha^k)}{2} & \frac{\cos(\theta^-_{sum} - \phi^-_s)}{2} \end{bmatrix} \begin{bmatrix} I^+_{sum} \\ I^-_{sum} \\ U^+_{sum} \\ U^-_{sum} \end{bmatrix}$$
$$+ U^{0DC}_{diff} \begin{bmatrix} -2I^\alpha_{sum} - 2I^0_{sum} \\ I^\alpha_{sum} + \sqrt{3}I^\beta_{sum} - 2I^0_{sum} \\ I^\alpha_{sum} - \sqrt{3}I^\beta_{sum} - 2I^0_{sum} \end{bmatrix} \tag{2.26}$$

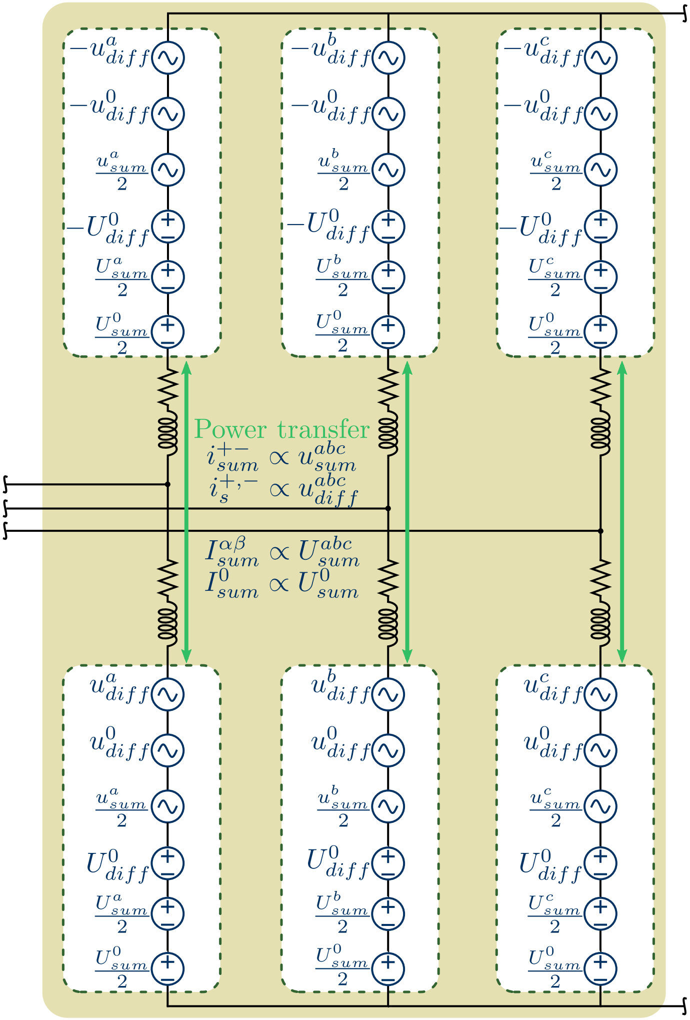

Fig. 2.5: DOFs required for transferring power between the upper and lower arms of the MMC.

Compared to the previous power balancing equations, the upper and lower arms' power transfer present interesting insights regarding interactions among different components and the usage of the last DOF remaining. Next, the main highlights of the vertical power transfer are described:

- Similarly to the horizontal power sharing scenario, the differential voltages play partial role in the vertical power transfer.
- Although it is assumed that the additive and differential compo-

nents are decoupled, they may interact during the horizontal power transfer.

- This interaction can be seen by the product between the differential and additive AC DOFs with the additive and differential AC current components, respectively.

- The last DOF remaining U_{diff}^{0DC} can be used to enhance the vertical power transfer by multiplying it with the MMCs DC additive currents.

Overall, the authors recommendation is to define the AC additive DOFs $\underline{U}_{sum}^{+-}$ and the DC differential one U_{diff}^{0DC} based on the desired set-points for the horizontal power balancing. As the other DOFs are already defined considering other power transfer conditions. The roles of the 12 DOFs in the power transfer are summarized in Table 2.1 while Table 2.2 highlights the authors' recommendations of which DOF should be selected for each power transfer condition (note that the DOFs not included in the table are set to zero).

Table 2.1: DOFs summary.

DOF	**Power Transfer**		
	$P_t^{DC} \to P_t^{AC}$	$P_{x\to y}$	$P_{u\to l}^{k}$
$\underline{U}_{diff}^{+,-}$	✓	✓	✓
$\underline{U}_{diff}^{0}$	×	✓	✓
$\underline{U}_{sum}^{+,-}$	✓ (losses)	✓	✓
$\underline{U}_{sum}^{0}$	×	×	×
$U_{diff}^{\alpha\beta}$	×	×	×
U_{diff}^{0DC}	×	×	✓
$U_{sum}^{\alpha\beta}$	✓ (losses)	✓	✓
U_{sum}^{0}	✓	✓	✓

Table 2.2: Recommendation of which DOF's to employ for the different power transfers.

DOF	**Power Transfer**		
	$P_t^{DC} \rightarrow P_t^{AC}$	$P_{x \rightarrow y}$	$P_{u \rightarrow l}^k$
$\underline{U}_{diff}^{+,-}$	✓	×	×
U_{sum}^0	✓	×	×
$\underline{U}_{diff}^0$	×	✓	×
$U_{sum}^{\alpha\beta}$	×	✓	×
$\underline{U}_{sum}^{+,-}$	×	×	✓
U_{diff}^{0DC}	×	×	✓

2.5 Interaction between the DOFs

In this section, the internal power transfer between legs and arms of the MMC is analyzed not only to validate the internal power equations but also to provide further details of how the several DOFs of the converter interact within one another. Even though some interactions were intuitive based on the traditional internal power equations, others were not observed since the classical methods were unable to exploit all the DOFs of the converter.

For this analysis, the converter is considered to be operated in steady-state and balanced DC and AC networks conditions[1], having $\underline{U}_{diff}^{+-}$ and U_{sum}^0 activated and regulated to fixed values in order to maintain nominal active power to be transferred between the DC and AC grids (default case). The remaining DOFs are switched *ON* and *OFF* following the order presented in Table 2.3, which 1 represents when the DOF is activated and 0 when it is not. The MMC specifications are similar to the parameters of the converter station employed in the HVDC link between France and Spain (INELFE), shown in Table 2.4. In additions, $I_s^{\alpha\beta 0}$ and $\underline{I}_s^0$ are set to be equal to zero throughout the operation. The upper and lower arms power transfer values for each phase is displayed in Figs. 2.6 to 2.8 and in Figs. 2.9 to 2.11 the power transfer between legs is shown. For each case study, bar plots with different colors are used to represent

---

[1] Note that the proposed reference calculation can be used for any AC and DC grid voltage scenarios.

the amount of power transferred by each DOF vertically (Figs. 2.6 to 2.8) or horizontally (Figs. 2.9 to 2.11). Note that the total amount of power transferred in each case may be different as they might be using additional or fewer DOFs.

Table 2.3: Activated DOFs.

Case	$\underline{U}_{diff}^{+-}$	U_{sum}^{0}	$U_{sum}^{\alpha\beta}$	$\underline{U}_{sum}^{+-}$	$\underline{U}_{diff}^{0AC}$	U_{diff}^{0DC}
Case I (default)	1	1	0	0	0	0
Case II	1	1	0	0	0	1
Case III	1	1	0	0	1	0
Case IV	1	1	0	0	1	1
Case V	1	1	0	1	0	0
Case VI	1	1	0	1	0	1
Case VII	1	1	0	1	1	0
Case VIII	1	1	0	1	1	1
Case IX	1	1	1	0	0	0
Case X	1	1	1	0	0	1
Case XI	1	1	1	0	1	0
Case XII	1	1	1	0	1	1
Case XIII	1	1	1	1	0	0
Case XIV	1	1	1	1	0	1
Case XV	1	1	1	1	1	0
Case XVI	1	1	1	1	1	1

Table 2.4: System parameters.

Parameter	**Symbol**	**Value**	**Units**
Rated power	S	1000	MVA
Rated power factor	$\cos\phi$	0.95 (c)	-
AC-side rated voltage (Line-to-Line RMS)	$\underline{U}_g$	325	kV
HVDC link voltage	U^{DC}	$\pm$320	kV
Phase reactor impedance	$\underline{Z}_s$	0.005+j 0.18	pu
Arm reactor impedance	$\underline{Z}_a$	0.01+j 0.15	pu
Converter modules per arm	N_{u,l_a}^{k}	433	-
Submodule capacitance	C_{SM}	9.5	mF
AC differential voltage	$\underline{U}_{diff}^{+}$	$1 \underline{/0^{o}}$	pu
AC differential voltage	$\underline{U}_{diff}^{-}$	0	pu
AC differential voltage	$\underline{U}_{diff}^{0AC}$	$0.2 \underline{/60^{o}}$	pu
DC differential voltage	U_{diff}^{0DC}	0.01	pu
AC additive voltage	$\underline{U}_{sum}^{+}$	$0.27 \underline{/0^{o}}$	pu
AC additive voltage	$\underline{U}_{sum}^{-}$	0	pu
DC additive voltage	U_{sum}^{α}	0.1	pu
DC additive voltage	U_{sum}^{β}	0.2	pu
DC additive voltage	U_{sum}^{0}	0.01	pu

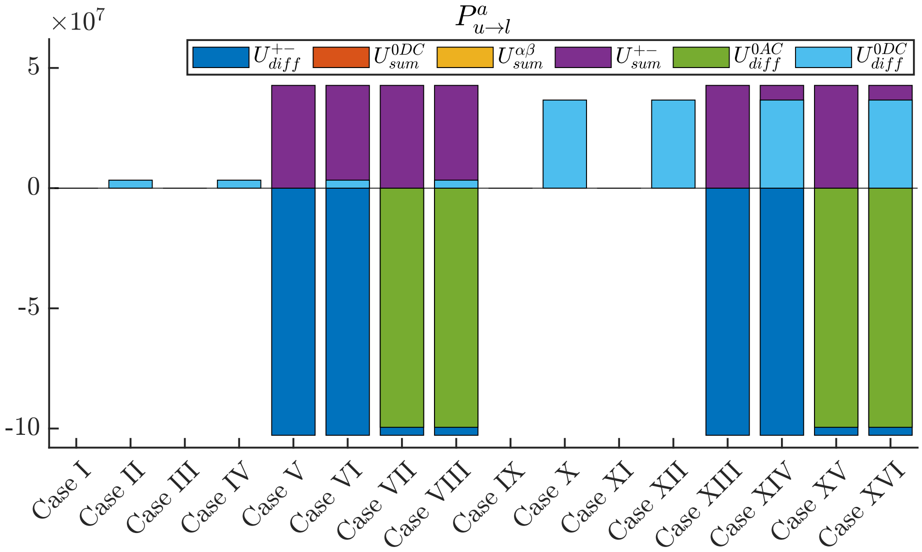

Fig. 2.6: Arm power transfer for phase a.

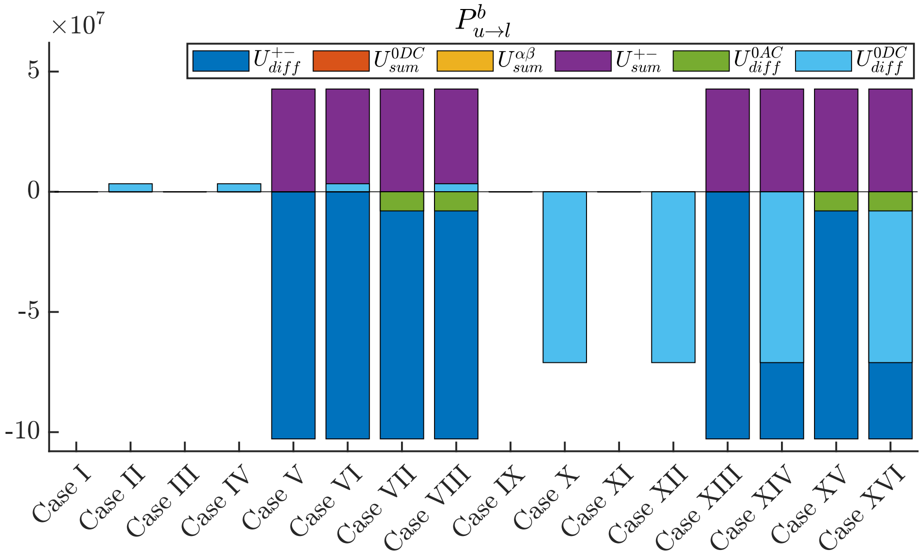

Fig. 2.7: Arm power transfer for phase b.

2.5.1 Case study I

When the DOFs $\underline{U}^{+-}_{diff}$ and U^{0}_{sum} are different than zero, they enable power transfer between the AC grid and the converter ($\underline{U}^{+-}_{diff}$) and between the MMC and the DC grid (U^{0}_{sum}). The values of these DOFs are set based on the amount of active/reactive power to be shared with

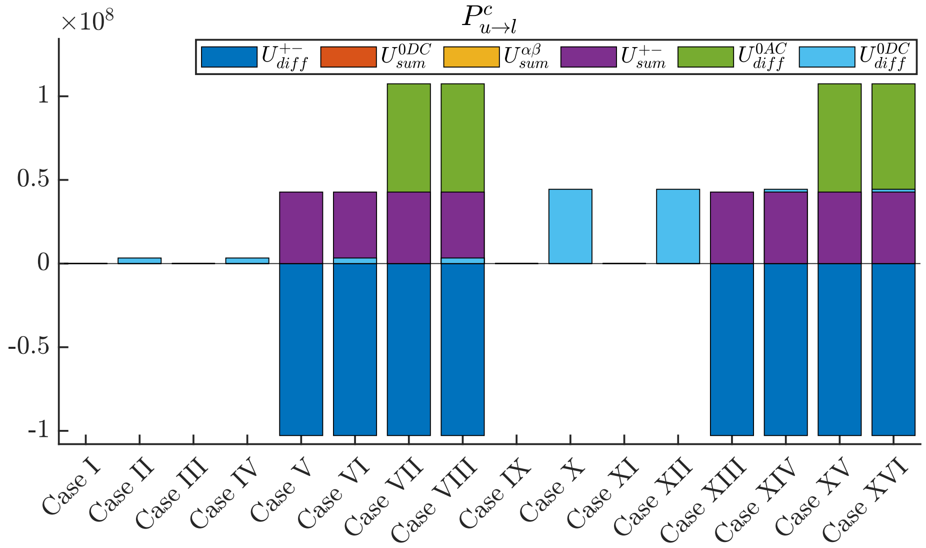

Fig. 2.8: Arm power transfer for phase c.

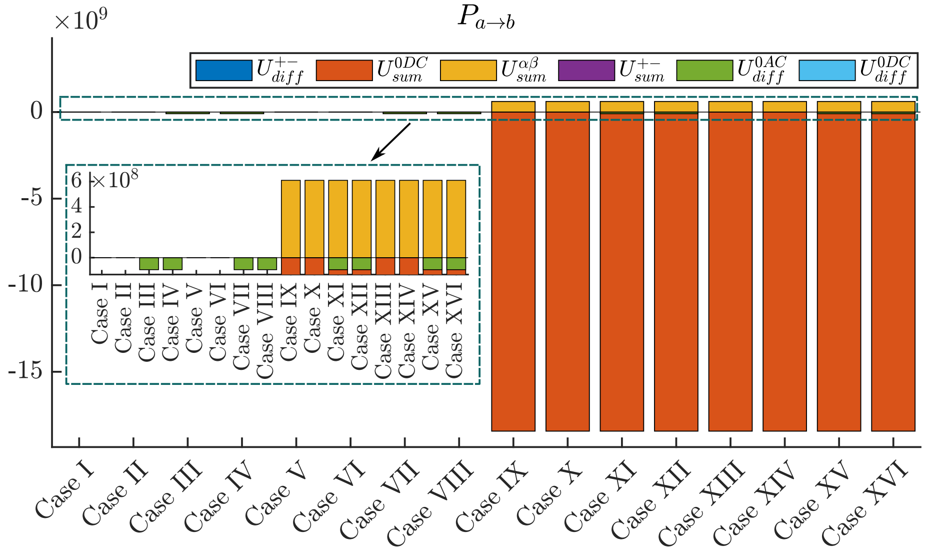

Fig. 2.9: Leg power transfer from phase a to b.

the AC network. However, as demonstrated in Sections 2.4, those DOFs play partial role in the phase-leg power sharing (see Section 2.4.4) or in the power transfer between the converters arms by interacting with the additive AC current (see Section 2.4.5). Such interactions will be analyzed in the next case studies.

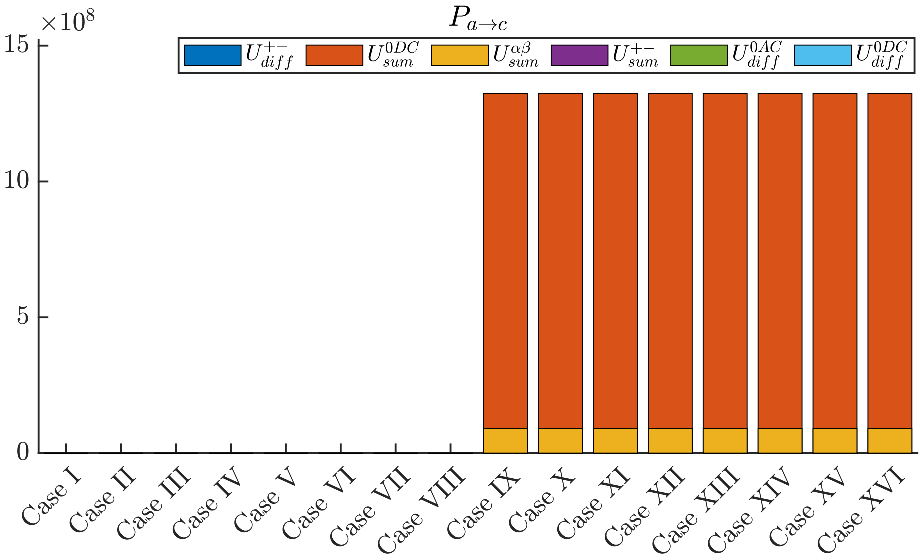

Fig. 2.10: Leg power transfer from phase a to c.

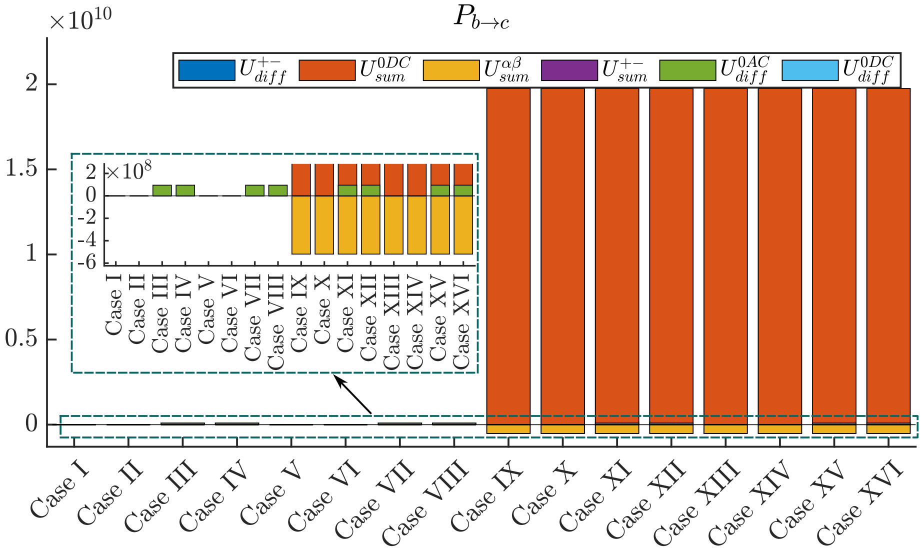

Fig. 2.11: Leg power transfer from phase b to c.

2.5.2 Case study II

When the DOF U_{diff}^{0DC} is activated, it allows different DC voltage levels between the upper and lower arms without affecting the DC current levels circulating in the converter (see Section 2.4.5). As a result, the MMC will have distinct power levels for its halves as it can be seen at the second columns in Figs. 2.6 to 2.8. The power difference between the arms for all three-phases is equal to $P^k_{u\to l} = 3.33$ MW, which is related to the interaction between U^{0DC}_{diff} and the DC zero-sequence additive current I^0_{sum}. As expected from the horizontal power balancing equations, this DOF cannot be used for power balancing between legs, this fact can be observed in Figs. 2.9 to 2.11, since all the power differences remained equal to zero. Finally, U^{0DC}_{diff} does not interfere with any of the remaining DOFs.

2.5.3 Case study III

When $\underline{U}^{0AC}_{diff}$ is in ON-state under balanced conditions, it allows different AC voltage levels within the MMC legs without compromising the inner currents as it is a zero-sequence component. Unlike the DC homopolar component, the ratio between the upper and lower arms voltages levels remains constant, since $U^k_{diff_u} = -U^k_{diff_l}$. As it can be observed in Figs. 2.6 to 2.8, there is no power difference between the halves of the converter regarding this DOF, $P^k_{u\to l} = 0$. Such outcome is in agreement with (2.26), as the AC currents circulating through the converter are strictly related to $\underline{U}^{+-}_{diff}$. And, to transfer power between the upper and lower arms of the converter using $\underline{U}^{0AC}_{diff}$, it would be necessary the circulation of AC additive currents, which are now zero since $\underline{U}^{+-}_{sum}$ is in OFF-state.

Regarding power sharing among the phase-legs of the converter, shown in Figs. 2.9 to 2.11, it can be noted that $\underline{U}^{0AC}_{diff}$ enables power transfer. The power values for this case study $P_{a\to b} = -95$ MW, $P_{a\to c} = 0$ and $P_{b\to c} = 95$ MW. This happens as there is AC current flowing through the converter due to $\underline{U}^{+-}_{diff}$. Thus, the magnitude of power sharing is related to the product between $\underline{U}^{0AC}_{diff}$ and $\underline{I}^{+-}_{s}$, as demonstrated in (2.24). No power sharing is observed regarding $\underline{U}^{+-}_{diff}$ as it will be strictly zero, since $\underline{U}^{-}_{diff} = 0$ and $\underline{I}^{-}_{s} = 0$ which is in agreement with (2.24). If negative-sequence differential voltage components were applied, the power transfer between the phase-legs of the converter would present two components, one regarding $\underline{U}^{0AC}_{diff}$ and another one due to $\underline{U}^{+-}_{diff}$.

2.5.4 Case study IV

This is the first case in which more than one DOF is used, besides $\underline{U}^{+-}_{diff}$ and U^0_{sum}. Under this condition, the AC and DC homopolar components of the differential voltages are activated. As expected from (2.24) and (2.26) and noted in Figs. 2.6 to 2.11, such DOFs do not interact with each other and with any other quantities only affecting the power transfer between legs due to $\underline{U}_{diff}^{0AC}$ and between upper and lower halves as $U_{diff}^{0DC} \neq 0$, with $P_{u\rightarrow l}^{k} = 3.33$ MW, $P_{a\rightarrow b} = -95$ MW, $P_{a\rightarrow c} = 0$ and $P_{b\rightarrow c} = 95$ MW.

2.5.5 Case study V

In this case, $\underline{U}_{sum}^{+-}$ is activated. As described in Section 2.4.5 and shown in Figs. 2.6 to 2.8, the addition of $\underline{U}_{sum}^{+-}$ causes power transfer between the upper and lower arms of the converter. This power transfer happens due to the interactions between the AC additive and differential currents with the AC differential and additive voltages, respectively. The upper and lower power transfer caused by $\underline{U}_{diff}^{+-}\underline{I}_{sum}^{+-}$ is equal to $P_{u\rightarrow l}^{k} = -102.031$ MW, whereas $\underline{U}_{sum}^{+-}\underline{I}_{s}^{+-}$ leads to a power transfer equals to $P_{u\rightarrow l}^{k} = 42.75$ MW.

Now, as the $\underline{U}_{diff}^{-} = \underline{U}_{sum}^{-} = 0$ and the other DOFs which would influence the phase-leg power sharing are deactivated, the resultant power transferred among the phase-legs of the converter is strictly zero as shown in Figs. 2.9 to 2.11. Such outcome is in agreement with the theoretical analysis of power equations derived in Section 2.4.4.

2.5.6 Case study VI

For case VI, the addition of U_{diff}^{0DC} with the other DOFs from case V will not cause any new interaction as it can be noted in Figs. 2.6 to 2.11, consequently the non-zero power levels are the same as the previous case studies. The DC homopolar voltage component only affects the power regarding itself, and no power difference among the phase-legs is obtained, as previously concluded.

2.5.7 Case studies VII and VIII

For cases VII and VIII, beside the conclusions drawn in the previous cases, a new interaction is observed between $\underline{U}_{diff}^{0AC}$ and $\underline{U}_{sum}^{+-}$. As expected from the theoretical analysis presented in (2.26) and observed in Figs. 2.6 to 2.8, the AC additive currents generated by $\underline{U}_{sum}^{+-}$ interact with $\underline{U}_{diff}^{0AC}$. Thus, power transfer between the upper and lower arms of the converter can be achieved, for Case VII: $P_{u\rightarrow l}^{a} = -159.53$ MW, $P_{u\rightarrow l}^{b} = -68.018$ MW and $P_{u\rightarrow l}^{c} = 47.392$ MW, while for Case VIII: $P_{u\rightarrow l}^{a} = -156.2$ MW, $P_{u\rightarrow l}^{b} = -64.684$ MW and $P_{u\rightarrow l}^{c} = 50.726$ MW. The power shared among the phase-legs is the same as presented in case study IV.

2.5.8 Case study IX

In this case, the DC non-homopolar components of the additive voltage are enabled $U_{sum}^{\alpha\beta} \neq 0$. As described in Section 2.4, such DOF can be used to balance the power mismatches between the MMC phase-legs, as it allows different DC current levels to flow in each leg (see Section 2.4.4) and will not affect the power transfer between upper and lower arms, which can be noted from Figs. 2.6 to 2.8. For the horizontal power transfer (see Figs. 2.9 to 2.11), when these DOFs are employed, the power shared among the phase-legs of the converter are being equal to $P_{a\rightarrow b} = -17.817$ GW, $P_{a\rightarrow c} = 1.4131$ GW and $P_{b\rightarrow c} = 19.23$ GW.

2.5.9 Case study X

Due to the presence of unbalanced DC currents flowing through the converter, the power difference between the upper and lower arms for each phase-leg will be different when the DOF U_{diff}^{0DC} is activated, as it is shown in Figs. 2.6 to 2.8. However, as detailed earlier, the DC homopolar component of the differential voltage does not affect the power balance within the converter phase-legs, which it can be observed in 2.9 to 2.11, since it maintains the same profile as Case IX.

2.5.10 Case studies XI to XVI

The magnitude of power transferred between arms and phase-legs caused by the interactions of the DOFs will be similar then the ones observed in the previous cases.

2.5.11 Observations

As an overall observation of the several case studies presented, the following interactions between the DOFs can be stated:

- The positive- and negative-sequence components of the AC differential voltage $\underline{U}_{diff}^{+-}$ influence the vertical power transfer (see Cases V to VIII and XIII to XVI) as it interacts with the currents generated by the AC additive DOFs $\underline{U}_{sum}^{+-}$. However, neither $\underline{U}_{diff}^{+-}$ or $\underline{U}_{sum}^{+-}$ affect the horizontal power transfer.
- The DOF U_{diff}^{0} only affects the vertical power transfer. To do so, this DOF interacts with the DC currents generated by the DC additive voltage $U_{sum}^{\alpha\beta 0}$.

- The zero-sequence AC differential voltage component $\underline{U}^{0}_{diff}$ interferes in both vertical and horizontal power transfer. For the vertical one, the effect of this DOF is only noted when the DOF $\underline{U}^{+-}_{sum}$ is activated, as the power transferred using $\underline{U}^{0}_{diff}$ is produced by its interactions with the currents generated by $\underline{U}^{+-}_{sum}$. Whereas, for the horizontal power transfer, $\underline{U}^{0}_{diff}$ interacts with the currents generated by $\underline{U}^{+-}_{diff}$.

- The DC additive DOFs actively affect the horizontal power transfer.

2.6 Validation of the mathematical expressions

In this section, the time-domain profile of the power mismatch expressions given in (2.24) and (2.26) are compared with the MMC's measured power differences during different AC network voltage sag conditions. The MMC is assumed to be operated in steady-state conditions with all the DOFs activated (Case XVI). Note that the values for the positive- and negative-sequence components of the AC differential voltage are obtained in order to maintain the desired power flow between the AC and DC networks, which will vary from the values in Table IV due to the unbalanced characteristics of the faults imposed in the AC side of the converter. Furthermore, the other DOF values are kept constant to the ones shown in Table IV that were only selected to demonstrate their effects in the power balancing of the converter and not to induce the MMC to achieve internal power balance since such goal can only be accomplished by the addition of energy-based controllers.

In Figs. 2.12 and 2.13, the time-domain waveforms for the AC voltage and currents are shown as well as the correlation between the measured and the calculated internal power mismatches during unbalanced AC network voltage sags. In Fig. 2.12 a type C voltage sag [51] is imposed into the AC network, resulting in $\underline{U}^{+}_{diff} = 0.6191$ pu to be equal to and $\underline{U}^{-}_{diff} = 0.2721$ pu to be equal to while in Fig. 2.13 a Single-Line-to-Ground (SLG) fault is considered ($\underline{U}^{+}_{diff} = 0.6062$ pu and $\underline{U}^{-}_{diff} = 0.2858$ pu). As it can be noticed, during the transient, the calculated value of the power mismatches presents a different profile in comparison to the measured one, which is more evident for the upper and lower arm power mismatch. However, it is clear that average value for the calculated and measured power mismatches are the same, which validates the expressions (2.24) and (2.26).

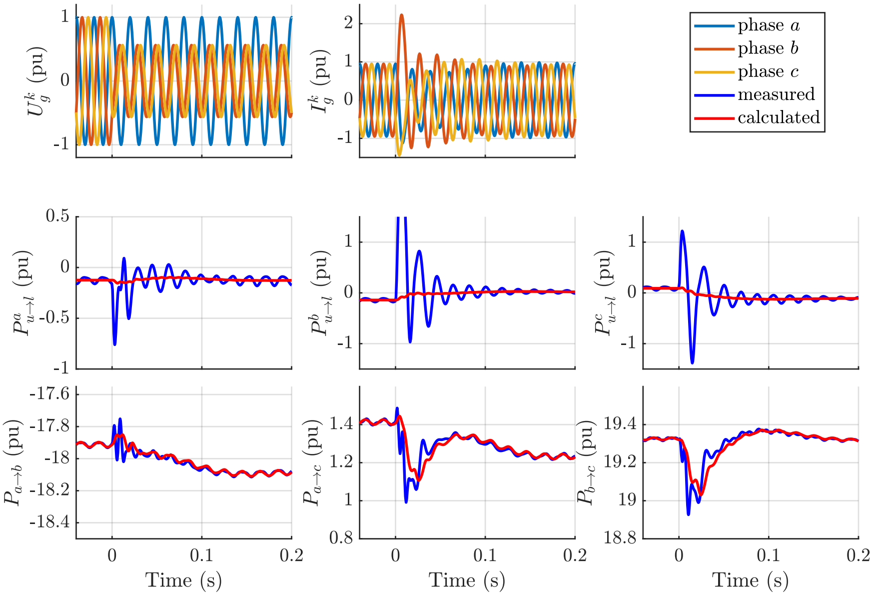

Fig. 2.12: Time-domain waveforms comparison for the internal power mismatch during a type C fault.

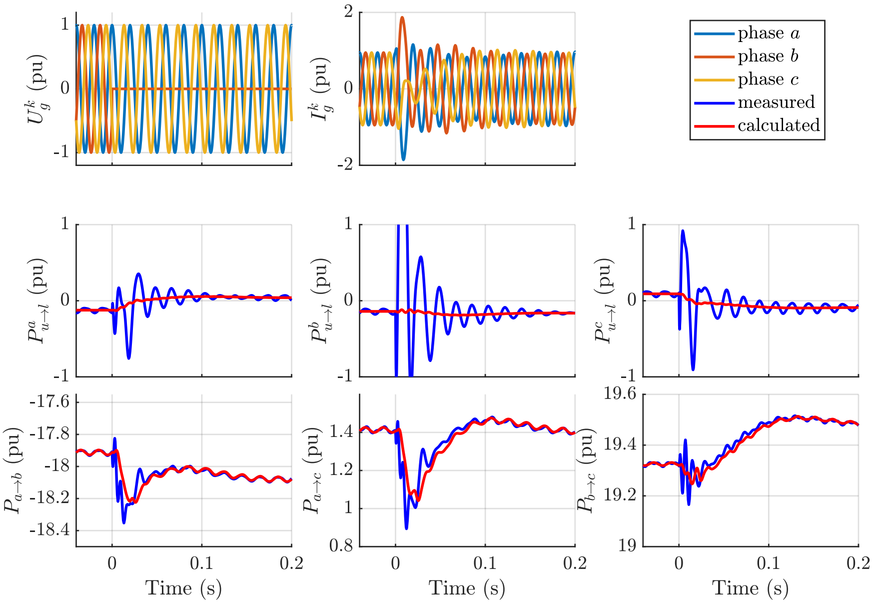

Fig. 2.13: Time-domain waveforms comparison for the internal power mismatch during a SLG fault.

2.7 Conclusion

A comprehensive analysis of the interactions caused by the several DOFs in the internal energy balancing of the MMC has been presented. Firstly, a steady-state analysis of the converter is performed to identify the DOFs of the converter. Then, an in-depth parametrization of the per-arm additive and differential voltage and current quantities has been developed. Based on this quantities, the expressions for the total power shared between the AC/DC networks, the powers transferred vertically and horizontally have been derived. The equations have indicated that although the additive and differential circuits are decoupled, their quantities interact with each other in order to achieve internal energy balancing, specially for the vertical transfer. To validate the theoretical analysis, simulation results have been carried out for an average model of the MMC, whereby different case studies proved the existence of the aforementioned power transfer interactions.

Chapter 3

Control of Modular Multilevel Converter under singular voltage sags

This chapter is a revised version of the following publication:
[**J2**] D. Westerman Spier, E. Prieto-Araujo, J. López-Mestre and O. Gomis-Bellmunt, "Improved current reference calculation for MMCs internal energy balancing control", in *IEEE Transactions on Power Delivery*, 2020.

3.1 Introduction

For a proper operation, all the MMC's DOFs must be properly regulated to ensure that the several magnitudes of the converter (i.e. the AC and DC networks currents, circulating current, submodule capacitor voltages) are within a desired level [52, 53]. As observed in the previous chapter, if the DOFs are improperly used, they can cause uneven power exchanges between the converter's arms and phase-legs leading to high internal energy deviations, especially during unbalanced AC network voltage conditions. Such issue must be quickly compensated to avoid tripping the converter.

Relevant reference calculation approaches and control strategies have been proposed to analyze and mitigate the effects of unbalanced AC network voltages. In [40], the controllers were derived targeting the horizontal (between phase-legs) energy regulation of the converter during AC single-line-to-ground fault. Still focusing on the phase-leg balancing of the MMC, [41] improves it through AC zero-sequence voltage injection while [37] analyzes the energy dynamic response for different DC circulating current scenarios. By considering not only the horizontal balancing but also the energy transfer between the upper and lower arms, further improvements can be achieved in the transient response of the converter [46]. References [36, 38, 43] derive distinct methods to perform the vertical energy balance of the MMC, but they only consider the DC characteristics of the circulating current. Authors in [39, 44, 45] employ both AC and DC components of the circulating current in their control design. In [44], the MMC's AC circulating current reference calculation is performed based only on the positive sequence of the AC grid voltage, whereas [39] also uses the negative sequence component. Still, the former proposals neglected the impact that the equivalent impedance of the MMC causes in the arms' applied voltages. Such influence is considered in [45], whereby an optimization algorithm using a linear matrix inequality approach is proposed to calculate the circulating current reference.

Although the previous methods are capable of controlling the MMC under unbalanced AC network conditions, during unbalanced scenarios whereby the positive and negative components of either the AC grid voltages or the MMC's internal voltages are equal, they might result in singularities in the current reference calculation. This problem was addressed for two-level VSCs by [54], and possible solutions were proposed for MMC applications during the former AC grid voltage sag in [33].

To the best of the authors knowledge, a control strategy that is capable of dealing with different unbalanced AC voltage sags (in particular internal singular voltage sags and singular AC network faults), while maintaining the upper and lower arms energies balanced has not been proposed yet. Another research gap considered in this chapter regards the addition of the internal impedance effects on the AC additive voltage during the derivation of the MMC's circulating current references. Next, the main contributions of this chapter are highlighted:

- Comparison among different AC additive current reference calculations and their potential usage during singular voltage condition.

- The DC differential zero-sequence voltage component U_{diff}^{0DC} is employed to enhance the power balancing between the upper and lower arms throughout the operation of the converter (balanced or unbalanced).

- Improvements in the solutions proposed in [33] with the addition of U_{diff}^{0DC} and the MMC's equivalent impedance.

- The degrees of freedom of the MMC are fully exploited by the current reference calculations.

- Comprehensive additive current reference calculation able to operate in any grid voltage condition.

The proposed reference calculation is compared with different methods by means of time-domain simulation results for distinct AC grid and internal singular voltage sag conditions. In addition, the effects of U_{diff}^{0DC} are also analyzed according to the reference calculation approach employed.

3.2 MMC control system

In this section, the overall control system to regulate the MMC and the methodology to calculate the additive and AC network current references are presented. The employed control scheme, shown in Fig. 3.1, uses the design procedures derived in [39] and can be divided into two main parts: the AC grid current control and the circulating current control. For the AC grid current stage, the current references are calculated based on the active and reactive power set-points required by the TSO and the magnitude of the positive-sequence component of the AC network voltage. Then, such references are employed into the grid side current control loops. The energy controllers are designed to maintain the internal energy balance of the converter. This is achieved through six different control loops which regulates the MMC's total internal energy E_t, the energy difference between the converter's phase-legs $E_{a\rightarrow b}$ and $E_{a\rightarrow c}$ and the energy mismatch between the converter's arms $E_{u\rightarrow l}^{k}$. Such energy regulators result in the power references necessary to calculate the AC and DC inner current set-points, highlighted in yellow in Fig. 3.1. These current references can be obtained through different methods according to the quantities that are used in the calculation (see method selection in Fig. 3.1 and Sections 3.3 and 3.4), which are later tracked by the additive current controllers.

For the sake of completeness, the reference calculation procedures for the AC grid currents and for the DC component of the additive currents are briefly described next, which more details can be found in [39]. On the other hand, a comprehensive analysis of different methods to calculate the current references for the AC component of the additive current is given. In addition, such approaches are compared regarding their applicability during faults and exploitation of the MMC's degrees of freedom.

3.2.1 AC network current reference calculation

Under balanced conditions, the AC grid currents present a symmetrical profile. However, during unbalanced AC voltage sags, the three-

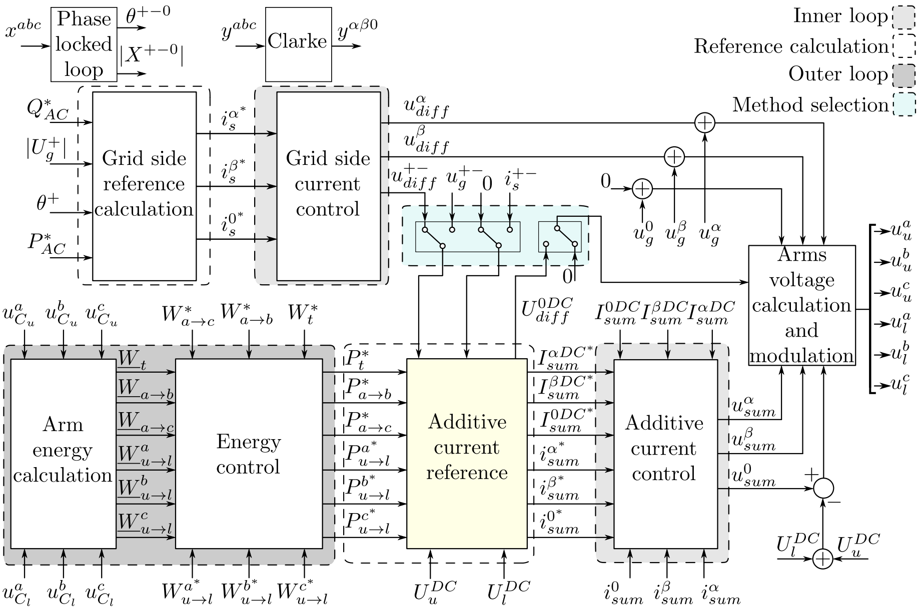

Fig. 3.1: Overall control scheme of the MMC converter for grid-following applications.

phase system may have different voltage levels for each phase (due to the presence of negative-sequence components), which might result in unbalanced currents circulating through the AC network. In general, the AC grid current references are calculated by considering only the positive-sequence of the AC grid voltages, either for balanced or unbalanced scenarios [55].

3.2.2 Additive current reference calculation

Generally, the DC components of the additive current are used to regulate the power transfer among the phase-legs of the converter. Whereas the AC components are employed to control the power exchanged between the MMC's upper and lower arms (vertical balancing) as discussed in Chapter 2.

DC component of the additive current

The DC terms of the additive current can be applied in the regulation of the energy exchanged horizontally. In addition, notch filters must be used to eliminate the line and double-line frequency power components coming from the energy controllers [39].

AC component of the additive current

To calculate the AC additive current references it is necessary to obtain a mathematical expression relating the power difference between the MMC's upper and lower halves with their respective applied voltages. At one hand, the arm's applied voltages can be considered to be equal to the AC network voltage (assuming that the equivalent impedance of the converter is small). The main advantages of such approach regards its simplicity and straightforwardness, since it uses the measurements from the AC system. However, this method presents a discontinuity when the positive- and negative-sequence components of the AC grid voltages are equal or almost equal (singular condition, see Table 3.1) [33]. As a consequence, the additive current references saturate, compromising the vertical energy balancing controller. Another candidate solution would to employ the differential voltages resultant from the grid side current control as the arm's applied voltages, but as it will be demonstrated later, this strategy also fails if the internal voltages present singular characteristics.

3.3 Comparison among different AC additive current reference calculation strategies

In this section, different methods to calculate the AC additive current references are presented. These approaches vary according to the voltages that are considered to be applied into the MMC's arms (AC grid or differential voltages). For balanced and several unbalanced network conditions, the distinct strategies can maintain the converter stable and provide proper current references. However, certain unbalanced AC grid voltage sags may lead to internal singular voltage conditions that must also be addressed during the derivation of the additive current references to avoid discontinuities of the system.

3.3.1 Internal singular voltage sag analysis

An internal singular voltage event is defined when the positive-sequence component of the AC differential voltage is equal to the negative one ($\underline{U}^{+}_{diff} = \underline{U}^{-}_{diff}$). In order to derive the expression for such fault, let's first assume that the AC differential voltages are calculated as [56]

$$\underline{U}^{+}_{diff} = \underline{U}^{+}_{g} + \underline{Z}_{eq}\underline{I}^{+}_{s} \tag{3.1a}$$

$$\underline{U}^{-}_{diff} = \underline{U}^{-}_{g} + \underline{Z}_{eq}\underline{I}^{-}_{s} \tag{3.1b}$$

Table 3.1: Singular AC network voltage faults [33].

Type	Voltages abc	Voltages $+-0$	Phasors abc
A	$\underline{U}_g^a = 0$ $\underline{U}_g^b = 0$ $\underline{U}_g^c = 0$	$\underline{U}_g^+ = 0$ $\underline{U}_g^- = 0$ $\underline{U}_g^0 = 0$	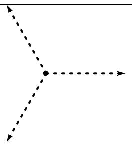
B	-	-	-
C	$\underline{U}_g^a = E_1$ $\underline{U}_g^b = -\frac{1}{2}E_1$ $\underline{U}_g^c = -\frac{1}{2}E_1$	$\underline{U}_g^+ = \frac{1}{2}E_1$ $\underline{U}_g^- = \frac{1}{2}E_1$ $\underline{U}_g^0 = 0$	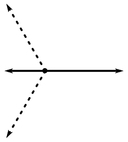
D	$\underline{U}_g^a = 0$ $\underline{U}_g^b = -\frac{1}{2}jE_1\sqrt{3}$ $\underline{U}_g^c = +\frac{1}{2}jE_1\sqrt{3}$	$\underline{U}_g^+ = \frac{1}{2}E_1$ $\underline{U}_g^- = -\frac{1}{2}E_1$ $\underline{U}_g^0 = 0$	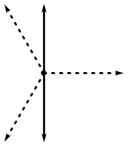
E	$\underline{U}_g^a = E_1$ $\underline{U}_g^b = 0$ $\underline{U}_g^c = 0$	$\underline{U}_g^+ = \frac{1}{3}E_1$ $\underline{U}_g^- = \frac{1}{3}E_1$ $\underline{U}_g^0 = \frac{1}{3}E_1$	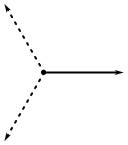
F	$\underline{U}_g^a = 0$ $\underline{U}_g^b = j\frac{\sqrt{3}}{3}E_1$ $\underline{U}_g^c = j\frac{\sqrt{3}}{3}E_1$	$\underline{U}_g^+ = \frac{1}{3}E_1$ $\underline{U}_g^- = -\frac{1}{3}E_1$ $\underline{U}_g^0 = 0$	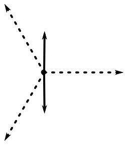
G	$\underline{U}_g^a = \frac{2}{3}E_1$ $\underline{U}_g^b = -\frac{1}{3}E_1$ $\underline{U}_g^c = -\frac{1}{3}E_1$	$\underline{U}_g^+ = \frac{1}{3}E_1$ $\underline{U}_g^- = \frac{1}{3}E_1$ $\underline{U}_g^0 = 0$	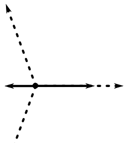

The scenario where $\underline{U}_{diff}^{+} = \underline{U}_{diff}^{-}$ is obtained by equating (3.1a) and (3.1b). As a result, an expression that describes in which condition the converter's applied voltages present singular behavior is given as follows

$$\underline{U}_{g}^{-} = \underline{U}_{g}^{+} + \underbrace{\underline{Z}_{eq}\left(\underline{I}_{s}^{+} - \underline{I}_{s}^{-}\right)}_{\text{internal factor}} \tag{3.2}$$

As mentioned in Section 3.2.1, the AC grid controllers are designed to inject only positive-sequence current component into the grid, thus $\underline{I}_{s}^{-} = 0$. Furthermore, it can be observed that this type of fault not only depends on the AC grid voltage characteristics but is also affected by the interaction between the MMC's equivalent impedance and the AC grid currents. In this chapter, it is considered that the internal factor is constant, since the controllers will keep injecting the same positive-sequence current levels into the AC grid throughout the converter's operation.

3.3.2 Method 0 - Initial approach $\underline{U}_{u,l}^{k} = \underline{U}_{g}^{k}$

This methodology is the most straightforward one to calculate the AC additive current references of the MMC. It assumes that the equivalent impedance of the converter is small and by doing so, the AC arm voltage can be considered equal to the AC grid voltage. However, during AC grid faults where the positive-sequence voltage component is equal to the negative one this method fails [39]. Such condition arises because the current reference calculation will present a discontinuity in this operating point. As a consequence, it will try to impose very high AC additive currents to circulate through the MMC, which must be disconnected to avoid damaging the converter.

3.3.3 Method 1 - Method 0 considering U_{diff}^{0DC}

This reference calculation applies the techniques developed in [33] employing U_{diff}^{0DC}. Next, the method's working principle along with the calculation and regulation of U_{diff}^{0DC} are described.

Working principle

This method removes one of the DOFs from the AC additive current that does not contribute to the power exchanged within the MMC arms. By doing so, the discontinuity is avoided but there will be a sustained constant energy deviation between the phase-legs of the converter throughout the fault. This approach can be further improved by replacing the degree of freedom that was lost with the DC differential zero-sequence voltage component U_{diff}^{0DC}.

Regulation of U_{diff}^{0DC}

During balanced conditions, this voltage is equal to zero as both upper and lower arms have the same DC voltage level. Under transients, on the other hand, U_{diff}^{0DC} is different than zero and its magnitude can be applied into the MMC's arms to improve the energy balancing between them. Such degree of freedom can be obtained as

$$U_{diff}^{0DC} = \frac{P_{u\rightarrow l}^{a} + P_{u\rightarrow l}^{b} + P_{u\rightarrow l}^{c}}{3I_{sum}^{0DC}} \tag{3.3}$$

where $P_{u\rightarrow l}^{abc}$ are the power difference between the upper and lower arms and $I_{sum}^{0DC} \neq 0$ (to avoid discontinuities). By using this degree of freedom, the energy deviations are eliminated and controlled power can be transmitted within the MMC's arms, enhancing the converter response during singular AC grid voltage conditions (see Section 3.5). In Fig. 3.2, the control structure employed in the regulation of U_{diff}^{0DC} is depicted. As aforementioned, the unregulated value of U_{diff}^{0DC} is calculated based on the equation shown above, and compared to its desired magnitude (set to be equal to zero), resulting in the error $\boldsymbol{e}$. This error goes to a PI controller, which is designed to quickly compensate any voltage disparity caused by the zero-sequence power mismatch between the upper and lower arms of the converter. By doing so, the sustained energy deviations observed when other control methods are used, as it was pointed out by [33], can be eliminated. The controller gains employed in this chapter are set to be equal to $k_p = 0.25$ and $k_i = 12$, whereby the gain selection was done based on the response of U_{diff}^{0DC} for different AC and internal singular voltage sag conditions. Finally, a saturation block is added as a safety factor to prevent high values of U_{diff}^{0DC} which would result in overmodulations.

3.3.4 Method 2 - Arm voltages equal to the DC and AC differential voltages $\underline{U}_{u,l}^{+-} = \underline{U}_{diff}^{+-} + U_{diff}^{0DC}$

An alternative solution to the former problems would be to replace the AC grid voltages by the positive- and negative-sequence components of

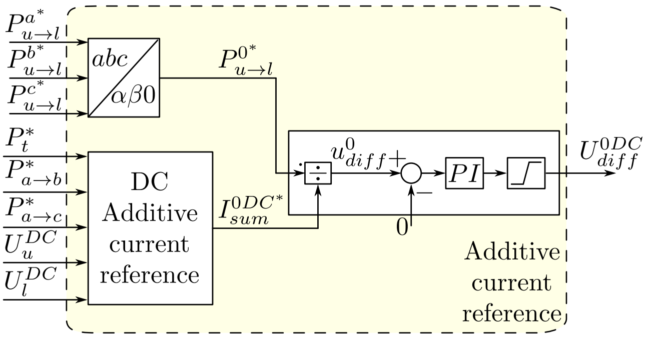

Fig. 3.2: U^{0DC}_{diff} control structure.

the internal differential voltages of the converter. Consequently, the MMC equivalent impedance will not be neglected, having a more realistic AC voltage level in the converter's arms. For this strategy, however, the differential voltage controllers should be fast enough to avoid inaccuracies due to the interactions between the two regulators [57]. Nevertheless, even if such requirements are fulfilled, in a situation where the MMC's internal differential voltages are equal, $U^+_{diff} = U^-_{diff}$, the discontinuity will also occur and the vertical energy balancing of the converter will be compromised.

3.3.5 Method 3 - Method 1 with $\underline{U}^{+-}_{u,l} = \underline{U}^{+-}_{diff} + U^{0DC}_{diff}$

Now, the principles in Method 1 are extended by considering that the arm's applied voltages are equal to the differential ones. If only the AC differential terms are employed, during fault event where $U^+_{diff} = U^-_{diff}$, the continued energy deviation would also be observed and would be compensated with the zero sequence DC differential voltage. However, as it will be shown in Section 3.5, the energy drifts will cause the U^{0DC}_{diff} controllers to saturate due to the limited voltage application range. Consequently, the vertical energy regulators will not be able to compensate the power transferred within the converter's arms, leading to the eventual disconnection of the system.

3.4 Method 4 - Proposed approach considering the additive and differential voltage components in the arm

The previous methods present distinct strategies to calculate the AC additive current by using different quantities as the applied voltages in the

MMCs arms. But, they share the same characteristic where the additive voltage effects in the arm are neglected. At one hand, it seems that such voltage cannot be part of the AC additive current references without an iterative control method. However, using a simple mathematical substitution, which does not require any optimization, iterative control or violate any constraint imposed in the steady-state analysis, it is possible to obtain an expression that can be employed as such reference calculation for any AC grid or arm singular voltage sag condition. Although the applied voltages DOFs, currents and power transfers have been defined in the previous chapter, for the sake of easing the understanding the proposed method, they are rewritten in this chapter as

$$\underline{U}^{k}_{u,l} = \mp \underline{U}^{k}_{diff} + \frac{\underline{U}^{k}_{sum}}{2} \tag{3.4a}$$

$$\begin{aligned} u^{k}_{u,l}(t) = \sqrt{2}\Bigg(& \mp U^{+}_{diff}\cos\left(\omega t + \theta^{+}_{diff} + \alpha^{k}\right) \mp \\ & \mp U^{-}_{diff}\cos\left(\omega t + \theta^{-}_{diff} - \alpha^{k}\right) + \frac{U^{+}_{sum}}{2}\cos\left(\omega t + \theta^{+}_{sum} + \alpha^{k}\right) + \\ & + \frac{U^{-}_{sum}}{2}\cos\left(\omega t + \theta^{-}_{sum} - \alpha^{k}\right)\Bigg) + \left(\frac{U^{kDC}_{sum}}{2} \mp U^{0DC}_{diff}\right) \end{aligned} \tag{3.4b}$$

where the sign ∓ indicates that the AC differential DOFs for the upper arms are negative, $u^{k}_{u} = -u^{k}_{diff} + \frac{u^{k}_{sum}}{2}$, while for the lower arms the AC differential DOFs are positive, $u^{k}_{l} = u^{k}_{diff} + \frac{u^{k}_{sum}}{2}$. $\alpha^{a} = 0, \alpha^{b} = -\frac{2\pi}{3}, \alpha^{c} = \frac{2\pi}{3}$ and $k \in \{a, b, c\}$. θ^{+}_{diff} and θ^{-}_{diff} are the phase-angles of the positive and negative sequence components of the AC differential DOFs, whereas θ^{+}_{sum} and θ^{-}_{sum} are the phase-angles for the positive- and negative-sequence AC additive DOF. Whereas, the upper and lower arms currents can be described as follows

$$\underline{I}^{k}_{u,l} = \pm \frac{\underline{I}^{k}_{s}}{2} + \underline{I}^{k}_{sum} \tag{3.5a}$$

$$\begin{aligned} i^{k}_{u,l}(t) = \sqrt{2}\Bigg(& \pm \frac{I^{+}_{s}}{2}\cos\left(\omega t + \phi^{+}_{s} + \alpha^{k}\right) \pm \\ & \pm \frac{I^{-}_{s}}{2}\cos\left(\omega t + \phi^{-}_{s} - \alpha^{k}\right) + I^{+}_{sum}\cos\left(\omega t + \phi^{+}_{sum} + \alpha^{k}\right) + \\ & + I^{-}_{sum}\cos\left(\omega t + \phi^{-}_{sum} - \alpha^{k}\right)\Bigg) + I^{kDC}_{sum} \end{aligned} \tag{3.5b}$$

where similarly to the arms' applied voltages, the sign ± is an indication that $i_u^k = \frac{i_s^k}{2} + i_{sum}^k$ and $i_l^k = -\frac{i_s^k}{2} + i_{sum}^k$. Furthermore, ϕ_s^+ and ϕ_{sum}^+ are the phase-angles of the positive-sequence additive and AC grid currents, respectively, while ϕ_s^- and ϕ_{sum}^- are the phase-angles of the negative-sequence current components. Having defined the upper and lower arms voltages and currents with the additive and differential quantities, it is possible to describe the power difference between the upper and lower arms as

$$P_{u\to l}^k = P_u^k - P_l^k = \mathrm{Re}\left\{ \underline{U}_u^k \underline{I}_u^k - \underline{U}_l^k \underline{I}_l^k \right\} + U_u^{kDC} I_u^{kDC} - U_l^{kDC} I_l^{kDC} \tag{3.6}$$

Replacing (3.4b) and (3.5b) in (3.6), the power differences are obtained in matrix form as follows

$$P_{u\to l}^k = \begin{bmatrix} U_{diff}^+ \\ U_{diff}^- \\ I_s^+ \\ I_s^- \end{bmatrix}^T \begin{bmatrix} A_{11} & A_{12} & A_{13} & A_{14} \\ A_{21} & A_{22} & A_{23} & A_{24} \\ A_{31} & A_{32} & A_{33} & A_{34} \\ A_{41} & A_{42} & A_{43} & A_{44} \end{bmatrix} \begin{bmatrix} I_{sum}^+ \\ I_{sum}^- \\ U_{sum}^+ \\ U_{sum}^- \end{bmatrix} - 2U_{diff}^{0DC} I_{sum}^{0DC} \begin{bmatrix} 1 \\ 1 \\ 1 \end{bmatrix} \tag{3.7}$$

$$A_{11} = -2\cos(\theta_{diff}^+ - \phi_{sum}^+), \quad A_{12} = -2\cos(\theta_{diff}^+ - \phi_{sum}^- - \alpha^k), \quad A_{13} = A_{14} = 0$$

$$A_{21} = -2\cos(\theta_{diff}^- - \phi_{sum}^+ + \alpha^k), \quad A_{22} = -2\cos(\theta_{diff}^- - \phi_{sum}^-), \quad A_{23} = -Z_a$$

$$A_{31} = A_{32} = 0, \quad A_{33} = \frac{\cos(\theta_{sum}^+ - \phi_s^+)}{2}, \quad A_{34} = \frac{\cos(\theta_{sum}^- - \phi_s^+ + \alpha^k)}{2}$$

$$A_{41} = A_{42} = 0, \quad A_{43} = \frac{\cos(\theta_{sum}^+ - \phi_s^- - \alpha^k)}{2}, \quad A_{44} = \frac{\cos(\theta_{sum}^- - \phi_s^-)}{2}$$

It can be observed that the left matrix consists of the AC grid currents and differential voltages whereas the far right matrix contains the additive voltages and currents. Furthermore, the phase-angle differences for each power element indicates an interaction between the additive and differential quantities. Although (3.7) can express the power transfer between the upper and lower arms of the converter, employing it in a control strategy to calculate the AC components additive current references might be challenging as it would require iterative calculation methods.

A simple approach would be to neglect the additive voltages and to consider only the differential terms in the reference calculation. However, as discussed in Section 3.3, this approximation fails during internal singular voltage sag conditions. In order to overcome such issue and to increase the operating range of the converter, the proposed reference calculation substitute $\underline{U}^{+-}_{sum}$ by an equation containing the arm impedance and the additive current, yielding

$$\underline{U}^{+}_{sum} = -2Z_a I^{+}_{sum}\underline{/\rho + \phi^{+}_{sum}} \tag{3.8a}$$

$$\underline{U}^{-}_{sum} = -2Z_a I^{-}_{sum}\underline{/\rho + \phi^{-}_{sum}} \tag{3.8b}$$

where ρ is the phase-angle of the arm impedance $\underline{Z}_a$. Replacing the additive voltages in (3.4b) with the new expressions from (3.8), the final equations for the vertical power transfer are obtained and expressed in (3.9).

$$P^{k}_{u\rightarrow l} = \begin{bmatrix} U^{+}_{diff} \\ U^{-}_{diff} \\ I^{+}_{s} \\ I^{-}_{s} \end{bmatrix}^{T} \begin{bmatrix} B_{11} & B_{12} \\ B_{21} & B_{22} \\ B_{31} & B_{32} \\ B_{41} & B_{42} \end{bmatrix} \begin{bmatrix} I^{+}_{sum} \\ I^{-}_{sum} \end{bmatrix} - 2U^{0DC}_{diff} I^{0DC}_{sum} \begin{bmatrix} 1 \\ 1 \\ 1 \end{bmatrix} \tag{3.9}$$

$$B_{11} = -2\cos\left(\theta^{+}_{diff} - \phi^{+}_{sum}\right), \quad B_{12} = -2\cos\left(\theta^{+}_{diff} - \phi^{-}_{sum} - \alpha^{k}\right)$$

$$B_{21} = -2\cos\left(\theta^{-}_{diff} - \phi^{+}_{sum} + \alpha^{k}\right), \quad B_{22} = -2\cos\left(\theta^{-}_{diff} - \phi^{-}_{sum}\right)$$

$$B_{31} = -Z_a\cos\left(\rho + \phi^{+}_{sum} - \phi^{+}_{s}\right), \quad B_{32} = -Z_a\cos\left(\rho + \phi^{-}_{sum} - \phi^{+}_{s} - \alpha^{k}\right)$$

$$B_{41} = -Z_a\cos\left(\rho + \phi^{+}_{sum} - \phi^{-}_{s} + \alpha^{k}\right), \quad B_{42} = -Z_a\cos\left(\rho + \phi^{-}_{sum} - \phi^{-}_{s}\right)$$

Comparing (3.7) and (3.9), it can be noted that the substitution does not change the number of terms in the new power transfer equations;

thus, the degrees of freedom of the converter are still being fully exploited. The three vertical power quantities $\left(P^a_{u\rightarrow l}, P^b_{u\rightarrow l}, P^c_{u\rightarrow l}\right)$ are adjusted based on four parameters $\left(I^+_{sum}, I^-_{sum}, \phi^+_{sum}, \phi^-_{sum}\right)$, since the AC grid current and the AC differential voltage magnitudes are given values that are regulated independently of the internal powers. By choosing that the reactive component of the positive additive current is equal to zero ($\sin(\phi^+_{sum}) = 0$), (3.9) can be reduced to

$$\underbrace{\begin{bmatrix} P^a_{u\rightarrow l} \\ P^b_{u\rightarrow l} \\ P^{ac}_{u\rightarrow l} \end{bmatrix}}_{\text{P}} = \underbrace{\begin{bmatrix} M_{11} & M_{12} & M_{13} \\ M_{21} & M_{22} & M_{23} \\ M_{31} & M_{32} & M_{33} \end{bmatrix}}_{\text{M}} \underbrace{\begin{bmatrix} I^-_{sum}\cos\phi^-_{sum} \\ I^-_{sum}\sin\phi^-_{sum} \\ I^+_{sum}\cos\phi^+_{sum} \end{bmatrix}}_{I^{AC}} - 2U^{0DC}_{diff}\, \underbrace{I^{0DC}_{sum}\begin{bmatrix} 1 \\ 1 \\ 1 \end{bmatrix}}_{I^{DC}} \tag{3.10}$$

where,

$$M_{11} = Z_{arm}\left(-I^+_s\cos\left(\rho - \phi^+_s\right) - I^-_s\cos\left(\rho - \phi^-_s\right)\right) - 2U^+_{diff}\cos\left(\theta^+_{diff}\right) - 2U^-_{diff}\cos\left(\theta^-_{diff}\right)$$

$$M_{12} = Z_{arm}\left(I^+_s\sin\left(\rho - \phi^+_s\right) + I^-_s\sin\left(\rho - \phi^-_s\right)\right) - 2U^+_{diff}\sin\left(\theta^+_{diff}\right) - 2U^-_{diff}\sin\left(\theta^-_{diff}\right)$$

$$M_{13} = M_{11}$$

$$\begin{aligned} M_{21} = Z_{arm}&\left(I^+_s\cos\left(\rho - \phi^+_s - \frac{2\pi}{3}\right) - I^-_s\cos\left(\rho - \phi^-_s\right)\right) - \\ &- 2U^+_{diff}\cos\left(\theta^+_{diff} + \frac{2\pi}{3}\right) - 2U^-_{diff}\cos\left(\theta^-_{diff}\right) \end{aligned}$$

$$\begin{aligned} M_{22} = Z_{arm}&\left(-I^+_s\cos\left(\rho - \phi^+_s - \frac{\pi}{6}\right) + I^-_s\sin\left(\rho - \phi^-_s\right)\right) - \\ &- 2U^+_{diff}\cos\left(\theta^+_{diff} + \frac{\pi}{6}\right) - 2U^-_{diff}\sin\left(\theta^-_{diff}\right) \end{aligned}$$

$$\begin{aligned} M_{23} = Z_{arm}&\left(-I^+_s\sin\left(\rho - \phi^+_s\right) - I^-_s\cos\left(\rho - \phi^-_s + \frac{2\pi}{3}\right)\right) - \\ &- 2U^-_{diff}\cos\left(\theta^-_{diff} - \frac{2\pi}{3}\right) - 2U^+_{diff}\cos\left(\theta^+_{diff}\right) \end{aligned}$$

$$\begin{aligned}M_{31} = Z_{arm} &\left(-I_s^+ \cos\left(\rho - \phi_s^+ + \frac{2\pi}{3}\right) - I_s^- \cos\left(\rho - \phi_s^-\right)\right) - \\ &- 2U_{diff}^+ \cos\left(\theta_{diff}^+ - \frac{2\pi}{3}\right) - 2U_{diff}^- \cos\left(\theta_{diff}^-\right)\end{aligned}$$

$$\begin{aligned}M_{32} = Z_{arm} &\left(I_s^+ \cos\left(\rho - \phi_s^+ + \frac{\pi}{6}\right) + I_s^- \sin\left(\rho - \phi_s^-\right)\right) + \\ &+ 2U_{diff}^+ \cos\left(\theta_{diff}^+ - \frac{\pi}{6}\right) - 2U_{diff}^- \sin\left(\theta_{diff}^-\right)\end{aligned}$$

$$\begin{aligned}M_{33} = Z_{arm} &\left(-I_s^+ \cos\left(\rho - \phi_s^+\right) - I_s^- \cos\left(\rho - \phi_s^- - \frac{2\pi}{3}\right)\right) - \\ &- 2U_{diff}^- \cos\left(\theta_{diff}^- + \frac{2\pi}{3}\right) - 2U_{diff}^+ \cos\left(\theta_{diff}^+\right)\end{aligned}$$

Based on the vertical power references provided by the energy controllers, the AC additive current references can be obtained from (3.10) as

$$\begin{aligned}&\begin{bmatrix} I_{sum}^- \cos\phi_{sum}^- \\ I_{sum}^- \sin\phi_{sum}^- \\ I_{sum}^+ \cos\phi_{sum}^+ \end{bmatrix} = 2U_{diff}^{0DC} I_{sum}^{0DC} \begin{bmatrix} 1 \\ 1 \\ 1 \end{bmatrix} + \frac{1}{\det M} \\ &\begin{bmatrix} M_{22}M_{33} - M_{23}M_{32} & M_{13}M_{32} - M_{12}M_{33} & M_{12}M_{23} - M_{13}M_{22} \\ M_{23}M_{31} - M_{21}M_{33} & M_{11}M_{33} - M_{13}M_{31} & M_{11}M_{23} - M_{13}M_{21} \\ M_{21}M_{32} - M_{22}M_{31} & M_{12}M_{31} - M_{11}M_{32} & M_{11}M_{22} - M_{12}M_{21} \end{bmatrix} \begin{bmatrix} P_{u\to l}^a \\ P_{u\to l}^b \\ P_{u\to l}^{ac} \end{bmatrix}\end{aligned} \tag{3.11}$$

The determinant of matrix M, during an internal singular voltage sag condition and considering that the AC grid current consists only of positive-sequence component, is equal to

$$\begin{aligned}\det M = &- \frac{3Z_{arm}^3 {I_s^+}^3 \sqrt{3}\cos(\rho - \phi_s^+)}{2} - \\ &- 3U_{diff}^+ \sqrt{3} {I_s^+}^2 Z_{arm}^2 \cos(2\rho - 2\phi_s^+ + \theta_{diff}^+) - \\ &- 6I_s^+ \sqrt{3} {U_{diff}^+}^2 Z_{arm} \cos(2\theta_{diff}^+ + \rho - \phi_s^+) - \\ &- 6I_s^+ \cos(\rho - \phi_s^+) \sqrt{3} {U_{diff}^+}^2 Z_{arm} - 6{I_s^+}^2 \cos(\theta_{diff}^+) \sqrt{3} U_{diff}^+ Z_{arm}^2\end{aligned} \tag{3.12}$$

As some TSOs demand the injection of reactive currents to provide voltage support [58, 59] or active currents for frequency support [60] to the faulted phases throughout voltage sag events, the positive-sequence component of the AC grid current I_s^+ will generally be different than zero. Therefore, the suggested reference calculation will not present any discontinuities during internal singular voltage sag conditions, as it can be noted from (3.12). Finally, the main characteristics of the different AC additive current reference calculation methods are summarized in Table 3.2.

Table 3.2: Methods summary.

Characteristics	**Method**				
	0	1	2	3	4
MMC equivalent impedance	✗	✗	✓	✓	✓
No energy drifts among phase-legs	✓	✗	✓	✗	✓
Used for any voltage sag condition	✗	✗	✗	✗	✓
Additive voltage effects	✗	✗	✗	✗	✓
Degrees of freedom are fully exploited	✗	✗	✗	✗	✓

3.5 Case study

In this section, time-domain simulations are carried out in Matlab® Simulink to analyze the performance of the different reference calculation methods during AC grid (Section 3.5.1) and internal singular (Section 3.5.2) voltage sag conditions. The simulations are performed considering an accelerated model of the MMC [61] and employing the Nearest Level Control (NLC) technique to calculate the number of active submodules in each arm [62]. In addition, the converter is considered to be operating under balanced AC grid conditions when the fault occurs. Both fault events last three seconds (starting at $t = 2$ s and restored at $t = 5$ s) [1] to verify if the methods are able to keep the converter operational and to highlight the differences among them. Table 3.3 details the system parameters for the case studies.

3.5.1 AC grid singular voltage condition

This case study is performed to illustrate the different dynamic behaviors that the converter will present according to the AC additive current reference calculation method used during an AC grid singular voltage

---

[1] Note that for real networks, the maximum allowed time for fault-ride through would be equal to 250 ms [63].

Table 3.3: System parameters.

Parameter	**Symbol**	**Value**	**Units**
Rated power	S	1000	MVA
Rated power factor	$\cos\phi$	0.95 (c)	-
AC-side rated voltage	$\underline{U}_g$	325	kV
HVDC link voltage	U^{DC}	±320	kV
Phase reactor impedance	$\underline{Z}_s$	0.005+j 0.18	pu
Arm reactor impedance	$\underline{Z}_{arm}$	0.01+j 0.15	pu
Converter modules per arm	N^k_{u,l_a}	433	-
Submodule capacitance	C_{SM}	9.5	mF

condition type C [33]. Under such fault event, the positive- and negative-sequence AC network voltage components have the same magnitude and phase-angle. In Fig. 3.3, the MMC's internal energy transfer is shown for each phase throughout the simulation. It can be observed that only Method 0 leads to the disconnection of the converter which is in agreement with the theoretical analysis (see Section 3.3). Furthermore, when the fault occurs, a short sustained drift in the energy transfer between the arms of phase a ($E^a_{u\rightarrow l}$) for Methods 1 and 3 is noted. This happens because the DC differential zero-sequence voltage U^{0DC}_{diff} controller saturates while attempting to eliminate the energy difference between the phase-legs of the converter, as shown in Fig. 3.4. Otherwise, the modulation strategy might result in negative voltage levels to be applied into the SMs, which is not possible considering that half-bridge topologies are employed. If full-bridge SMs are considered, negative voltages could be imposed improving the dynamic response of the internal energy balancing.

In Fig. 3.5, the time-domain waveforms for the upper and lower power mismatches obtained employing (3.9) are shown. The vertical power transfer regarding U^{0DC}_{diff} is depicted in green, whereas the average AC power mismatches between the upper and lower arms is highlighted in red and the total value is represented as the blue continuous line. Among the fault occurrence and clearance transients highlighted in the figure, the DC component contribution is more evident during the fault event for phase a. Due to the characteristics of the fault and the AC grid current controller design, the active power injected in the faulted phases b and c is reduced, which is reflected inside the converter as a reduction in the DC additive circulating current levels for those phases. As a result, even though the DC zero-sequence voltage component is common for all the three phases, its effect is more significant for phase a since its DC additive current level is maintained constant during the fault event.

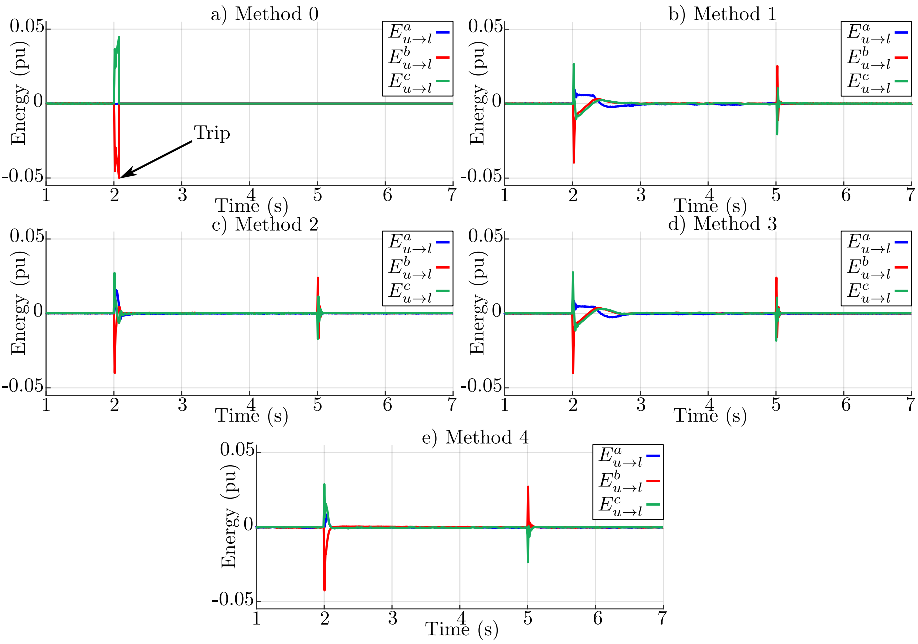

Fig. 3.3: Energy difference between the MMC arms during AC grid voltage singular condition.

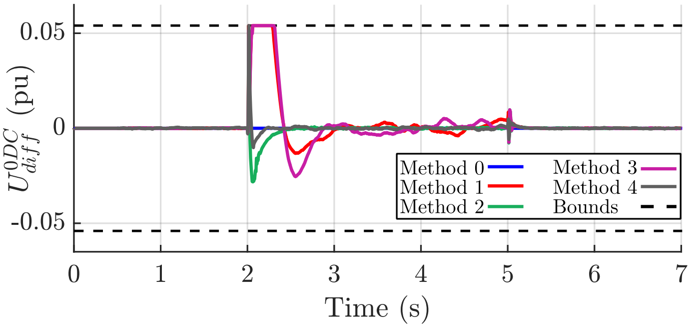

Fig. 3.4: U^{0DC}_{diff} levels during AC grid singular voltage sag for the different reference calculation methods.

Finally, it can be better noted during the fault occurrence transient for phase a that the power provided by U^{0DC}_{diff} provides a negative component which reduces the high oscillations caused by the AC power part in the total vertical power transfer.

3.5.2 Internal singular voltage condition

The objective of this case study is to show that the proposed AC additive current reference calculation can avoid the discontinuity of the system even during internal singular voltage sags. The AC grid voltages for this

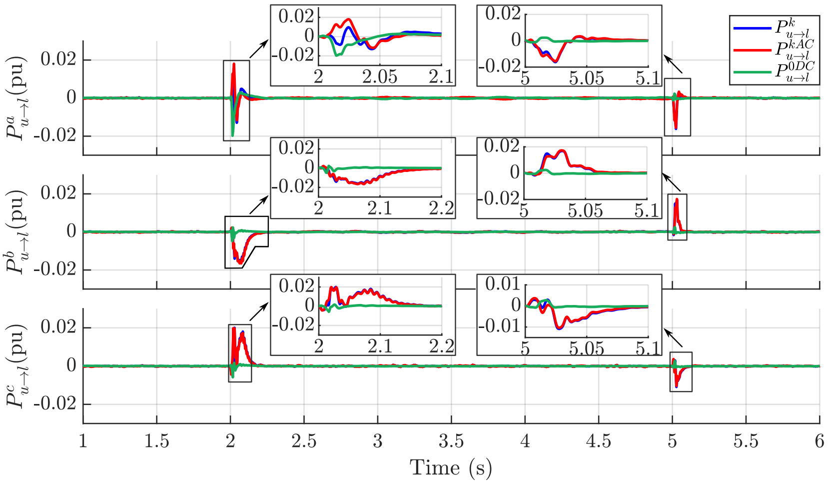

Fig. 3.5: Vertical power transfer during AC network singular voltage sag condition.

fault are calculated based on the expression given in (3.2), assuming an internal factor equals to $\underline{Z}_{eq}\underline{I}_s^+ = 0.24\underline{/87.75^o}$ pu and $\underline{U}_g^+ = 0.5\underline{/0^o}$ pu, resulting in the positive- and negative-sequence AC differential voltages to be equal to $\underline{U}_{diff}^+ = \underline{U}_{diff}^- = 0.56\underline{/25.49^o}$. The energy transfer profiles for each phase are shown in Fig. 3.6 for all the different reference calculation methods. It can be noted that, although Method 0 fails for AC grid singular voltage sag, it is capable of handling the internal singular voltage condition along with Method 4.

Regarding the DC zero-sequence differential voltage, Method 0 does not use it whereas all the other methods present either short or long saturation periods, as it can be seen in Fig. 3.7. Method 2 is saturated for the maximum and minimum voltage levels, but it is not able to improve the energy regulation, leading to the system disconnection. Methods 1 and 3 result in a sustained saturation, but they also fail to track the desired energy references. Although U_{diff}^{0DC} is also saturated using Method 4, it is quickly recovered.

In Fig. 3.8, the waveforms of the MMC quantities are presented showing its dynamic behavior during the fault event and when it is cleared. It can be noted that the arms applied voltages for phase b and c become equal for this type of fault. In addition, all the voltages applied to the converter are higher than zero ($0 \leqslant U_{u,l}^k$), which is obtained since the U_{diff}^{0DC} is saturated. Finally, Method 4 was the only AC additive current reference calculation approach that avoided the converter to be tripped for both AC grid and internal singular voltage sag condition.

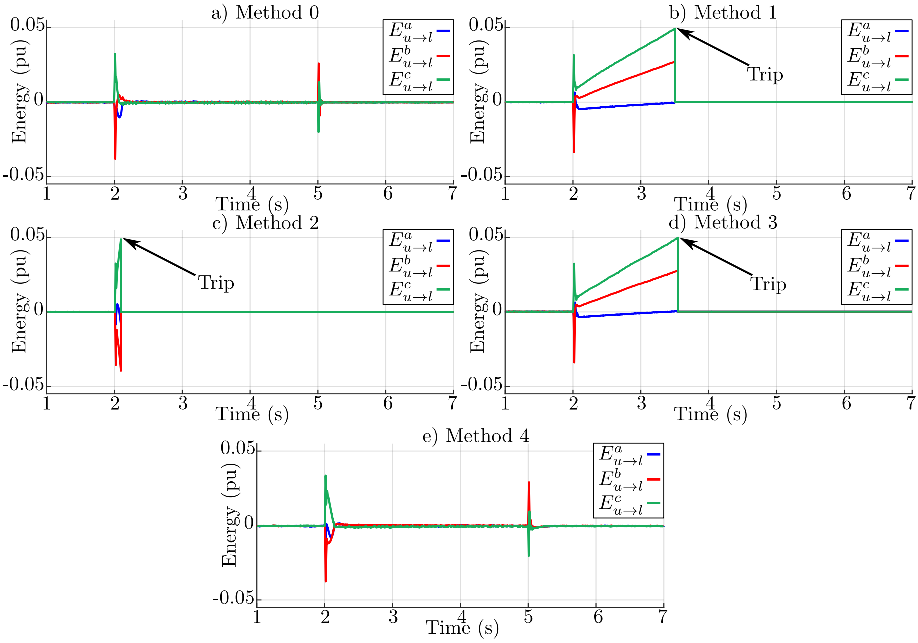

Fig. 3.6: Energy difference between the MMC arms during internal singular voltage sag condition.

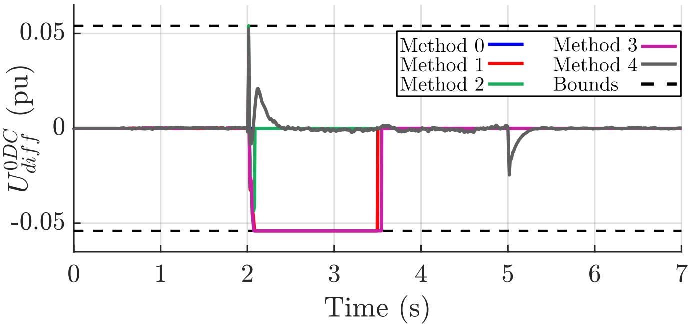

Fig. 3.7: U^{0DC}_{diff} levels during internal singular voltage sag for the different methods.

3.5.3 Other singular fault scenarios

In this section, the proposed method is compared with the other approaches for different types of internal and AC network singular voltage sag conditions. The simulations conducted focused on the upper and lower arms' energy mismatch throughout the operation of the converter to further validate the proposed method. In Figs. 3.9 to 3.12 the results obtained during AC grid singular voltage sags D to G [33] are shown,

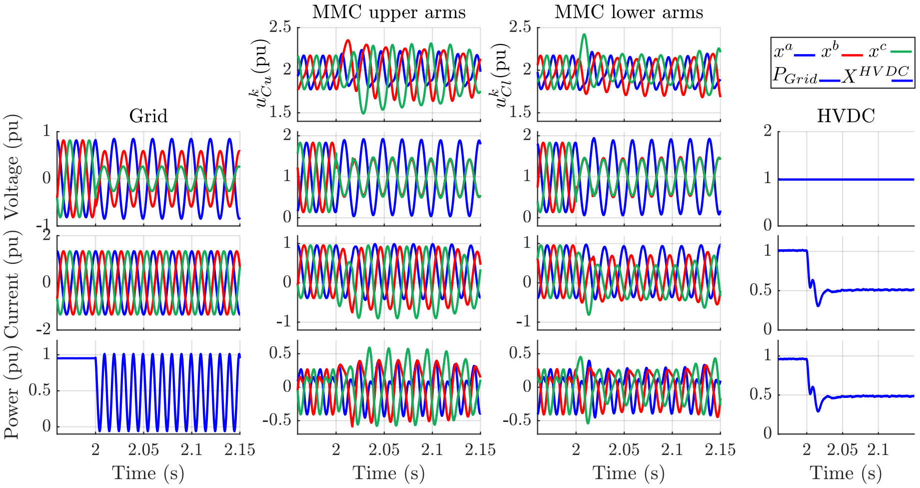

(a) Transition from normal operation to fault event.

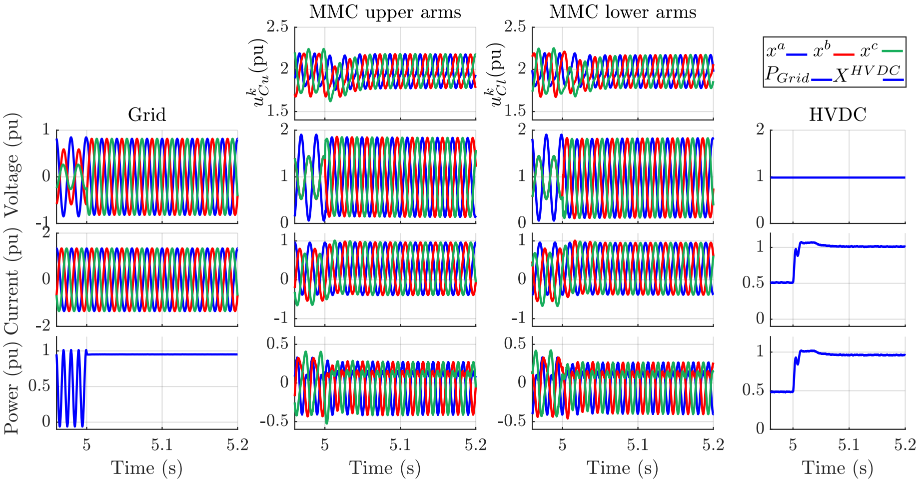

(b) Fault to normal.

Fig. 3.8: MMC waveforms during fault transients when Method 4 is employed. a) Fault is applied to the system and, b) Fault event is cleared.

whereas Figs. 3.13 to 3.16 depict similar voltage sags, however reflected to the applied arm voltages of the converter characterizing $U^+_{diff} = U^-_{diff}$.

The results confirm the conclusions drawn for the type C singular voltage sags. Regarding the AC grid singular conditions, it can be noted that Method 0 result in eventual disconnections of the converter (faults C

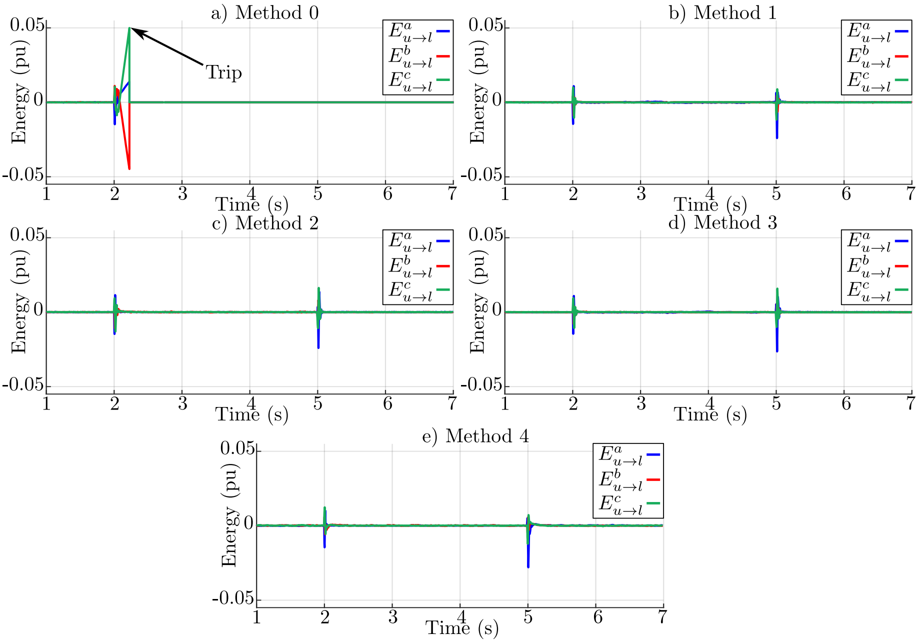

Fig. 3.9: Energy mismatches for AC network voltage singular type D.

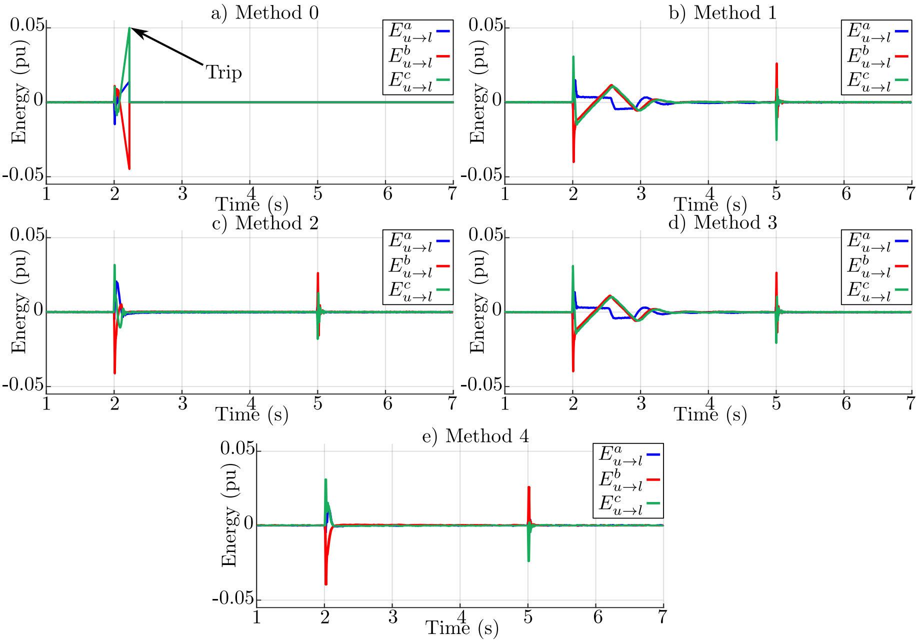

Fig. 3.10: Energy mismatches for AC network voltage singular type E.

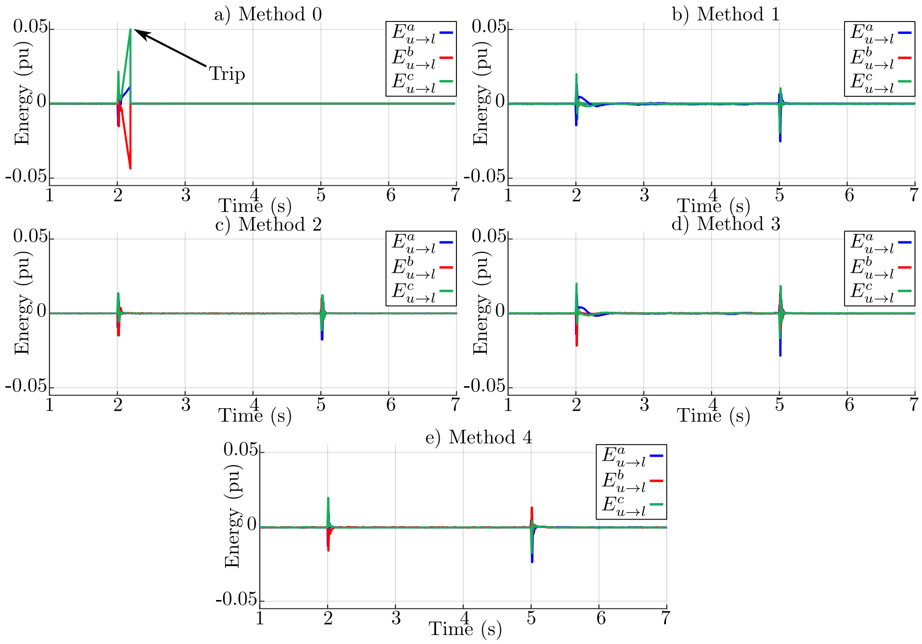

Fig. 3.11: Energy mismatches for AC network voltage singular type F.

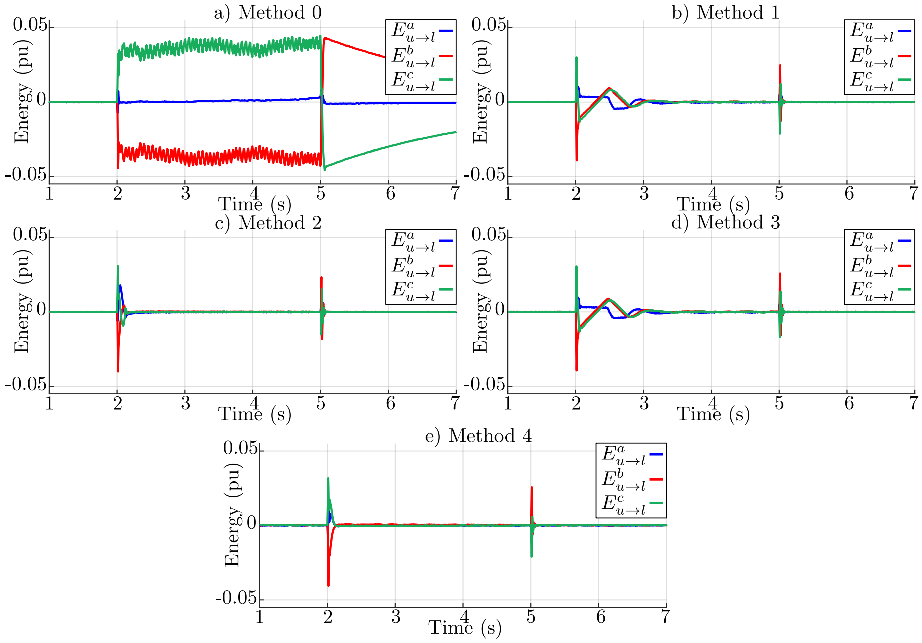

Fig. 3.12: Energy mismatches for AC network voltage singular type G.

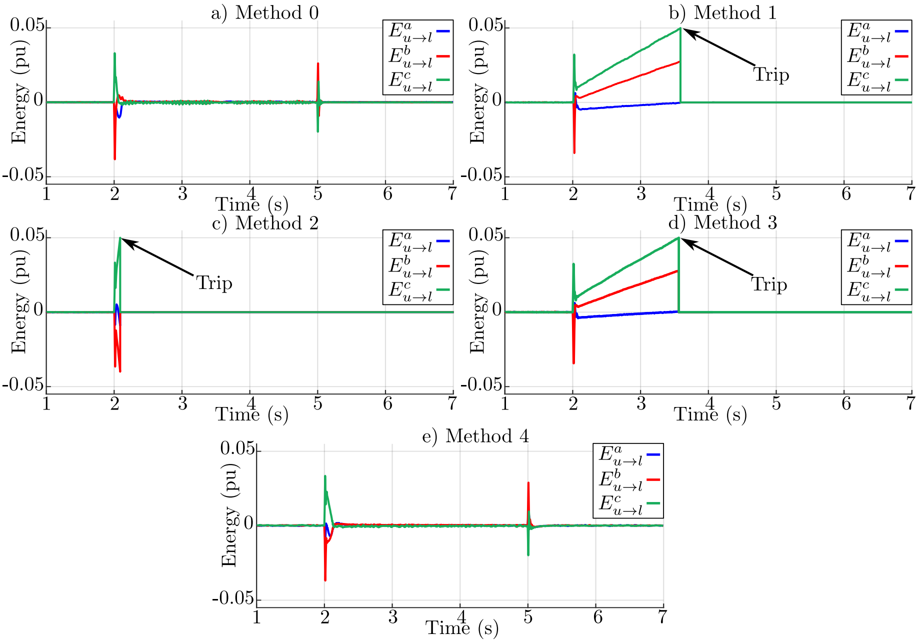

Fig. 3.13: Energy mismatches for internal voltage singular type D.

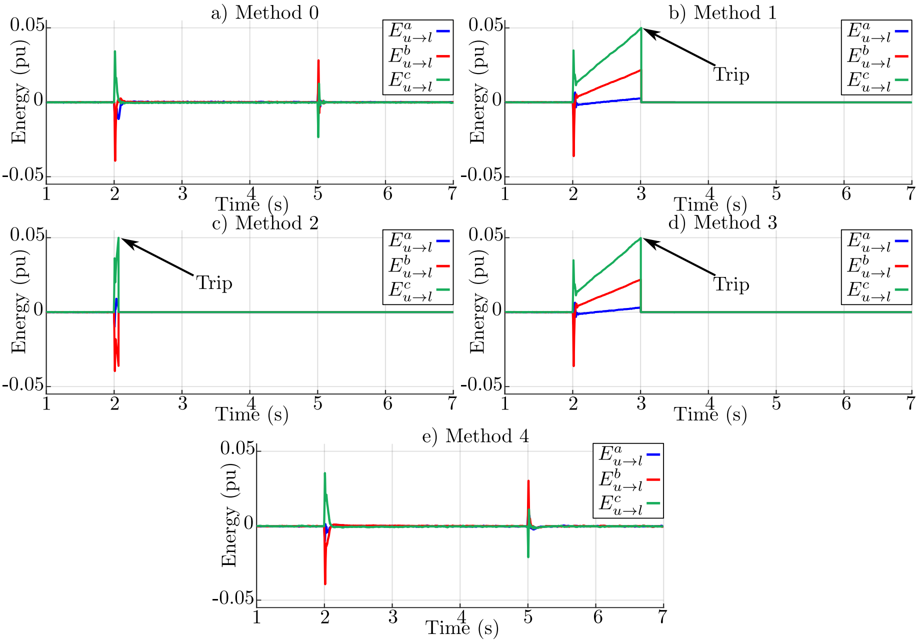

Fig. 3.14: Energy mismatches for internal voltage singular type E.

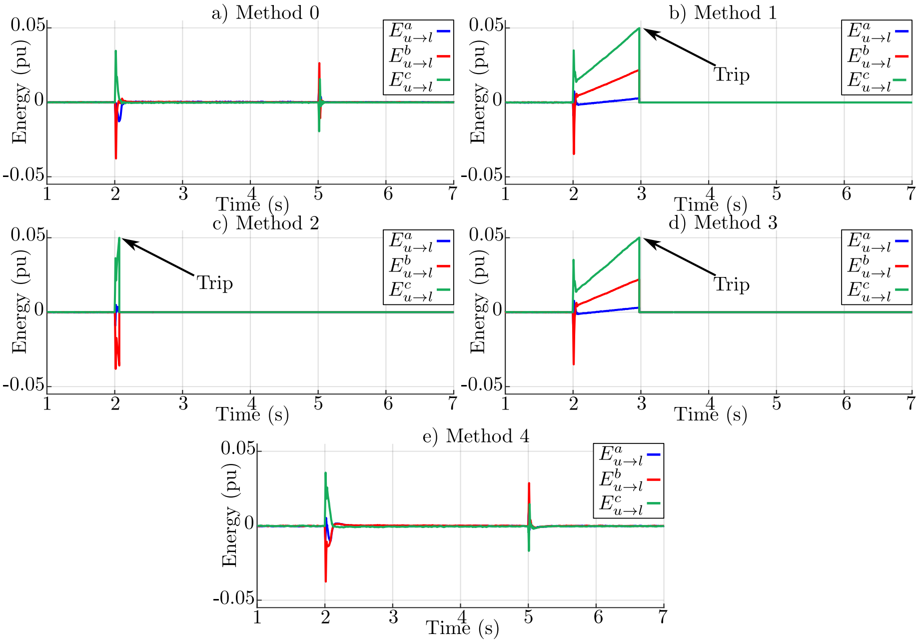

Fig. 3.15: Energy mismatches for internal voltage singular type F.

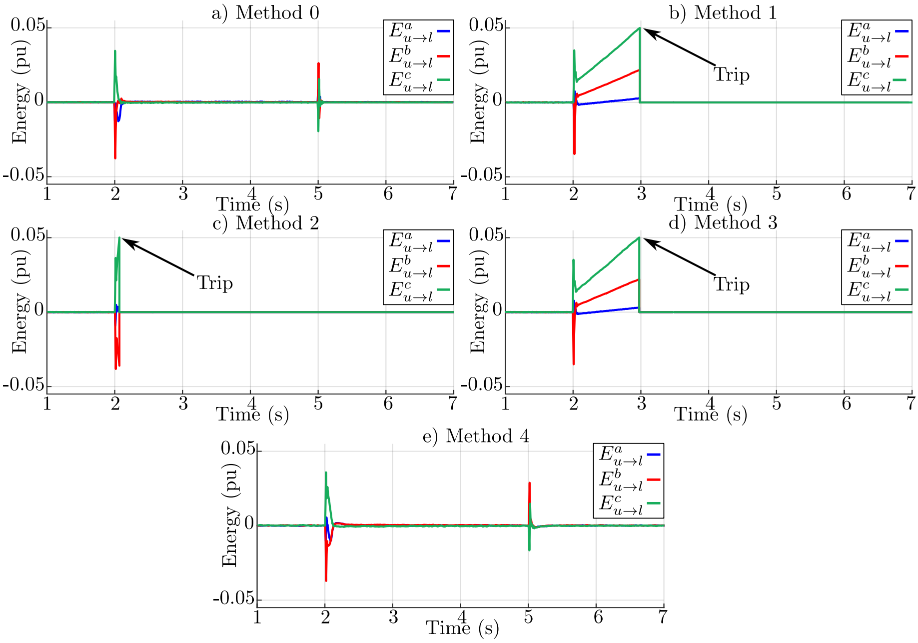

Fig. 3.16: Energy mismatches for internal voltage singular type G.

to F), but it is able to marginally maintain the system operating during a type G fault. However, this method results in undesired sustained energy drifts during the aforementioned fault. In terms of Methods 1 and 3, during faults E and G, specifically, sustained energy drifts are observed for phase a, while the remaining phases present slow dynamics. Methods 2 and 4 have faster dynamics, quickly compensating the energy deviations.

During internal singular voltage conditions, Methods 1 to 3 are unable to regulate the converter, resulting in eventual protection trips (between 1 to 1.5 s after the fault's occurrence for Methods 1 and 3 and within 100 ms for Method 2). On the other hand, Methods 0 and 4 are capable of managing the energy drifts caused by these faults. Finally, it should be mentioned that for all types of fault conditions presented, the proposed Method 4 was the only approach able to compensate the occurrences allowing the converter to safely reach steady-state conditions.

3.5.4 Internal parameters deviations

In this case study, the performance of the proposed method 4 is analyzed considering parameters deviations in the arm impedances of the MMC during an internal singular voltage sag condition type D (see Section 3.3.1 and [33]). For the different internal parameter set-ups simulated, it is considered that both reference calculations and design of the controller gains are done based on the parameters given in Table 3.3. The effects of the arm impedance deviations are analyzed into two different set-ups. In the first one, unbalanced errors within ±5% are considered, where in the second case the asymmetry can achieve errors up to ±10%. The arm impedance values for the different asymmetric cases are highlighted in Table 3.4. Finally, the analysis is performed through time-domain simulations of the main quantities of the converter, as well as its internal energy.

Table 3.4: Arm impedance values for Case study D.

Deviation of ±5%	Deviation of ±10%
$Z_u^a = Z_{arm} - 0.05Z_{arm}$	$Z_u^a = Z_{arm} - 0.015Z_{arm}$
$Z_u^b = Z_{arm} - 0.01Z_{arm}$	$Z_u^b = Z_{arm} - 0.1Z_{arm}$
$Z_u^c = Z_{arm} + 0.02Z_{arm}$	$Z_u^c = Z_{arm} + 0.13Z_{arm}$
$Z_l^a = Z_{arm} + 0.03Z_{arm}$	$Z_l^a = Z_{arm} + 0.05Z_{arm}$
$Z_l^b = Z_{arm} + 0.015Z_{arm}$	$Z_l^b = Z_{arm} + 0.1Z_{arm}$
$Z_l^c = Z_{arm} + 0.025Z_{arm}$	$Z_l^c = Z_{arm} - 0.08Z_{arm}$

where $Z_{u,l}^k$ is the upper and lower arms impedances, with $k \in \{a, b, c\}$.

In Figs. 3.17 and 3.18, the waveforms for the ±5% deviations are depicted. It can be noted that the arm impedance errors do not interfere with the proposed method, since it is still capable of maintaining the proper operation of the system even during the fault. Now, the errors are increased to ±10% and the results are shown in Figs. 3.19 and 3.20. It can be observed that although the arm impedances present high asymmetric values, leading 100Hz oscillations in the power in the AC-side of the converter, such asymmetry does not affect the DC-side. If the reference calculations and the controllers are not properly designed, under such impedance condition, undesired 50Hz oscillations would appear in the DC-side current. Finally, comparing the energy plots during both unbalance scenarios, it is clear that the most severe case presents higher energy deviation among the phase-legs of the converter, but such deviation can be compensated during the steady-state and does not affect the overall performance of the MMC.

3.5.5 Distinctions among the reference calculation methods

In this section, the main differences among the presented methods and the requirements for their implementation in a real system are discussed. The fundamental disparities among Methods 0 to 4 regard the consideration of the arms' and AC network's impedances effects and the usage of U_{diff}^{0DC}. Method 0 neglects both impedances and it is the only one that does not consider U_{diff}^{0DC} in its vertical power equations. For Method 1, complex mathematical techniques to remove the degrees of freedom that do not contribute in the power transfer are required but still it does not acknowledge the impedances effects. Methods 2 and 3 extended the techniques applied in Methods 0 and 1, respectively, by considering the impedance impacts in the differential voltages. In Method 4, the impedances contributions are respected not only for the differential voltages but also for the additive ones.

From an implementation perspective, the previous methods present contrasting degrees of complexity. Regarding hardware requirements (e.g. sensors for measurements), all methods share similar control structures and would require similar measurements. For the methods regulating the DC differential zero-sequence voltage, no extra sensors are needed, since such quantity is calculated based on existing measurements. Considering the computational aspect, the implementation of Method 0 is the easiest one among the presented approaches as the most complex mathematical operation required is the inversion of a 3x3 matrix. Method 2 presents a slightly higher complexity level compared to Method

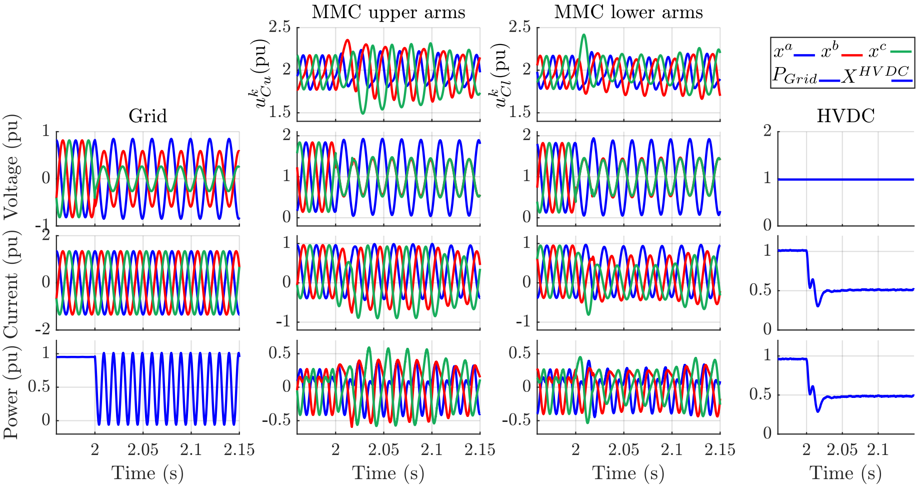

(a) Transition from normal operation to fault event.

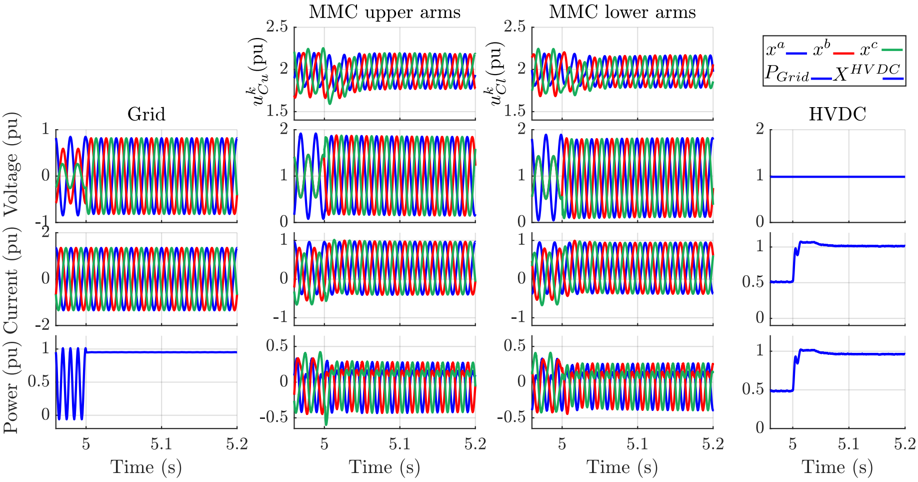

(b) Fault to normal.

Fig. 3.17: MMC waveforms during fault an interior singular voltage sag type D considering unbalanced arm impedances conditions within ±5% error . a) Fault is applied to the system and, b) Fault event is cleared.

0 due to two main factors; 1- the usage of the differential quantities and the DC additive currents (the magnitude and phase-angle of the differential voltages, as well as the DC current magnitudes can be obtained through basic operations and digital filters performed internally by the micro-controller), 2- the regulation of U^{0DC}_{diff}. Methods 1 and 3, although

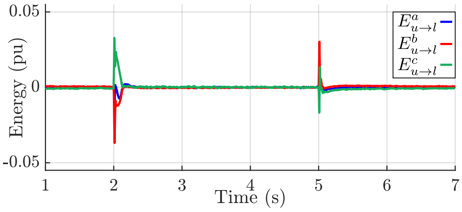

Fig. 3.18: Energy mismatches considering arm impedance unbalances within ±5%.

use different voltages in the calculations (AC grid and the AC differential voltages, respectively), they both require to compute the Moore-Penrose pseudoinverse in order to obtain their current references. Such complex mathematical operation is not required by Method 4. In this Method, the same procedures employed in Method 2 to obtain the differential voltages and DC additive currents are used only requiring an extra operation in the micro-processor to obtain the magnitudes and phase-angles of the AC additive currents. By having these values, the last operation required by the proposed Method 4 would be to solve equation (3.11).

In Table 3.5, the different measurements and the mathematical operations required by each method are highlighted. In summary, Method 0 is the most straight-forward and simplest to implement among all. Method 2 and 4 does not significantly increase the computational burden, whereas Methods 1 and 3 are the ones which require the highest computational burden, due to the Moore-Penrose pseudoinverse calculation. Finally, only Method 4 was capable of handling all the different fault case scenarios analyzed.

Table 3.5: Distinction among Methods.

Additional operation and control	**Method**				
	0	1	2	3	4
Control of U_{diff}^{0DC}	×	✓	✓	✓	✓
Magnitude and phase-angle of u_{diff}^{+-}	×	×	✓	✓	✓
Calculation of the Moore-Penrose pseudo matrix	×	✓	×	✓	×
Extra matrix to remove the AC additive current component	×	✓	×	✓	×
Arm impedance value	×	×	×	×	✓
Magnitude and phase-angle of u_g^{+-}	✓	✓	×	×	×
Inversion and solution of 3x3 matrix	✓	✓	✓	✓	✓

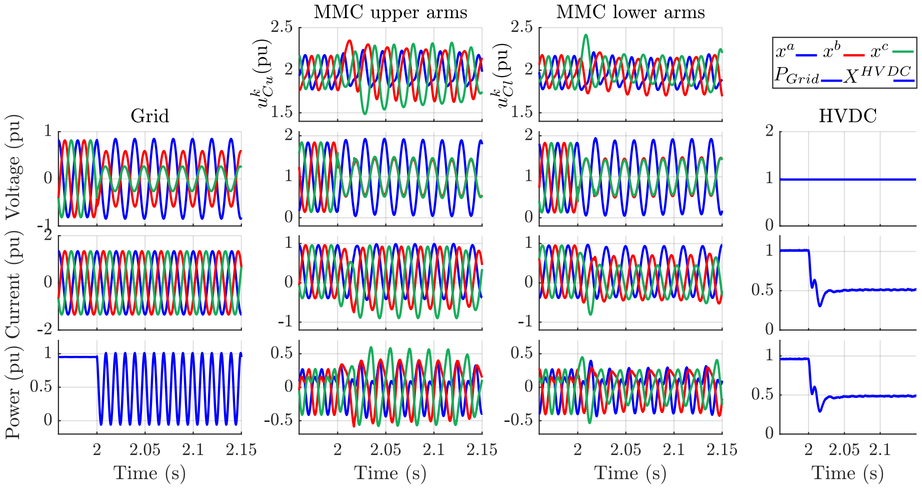

(a) Transition from normal operation to fault event.

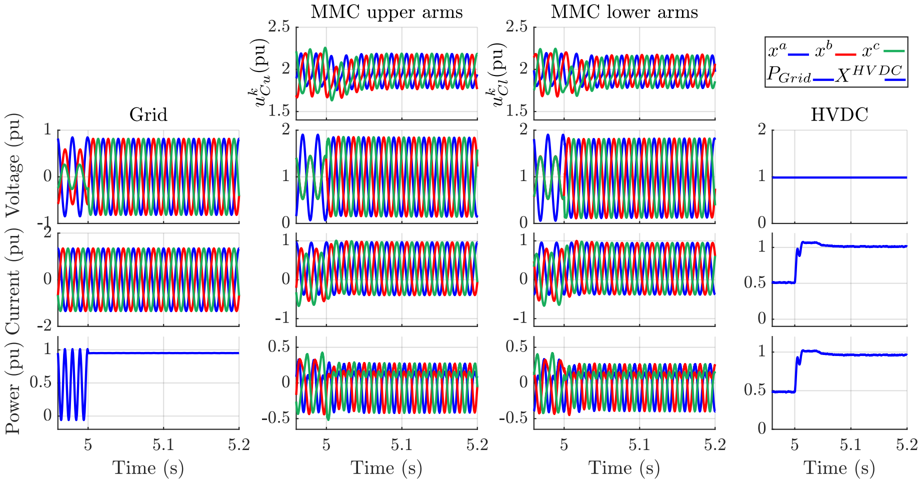

(b) Fault to normal.

Fig. 3.19: MMC waveforms during fault an interior singular voltage sag type D considering unbalanced arm impedances conditions within ±10% error . a) Fault is applied to the system and, b) Fault event is cleared.

3.6 Conclusions

An improved inner current reference calculation method for MMCs operating under normal and unbalanced network conditions has been presented. Particularly, the MMC operation during AC grid or internal singular voltage sag conditions. Such fault events are quite challenging to

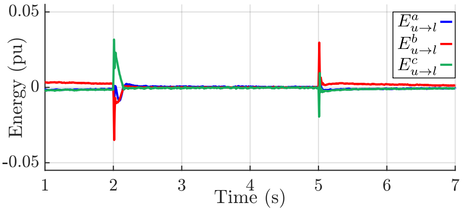

Fig. 3.20: Energy mismatches considering arm impedance unbalances within ±10%.

handle as they might lead to the eventual disconnection of the system by trying to impose high inner current references. The reference calculation has been formulated on the *abc* additive and differential reference frames and it enables to calculate the arms' energy transfer considering all the degrees of freedom of the MMC; thus, the effects of the MMC's and AC side impedances are regarded. This is achieved through a mathematical substitution which does not require any iterative calculation method or optimization, whereby the AC additive voltage is replaced by the voltage drop in arms' impedance caused by the additive currents. Simulation results validate that the proposed reference calculation technique is able to provide the adequate converter references and to maintain the converter operating during both AC grid and internal singular voltage conditions.

Chapter 4

Optimization-based current reference calculation for MMCs

This chapter is related to the following publications:

[**J1**] D. Westerman Spier, E. Prieto-Araujo, J. López-Mestre and O. Gomis-Bellmunt, "Optimal Current Reference Calculation for MMCs Considering Converter Limitations", in *IEEE Transactions on Power Delivery*, vol. 36, no. 4, pp. 2097-2108, Aug. 2021.
[**C1**] D. Westerman Spier, J. López-Mestre, E. Prieto-Araujo and O. Gomis-Bellmunt, "Steady-State Analysis of the Modular Multilevel Converter", *IECON 2019 - 45th Annual Conference of the IEEE Industrial Electronics Society*, 2019, pp. 4861-4866.
[**C2**] D. Westerman Spier, J. López-Mestre, E. Prieto-Araujo and O. Gomis-Bellmunt, "Analytic estimation of the MMC sub-module capacitor voltage ripple for balanced and unbalanced AC grid conditions", 3^o *Simpósio Ibero-Americano em Microrredes Inteligentes com Integração de Energias Renováveis*, Oct. 2019, pp. 1-6.

4.1 Introduction

Up to now, it has been demonstrated the roles of the DOFs in the internal energy balance of the converter and how they can be used to enhance its controllability during balanced and unbalanced scenarios. Still, further improvements can be achieved when optimization techniques are employed to calculate the DOF's and the currents imposed by them. In [38], an optimization algorithm based on Lagrange multipliers is proposed to calculate the MMC circulating current considering the positive-, negative- and zero-sequence components of the AC side of the converter.

The aforementioned methods showed in Chapters 2 and 3 can accurately represent and exploit the MMC's DOFs in the differential and additive reference frame. But, they might not be straightforwardly usable in an optimization environment where constraints in the natural *abc* frame should be imposed to individual arm quantities. A natural *abc* per arm modelling approach provides a direct identification of the quantities of the converter. Based on this approach, references [64, 65] proposed a steady-state analysis of the MMC focusing on the AC arm quantities, while considering per phase model of the DC ones, without analyzing DC unbalances.

In terms of converter operation, during unbalanced faults the MMC control should be able to prioritize the AC current components (active or reactive) to be injected into the network to meet the requirements imposed by the grid codes. For instance, reference [60] prioritizes the active current components, whereas [58,59] main concern is the injection of reactive current to provide voltage support during the fault. In addition, these conditions should be met without violating any of the voltage and current limitations of the converter.

To the best of the authors knowledge, a general optimization problem to calculate the converter references, using a complete per arm MMC model running on the natural *abc* reference frame, able to meet the grid operator specifications while considering the constraints of the MMC (arm currents, voltages and SM voltages) for any grid AC and DC voltage condition, has not been proposed yet. Next, the main contributions of this chapter are detailed:

- Development of a natural *abc* reference frame steady-state model including all the MMC degrees of freedom.

- Formulation of an optimization-based reference calculation problem using the steady-state developed model, to guarantee an optimal MMC operation under any network voltage conditions and grid operator requirements, considering the converter limitations.

The suggested reference calculation optimization problem ensures that:

- The AC currents are as close as possible to the grid code requirements, without exceeding the MMC limits.

- The internal currents of the converter are limited per arm simultaneously considering both AC and DC components.

- Converter applied voltages do not exceed the limitations of the MMC arms.

- SM capacitors' voltages do not exceed their voltage limitation. This constraint is imposed using an equivalent arm capacitor modelling which includes the corresponding voltage fluctuation (assuming that an adequate sorting algorithm is implemented).

- The degrees of freedom of the MMC are fully exploited by the optimization to be as close as possible to the operator requirements.

- Any AC grid operator requirement can be fulfilled, prioritizing either active or reactive current component. In this chapter, the reactive AC current is prioritized to provide voltage support to the faulted network.
- It can be used for different MMC SM configurations (half-bridge, full-bridge, hybrid), as long as the MMC limits are adapted according to each equivalent arm voltage condition.

To validate the proposed optimization-based reference calculation, different case studies are included to show the optimization performance and to highlight the effect of the imposed constraints. In addition, the output values from the steady-state model are compared with time domain simulations (once steady-state is reached) for different grid voltage conditions, showing adequate results.

4.2 Steady-state modelling and analysis

Although the steady-state model has been derived in Chapter 2, for the sake of completeness, in this section, the steady-state equations that later are used as part of the optimization formulation are depicted.

4.2.1 AC network currents

Based on the converter steady-state values, the grid currents $\underline{I}_s^k$ can be obtained

$$\underline{I}_s^k = \left(\frac{\underline{S}^k}{\underline{U}_g^k}\right)^* = \frac{P^k - jQ^k}{\underline{U}_g^{k*}} \tag{4.1}$$

Using (4.1), the calculation of $\underline{I}_s^k$ may result in zero sequence components $\underline{I}_s^0$ for a generic unbalanced AC voltage condition, which cannot flow due to the three-wire AC connection[1]. To impose this condition in the model, one option is to remove the zero-sequence keeping the positive and negative sequence components [66]. Current $\underline{I}_s^k$ will be subsequently used in the following section as an input to solve the steady-state model.

---

[1] Note that the AC current reference calculation (4.1) would not be used in a real converter operation, in which grid code requirements would impose the AC current set-point values based on the defined grid conditions, as it is detailed in Sections 4.3 and 4.4. In this case, equation (4.1) is included in this section so that the analysis stands on its own, being an input for the model.

4.2.2 AC MMC circuit analysis

Fig. 4.1 shows the AC circuit which can be derived from the general scheme of the converter (see Chapter 2) short-circuiting the DC voltage sources and considering the AC component of the arm applied voltages.

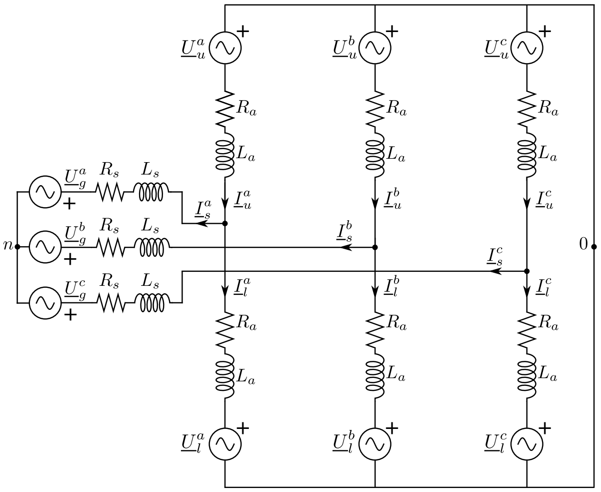

Fig. 4.1: AC model of the MMC.

Applying the Kirchhoff Current Law (KCL) in the middle point of the MMC arms and involving the currents calculated in (4.1), the relation between the arm currents is obtained as

$$\underline{I}_s^k = \underline{I}_u^k - \underline{I}_l^k \tag{4.2}$$

To prevent the circulation of AC current through the DC network, no AC zero sequence arms' current component must be flowing through the MMC. This restriction can be met by imposing that the sum of the upper arms' AC currents is equal to zero, as

$$\underline{I}_u^a + \underline{I}_u^b + \underline{I}_u^c = 0 \tag{4.3}$$

Note that, no additional equation is required to eliminate the zero sequence current component from the lower arms, as it can be directly obtained by combining (4.2), (4.3) while assuming no zero sequence in the grid currents (three-wire connection).

The AC voltage equations for the MMC arms (see Fig. 4.1) can be obtained through Kirchhoff Voltage Law (KVL), as

$$\underline{U}_{0n} = \underline{U}_g^k + \underline{Z}_s(\underline{I}_u^k - \underline{I}_l^k) + \underline{Z}_a\underline{I}_u^k + \underline{U}_u^k \tag{4.4}$$

$$\underline{U}_{0n} = \underline{U}_g^k + \underline{Z}_s(\underline{I}_u^k - \underline{I}_l^k) - \underline{Z}_a\underline{I}_l^k - \underline{U}_l^k \tag{4.5}$$

where, $\underline{U}_{0n}$ is the voltage between the 0 DC reference node and the neutral n of the AC three-phase system and, $\underline{Z}_s$ and $\underline{Z}_a$ are the phase reactor and MMC's arm impedances, respectively.

The last equation to be included in the AC analysis is the power difference between the arms, which is required to conduct a first steady-state analysis. In this case, it can be assumed that the upper and lower arms exchange the same amount of active and reactive power, as

$$P_u^k - P_l^k = 0 \rightarrow U_{u_r}^k I_{u_r}^k + U_{u_i}^k I_{u_i}^k = U_{l_r}^k I_{l_r}^k + U_{l_i}^k I_{l_i}^k \tag{4.6}$$

$$Q_u^k - Q_l^k = 0 \rightarrow U_{u_r}^k I_{u_i}^k - U_{u_i}^k I_{u_r}^k = U_{l_r}^k I_{l_i}^k - U_{l_i}^k I_{l_r}^k \tag{4.7}$$

with $P_{u,l}^k$ and $Q_{u,l}^k$ as the upper and lower arms active and reactive power, respectively. Later, (4.6) and (4.7) will not be part of the optimization, as they will be considered a degree of freedom of the converter, as discussed in Section 4.4.

4.2.3 DC MMC circuit analysis

For the DC part of the MMC, an analogous analysis to the AC circuit is developed. The DC model is shown in Fig. 4.2, where only DC voltages are applied to the system, short-circuiting the AC sources and inductances.

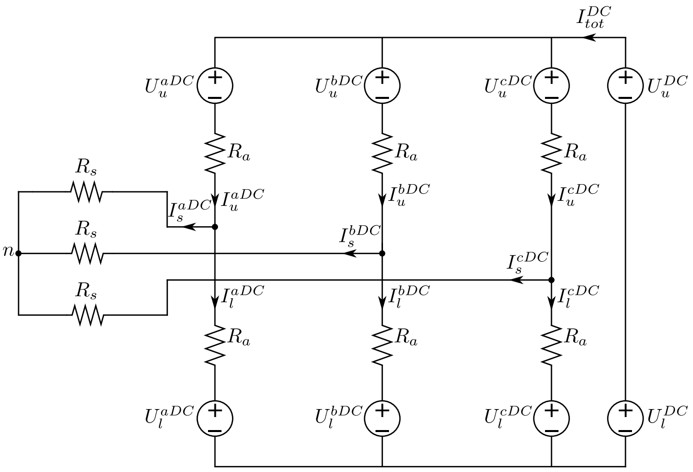

Fig. 4.2: DC model of the MMC.

In order to avoid the circulation of DC components into the AC network, I_s^{kDC} is regulated to be equal to zero. Therefore, $I_u^{kDC} = I_l^{kDC} =$

I^{kDC}, with $k \in (a, b, c)$. The voltage equations can be written as follows

$$U_u^{DC} + U_l^{DC} = U_u^{kDC} + U_l^{kDC} + 2R_a I^{kDC} \tag{4.8}$$

Also, the total DC current of the system I_{tot}^{DC} can be obtained as

$$I_{tot}^{DC} = I^{aDC} + I^{bDC} + I^{cDC} \tag{4.9}$$

4.2.4 Steady-state AC/DC power balance equations

In steady-state conditions, the AC and DC active power exchanged in each of the arms (voltage sources) should be equal, if the semi-conductor losses are neglected. Obviously, this is not feasible with instantaneous values (as the arm single-phase AC power is non-constant). However, it is possible to impose an equality between the AC average power (calculated in the phasor domain) and the DC power. If this condition is not achieved, the energy in the arm cells would either charge or discharge the equivalent arm capacitors (increasing/decreasing the stored energy) and therefore, steady-state conditions would not hold. This constraint can be mathematically expressed as

$$P_{u,l}^{kAC} = P_{u,l}^{kDC} \rightarrow U_{u,l_r}^{k} I_{u,l_r}^{k} + U_{u,l_i}^{k} I_{u,l_i}^{k} = U_{u,l}^{kDC} I^{kDC} \tag{4.10}$$

4.2.5 Equivalent arm capacitor voltage fluctuation

Next, an estimation of the equivalent arm capacitor voltage ripple is performed to verify that the SM capacitor voltages do not exceed their design limitations. The energy stored in each arm of the converter is directly dependable on the power flowing through the MMC. Under balanced AC network conditions, the average energy stored in each arm is equal, also showing similar ripple profiles per arm (phase-shift difference). However, during unbalanced scenarios, the MMC arms may present high energy deviations, leading to variations of the energy stored within them, which might eventually exceed the design limitations. Consequently, the energy stored in each arm, therefore in each SM (assuming an adequate sorting algorithm), must be kept within a certain range to ensure a proper operation of the MMC.

To mathematically represent the equivalent arm voltage fluctuation, the Arm Averaged Model (AAM) [67] is used. This model represents each arm as an equivalent capacitor that is charged/discharged depending on the power exchanged by each arm, which is reflected as a charging/discharging current. This way, the entire arm can be represented as an equivalent capacitor. Based on the AAM equivalent arm model, a mathematical procedure to derive a generalized estimation for the maximum and minimum voltage ripple for the equivalent arm capacitor is presented.

Instantaneous MMC arm power

To calculate the equivalent arm capacitor voltage ripple, firstly, the instantaneous power for the upper and lower arms of the MMC should be obtained as

$$\begin{aligned} p_{u,l}^{k}(t) = u_{u,l}^{k}(t) i_{u,l}^{k}(t) = \Big(U_{u,l}^{kDC} + \hat{U}_{u,l}^{k} \cos(\omega t + \psi_{u,l}^{k}) \Big) \\ \Big(I_{u,l}^{kDC} + \hat{I}_{u,l}^{k} \cos(\omega t + \delta_{u}^{k}) \Big) \end{aligned} \tag{4.11}$$

where $I_{u,l}^{kDC}$ are the upper and lower DC currents flowing through the MMC arms, $\delta_{u,l}^{k}$ and $\psi_{u,l}^{k}$ are the upper and lower arms' currents and voltages phase-angles, respectively. It can be noted that the power will have components at zero, ω and 2ω pulsations. The sum of the constant zero frequency power of the AC and DC sources must be zero in steady-state conditions, to avoid energy deviation in the arm. Therefore, the upper and lower arms' powers can be reduced to

$$\begin{aligned} p_{u,l}^{k}(t) = U_{u,l}^{kDC} \hat{I}_{u,l}^{k} \cos(\omega t + \delta_{u,l}^{k}) + \\ + I_{u,l}^{kDC} \hat{U}_{u,l}^{k} \cos(\omega t + \psi_{u,l}^{k}) + \frac{\hat{U}_{u,l}^{k} \hat{I}_{u,l}^{k}}{2} \cos(2\omega t + \delta_{u,l}^{k} + \psi_{u,l}^{k}) \end{aligned} \tag{4.12}$$

Arms maximum energy and voltage calculation

The voltage in a capacitor presents a profile that is related to its energy. One way to find the maximum and minimum values of the equivalent arm capacitor voltage is to obtain the peak values of the arm energy. The equation for the instantaneous energy flowing through the MMC arms can be expressed as (integrating (4.12) over time)

$$\begin{aligned} E_{u,l}^{k}(t) = \frac{U_{u,l}^{kDC} \hat{I}_{u,l}^{k}}{\omega} \sin(\omega t + \delta_{u,l}^{k}) + \\ + \frac{I_{u,l}^{kDC} \hat{U}_{u,l}^{k}}{\omega} \sin(\omega t + \psi_{u,l}^{k}) + \frac{\hat{U}_{u,l}^{k} \hat{I}_{u,l}^{k}}{4\omega} \sin(2\omega t + \delta_{u,l}^{k} + \psi_{u,l}^{k}) \end{aligned} \tag{4.13}$$

The upper and lower arm energies, shown in (4.13), have terms that oscillate at the fundamental frequency and a second order one. As stated in the comprehensive analysis developed in [68], the actual maximum energy stored in the equivalent arm capacitor, and consequently its maximum voltage ripple, cannot be found without iterative methods. But, the absolute maximum energy bound for the upper and lower arms can be obtained through trigonometric assumptions, which are discussed next. First, let's combine the first order frequency terms into a single expressions based on the following expression

$$\begin{aligned} &A\sin(\omega t+\alpha)+B\sin(\omega t+\beta)= \\ &=\underbrace{\sqrt{\left[A\cos(\alpha)+B\cos(\beta)\right]^2+\left[A\sin(\alpha)+B\sin(\beta)\right]^2}}_{\mathrm{X}}\cdot \\ &\cdot\sin\left\{\omega t+\underbrace{\tan^{-1}\left[\frac{A\sin(\alpha)+B\sin(\beta)}{A\cos(\alpha)+B\cos(\beta)}\right]}_{\Psi}\right\} \end{aligned} \tag{4.14}$$

Observing (4.14), it is clear that the resultant expression represents a vector with maximum magnitude equals to X with a phase of Ψ. Therefore, the maximum ripple energy value for the terms at the fundamental frequency can be found by replacing the elements from (4.13) in X, such as

$$E^k_{u,l_{max_f}}=\left(\begin{aligned}&\left[\frac{U^{kDC}_{u,l}\hat{I}^k_{u,l}}{\omega}\cos(\delta^k_{u,l})-\frac{I^{kDC}_{u,l}\hat{U}^k_{u,l}}{\omega}\cos(\theta^k_{u,l})\right]^2+\\&+\left[\frac{U^{kDC}_{u,l}\hat{I}^k_{u,l}}{\omega}\sin(\delta^k_{u,l})-\frac{I^{kDC}_{u,l}\hat{U}^k_{u,l}}{\omega}\sin(\theta^k_{u,l})\right]^2\end{aligned}\right)^{1/2} \tag{4.15}$$

Therefore the upper and lowers instantaneous energies can be described as,

$$E^k_{u,l}(t)=E^k_{u,l_{max_f}}\sin(\omega t+\Psi^k_{u,l})+E^k_{max_{2f}}\sin(2\omega t+\delta^k_{u,l}+\theta^k_{u,l}) \tag{4.16}$$

where, $\Psi^k_{u,l}$ are the upper and lower phase shifts for phase k obtained using (4.14) and $E^k_{max_{2f}} = \left|-\hat{U}^k_{u,l}\hat{I}^k_{u,l}/4\omega\right|$.

Although the maximum value of the arms energy at the fundamental frequency was obtained, there is still a need to combine them with the second-order components to achieve a general equation that can estimate the maximum energy ripple of the upper and lower arms. Equation (4.16) will be maximized when $\sin(\omega t + \Psi^k_{u,l}) = \sin(2\omega t + \delta^k + \theta^k) = 1$; thus,

$$E^{kAC}_{u,lmax} = E^k_{u,lmax_f} + E^k_{max_{2f}} \tag{4.17}$$

To comply with the conditions in (4.17), the angles for the first and second order terms must meet the following condition,

$$\begin{aligned}
\omega t + \Psi^k_{u,l} &= \pi/2 + n_1\pi, \text{for } n_1 \in \mathbb{Z}, && \text{(4.18a)}\\
2\omega t + \delta^k + \theta^k &= \pi/2 + n_2\pi, \text{for } n_2 \in \mathbb{Z} && \text{(4.18b)}\\
\pi/2 + n_1\pi - \Psi^k_{u,l} &= \left(\pi/2 + n_2\pi - (\delta^k + \theta^k)\right)/2 && \text{(4.18c)}\\
\pi + 2n_1\pi - 2\Psi^k_{u,l} &= \pi/2 + n_2\pi - (\delta^k + \theta^k) && \text{(4.18d)}\\
\pi/2 + (2n_1 - n_2)\pi &= 2\Psi^k_{u,l} - (\delta^k + \theta^k) && \text{(4.18e)}\\
2\Psi^k_{u,l} - (\delta^k + \theta^k) &= \pi/2 + n\pi && \text{(4.18f)}
\end{aligned}$$

However, when such condition is not held, the maximum energy level calculated with (4.18) presents a value deviation. This error is affected by the magnitudes of the energy terms, as well as the phase displacement between them. In Figs. 4.3 and 4.4, it can be observed that the maximum energy value and, consequently, the minimum error (see (4.18)) happens when the angles for the second order is equal to $\left(\delta^k_{u,l} + \psi^k_{u,l}\right) = 90^o$ or for high energy ratios. Where, the highest energy deviation occurs when there is no phase between, $E^k_{u,lmax_f}$ and $E^k_{max_{2f}}$ and small energy ratio, having a value equals to 15%.

The upper and lower arms maximum energy ripple will be expressed considering the worst-case scenario, as depicted in (4.19) , in which the sum of the angles is equal to $\pi/2$. Although this analysis cannot calculate the actual energy point, the energy error can be used as a safety parameter since the estimated maximum value will always be lower than the actual maximum. Therefore, it can be ensured that for any operating point, the maximum equivalent arm capacitor voltage fluctuation

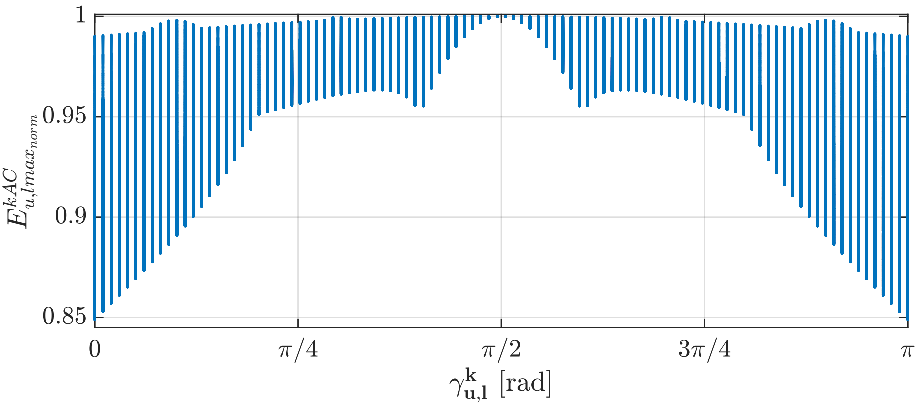

Fig. 4.3: Effects of the phase-angles and the maximum energy ripple bound.

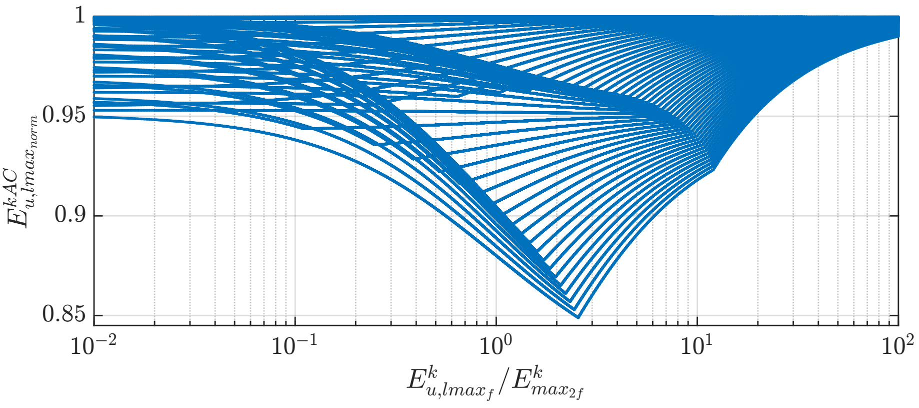

Fig. 4.4: Effects of the ratio between the line and double-line frequency terms and the maximum energy ripple bound.

obtained through 4.18 will always be within their design limits.

$$E^{kAC}_{u,l_{max}} = \sqrt{\left[\frac{U^{kDC}_{u,l}\hat{I}^{k}_{u,l}}{\omega}\cos(\delta^{k}_{u,l}) + \frac{I^{kDC}_{u,l}\hat{U}^{k}_{u,l}}{\omega}\cos(\psi^{k}_{u,l})\right]^2 + \left[\frac{U^{kDC}_{u,l}\hat{I}^{k}_{u,l}}{\omega}\sin(\delta^{k}_{u,l}) + \frac{I^{kDC}_{u,l}\hat{U}^{k}_{u,l}}{\omega}\sin(\psi^{k}_{u,l})\right]^2} + \left|\frac{\hat{U}^{k}_{u,l}\hat{I}^{k}_{u,l}}{4\omega}\right| \tag{4.19}$$

As aforementioned, the analysis considers that the MMC is operated in steady-state conditions and, as a result, the capacitors can be considered fully charged. For this reason, they already present an average energy level for the upper and lower arms (4.20). Moreover, this energy reference must be taken into account when the arm capacitor voltage ripple is calculated.

$$E^k_{u,l_{ref}} = \frac{C_{SM}}{2} N^k_{u,l_a} U^2_{SM} \tag{4.20}$$

where U_{SM} is average SM nominal voltage, C_{SM} is the SM capacitance and N^k_{u,l_a} is the number of SMs available in the arm. Therefore, the maximum and minimum values for the upper and lower arms energy can be obtained adding (4.19) and (4.20), described as

$$E^k_{u,l_{max,min}} = \underbrace{E^k_{u,l_{ref}}}_{\text{DC term (4.20)}} \pm \underbrace{E^{kAC}_{u,l_{max}}}_{\text{peak of the AC part (4.19)}} \tag{4.21}$$

Even though several operating conditions will result in equivalent arm capacitor energy fluctuations that are asymmetric regarding their DC component, the maximum and minimum energy bounds for any operating point will always present a symmetric pattern (since they are derived considering the highest energy ripple scenario). Furthermore, (4.21) will be used in the formulation of the optimization problem to avoid not only over-modulations but also exceeding equivalent arm capacitors and SM capacitors over-voltages in the MMC, as will be shown in Section 4.4 and 4.5. Based on the maximum and minimum energy levels $E^k_{u,l_{max,min}}$, the admissible voltage magnitudes of the equivalent arms' capacitors can be expressed as

$$U^k_{Cu,l_{max,min}} = \sqrt{\frac{2E^k_{u,l_{max,min}} N^k_{u,l_a}}{C_{SM}}} \tag{4.22}$$

Complete model

The full non-linear steady-state model for the MMC, with $k \in (a, b, c)$, can be summarized as,

- 72 quantities given as:
  - 13 complex AC quantities: $\underline{U}^k_{u,l}$, $\underline{U}_{0n}$, $\underline{I}^k_{u,l}$
  - 46 DC quantities: $U^{kDC}_{u,l}, I^{kDC}, I^{DC}_{tot}$, $E^{kAC}_{u,l_{max}}$, $E^k_{u,l_{ref}}$ $E^k_{u,l_{max,min}}$, $U^k_{Cu,l_{max,min}}$
- 72 equations divided as:
  - 10 complex linear AC equations: (4.2) to (4.5)
  - 4 linear DC real equations: (4.8), (4.9)
  - 48 non-linear real equations: (4.6), (4.7), (4.10), (4.19-4.22)

The model will require the following inputs

- AC and DC system voltages: $\underline{U}_g^k$, $U_{u,l}^{DC}$.
- AC network current $\underline{I}_s^k$ obtained using (4.1), based on P^k, Q^k and $\underline{U}_g^k$, eliminating the zero sequence component $\underline{I}_s^0$.
- SM characteristics: U_{SM}, C_{SM}, N_{u,l_a}^k.

This model can be used to calculate the steady-state quantities of the MMC for any grid voltage condition. This chapter will adapt it in Section 4.4 to use it as part of an optimization-based reference calculation problem. It will also be employed to calculate the pre-fault values of the system, to be added as initial conditions for the optimization algorithm.

4.3 Grid support requirements

This section details the calculation of the AC side currents dictated by the operators' grid codes. During an AC grid voltage fault, the MMC must be able to inject or absorb reactive current ΔI_r from the AC grid in order to provide voltage support. According to the Spanish grid code [59] (taken as example), the magnitude of ΔI_r (in pu basis) to be injected into the grid varies according to AC system RMS voltage levels as follows

1. $U_{min1} \leqslant U_g^k \leqslant U_{max1} \rightarrow \Delta I_r^k = 0$
2. $U_{min2} \leqslant U_g^k < U_{min1} \rightarrow \Delta I_r^k = \frac{\Delta I_{rmax}(U_{min1} - U_g^k)}{U_{min1} - U_{min2}}$
3. $U_g^k < U_{min2} \rightarrow \Delta I_r^k = \Delta I_{rmax}$

Under a balanced fault, the injection of reactive currents presents a symmetrical profile. However, in an unbalanced AC voltage sag condition, the three-phase system may have different voltage levels in each of its phases [51]. The phasor representation of the AC network voltages during different voltage sags is shown in Table. 4.1, where E_1 is the pre-fault voltage and V is the voltage of the faulted phase.

A common solution to provide voltage support is based on the decomposition of the faulted network voltage into positive, negative and zero sequence components. Then, the magnitude of the reactive current to be injected is selected based only on the magnitude of the positive sequence voltage component, which this chapter will refer as Strategy I. However, this methodology is unable to provide full voltage support to the faulted grid. Furthermore, by disregarding the negative and zero voltage sequence components, healthy phases might receive unnecessary

Table 4.1: Phasor representation of AC network voltage sags.

Type	Voltages	Phasors *abc*
A	$\underline{U}_g^a = V$ $\underline{U}_g^b = -\frac{1}{2}V - \frac{1}{2}jV\sqrt{3}$ $\underline{U}_g^c = -\frac{1}{2}V + \frac{1}{2}jV\sqrt{3}$	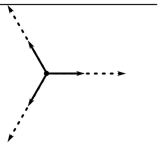
B	$\underline{U}_g^a = V$ $\underline{U}_g^b = -\frac{1}{2}E_1 - \frac{1}{2}jE_1\sqrt{3}$ $\underline{V}^c = -\frac{1}{2}E_1 + \frac{1}{2}jE_1\sqrt{3}$	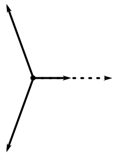
C	$\underline{U}_g^a = E_1$ $\underline{U}_g^b = -\frac{1}{2}E_1 - \frac{1}{2}jV\sqrt{3}$ $\underline{U}_g^c = -\frac{1}{2}E_1 + \frac{1}{2}jV\sqrt{3}$	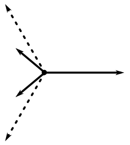
D	$\underline{U}_g^a = V$ $\underline{U}_g^b = -\frac{1}{2}V - \frac{1}{2}jE_1\sqrt{3}$ $\underline{U}_g^c = -\frac{1}{2}V + \frac{1}{2}jE_1\sqrt{3}$	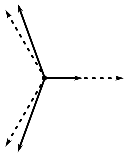
E	$\underline{U}_g^a = E_1$ $\underline{U}_g^b = -\frac{1}{2}V - \frac{1}{2}jV\sqrt{3}$ $\underline{U}_g^c = -\frac{1}{2}V + \frac{1}{2}jV\sqrt{3}$	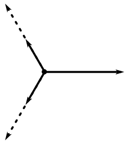
F	$\underline{U}_g^a = V$ $\underline{U}_g^b = -\frac{1}{2}V - \left(\frac{1}{3}E_1 + \frac{1}{6}V\right) j\sqrt{3}$ $\underline{U}_g^c = -\frac{1}{2}V + \left(\frac{1}{3}E_1 + \frac{1}{6}V\right) j\sqrt{3}$	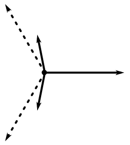
G	$\underline{U}_g^a = \frac{2}{3}E_1 + \frac{1}{3}V$ $\underline{U}_g^b = -\frac{1}{3}E_1 - \frac{1}{6}V - \frac{1}{2}jV\sqrt{3}$ $\underline{U}_g^c = -\frac{1}{3}E_1 - \frac{1}{6}V + \frac{1}{2}jV\sqrt{3}$	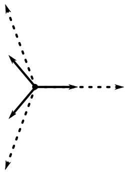

voltage support leading to over-voltages in the system. The opposite scenario may also happen, where the faulted phases might require full voltage support but, the value of the reactive current calculated based only on the positive sequence voltage component is insufficient.

Another possible solution would be to consider all the three symmetrical (positive, negative and zero) AC voltages components, which would be the ideal case, as the phases would receive the exact amount of reactive and active power in accordance to the grid code, named Strategy II. Such condition may be infeasible since the AC system consists of three-wires and this strategy might try to impose zero sequence current component into the AC network. For both strategies (I and II), if the magnitude of the AC current references exceeds the AC grid current limitations I_{max}^{AC}, they must be reduced while keeping their phasorial angle constant.

In order to provide a better voltage support, an additional strategy is suggested to adjust each individual phase current to be as close as possible to the grid code (active and specially reactive) power support requests, without violating the converter constraints and limits. Firstly, the pre-fault active and reactive AC grid current components are obtained as

$$\begin{bmatrix} I_{P_{pre}}^{k} \\ I_{Q_{pre}}^{k} \end{bmatrix} = \begin{bmatrix} \cos(\theta_{pre}^{k}) & \sin(\theta_{pre}^{k}) \\ -\sin(\theta_{pre}^{k}) & \cos(\theta_{pre}^{k}) \end{bmatrix} \cdot \begin{bmatrix} I_{spre_r}^{k} \\ I_{spre_i}^{k} \end{bmatrix} \tag{4.23}$$

where θ_{pre}^{k} and $\underline{I}_{spre}^{k}$ are the phase-angles of the AC grid voltages and the AC grid currents during pre-fault conditions (obtained using (3)), respectively. The support current to fulfill the grid code requirements is calculated by adding the additional required reactive current to the pre-fault reactive current component, as $I_{sup}^{k} = \Delta I_{r}^{k} + I_{Q_{pre}}^{k}$. This magnitude is expressed as a phasor, which has to be properly placed in relation to the faulted AC grid voltages to allow voltage support, as (considering $k \in (a, b, c)$)

$$\underline{I}_{sup}^{k} = I_{sup}^{k}(\cos(\theta_{F}^{k} + 90^{o}) + j\sin(\theta_{F}^{k} + 90^{o})) \tag{4.24}$$

where θ_{F}^{k} is the phase-angle of the AC grid voltages during the fault. Note that the phase-angles during pre-fault and faulted conditions are obtained by means of phase locked-loops (PLLs), which must be fast enough to avoid undesirable dynamic interactions with other quantities of the MMC [69]. However, if $|I_{sup}^{k}| < I_{max}^{AC}$, the grid code demands the MMC to also inject active current components $\underline{I}_{P}^{k}$, which must have the same phase-angles as the faulted AC grid voltages, until the AC grid currents achieve nominal levels. This active current component can be described as

$$\underline{I}_P^k = I_P^k(\cos(\theta_F^k) + j\sin(\theta_F^k)) \tag{4.25}$$

where I_P^k is the magnitude of the AC active current, which is equal to the pre-fault active current component $I_{P_{pre}}^k$. As an example, for a type C fault [51], the voltages and current vectors are depicted in Fig. 4.5. For an easier understanding of the phasors, a pre-fault state with $I_{Q_{pre}}^k = 0$ has been chosen.

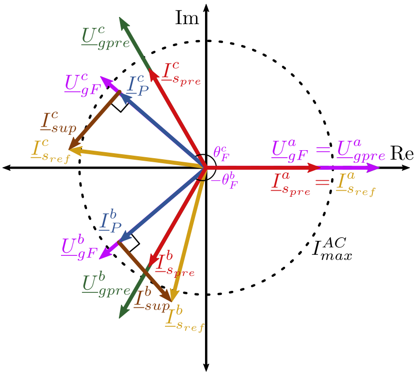

Fig. 4.5: Reactive current injection according to the utility grid voltage.

Although the addition of $I_{P_{pre}}^k$ may result in AC grid currents that are higher than the nominal levels or even exceeding the system limitations, an optimization problem is formulated to avoid those issues. To do so, the active I_P^k and reactive I_Q^k components have to be adjusted to calculate AC grid current references $\underline{I}_{s_{ref}}^k$ that do not exceed the design limitations. This can be achieved by adding to (4.23) the coefficients (α^k and β^k), which are used to adapt the amount of active and reactive currents to be injected per phase in case of reaching a limitation. Then, $\underline{I}_{s_{ref}}^k$ can be calculated as

$$\text{minimize W} = \lambda_1 \left(R_a \left(\sum_{k=a}^{c} {I_u^k}^2 + {I_l^k}^2 \right) + R_a \left(\sum_{k=a}^{c} {I_u^{kDC}}^2 + {I_l^{kDC}}^2 \right) \right) - \lambda_2 \left(\sum_{k=a}^{c} \alpha^k \right) - \lambda_3 \left(\sum_{k=a}^{c} \beta^k \right) \tag{4.26}$$

$$\begin{bmatrix} I_{s_{ref_r}}^k \\ I_{s_{ref_i}}^k \end{bmatrix} = \begin{bmatrix} \cos(\theta_F^k) & -\sin(\theta_F^k) \\ \sin(\theta_F^k) & \cos(\theta_F^k) \end{bmatrix} \cdot \begin{bmatrix} \alpha^k \cdot I_P^k \\ \beta^k \cdot I_Q^k \end{bmatrix} \tag{4.27}$$

where $I_Q^k = I_{sup}^k$. As mentioned above, the coefficients α^k and β^k can affect the active and reactive currents levels, respectively. Under normal operations, both parameters present their maximum level being equal to

1, which would not constraint neither the active nor the reactive powers. However, depending on the AC grid voltage conditions, these values should be modified to remove both the zero sequence current component of the unbalanced references and to meet the MMC limitations. Clearly, the selection of the six coefficients α^k and β^k is not a simple task as changing any of the coefficients will importantly affect the response of the converter towards the network. Thus, the reference calculation problem will be part of an optimization problem, which will ensure that the current references are as close as possible in terms of active and reactive powers to the grid code demands (enabling also active/reactive power prioritization). This strategy is named Optimal Strategy and the optimization problem used to calculate it is detailed in the next section.

4.4 Optimal reference calculation

In this section, an optimization algorithm is proposed to calculate the converter arm quantities to provide adequate grid support during balanced and unbalanced voltage conditions while ensuring that the converter operation is kept within its design and operating limits.

4.4.1 Optimization problem

The multi-objective function is defined in (4.26), where each term of the expression is multiplied by a weighting factor λ_x that is used to prioritize among converter arm inductance losses λ_1, active power λ_2 and reactive power λ_3. In this Chapter, $\lambda_3 \gg \lambda_2 \gg \lambda_1$ so that the reactive current is prioritized over the active current and the power losses (pushing β^k as close as possible to 1), respectively.

To ensure that all the technical constraints are fulfilled, the optimization problem is subjected to several linear and non-linear constraints. These mathematical restrictions are based on the equations of the steady-state model presented in Section 4.2. Specifically, (4.3), (4.4) and (4.5), together with the following linear constraints are part of the optimization problem, considering $k \in (a, b, c)$

$$\underline{I}^a_{s_{ref}} + \underline{I}^b_{s_{ref}} + \underline{I}^c_{s_{ref}} = 0 \tag{4.28a}$$

$$\underline{I}^k_{s_{ref}} = \underline{I}^k_u - \underline{I}^k_l \tag{4.28b}$$

$$U^{DC}_{u,l} = U^{kDC}_{u,l} + R_a I^{kDC}_{u,l} \tag{4.28c}$$

$$I^{kDC}_{s_{ref}} = I^{kDC}_u - I^{kDC}_l \tag{4.28d}$$

$$I_{tot}^{DC} = I_u^{aDC} + I_u^{bDC} + I_u^{cDC} \tag{4.28e}$$

Equation (4.28a) imposes that the AC current references have no zero sequence component, while (4.28b) describes the relation between the MMC AC currents. Equations (4.28c) and (4.28d) are included to guarantee that no DC current flows through the AC side of the converter. Finally, (4.28e) relates the MMC inner DC currents with the total DC one.

For the non-linear constraints, (4.27) is needed along with the AC/DC arm power balance equations

$$P_{u,l}^{kAC} = P_{u,l}^{kDC} \rightarrow U_{u,l_r}^{k} I_{u,l_r}^{k} + U_{u,l_i}^{k} I_{u,l_i}^{k} = U_{u,l}^{kDC} I_{u,l}^{kDC} \tag{4.29}$$

In addition to the expressions shown above, the energy equations for the upper and lower equivalent arm capacitors (4.19)-(4.21) are also required, since they are used to calculate the equivalent arms' capacitor voltages. Lastly, the converter limitations are imposed by the following inequalities

$$I_{s_{ref}}^{k} \leqslant I_{max}^{AC}, \quad I_{u,l}^{k} + I_{u,l}^{kDC} \leqslant I_{max}^{arm} \tag{4.30a}$$

$$U_{Cu,l_{max}}^{k} \leqslant U_{C_{max}} \tag{4.30b}$$

$$0 \leqslant U_{u,l}^{kDC} + \sqrt{2} U_{u,l}^{k} \leqslant U_{Cu,l_{min}}^{k} \tag{4.30c}$$

$$0 \leqslant \alpha^{k} \leqslant 1, \quad 0 \leqslant \beta^{k} \leqslant 1 \tag{4.30d}$$

where I_{max}^{AC} is the maximum current that can be injected into the AC grid, I_{max}^{arm} is the maximum current which can circulate through the MMC arms, and $U_{C_{max}}$ is the peak value that the equivalent arms' capacitors voltage can achieve, that can be directly related to each SM voltage. Equation (4.30a) limits the maximum currents that can be injected into the AC grid and that can flow through the MMC arms. The inequality (4.30b) ensures that the equivalent arm capacitor voltages do not exceed their maximum voltage bound, whereas (4.30c) is used to guarantee that the applied voltages are higher than the minimum allowed voltage (left-hand side of the equation) and to avoid over-modulations (right-hand side). If full-bridge SMs were considered, the left value of (4.30c) should be replaced from 0 to $-U_{Cu,l_{min}}^{k}$. Finally, the weights α^k and β^k are limited as shown in (4.30d). The optimization will try to maximize these weights (max. equal to 1), consequently being as close as possible to the desired current references imposed by the grid code, respecting the system constraints.

4.4.2 Complete optimization model and methodology

The complete optimization model is summarized below.

- 90 MMC quantities:
  - 16 AC quantities: $\underline{U}_{u,l}^{k}, \underline{U}_{0n}, \underline{I}_{u,l}^{k}, \underline{I}_{s_{ref}}^{k}$
  - 58 DC quantities: $U_{u,l}^{kDC}, I_{u,l}^{kDC}, I_{s_{ref}}^{kDC}, I_{tot}^{DC}, \alpha^{k}, \beta^{k}, E_{u,l_{max}}^{kAC}, E_{u,l_{ref}}^{k}, E_{u,l_{max,min}}^{k}, U_{Cu,l_{max,min}}^{k}$
- 80 equations divided in:
  - 11 complex linear AC equations: (4.3), (4.4), (4.5), (4.28a), (4.28b)
  - 10 linear DC equations: (4.28c-4.28e)
  - 48 non-linear equations: (4.19-4.22), (4.27), (4.29)
- 39 inequalities: (4.30a-4.30d)

The optimal model will require the following inputs:

- AC and DC system voltages: $\underline{U}_{g}^{k}$, $U_{u,l}^{DC}$.
- AC network current in the form of active I_{P}^{k} and reactive I_{Q}^{k} currents, which are obtained using the pre-fault AC current and voltage levels, the reactive current required by the grid code I_{sup}^{k} and the AC grid phase-angles during the fault θ_{F}^{k}.
- SM type and characteristics: U_{SM}, C_{SM}, N_{u,l_a}^{k}.

The different steps to run the optimization algorithm are:

1. Define the pre-fault and fault condition scenarios.
2. Obtain of the pre-fault MMC steady-state quantities.
3. Calculate the active and reactive current set-points required by the grid code $\underline{I}_{P}^{k}$ and $\underline{I}_{Q}^{k}$, see (4.23-4.25).
4. Determine the weighting factors λ_x of the multi-objective function.
5. Introduce the MMC parameters and limitations.
6. Run the optimization algorithm using equations detailed above.

The optimization algorithm could be implemented following two different strategies as shown in Fig. 4.6. The first approach is to perform an online optimization, detailed in Fig. 4.6a, which could be executed using computers, DSPs or FPGAs. The algorithm receives the real-time magnitudes of the HVDC system and it calculates the AC grid, DC and

AC arm current references that track the set-points imposed by the TSO while keeping the internal energy of the converter balanced and within the imposed boundaries. Then, conventional MMC inner and grid current controllers could be used to achieve the desired current references.

Another approach would be to run the optimization offline, see Fig. 4.6b. The optimization is executed offline considering multiple operational points of the converter, saving all the results. These results could be stored as a data table in the memory of a processor unit. Then, whenever this device receives the real-time data from the HVDC system, it is possible to interpolate the desired current control references from the data table which are sent to the different MMC current regulators.

The first configuration ensures that the optimal references are obtained for the specific point of operation, but requires to run the optimization online with the corresponding computational burden. The second option only requires to correlate the actual operating point with the corresponding one in the data table, but it may have some errors depending on the size of the data set up in this table (which might be limited by the memory available in the microcontroller).

4.5 Case Study

In this section, the results of the proposed optimization-based reference calculation algorithm are shown in voltage sag (case A) and constrained (cases B and C) scenarios. The optimization problem is solved using Matlab® *fmincon* function (interior-point based method [70]), since it can deal with constrained nonlinear multi-variable problems. In addition, the optimization results are also applied to a MMC time-domain simulation model developed in Matlab Simulink®. The steady-state simulation waveforms and the optimization output are compared to confirm the applicability of the suggested method and to verify that the MMC constrains (currents and voltages limits) are respected. Table 4.2 details the system parameters for the case studies.

4.5.1 Case A: Optimal reference calculation in AC voltage sags

This case study is performed to illustrate how the suggested optimal reference calculation is able to provide adequate grid support, compared with the conventional Strategy I and the ideal grid code support Strategy

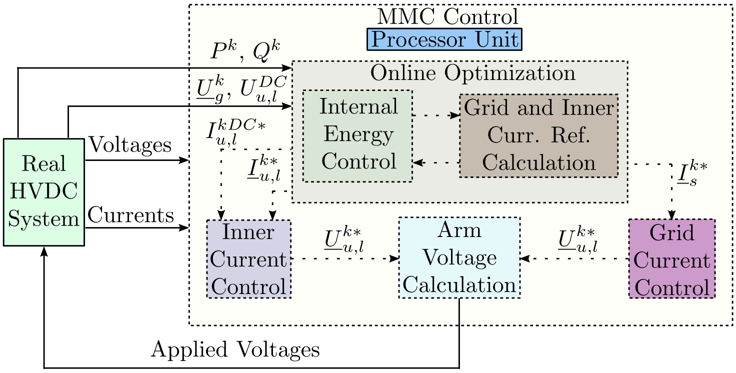

(a) Online optimization.

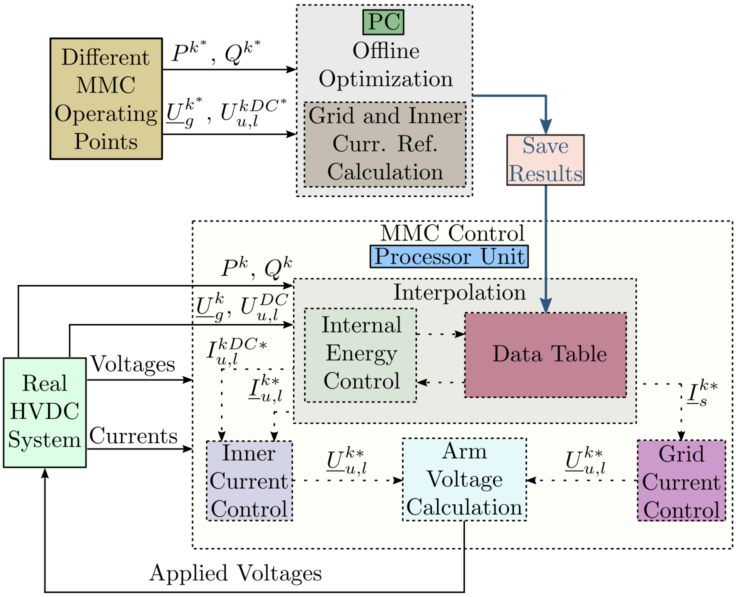

(b) Offline optimization.

Fig. 4.6: Application scenarios for the proposed optimization algorithm.

II[2] (see Section 4.3). The MMC is considered to be operating in the following steady-state pre-fault conditions: grid voltage $|\underline{U}_g^k| = 1$ pu and active and reactive power set-points $P^k = 0.32$ pu and $Q^k = 0$. Then, balanced and unbalanced AC voltage sags (type A, C and F) are imposed, with faulted voltage V equal to 0.3 pu [51]. The Spanish grid

---

[2] Strategy I provides only positive sequence support, based on positive sequence voltage, while Strategy II provides the ideal per phase support following the grid code, including the zero sequence (it is used only as a reference, as it is not implementable).

Table 4.2: System parameters.

Parameter	**Symbol**	**Value**	**Units**
Rated power	S	526	MVA
Rated power factor	$\cos\phi$	0.95 (c)	-
AC-side voltage	$\underline{U}_{gRMS}$	184.75	kV
HVDC link voltage	U^{DC}	±320	kV
Phase reactor impedance	$\underline{Z}_s$	0.02+j 0.1	pu
Arm reactor impedance	$\underline{Z}_a$	0.01+j 0.08	pu
Converter modules per arm	$N^k_{a_{u,l}}$	400	-
Average module voltage	U_{SM}	1.6	kV
SM capacitance	C_{SM}	8	mF
Grid code voltage 1	U_{min1}	0.9	pu
Grid code voltage 2	U_{min2}	0.6	pu
Grid code voltage 3	U_{max1}	1.05	pu
Max reactive current	ΔI_{rmax}	1	pu
Optimal weighting factor 1	λ_1	10^{-9}	-
Optimal weighting factor 2	λ_2	1	-
Optimal weighting factor 3	λ_3	10^6	-
Maximum MMC arm current	I^{arm}_{max}	0.77	pu
Maximum AC grid current	I^{AC}_{max}	1	pu

code is used to implement the different reference calculation strategies (see values in Table 4.2).

Firstly, imposing the balanced AC voltage sag condition (type A [51]) results in same voltage levels for the three phases equal to $|U^k_g| = 0.3$ pu. Based on the grid code, as $|U^k_g| < U_{min2}$ (see Section 4.3 and Table 4.2), all phases of the AC system must receive full support from the MMC. Secondly, the unbalance type C fault (single-line to ground (SLG)) condition is imposed, leading to the following voltages $|U^a_g| = 1$ pu and $|U^{bc}_g| = 0.56$ pu. Based on the grid code, phases *b* and *c* require maximum reactive current injection while phase *a* AC current should be kept constant. Finally, the unbalanced type F fault (line-to-line to ground (LLG)) scenario is imposed. During this event, the voltages of the three phases are $|U^a_g| = 0.3$ pu and $|U^{bc}_g| = 0.68$ pu. As a result, phase *a* requires full voltage support, whereas the remaining phases only demand partial support from the converter. Whereas the phasor form of the AC voltages, as well as the per-phase AC current references are compared for each strategy and depicted in Fig. 4.7.

For the different AC voltage sag conditions, shown in Fig. 4.7a, the output of the optimal reference calculation strategy is compared with Strategies I and II (calculated without applying optimization as detailed in Section 4.3). Figs. 4.7b to 4.7d depict the phasor representation

Table 4.3: Comparison of the active and reactive powers using the different strategies.

Fault type	**Phase**	P_g^k [pu]			Q_g^k [pu]		
		Opt.	Str. I	Str. II	Opt.	Str. I	Str. II
A	a	0	0	0	−0.1000	−0.1000	−0.1000
	b	0	0	0	−0.1000	−0.1000	−0.1000
	c	0	0	0	−0.1000	−0.1000	−0.1000
C	a	0.3011	0.1198	0.3167	0	−0.1806	0
	b	0	0.1198	0	−0.0341	−0.1806	−0.1878
	c	0.1784	0.1198	0	−0.05864	−0.1806	−0.1878
F	a	0.0150	0	0	−0.0988	−0.1778	−0.1000
	b	0.1548	0	0.1548	−0.1659	−0.1778	−0.1659
	c	0	0	0.1548	−0.1659	−0.1778	−0.1659

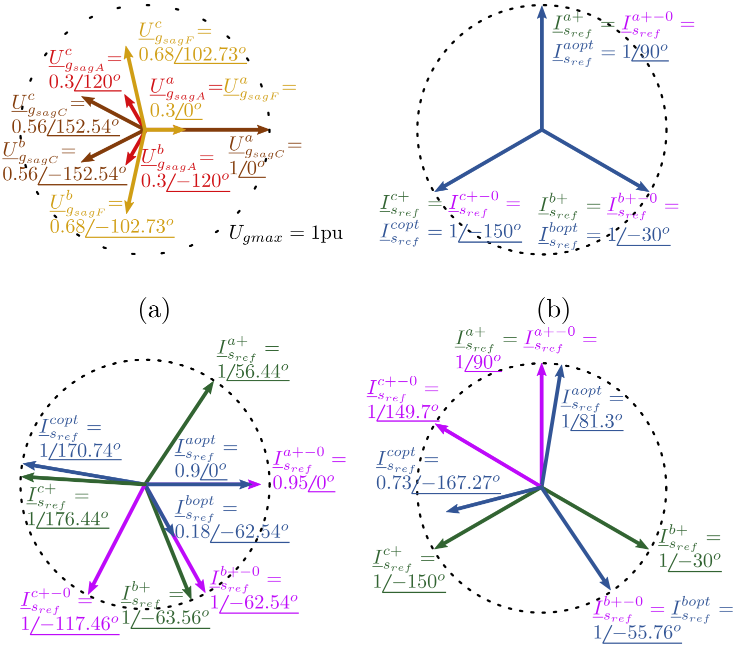

(a) (b) (c) (d)

Fig. 4.7: Grid AC voltages and currents phasor representation for different AC grid conditions. a) Voltages for each voltage sag (A-red, C-brown, F-yellow), b) Currents for sag type A, c) Currents for sag type C and, d) Currents for sag type F. Strategy I - green. Strategy II - pink. Optimal strategy - blue.

of the AC grid current references obtained implementing the different strategies for the case study faults. Strategy I ($I_{s_{ref}}^{k+}$) is represented using green phasors, Strategy II ($I_{s_{ref}}^{k+-0}$) is depicted using pink phasors and the optimized current references ($I_{s_{ref}}^{kopt}$) are illustrated using blue phasors. The dashed circle symbolizes the AC grid current limits I_{max}^{AC}. Moreover, the per-phase active and reactive powers during the faults are presented in Table 4.3 to compare the power injection performance of the different strategies.

Fig. 4.7b and the powers presented in Table 4.3 show that the three reference calculation strategies lead to the same result for a balanced voltage sag as the grid voltages only present positive sequence component. It can be observed that all the grid currents are 90^o degrees phase-shifted in comparison with their phase-voltage (full voltage support), which is also in agreement with the power results as $P_g^k = 0$ and $Q_g^k = 0.100$ pu. In terms of the optimal strategy results, the active and reactive coefficients for this case are $\alpha^k = 1^{-5}$ and $\beta^k = 0.999$, thus achieving a maximization of the reactive power injection. Finally, for such voltage sag condition, any of the presented strategies will completely fulfill the grid code requirements.

For fault type C, which the results are shown in Fig. 4.7c, it can be noticed that for the healthy phase (phase a), the optimization algorithm has a similar response to Strategy II. The obtained coefficients are $\alpha^a = 0.951$ and $\beta^a = 1$, meaning that phase a current is almost not limited (it is the healthy one), and only a small reduction is applied to the active current component. To fully comply with the grid code requirements, the reactive optimal coefficient should be $\beta^{bc} = 1$ for phases b and c to provide full reactive support, also implying that $\alpha^{bc} = 0$ (no current room left for active power). However, in order to meet all the constraints imposed in the formulation of the optimization problem, such coefficients are unfeasible. Phase b resulted in $\alpha^b = 0$ and $\beta^b = 0.18$, thus injecting no active power and only a constrained amount of reactive power. Whereas, for phase c, the optimization kept $\alpha^c = 1$ and reduced $\beta^c = 0.312$, thus providing active power and partial reactive power support. Note that, as the ideal support to be provided (Strategy II) is highly unbalanced (pink phasors in Fig. 4.7b), even though the optimization algorithm attempts to keep α^k and β^k values as close as possible to 1, this condition cannot be achieved due to the system and converter imposed constraints.

Further conclusions can be drawn observing the reactive and active powers injected during the voltage sag type C. As it can be noticed in Table 4.3, the amount of active power injected for phase a using the optimal algorithm is similar to the one imposed by the grid code requirement

(Strategy II), whereas Strategy I leads to a larger error. Furthermore, Strategy I has high reactive power injection, which might result in undesirable over-voltages in phase a. For phase b, the active power given by the proposed optimization method also shows better performance in comparison to Strategy I. However, due to the fault characteristics and the converter constraints, the optimization algorithm cannot achieve the levels imposed by the grid operator (shown in Strategy II) for P_g^c, Q_g^b and Q_g^c. Although the optimization is unable to fully satisfy the grid code requirement, it still is a more suitable option for such fault as it might avoid causing over-voltages in the AC system as could occur when Strategy I is employed.

For type F fault (see Fig. 4.7d), according to the grid code, phase a requires full voltage support, whereas partial support is needed by the other phases. The optimal coefficients for phase a are equal to $\alpha^a = 0.158$ and $\beta^a = 0.988$, indicating that the optimization algorithm presented similar response compared to Strategy II. Moreover, $\underline{I}_{s_{ref}}^{bopt}$ is in perfect agreement with the grid code requirement, with $\alpha^b = 0.718$ and $\beta^b = 1$ (partial reactive support requirement). However, it can be noted that $\underline{I}_{s_{ref}}^{copt}$ is deviated from the ideal support (Strategy II) in terms of angle and magnitude. This happens as the optimization must comply with the imposed constraints, leading to weights equal to $\alpha^c = 0$ and $\beta^c = 1$, which means that it is only providing reactive current support, without injecting active power (in accordance to the reactive power prioritization). In summary, the optimal references obtained are able to meet the reactive power support requirements as $\beta^k \approx 1$ for all phases, while active power is maximized whenever possible, without violating any of the converter constraints. Finally, it can be observed in Table 4.3 that the optimization algorithm presents superior performance compared to Strategy I for all phases, as the usage of Strategy I would lead not only to undesirable over-voltages in the AC network but also to higher mismatches in the active power levels.

Next, the steady-state time-domain simulation results are analyzed once the obtained optimal references are applied to the converter model to verify the applicability and correctness of the model. The response of the proposed optimization algorithm (continuous lines) is compared with the waveforms of an averaged model of the MMC (dashed lines) during a type C fault, as shown in Fig. 4.8. The design limits for the arms voltage and currents, as well as the maximum allowed value for the AC grid current and maximum and minimum equivalent arm capacitor voltage ripple are represented as dotted lines. The instantaneous powers of the

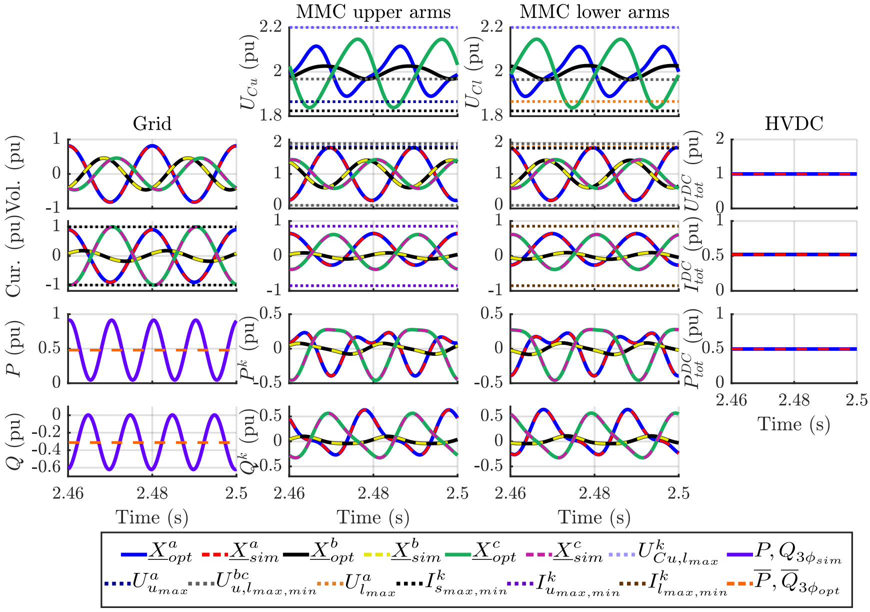

Fig. 4.8: Steady-state waveforms of the MMC quantities during a type C fault.

upper arms, lower arms and the HVDC network are shown for all case-studies based on the results obtained both from the solution of the optimization problem and from the time-domain simulations. Moreover, the active and reactive powers exchanged with the AC grid are depicted in two different manners. The average active and reactive power references given by the optimization are shown as dashed orange lines, whereas the instantaneous powers are depicted as continuous magenta lines (left-bottom part). In Fig. 4.8, due to the unbalanced characteristic of fault, the instantaneous powers injected into the AC grid present double-line frequency oscillations. However, these oscillations are mitigated by the MMC and are not reflected into the DC network. As it can be observed, the quantities obtained from the optimization are in close agreement with the MMC averaged model, thus confirming its applicability. In addition, the AC grid currents profile match their phasorial representation (see Fig. 4.7c). Lastly, all the MMC quantities are within the design limits, since no waveform is surpassing its corresponding restriction, although some of them are hitting some limitations (e.g. AC current limits), due to the optimization performance and imposed constraints.

4.5.2 Saturation in the MMC arm voltages

The objective of this case study is to show the capability of the optimization method to operate with individual arm constraints. Assume that the MMC is operating in normal conditions with 400 available levels per arm (same AC voltage and power set-points as case A - pre-fault). Then, a contingency situation is imposed into the model causing a reduction of the working SMs in the upper arm for phase a ($N^a_{a_u}$) from 400 to 330. This condition will affect the equivalent arm capacitor voltage for the upper arm in phase a ($U^a_{C_u}$), thus limiting the voltage that can be applied with this arm. To operate in such constrained scenario, the suggested optimization formulation is used modifying only the number of available SMs.

Fig. 4.9 shows the optimization results being applied to the simulation model in such case. It can be seen that the stored energy (voltage) in phase a is importantly reduced (see Fig. 4.9 top-left graph), impacting both its DC and AC voltage levels. In order to avoid over-modulation, the applied voltages in the upper arm of phase a are decreased and this also affects the applied voltage for the lower one, which must be adapted to fulfill the optimization constraints. Furthermore, phases b and c applied voltages are increased (to compensate the reduction in phase a) by the optimization algorithm targeting to meet the pre-contingency active and reactive power set-points. These voltages are incremented without entering over-modulation mode, as the optimization is limiting $\underline{U}^{bc}_{u,l}$ quantities to their respective maximum levels.

Even though the optimization attempts to achieve the pre-fault power set-point values, the converter limitations and constraints do not allow the MMC to reach the desired power levels, consequently the power flow through the MMC is reduced. This is reflected in the optimization coefficients setting them to $\alpha^k = 0.364$ and $\beta^k = 1$ (equal power/current per phase), which is constraining the active power injection to the AC side. In addition, although there is energy imbalance inside the converter, the optimization is capable of attaining steady-state conditions by establishing an internal power flow among the MMC phases (see Fig. 4.9 arm currents).

4.5.3 Maximum capacitor voltage fluctuation

This case study aims to demonstrate that the optimization is able to limit the maximum equivalent arms' capacitor voltages based on the estimation derived in Section 4.2.5. Considering that the MMC is again

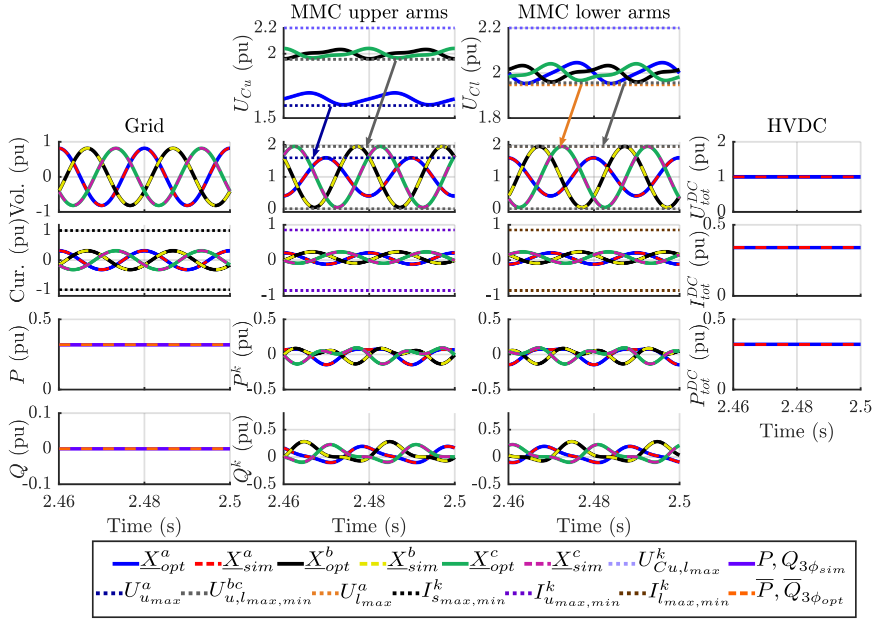

Fig. 4.9: MMC waveforms during constraint scenario for the arms voltages.

operated under pre-fault defined settings, two different maximum voltage ripple scenarios are applied to all the converter's arms. The optimization results for the two cases are shown in Fig. 4.10. For the first condition (see Fig. 4.10a), the maximum voltage ripple for all arms is equal to 10% of the arm voltage reference ($N_{a u,l}^k U_{SM} = 640$ kV), which represents the settings used in the previous case studies. Whereas, Fig. 4.10b displays the waveforms when the maximum ripple is reduced to 5%.

In the first case, the value of the maximum ripple is higher than the operating voltage stored in the equivalent arms' capacitors (see Fig. 4.10a), keeping a safety margin. Thus, the optimization coefficients are equal to $\alpha^k = 1$ and $\beta^k = 1$ (not limiting any power). However, if the maximum voltage limitation is reduced (see Fig. 4.10b), the optimization decreases the active power exchanged by the converter ($\alpha^k = 0.74$ and $\beta^k = 1$) to maintain the converter within its acceptable limits. The reduction in the amount of active power injected into the AC system happens due to the necessity of decreasing the stored energy magnitudes in the equivalent arm capacitors to avoid exceeding the design limitation. Otherwise, there is no possible alternative to limit the equivalent arm capacitor voltage ripple to the imposed level, which is in agreement with (4.19) and (4.20). Also, it can be confirmed that the ripple estimation used in the optimization is valid, as the maximum and minimum equivalent arm capacitor voltages are kept within the bounds imposed via (4.22) (see the top graphs of Fig. 4.10b). Finally, the errors for the maximum and minimum equivalent arm capacitor voltage between the actual value (obtained based on the analytical expression regarding the first and second order frequency terms (4.13)) and the maximum and minimum bounds (4.22) are: $e_{max} = 0.5\%$ and $e_{min} = 1.34\%$ considering maximum allowed voltage ripple equals to 10%, whereas $e_{max} = 0.46\%$ and $e_{min} = 1\%$ when the maximum allowed ripple is reduced to 5%.

4.6 Conclusion

An optimization-based reference calculation method for MMCs operating in normal and constrained situations (converter variables limited due to voltage or current limitations) has been presented. The optimization problem has been formulated based on the steady-state per arm approach model, which permits analyzing individually each converter arm while enabling to impose specific arm constraints. The limitations considered have been each individual arm currents and voltages and the SM capacitor voltages, in which the last one was obtained through an analytic estimation. In addition, the optimization algorithm has been formulated as a multi-objective problem, allowing to prioritize between active power, reactive power or converter arm losses reduction when the converter is operating in a constrained condition. Results show that the optimization algorithm is able to provide adequate converter references in different scenarios, such as unbalanced fault conditions, reduction of the arm available SMs or limited arm ripple operation. The optimization output references are validated using time-domain simulations, which in all cases revealed the correct operation of the converter, attempting to fulfil the grid code requirements while maintaining the converter within the defined voltage and current limits.

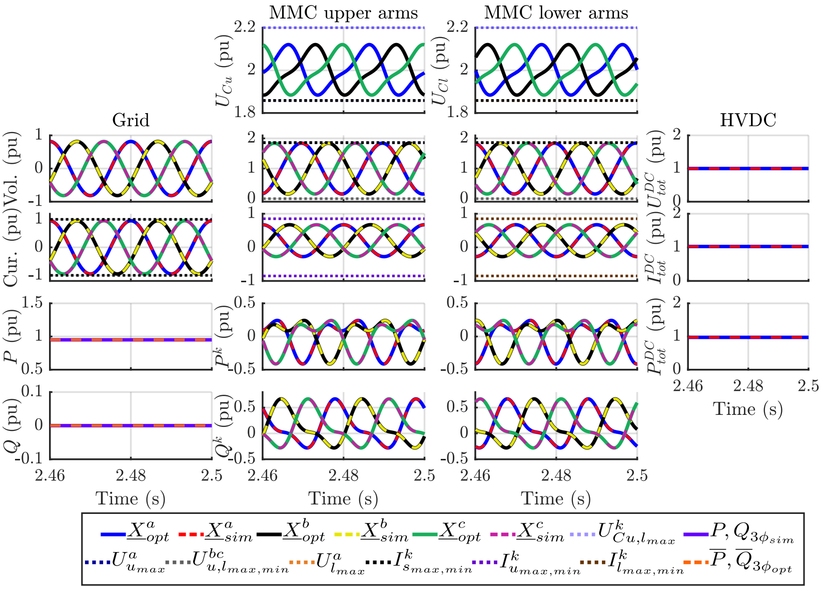

(a) Maximum ripple equals to 10%.

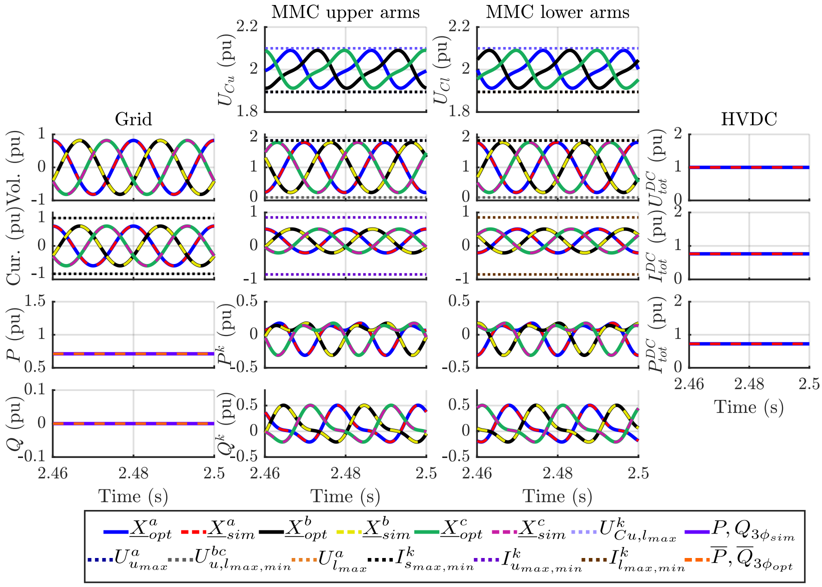

(b) Maximum ripple equals to 5%.

Fig. 4.10: Time-domain waveforms for the equivalent arms' capacitor voltages. a) Maximum ripple equals to 10% and, b) Maximum ripple equals to 5%.

Chapter 5

Real-time optimization-based reference calculation integrated control for MMCs

This chapter is based on the following publications:

[**J3**] D. Westerman Spier, J. M. Rodriguez-Bernuz, E. Prieto-Araujo, J. López-Mestre, A. Junyent-Ferré and O. Gomis-Bellmunt, "Real-time optimization-based reference calculation integrated control for MMCs considering converter limitations", in *IEEE Transactions on Power Delivery*, 2021.

[**C3**] D. Westerman Spier, E. Prieto-Araujo, J. López-Mestre and O. Gomis-Bellmunt, "Optimization-based reference calculation for Modular Multilevel Converters in balanced and unbalanced network conditions", *2021 23rd European Conference on Power Electronics and Applications (EPE'21 ECCE Europe)*, 2021, pp. 1-6.

5.1 Introduction

As it was concluded in the previous chapter, an optimization-based algorithm to calculate the MMC's references can improve the converter's operation and enhance its ability to provide voltage support during AC network fault conditions. However, it is still necessary to integrate such references in a proper control strategy to provide optimal regulation of the MMC-HVDC. Industrial practices given by Cigre suggest that the MMC's controllers should regulate the AC network currents, the circulating currents and the internal energy of the converter [71]. Under balanced grid conditions, traditional control strategies such as the circulating current suppressing control (CCSC) [72] can be used to keep the MMC's quantities close to their nominal values. But under scenarios where energy deviations occur for instance, during AC/DC power setpoints changes, the CCSC may present lower performance compared to strategies that regulate the MMC's SM capacitors energies [56]. Nevertheless, during unbalanced AC and/or DC faults, several quantities of the converter are importantly affected. The internal states of the converter must be properly compensated to maintain the system operating accordingly to the network operator requirements (e.g. providing frequency or voltage support to the grid) without transgressing the physical limitations of the converter.

Focusing on enhancing the performance of the MMC, several authors employed optimization algorithms as part of the control strategy. By doing so, the internal energy and circulating current limitations of the converter can be easily imposed in the formulation of the problem. In [38,73], different optimization problems are developed targeting the internal energy balancing and optimizing the circulating currents, which are later used in the control strategy. However, due to their high nonlinear characteristics (resulting in high computational burden), these models have to be used in an offline manner. Thus, the control variables required from the optimal algorithm are calculated prior their application into the real system. Further improvements can be achieved if the optimization problem can be solved in real-time. In [45], a real-time linear matrix inequality optimization problem is integrated with conventional AC grid and internal energy control strategies. But, the controller cannot compensate the MMC's internal energy producing undesired sustained deviations during unbalance AC faults. Model Predict Control (MPC) is also a potential candidate to optimize the MMC's operation. In [74, 75], different MPC methods are used to regulate the MMC during AC unbalanced faults. Although they elaborate a comprehensive control method for the AC grid current, the internal energy balancing is disregarded.

The different approaches presented above share similar AC grid current control methods which only considers the injection of positive-sequence active current component even during AC network voltage sags. Under these faults, the MMC must comply with the TSO's Fault Ride-Through (FRT) requirements, providing additional support to the network (e.g. frequency or voltage supports), by either injecting and/or absorbing active and/or reactive current components. Although these requirements are imposed by the TSOs of each country, in accordance to the European Network of Transmission System Operators (ENTSO-E) [76], there is a limited number of publications addressing this issue in HVDC systems [77–80]. However, they either cannot fully comply with the grid code or are more challenging to impose the TSO's regulations in their control strategy formulation.

To the best of the authors knowledge, a real-time optimization-based reference calculation algorithm integrated with a control for MMC-HVDC stations to provide adequate support to a faulted network while considering the converter limitations has not been proposed yet. Aiming to address these challenges, this chapter brings the following main contributions:

- Formulation of an optimization-based control strategy to ensure that the positive- and negative-sequences of the AC grid's active and reactive components are as close as possible to the grid code requirements, without exceeding the MMC's limits.
- The MMC's DC and AC circulating current components are limited simultaneously for each arm of the converter.
- The power mismatches between the converter's upper and lower arms, as well as among the phase-legs are considered simultaneously in the formulation of the algorithm.
- The computational burden of the algorithm is reduced by performing an LTV approximation of the system model. It is shown that this approach reduces the convergence time more than one order of magnitude compared to a nonlinear formulation; making the real-time implementation of the algorithm feasible.
- Definition of a strategy to achieve a seamless transition between the optimized and a conventional reference generator in the event that the optimization does not converge in the allowed time.

The proposed linearized optimization-based reference calculation algorithm integrated with the MMC's control strategy is analyzed theoretically and through detailed time-domain simulations.

5.2 Description of the optimization problem

This section describes the formulation of the optimization problem and the simplification applied to reduce its computational burden for real-time applications. It is first shown that the analysis of the MMC system leads to set of nonlinear equations. Thus, the preliminary nonlinear formulation of the optimization of the system is presented. Next, the LTV approximation is employed into the nonlinear model, which permits to formulate the optimization as a standard linear quadratic problem (QP) reducing the computational complexity. The schematic of the MMC is shown in the left-part of Fig. 5.1.

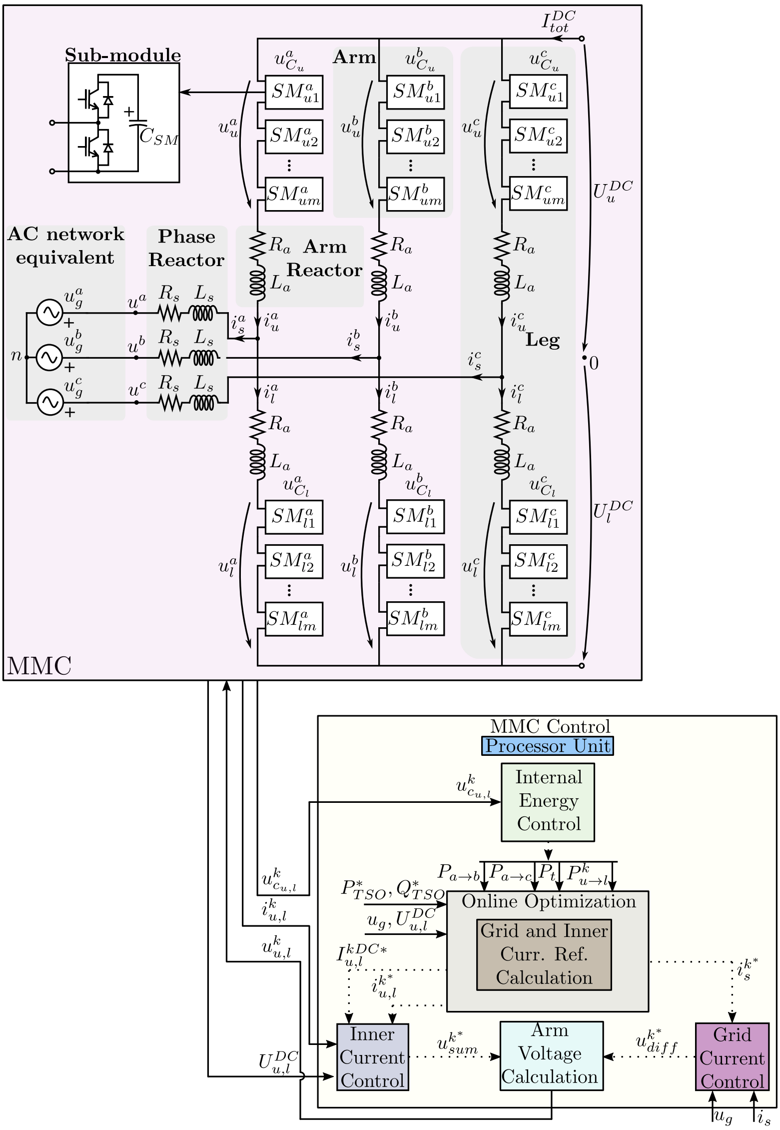

Fig. 5.1: MMC model with the proposed optimal control conceptualization.

5.2.1 Nonlinear model of the MMC

The nonlinear steady-state mathematical model of the MMC can be described as

$$\underline{U}_{0n} = \underline{U}_g^k + \underline{Z}_s(\underline{I}_u^k - \underline{I}_l^k) + \underline{Z}_a\underline{I}_u^k + \underline{U}_u^k \tag{5.1a}$$

$$\underline{U}_{0n} = \underline{U}_g^k + \underline{Z}_s(\underline{I}_u^k - \underline{I}_l^k) - \underline{Z}_a\underline{I}_l^k - \underline{U}_l^k \tag{5.1b}$$

$$\underline{I}_u^a + \underline{I}_u^b + \underline{I}_u^c = 0 \tag{5.1c}$$

$$\underline{I}_s^a + \underline{I}_s^b + \underline{I}_s^c = 0 \tag{5.1d}$$

$$\underline{I}_s^k = \underline{I}_u^k - \underline{I}_l^k \tag{5.1e}$$

$$\begin{bmatrix} I_{s_r}^{+,-} \\ I_{s_i}^{+,-} \end{bmatrix} = \begin{bmatrix} \cos(\theta^{+,-}) & -\sin(\theta^{+,-}) \\ \sin(\theta^{+,-}) & \cos(\theta^{+,-}) \end{bmatrix} \cdot \begin{bmatrix} \alpha^{+,-} \cdot I_P^{+,-} \\ \beta^{+,-} \cdot I_Q^{+,-} \end{bmatrix} \tag{5.1f}$$

$$\begin{bmatrix} \underline{I}_s^a \\ \underline{I}_s^b \\ \underline{I}_s^c \end{bmatrix} = \begin{bmatrix} 1 & 1 & 1 \\ \underline{p}^2 & \underline{p} & 1 \\ \underline{p} & \underline{p}^2 & 1 \end{bmatrix} \cdot \begin{bmatrix} I_{s_r}^{+} + j \cdot I_{s_i}^{+} \\ I_{s_r}^{-} + j \cdot I_{s_i}^{-} \end{bmatrix} \tag{5.1g}$$

$$\sum_{k=a}^{c} \left[\mathrm{Re}\Big\{ \underline{U}_u^k \underline{I}_u^k + \underline{U}_l^k \underline{I}_l^k \Big\} + U_u^{kDC} I_u^{kDC} + U_l^{kDC} I_l^{kDC} \right] = 0 \tag{5.1h}$$

$$P_{u\to l}^k = \mathrm{Re}\Big\{ \underline{U}_u^k \underline{I}_u^k - \underline{U}_l^k \underline{I}_l^k \Big\} + \left(U_u^{kDC} I_u^{kDC} - U_l^{kDC} I_l^{kDC} \right) \tag{5.1i}$$

$$\begin{aligned} P_{a\to b} = \mathrm{Re}\Big\{ & \left(\underline{U}_u^a \underline{I}_u^a + \underline{U}_l^a \underline{I}_l^a \right) - \left(\underline{U}_u^b \underline{I}_u^b + \underline{U}_l^b \underline{I}_l^b \right) \Big\} + \\ & \left(U_u^{aDC} I_u^{aDC} + U_l^{aDC} I_l^{aDC} \right) - \left(U_u^{bDC} I_u^{bDC} + U_l^{bDC} I_l^{bDC} \right) \end{aligned} \tag{5.1j}$$

$$\begin{aligned} P_{a\to c} = \mathrm{Re}\Big\{ & \left(\underline{U}_u^a \underline{I}_u^a + \underline{U}_l^a \underline{I}_l^a \right) - \left(\underline{U}_u^c \underline{I}_u^c + \underline{U}_l^c \underline{I}_l^c \right) \Big\} + \\ & \left(U_u^{aDC} I_u^{aDC} + U_l^{aDC} I_l^{aDC} \right) - \left(U_u^{cDC} I_u^{cDC} + U_l^{cDC} I_l^{cDC} \right) \end{aligned} \tag{5.1k}$$

$$I_s^{kDC} = I_u^{kDC} - I_l^{kDC} \tag{5.1l}$$

$$I_{tot}^{DC} = I_u^{aDC} + I_u^{bDC} + I_u^{cDC} \tag{5.1m}$$

$$U_u^{DC} + U_l^{DC} = U_u^{kDC} + U_l^{kDC} + 2R_a \left(I_u^{kDC} + I_l^{kDC} \right) \tag{5.1n}$$

$$2\left(-U_u^{aDC} + U_l^{aDC} \right) + \left(U_u^{bDC} - U_l^{bDC} + U_u^{cDC} - U_l^{cDC} \right) = 0 \tag{5.1o}$$

$$\left(U_u^{bDC} - U_l^{bDC} - U_u^{cDC} + U_l^{cDC} \right) = 0 \tag{5.1p}$$

with $\underline{p} = e^{j\frac{2\pi}{3}}$, $\theta^{+,-}$ being the AC grid voltage positive- and negative-sequences phase-angles and $I_p^{+,-}$ and $I_q^{+,-}$ as the positive- and negative-sequence active and reactive current components set-points to be injected/absorbed by the AC network which are demanded by the TSO, respectively. Equations (5.1a-5.1e) and (5.1l-5.1m) describe the AC and DC currents and the AC voltages in the converter, already included in the optimization problem in [80]. Expressions (5.1f-5.1g) are used to calculate the AC network current levels. Note that the coefficients $\alpha^{+,-}$ and $\beta^{+,-}$ are used to adequate the amount of active and reactive currents to be injected/absorbed by the AC network to avoid the converter to exceed its physical limitations. In addition, the values of these four coefficients have a direct effect on the AC grid current magnitudes and an indirect impact on other internal quantities of the MMC, which may cause them to exceed their limits. Thus, the selection of $\alpha^{+,-}$ and $\beta^{+,-}$ is performed by an optimization algorithm (see Section 5.2.2). Next, (5.1h-5.1p) introduce terms not accounted in [80]. Where, (5.1h) describes the steady-state condition, (5.1i-5.1k) define the power differences between arms and phase-legs and (5.1n-5.1p) characterize the DC voltages in the converter while eliminating possible DC voltages into the AC grid.

5.2.2 Nonlinear optimization problem

The multi-objective nonlinear optimization problem that enables the prioritization among the positive- and negative-sequence components of the active and reactive AC grid current and, at the same time, ensures that the MMC's quantities are kept within their design limits is given as follows

$$\max_{\substack{\underline{I}^k_{u,l}, I^{kDC}_{u,l}, \underline{U}^k_{u,l}, U^{kDC}_{u,l},\\ \underline{U}_{n0}, \alpha^{+,-}, \beta^{+,-}}} \quad \lambda_{I_p^+}\alpha^+ + \lambda_{I_q^+}\beta^+ + \lambda_{I_p^-}\alpha^- + \lambda_{I_q^-}\beta^- \tag{5.2a}$$

$$\text{s.t.} \quad (5.1a \text{ to } 5.1p) \tag{5.2b}$$

$$I^k_s \leqslant I^{AC}_{max} \tag{5.2c}$$

$$I^k_{u,l} + I^{kDC}_{u,l} \leqslant I^{arm}_{max} \tag{5.2d}$$

$$0 \leqslant U^k_{u,l} + U^{kDC}_{u,l} \tag{5.2e}$$

$$0 \leqslant \alpha^+ \leqslant 1 \tag{5.2f}$$

$$0 \leqslant \alpha^- \leqslant 1 \tag{5.2g}$$

$$0 \leqslant \beta^+ \leqslant 1 \tag{5.2h}$$

$$0 \leqslant \beta^- \leqslant 1 \tag{5.2i}$$

where, the OF, given in (5.2a), consists of four coefficients, $\alpha^{+,-}$ and $\beta^{+,-}$, which are employed to regulate the levels of positive- and negative-sequence active and reactive current components to be injected/absorbed by the AC grid, respectively, in order to comply with the grid operator requirements. These coefficients are be prioritized according to the values used in the optimal weights $\lambda_{I_p{}^{+,-}, I_q{}^{+,-}}$. The optimal weights in this chapter have been chosen based on the performance of the reactive current injection/absorption after running extensively simulations considering different faults and several different weights' combination. It was observed after those tests that the optimal performance that eases the prioritization and improve the convergence time it is when factor of at least 10^{-3}, regarding each λ_x is used. Then, to provide optimal voltage support to the network during AC network faults, the optimal weights are selected as $\lambda_{I_q^+} \gg \lambda_{I_q^-} \gg \lambda_{I_p^+} \gg \lambda_{I_p^-}$[1]. The equality constraints are set in (5.2b) and are based on the nonlinear steady-state model of the MMC (see Section 5.2.1). The maximum allowed current in the AC network and through the MMC's arms are imposed in (5.2c-5.2d) by setting the magnitudes of I_{max}^{AC} and I_{max}^{arm}, respectively. Since half-bridge SMs are considered in this analysis, the lower limit in (5.2e) is set as 0, as it is not possible to synthesize negative voltages. Nevertheless, negative values could be considered if full-bridge SMs were employed. Constraints (5.2f-5.2i) establish the maximum and minimum allowed values for the optimal weights $\alpha^{+,-}$ and $\beta^{+,-}$. Under normal conditions, these four quantities are equal to 1, but depending on the AC and DC network voltage conditions, their levels might change to meet the MMC limitations. Although the Spanish TSO [59] requirements have been described in Chapter 4, for the sake of completeness it is again described in this Chapter. Its impositions are to maximize the injection of reactive current during AC grid voltage sags. The magnitude of the additional reactive current component ΔI_r to be injected/absorbed by the grid varies according to the RMS voltage levels at the PCC as

$$U_{min1} \leqslant U_g \leqslant U_{max1} \rightarrow \Delta I_r = 0 \tag{5.3a}$$

$$U_{min2} \leqslant U_g < U_{min1} \rightarrow \Delta I_r = \frac{\Delta I_{rmax}(U_{min1} - U_g)}{U_{min1} - U_{min2}} \tag{5.3b}$$

$$U_g < U_{min2} \rightarrow \Delta I_r = \Delta I_{rmax} \tag{5.3c}$$

where the values of U_{min1}, U_{max1}, U_{min2} and ΔI_{rmax} are defined by the grid operator.

5.2.3 Linearization of the optimization problem

Although most of the equations presented in Section 5.2.2 are linear, the internal energy balance of the converter (5.1i-5.1k) and the overall energy balance of the system (5.1h) present a strong nonlinear relationship. This problem is similar in nature to the energy regulation problem discussed in [81] where an LTV approximation is proposed to reduce the computational burden of a nonlinear MPC controller. This same linearization

---

[1] Under unbalanced faults which require the injection of the positive-sequence and the absorption of the negative-sequence reactive components, the positive-sequence current to be injected will be 90^o leading the phase-angle of U_g^+, whereas the current to be absorbed for U_g^- must be lagging 90^o to mitigate its asymmetric effects. For grid operators that prioritize the active current injection (e.g. [60]), the relation should be modified as $\lambda_q^{+,-} \ll \lambda_p^{+,-}$.

strategy is implemented in [82] to design a predictive controller on an MMC controller; thus validating the scalability of the LTV approach to the MMC. Similarly, the LTV linearization is adopted here to tackle the large computational burden arisen from the nonlinear formulation of the prioritization algorithm.

Therefore, the nonlinear behaviour of the system is decomposed into two different subsystems: one that determines the nonlinear behaviour of the converter and is characterized by its steady-state trajectories, and an LTI system which describes the small-signal perturbations around the nonlinear steady-state points. This approximation resembles a classic Jacobian linearization. However, in this case, it is performed over steady-state varying trajectories instead of static DC quiescent point. Note that these steady-state trajectories can either be calculated within the optimization algorithm or come from an external source (see Section 5.4). Generically, the LTV approximation can be represented as

$$\begin{aligned} \frac{d}{dt}x &= \frac{d}{dt}\left(X+\hat{x}\right) = \frac{d}{dt}X + \frac{d}{dt}\hat{x} = f(x,u) \\ &\approx f(X,U) + \left.\frac{\partial f}{\partial x}\right|_{\hat{x},\hat{u}} (x-X) + \left.\frac{\partial f}{\partial u}\right|_{\hat{x},\hat{u}} (u-U) \\ &\approx \underbrace{f(X,U)}_{F_0} + \frac{\partial f(X,U)}{\partial x}\hat{x} + \frac{\partial f(X,U)}{\partial u}\hat{u} \end{aligned} \tag{5.4}$$

where x represents a vector containing the MMC's states $x \triangleq \Big[\underline{I}^{k}_{u[1]}, \underline{I}^{k}_{l[1]}, I^{kDC}_{u[1]}, I^{kDC}_{l[1]}, \underline{I}^{k}_{s[1]}, \alpha^{+}_{[1]}, \beta^{+}_{[1]}, \alpha^{-}_{[1]}, \beta^{-}_{[1]}, ..., \underline{I}^{k}_{u[N]}, \underline{I}^{k}_{l[N]}, I^{kDC}_{u[N]}, I^{kDC}_{l[N]}, \underline{I}^{k}_{s[N]}\Big]^{T}$, u accounts for the converter's control quantities $u \triangleq \Big[\underline{U}^{k}_{u[0]}, \underline{U}^{k}_{l[0]}, U^{kDC}_{u[0]}, U^{kDC}_{l[0]}, ..., \underline{U}^{k}_{u[N-1]}, \underline{U}^{k}_{l[N-1]}, U^{kDC}_{u[N-1]}, U^{kDC}_{l[N-1]}\Big]^{T}$ and $\mathbf{F}_0$ represents the steady-state trajectories (see Section 5.4).

Linearized OF and equality constraints

The OF and equality constraints of the linearized optimization problem are obtained by applying (5.4) in the expressions given in (5.2a-5.2b).

Linearized inequality constraints

The inequalities relating the optimal weights $\alpha^{+,-}$ and $\beta^{+,-}$ already have a linear profile; thus, applying (5.4) into (5.2f-5.2i) results in

$$\begin{aligned} &0 \leqslant \left(A^{+}+\hat{\alpha}^{+}\right) \leqslant 1, \quad 0 \leqslant \left(A^{-}+\hat{\alpha}^{-}\right) \leqslant 1, \\ &0 \leqslant \left(B^{+}+\hat{\beta}^{+}\right) \leqslant 1, \quad 0 \leqslant \left(B^{-}+\hat{\beta}^{-}\right) \leqslant 1 \end{aligned} \tag{5.5}$$

Unlikely the previous inequalities, the current and voltage inequality constraints in (5.2c-5.2e) have nonlinear circular characteristics, as they are calculated based on absolute values relating the real and imaginary parts of the current phasors. One possible way to linearize the aforementioned inequality constraints is to employ (5.4). But neglecting the high-order nonlinear terms may lead the MMC to exceed its current limitations or impose negative voltages into the arms (which is not possible considering that half-bridge structures are employed into the SMs).

In order to overcome the aforementioned drawbacks introduced by the linearization of the absolute value constraints, a potential solution is proposed based on the decomposition of these constraints into two complementary components in quadrature. Then, the sum of these two signals, modelled as sinusoidal trajectories, must always be within the maximum and minimum values imposed by the converter limitations (see (5.2c-5.2e)). Note that the accuracy of this approximation is now limited by the number of points N_{points} considered to represent these quadrature components (e.g. higher number of points results in higher accuracy; but, higher computational burden). The sine waves are mathematically described in (5.6) and represented (for different time instants) in Fig. 5.2.

$$\mathrm{Re} = (X_r + \hat{x_r})\cos(\omega n_k T_s), \quad \mathrm{Im} = (X_i + \hat{x_i})\sin(\omega n_k T_s) \tag{5.6a}$$

$$\mathrm{Mag} = (X_r + \hat{x_r})\cos(\omega n_k T_s) + (X_i + \hat{x_i})\sin(\omega n_k T_s) \tag{5.6b}$$

where $\omega = 100\pi$.

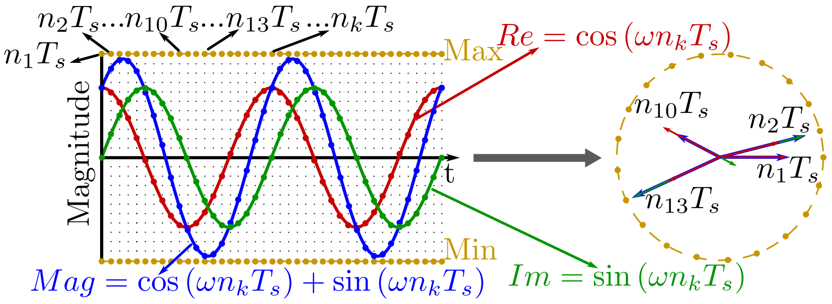

Fig. 5.2: Linearization for AC grid currents and arms' current and minimum applied voltage inequalities.

Therefore, applying (5.6) into the current inequalities in (5.2a), the linearized constrains to limit the AC grid and arm's currents and the minimum voltage to be applied to the arm's can be obtained and are expressed as

$$-I^{AC}_{max} \leqslant (I^k_{s_r} + \hat{i}^k_{s_r})\cos(\omega n_k T_s) + (I^k_{s_i} + \hat{i}^k_{s_i})\sin(\omega n_k T_s) \leqslant I^{AC}_{max} \tag{5.7a}$$

$$\begin{aligned}- I^{arm}_{max} \leqslant (I^{k}_{u,l_r} + \hat{i}^{k}_{u,l_r})\cos(\omega n_k T_s) + (I^{k}_{u,l_i} + \hat{i}^{k}_{u,l_i})\sin(\omega n_k T_s) + \\ (I^{kDC}_{u,l} + \hat{i}^{kDC}_{u,l}) \leqslant I^{arm}_{max}\end{aligned} \tag{5.7b}$$

$$\begin{aligned}0 \leqslant (U^{k}_{u,l_r} + \hat{u}^{k}_{u,l_r})\cos(\omega n_k T_s) + (U^{k}_{u,l_i} + \hat{u}^{k}_{u,l_i})\sin(\omega n_k T_s) + \\ (U^{kDC}_{u,l} + \hat{u}^{kDC}_{u,l})\end{aligned} \tag{5.7c}$$

5.3 Analysis of the linearized optimization problem

In this section, the presented linearized optimization algorithm is compared with a nonlinear optimization algorithm tuned with similar tolerance levels as the linear approximation, and a nonlinear algorithm tuned with very fine tolerance (case considered as the reference solution). The comparative analysis is performed in both normal and faulted AC grid voltage scenarios. The nonlinear problem is obtained using Matlab® *fmincon* function (Sequential Quadratic Program (SQP) based algorithm [83]) and the Operator Splitting Quadratic Program (OSQP) solver [84] is used to find the solution of the equivalent linearized problem. The comparison relies on two main aspects - accuracy (which relates to the OF and optimal weights' $\alpha^{+,-}$ and $\beta^{+,-}$ values) and convergence time T_{conv}, considering that different number of points are employed in the sinusoidal waveforms to calculate the inequality constraints (see Section 5.2.3). Based on these parameters, N_{points} is selected to be later used in the online optimization algorithm to calculate the MMC's current references (see Section 5.5).

5.3.1 Case 1 - Normal AC grid conditions

In this case study, the MMC is considered to be operated under an unconstrained scenario with normal AC grid voltage conditions. In the upper-left part of Fig. 5.3, the value of the OF is depicted. As it can be noted, both nonlinear and linear (regardless the number of points employed in the inequality constraints) models result in similar magnitude as the reference one. Regarding the convergence time, the solution of the nonlinear model is obtained in approximately 90 ms; in contrast, the linearized problem is solved within 2.5 ms (nearly 36 times faster, assuming $N_{points} > 5$). For the optimal weights, $\alpha^{+}_{ref} = \alpha^{+}_{lin} = 1$ while its nonlinear value has a small deviation being equal to $\alpha^{+}_{non} = 0.98$. Whereas for $\beta^{+,-}$, both nonlinear and linear optimization algorithms output the same number as the desired one $\beta^{+,-}_{ref} = 1$. Finally, for this AC network condition, any number of points above 5 could be selected to be employed in the online algorithm.

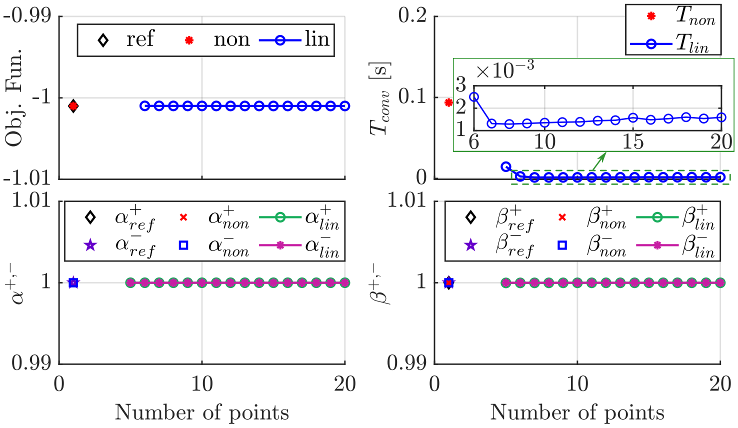

Fig. 5.3: Comparison between the nonlinear and linear models under normal AC grid operations and with relative and absolute tolerances equal to 10^{-3}.

5.3.2 Case 2 - Balanced AC grid fault

For this scenario, an analogous analysis is performed assuming that the AC network is under a balanced three-phase voltage sag. The OF value for both the nonlinear model and the linear optimization are in close-agreement with the desired one, as shown in Fig. 5.4. In addition, the convergence time is greatly improved by using the linearized model (around 35 times faster assuming $N_{points} \geqslant 6$). Regarding the optimal weights, both $\alpha^{+,-}_{non}$ and $\alpha^{+,-}_{lin}$ have similar values to the very fine tolerance optimization problem. For β, the nonlinear ones are equal to the reference magnitude, whereas β^{+}_{lin} have fluctuations around the desired point (respective to the number of points employed in the inequality constraints). Based on the analysis of the previous parameters, under this type of fault $N_{points} = 7$ would be an optimal number of points to be employed in the inequality constraints.

5.3.3 Case 3 - Unbalanced AC grid faults

The performance of the linearized model is analyzed considering an unbalanced AC voltage sag types C [51]. Observing Fig. 5.5a, it is clear that the linearized optimal weights present a disparity from their respective reference values, especially for α^{+}_{lin} and β^{+}_{lin}, regardless the number of points employed in the inequality constraints. Such mismatches can be reduced if the solver tolerances are tightened, as it shown in Fig. 5.5b. For the first case, the absolute and relative tolerances are set to be equal to 10^{-3}, whereas in the second one, the tolerances are reduced to 10^{-6}.

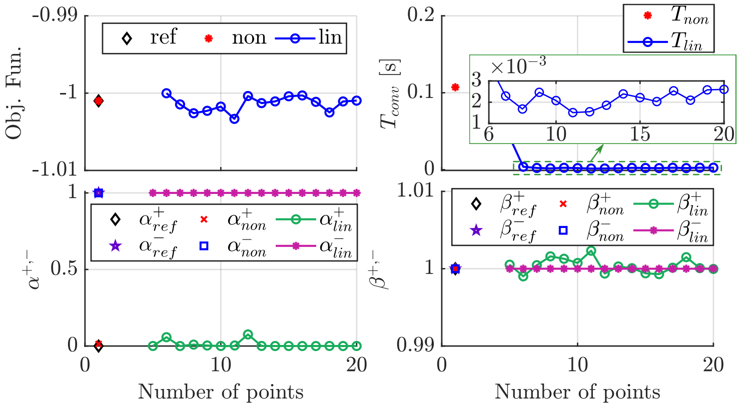

Fig. 5.4: Comparison between the nonlinear and linear optimization under balanced AC three-phase voltage sag.

Although the precision of the solver is improved, it is important to highlight that there is a trade off between the convergence time and the solver's precision. As it can be noted in Fig. 5.5, by tightening the solver's tolerance, the convergence time T_{conv} for the linearized model is increased reaching infeasible values to be used in the proposed optimization algorithm to calculate the MMC's current reference in online applications.

Finally, due to the responses of the linearized optimized model for balanced and unbalanced AC grid scenarios and the precision and convergence time of the solver, the number of points to be used in the online optimization algorithm is equal to $N_{points} = 7$ and the absolute and relative tolerances are set to 10^{-3}.

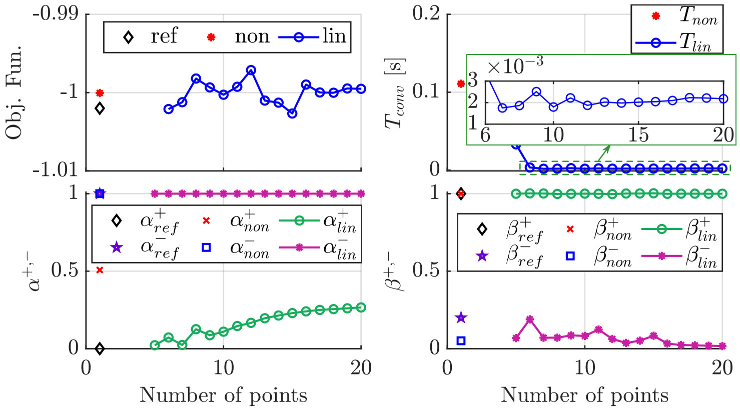

(a) Absolute and relative tolerances equal to 10^{-3}.

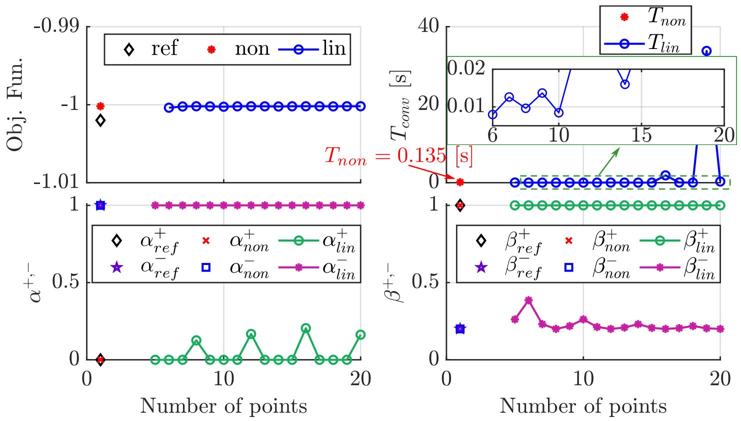

(b) Absolute and relative tolerances equal to 10^{-6}.

Fig. 5.5: Comparison between the nonlinear and linear optimization for a type C fault.

Still considering the same unbalanced voltage scenario, number of points and formulation of the linearized optimization problem, the time-to-solution of the algorithm is depicted in Fig. 5.6 considering different solvers. In this figure, only the solution time of the optimization algorithm is considered once all the matrices involved in the problem have been formulated; thus, the convergence time is smaller compared to the previous cases. It is clear that not only the selection of the former discussed parameters (e.g. tolerances, number of points) have an important impact on the convergence time of the optimization problem, but also the solver employed. Finally, the OSQP solver presented better performance among the different solvers, reducing the convergence time by more than one order of magnitude.

5.4 Integration with the controller

In this section, the optimization-based reference calculation algorithm is integrated with the overall control structure of the converter. The control scheme implemented is shown in Fig. 5.7 and uses the design procedures derived in [39]. This control strategy tracks the AC and DC current components in the stationary $\alpha\beta0$ reference frame and can be separated into three main parts: the AC grid and circulating currents controls and the internal energy regulators. The energy controllers are required to keep the internal energy of the converter balanced. This

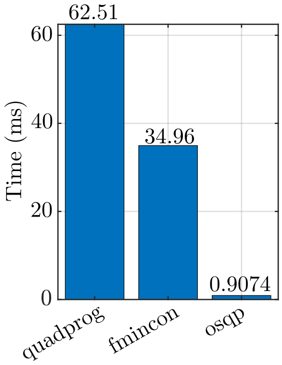

Fig. 5.6: Computation time required by different solvers. The comparison is performed running the algorithm on an Intel i7-4770 CPU @ 3.40 GHz.

is achieved by regulating the total energy of the converter E_t, the energy differences between the upper and lower arms $E^k_{u \rightarrow l}$ and among the MMC's phase-legs $E_{a \rightarrow b}$ and $E_{a \rightarrow c}$. These energy controls output the power set-points to calculate the non-optimal AC and DC circulating currents references. For the AC network currents, the non-optimal references are calculated based on the positive- and negative-sequence active and reactive current components demanded by the TSO and the magnitude of the positive- and negative-sequence components of the AC grid voltages. Besides the aforementioned non-optimal reference calculations, the online optimization-based reference calculation block is also added as part of the overall control scheme (highlighted in yellow color in Fig. 5.7). The selection between the optimal and the non-optimal references is performed by the enable block (blue color block in Fig. 5.7) whose working principle is described later.

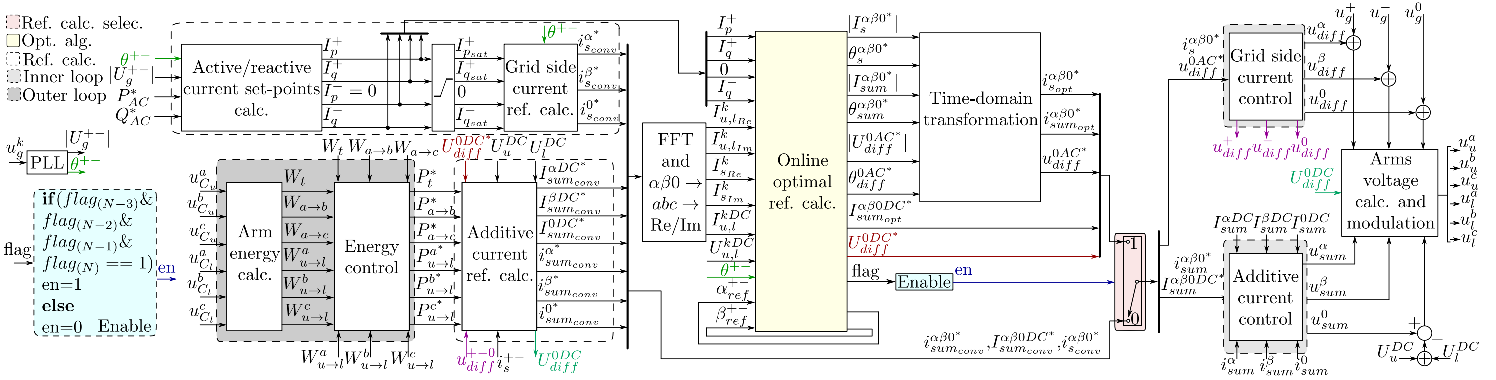

Fig. 5.7: Full control scheme of the MMC integrating the optimal reference calculation.

5.4.1 AC network current reference

The AC grid currents may present symmetrical or asymmetrical profiles under balanced and unbalanced conditions, respectively. This asymmetry is caused due to the presence of negative-sequence components, which must be taken into account during the reference calculation stage. As it can be noted in the upper part of Fig. 5.7, for both conventional and optimal calculation approaches, the positive- and negative-sequence components of the active and reactive currents are pre-calculated based on [55]. Now, these values will be used for both online and conventional reference calculation. For the online method, such quantities are directly used as input parameters for the optimization algorithm. On the other hand, for the conventional method, the active and reactive current components are first saturated to ensure that their magnitudes are within the design limitations of the converter. Then, the saturated currents are employed in the grid side reference calculation block, resulting in the traditional AC network current references $i_{s_{conv}}^{\alpha\beta0*}$ which will also be used as input parameters for the online calculation strategy as the steady-state trajectories required by the linearized model. Finally, depending on the output value of enable block, either the optimal $i_{s_{opt}}^{\alpha\beta0*}$ or the conventional $i_{s_{conv}}^{\alpha\beta0*}$ current references are sent to the grid side current control.

5.4.2 Additive current reference

The MMC's circulating currents contain both AC and DC components, which are employed to regulate the internal energy balance of the converter. Such inner current set-points are first calculated through the method described in [47] without considering the limitations of the converter. Then, these values are used as the steady-state trajectories of the online optimization algorithm. Although the trajectory levels may be exceeding the MMC's internal current limits, the optimization problem is derived in a manner that allows its small-signal values to adjust their magnitudes. Therefore, the final current value output by the optimization algorithm will be kept within the physical limitations of the converter (see Section 5.2.3).

According to the enable block's output, the additive current control block may either use the adequate saturated and optimized inner current $i_{sum_{opt}}^{\alpha\beta0}$ or the non-optimal values $i_{sum_{conv}}^{\alpha\beta0}$ as the current references required by the control strategy. In which, for the non-optimal values, hard saturation strategies are employed for both DC and AC $\alpha\beta0$ additive current components. However, such approach cannot ensure the optimal usage of the converter.

5.4.3 Backup reference calculation method

The enable block is responsible for integrating the optimization algorithm with the MMC's controllers. Its main objective is to ensure that the control scheme is maintained properly running even in a hypothetical scenario where the algorithm can not converge into a solution within the control time step. The desired output flag level is equal to 1, meaning that the optimization algorithm is able to converge into a solution that satisfies the problem constraints (see Section 5.2.3). The enable scheme keeps measuring the optimization flag and, if the flags are kept equal to 1 during the consecutive sample $T_N \rightarrow T_{N-3}$, used as a safety factor, then the optimal references are fed into the controllers. However, if at the time instant T_N the output flag is different than 1, the non-optimized references are imposed into the controllers.

While the optimal reference generator is over-ruled, the optimization problem keeps being solved in the background. If in the next time steps the algorithm is capable of solving the problem within the specified time, the enable block returns to feed the controller with the optimized references. Otherwise, the conventional non-optimized references are kept used until the optimization algorithm is able to converge satisfactorily; thus guaranteeing the safe operation of the system.

5.5 Results

This section presents the results obtained when the proposed optimization-based control is employed to regulate the MMC under different operating conditions. For the first case study, the amount of reactive and active currents injected into the AC grid during distinct voltage sags is compared. Cases II to IV present the time-domain waveforms of the MMC when it is operated under balanced and unbalanced AC and DC network voltage conditions. Finally, the performance of the optimization algorithm is analyzed based on its convergence time for the different AC grid voltage sags and DC unbalances. Even though in real networks the maximum allowed time for fault-ride through is 250 ms [63], the fault events under study are extended to 500 ms to validate the control scheme stability. The simulations are conducted on a computer with a 3.4 GHz Intel core i7-4770 processor with 16 GB of RAM using Matlab Simulink® considering an accelerated model of the MMC [61] and employing the NLC technique to calculate the number of active sub-modules in each arm [62]. The linear optimization problem is solved by the Operator Splitting Quadratic Program (OSQP) [84]. The time-domain waveforms are analyzed for the former conditions to confirm the applicability of the suggested method in real-time applications based on its performance for different requirements (e.g. convergence time and compliance with the MMC constraints). The system parameters employed for the case studies are detailed in Table 5.1.

Table 5.1: System parameters.

Parameter	**Symbol**	**Value**	**Units**
Rated power	S	1000	MVA
Rated power factor	$\cos\phi$	0.95 (c)	-
AC-side rated voltage	$\underline{U}_g$	325	kV
HVDC link voltage	U^{DC}	±320	kV
Phase reactor impedance	$\underline{Z}_s$	0.005+j 0.18	pu
Arm reactor impedance	$\underline{Z}_a$	0.01+j 0.15	pu
Converter modules per arm	$N^k_{u,l_{arm}}$	433	-
Sub-module capacitance	C_{SM}	9.5	mF
Sample time	T_s	10	μs
Optimization time step	T_{step}	2.5	ms
$I_q^{+,-}$ injection response time	t_1	30	ms
$I_q^{+,-}$ clearance response time	t_2	50	ms
Maximum reactive current	$I^{+,-}_{q_{max}}$	$\sqrt{2}$	pu
Optimal weighting factor 1	$\lambda_{I_p^+}$	10^{-6}	-
Optimal weighting factor 2	$\lambda_{I_q^+}$	1	-
Optimal weighting factor 3	$\lambda_{I_p^-}$	10^{-9}	-
Optimal weighting factor 4	$\lambda_{I_q^-}$	10^{-3}	-
Maximum MMC arm current	I^{arm}_{max}	1.0842	pu
Maximum AC grid current	I^{AC}_{max}	$\sqrt{2}$	pu

5.5.1 Case study I: AC grid current comparison

In this case study, the steady-state values obtained using the proposed optimization-based current reference calculation algorithm considering different prioritizations are compared with the grid code demands. The TSO's requirements do not take into account the limitations of the converter, focusing exclusively in the unsaturated injection of positive- and negative-sequence active and reactive current components (refereed as TSO's requirements). In the first prioritization scenario, named Proposal I, the proposed optimization method prioritizes the positive-sequence reactive and active components over the negative ones by employing optimal weights for the positive-sequence quantities higher than the negative ones as $\lambda_{I_q^+} = 1$, $\lambda_{I_p^+} = 10^{-3}$, $\lambda_{I_q^-} = 10^{-6}$ and $\lambda_{I_p^-} = 10^{-9}$. Next, in Proposal II, the values of the optimal weights are changed to $\lambda_{I_q^+} = 1$,

$\lambda_{I_q^-} = 10^{-3}$, $\lambda_{I_p^+} = 10^{-6}$ and $\lambda_{I_p^-} = 10^{-9}$ (as in Table I), prioritizing the reactive components over the active ones. Finally, the AC currents obtained from the previous schemes and the results gathered from the proposed linearized optimization are shown in Table 5.2 for several types of AC voltage sags considering $V = 0.3$ pu [51].

As it can be observed in Table 5.2, during the balanced fault scenario both Proposals I and II prioritize the injection of reactive current components over the active ones to provide full voltage support to the AC grid, as the converter has achieved its limitations. For the unbalanced AC grid faults type B to D, Proposal I can provide full positive-sequence voltage support to the grid and partial injection of positive-sequence active current, as the MMC reaches its AC grid current limitations. On the other hand, as Proposal II prioritizes the negative-sequence reactive current component over the positive-sequence active one, it is capable of providing not only full positive-sequence voltage support during all faults, but also full (Fault type B) and partial (Faults C and D) negative-sequence voltage support. However, as the converter has reached its AC grid current limitations, Proposal II cannot inject active current into the grid. Finally, for Faults type E to G, both Proposals I and II have equal responses as the TSO's requirements for the positive-sequence reactive current component already imposes the converter to reach its limits.

Table 5.2: Comparison of the steady-state active and reactive currents considering different prioritizations.

Fault Type	**Voltage Level** [pu]	$I_p^{+,-}$ [pu]			$I_q^{+,-}$ [pu]		
		TSO's requirement	Proposal I	Proposal II	TSO's requirement	Proposal I	Proposal II
A	$U_g^+ = 0.30$ $U_g^- = 0$	$I_p^+ = 0.95$ $I_p^- = 0$	$I_p^+ = 0$ $I_p^- = 0$	$I_p^+ = 0$ $I_p^- = 0$	$I_q^+ = -1$ $I_q^- = 0$	$I_q^+ = -1$ $I_q^- = 0$	$I_q^+ = -1$ $I_q^- = 0$
B	$U_g^+ = 0.767$ $U_g^- = 0.233$	$I_p^+ = 0.95$ $I_p^- = 0$	$I_p^+ = 0.896$ $I_p^- = 0$	$I_p^+ = 0.458$ $I_p^- = 0$	$I_q^+ = -0.444$ $I_q^- = 0.444$	$I_q^+ = -0.444$ $I_q^- = 0$	$I_q^+ = -0.444$ $I_q^- = 0.444$
C	$U_g^+ = 0.65$ $U_g^- = 0.35$	$I_p^+ = 0.95$ $I_p^- = 0$	$I_p^+ = 0.553$ $I_p^- = 0$	$I_p^+ = 0$ $I_p^- = 0$	$I_q^+ = -0.833$ $I_q^- = 0.833$	$I_q^+ = -0.833$ $I_q^- = 0$	$I_q^+ = -0.833$ $I_q^- = 0.276$
D	$U_g^+ = 0.65$ $U_g^- = 0.35$	$I_p^+ = 0.95$ $I_p^- = 0$	$I_p^+ = 0.553$ $I_p^- = 0$	$I_p^+ = 0$ $I_p^- = 0$	$I_q^+ = -0.833$ $I_q^- = 0.833$	$I_q^+ = -0.833$ $I_q^- = 0$	$I_q^+ = 0.833$ $I_q^- = 0.167$
E	$U_g^+ = 0.533$ $U_g^- = 0.233$	$I_p^+ = 0.95$ $I_p^- = 0$	$I_p^+ = 0$ $I_p^- = 0$	$I_p^+ = 0$ $I_p^- = 0$	$I_q^+ = -1$ $I_q^- = 0.444$	$I_q^+ = -1$ $I_q^- = 0$	$I_q^+ = -1$ $I_q^- = 0$
F	$U_g^+ = 0.533$ $U_g^- = 0.233$	$I_p^+ = 0.95$ $I_p^- = 0$	$I_p^+ = 0$ $I_p^- = 0$	$I_p^+ = 0$ $I_p^- = 0$	$I_q^+ = -1$ $I_q^- = 0.444$	$I_q^+ = -1$ $I_q^- = 0$	$I_q^+ = -1$ $I_q^- = 0$
G	$U_g^+ = 0.533$ $U_g^- = 0.233$	$I_p^+ = 0.95$ $I_p^- = 0$	$I_p^+ = 0$ $I_p^- = 0$	$I_p^+ = 0$ $I_p^- = 0$	$I_q^+ = -1$ $I_q^- = 0.444$	$I_q^+ = -1$ $I_q^- = 0$	$I_q^+ = 1$ $I_q^- = 0$

5.5.2 Case study II: Balanced AC voltage sag

This case study is conducted to illustrate the performance of the full control scheme under a three-phase AC network voltage sag. The MMC is considered to be operating under normal conditions: $P = 0.95$ pu, $Q = 0$ and $|U_g|^k = 1$ pu. Then, at $t = 0.5$ s a three-phase voltage sag is imposed into the AC system reducing the AC network voltage to 30% of its pre-fault value, and at $t = 1$ s the fault is cleared. Although the fault event happens in a abruptly manner, the injection of reactive current to provide voltage support to the grid must be done in agreement with the TSO's fault-ride through and magnitude requirements. According to the Spanish grid-code, if $|U_g| < 0.6$ pu, then the MMC must provide full voltage support to the system. The time-domain trajectories of the MMC states are displayed in Fig. 5.8, where the upper part shows the fault-ride through period and the bottom-half depicts the MMC's profile during the fault clearance course. In addition, it can be noted that both the AC and internal currents, as well as, the minimum allowed arms' applied voltages of the converter are respecting their limits (imposed during the formulation of the optimization problem) throughout the whole operation.

The TSO also demands that the reactive current injection must be done within 30 ms after the fault event [59] and that the pre-fault active and reactive current set-points must be restored within 50 ms after the fault is cleared. In Fig. 5.9, the positive- and negative-sequence active and reactive current components profiles are shown. It can be noted that the optimal control scheme is able to provide additional reactive current to the faulted grid within the time range requested by the TSO. In addition, due to the balanced characteristics of the fault, the optimization method resulted in $I^{+,-}_{p_{opt}} = 0$, $I^{-}_{q_{opt}} = 0$ and $I^{+}_{q_{opt}} = -1$ pu (full voltage support).

5.5.3 Case study III: Unbalanced AC voltage sags

Similarly to the previous scenario, this case study analyzes the online control scheme under an unbalanced voltage sag type C, with $V = 0.3$ pu . The fault event and its clearance happen under same pre-fault conditions and times, as presented previously. Under this type fault, the grid voltages are equal to $|U_g^+| = 0.65$ pu and $|U_g^-| = 0.35$ pu; thus, based on the Spanish grid-code, the MMC should provide partial positive- and negative-sequences reactive current components to the AC network. In Fig. 5.10, the MMC's waveforms are displayed and it can be

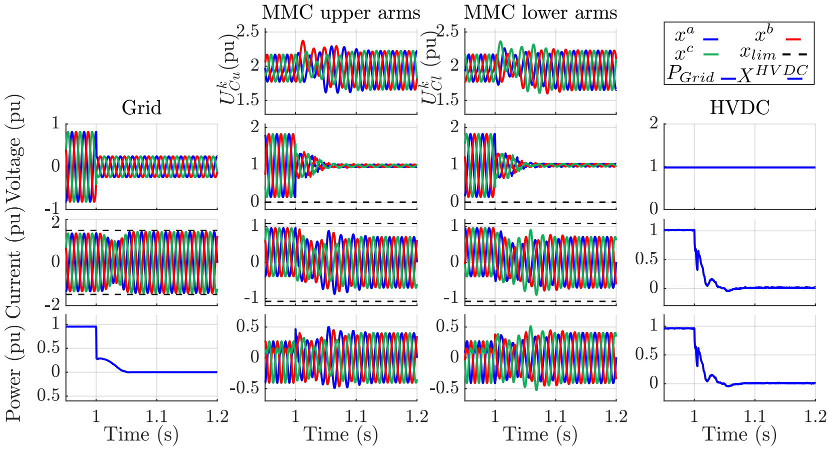

(a) Normal to fault.

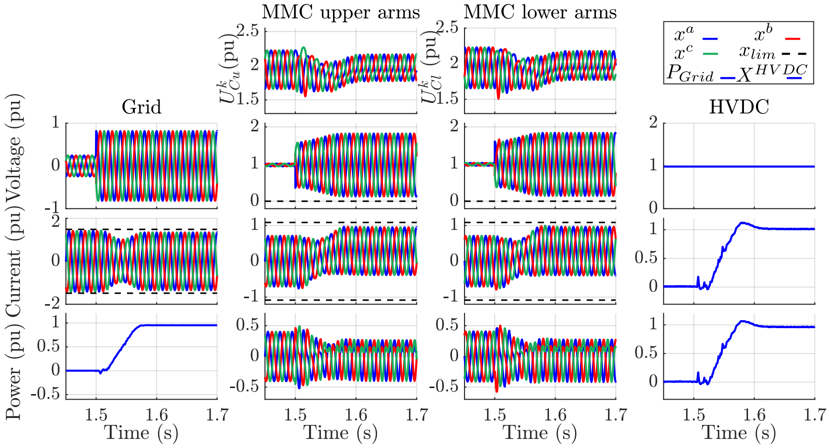

(b) Fault to normal.

Fig. 5.8: Time-domain waveforms for MMC's main quantities during balanced voltage sag. a) From normal to fault scenario, b) From fault to normal operations.

observed that the converter's quantities are also kept within their limits. Differently from the previous case, during this fault condition there is a double-line oscillations in the AC grid power caused by the unbalanced characteristics of the fault. But, such fluctuations are not reflected to the DC side of the converter since the MMC energy storage cells can mitigate these effects.

In Fig. 5.11 the energy mismatches between the upper and lower arms, as well as among the phase-legs of the converter are displayed. It can

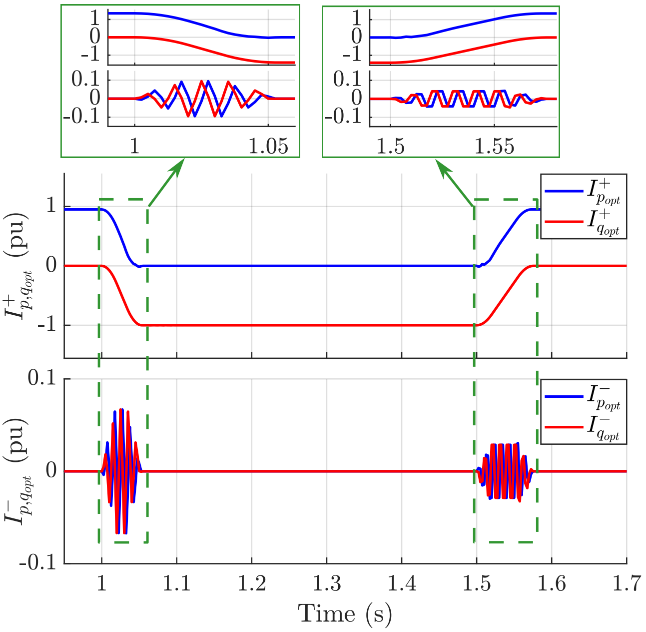

Fig. 5.9: $I^{+}_{p,q}$ and $I^{-}_{p,q}$ profiles during a three-phase fault.

be observed that the proposed optimal control strategy is capable of compensating the energy deviations during the fault and the transitory profile is kept below 0.05 pu (avoiding the converter protections to trip).

Now, the effects of the delays caused by the solving time of the optimization algorithm are analyzed during a SLG fault scenario. It can be noted from Fig. 5.12 that during steady-state conditions, the delays have no effect as the waveforms considering the delays are in close agreement with the ideal ones. During transients, it is clear from Fig. 5.12a that the delayed upper arm currents present small deviations in contrast to the ideal trajectories. However, such deviations have negligible impact in the AC grid currents injected/absorbed by the converter during the fault as the ideal waveforms are matching the delayed ones (see Fig. 5.12b). In addition, all the other results presented in the chapter indicate a better performance of proposed optimization-based reference calculation integrated control in contrast to other control methods (see Section 5.6).

5.5.4 Case IV - HVDC voltage unbalance

For this case study, the DC and AC grids are considered to be operated under balanced nominal conditions, when the MMC's upper DC pole

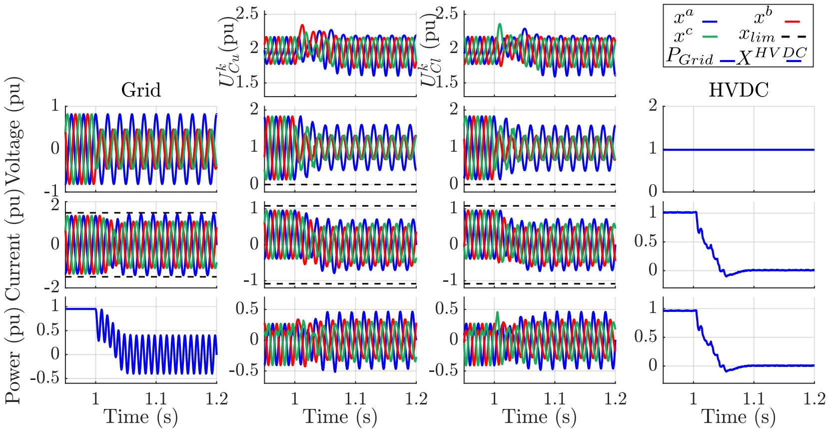

(a) Normal to fault.

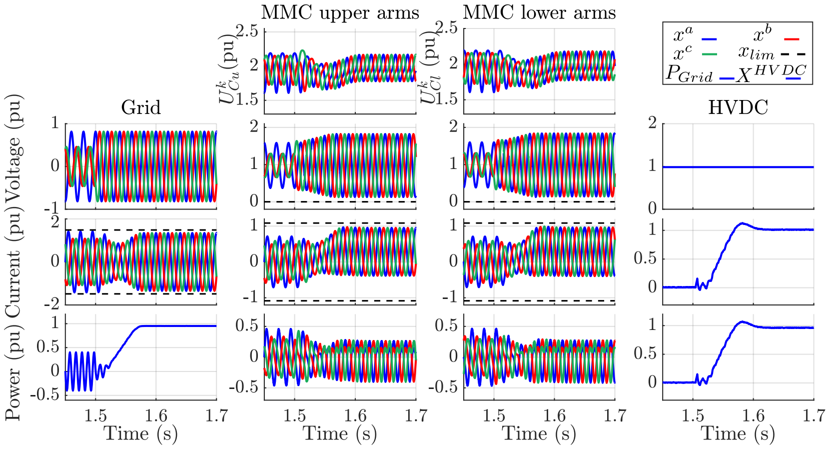

(b) Fault to normal.

Fig. 5.10: Time-domain waveforms for MMC's main quantities during a type C fault. a) From normal to fault scenario, b) From fault to normal operations.

suffers a voltage drop (from 320 kV to 256 kV). Such event may arise, for example, in bipolar HVDC multiterminal configurations, where one converter of the system (which is far from the MMC under study) suffers a DC fault. During the fault ride through or blockage stage, as a consequence, other parts of the DC system may observe DC voltage unbalances.

The first thing that can be noted in Fig. 5.13(a) is that when the DC voltage unbalance happens, the HVDC current injected into the MMC increases to maintain the active power level demanded by the AC net-

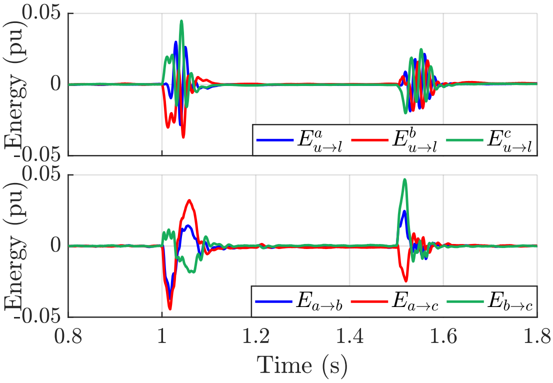

Fig. 5.11: Internal energy profiles during a type C fault.

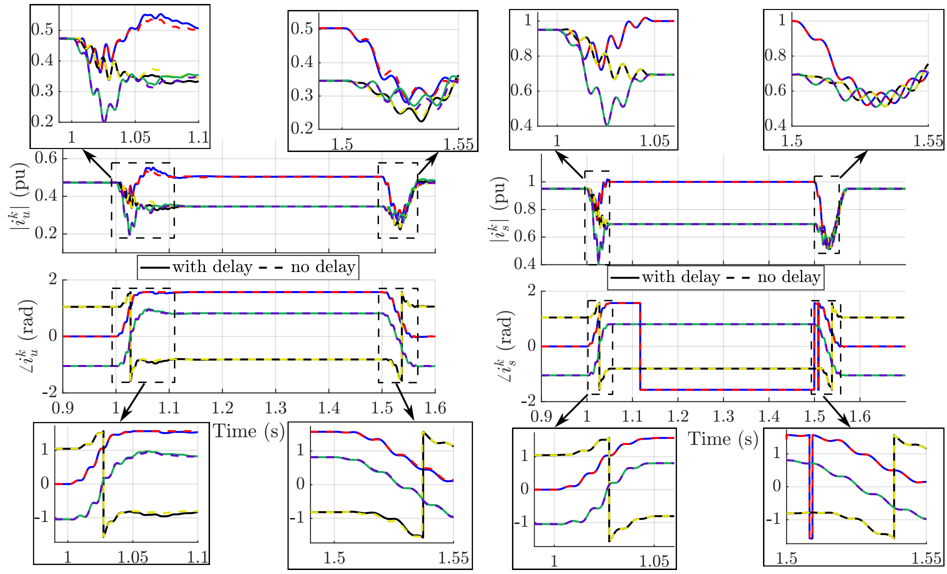

(a) MMC's upper arms currents.

(b) AC grid currents.

Fig. 5.12: Optimization convergence time impact comparison in the optimal references during SLG fault.

work. The DC voltage and current deviations are reflected to the internal quantities of the converter rising the current levels circulating through the MMC's arms, which are maintained within the limitations of the converter by the optimization algorithm. Whereas, the arms applied voltages are decreased to their minimum allowed value set to be equal to zero, as the SMs are based on half-bridge topologies. If other SM structures are considered, such as the full-bridge ones, negative voltages could be applied into the arms of the converter; thus, the minimum allowed arm voltages would be modified to values below zero (e.g. $U^k_{u,l_{min}} < 0$). In addition, AC grid currents and, consequently, the AC network power are kept constant throughout the fault due to the optimal control strategy. Similarly, when the fault is cleared, as it is shown in 5.13(b), the DC side and internal quantities of the converter are set back to normal operating levels, while no change is observed in the AC side.

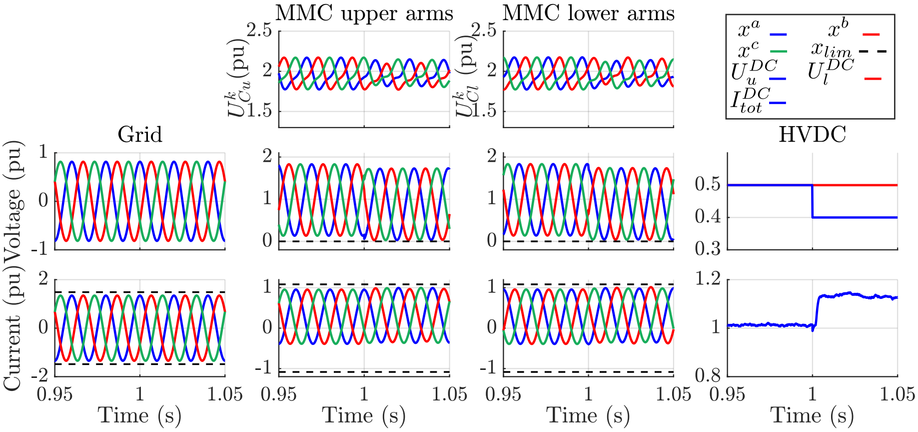

(a) Normal to fault.

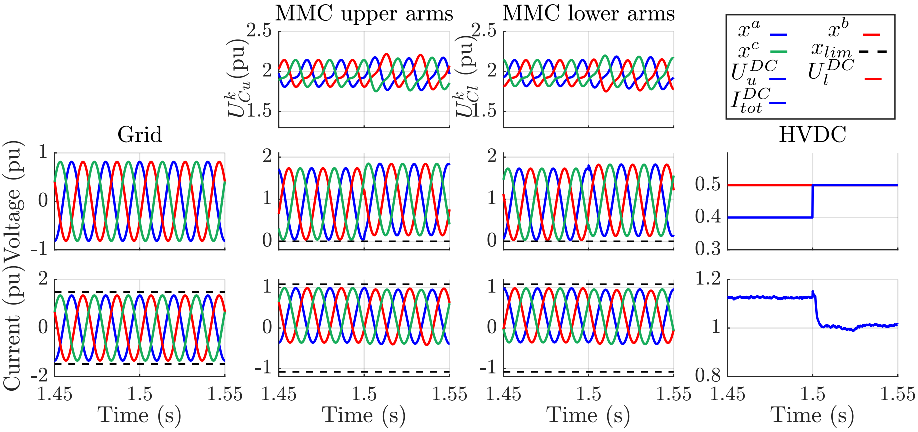

(b) Fault to normal.

Fig. 5.13: Time-domain waveforms for MMC's main quantities. a) From normal to fault scenario, b) From fault to normal operations.

5.5.5 Analysis of the optimization-algorithm convergence time for different AC and DC voltage unbalance conditions

In this section, the convergence time of the optimization algorithm employed in online applications contemplating different AC and DC network voltage conditions are highlighted. The AC grid voltage sags consider $V = 0.3$ pu, whereas for the DC unbalances the same scenarios as Section 5.5.4 is used. The purpose of these tests is to confirm that the proposed optimal control strategy can find an optimal solution within each control time step. In Fig. 5.14, the probability of finding an optimal solution within a specific time-interval is depicted, in which each bar corresponds to a time-interval of 500 μs. As it can be noted, for the several cases analyzed, the probability of occurrence within 2.5 ms is above 99%. Furthermore, the probability of occurrence within 1.5 ms is also above 99% when the converter is operated under normal conditions or during the DC voltage unbalance presented in Section 5.5.4). For the AC grid voltage sags, the balanced case has the highest probability of occurring within 1.5 ms (more than 80%). Finally, for the unbalanced AC network faults, the probability of finding an optimal solution within 1.5 ms is above 62%.

5.6 Comparison with other control methods

In this section, the proposed optimization-based reference calculation integrated control is compared with two different MMC control strategies. The first control strategy for comparison is the CCSC (C1) [72], whereas the second one is an energy-based control (C2) [47]. The main difference between strategy C2 and the proposed method is how the controller references are calculated, as they both have the same controllers with the same gains. When C2 is employed, the references are calculated based on additive and differential components of the converter, while the proposed approach calculates the references in the natural *abc* reference frame through the proposed linearized optimization algorithm. During scenarios where the optimization-algorithm fails to converge, the references provided to the controllers are the same as the ones used in C2 (see Section 5.4.3).

Both strategies C1 and C2 include positive- and negative-sequence AC grid and circulating current controllers and reactive/active AC network currents prioritization based on Cigre B4.70 [71]. The different case studies compare the MMC's responses during different fault and constrained scenarios, assuming the values shown in Table I and that the converter

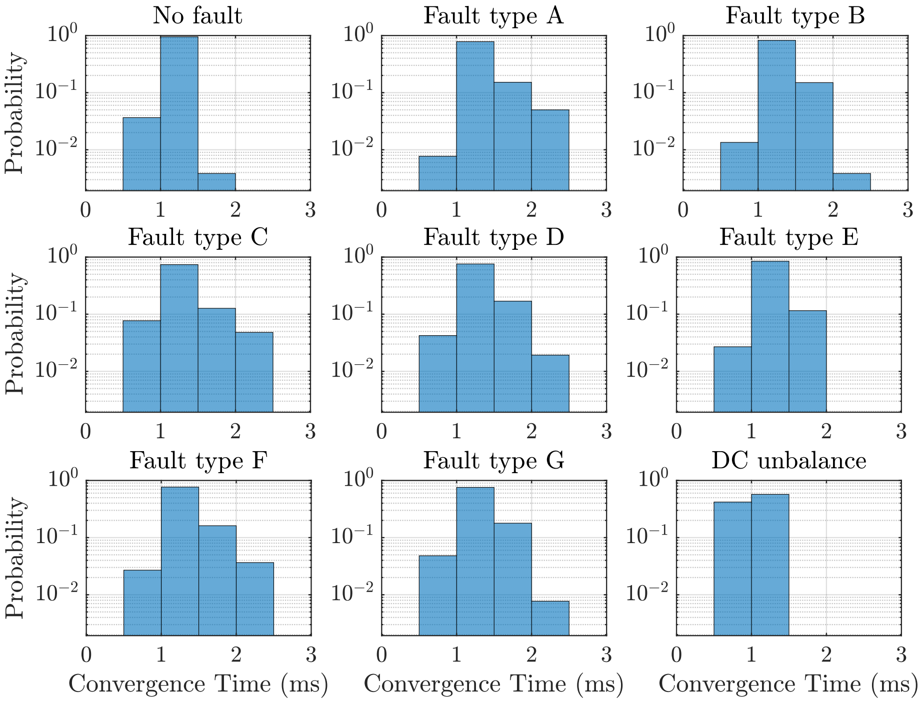

Fig. 5.14: Convergence time histogram for different AC/DC network conditions.

must inject/absorb reactive currents in order to provide voltage support to the network to comply with the grid-code requirements [59]. For all the following case studies, the MMC is firstly considered to be operating in normal AC network conditions, when at $t = 1$ s a SLG fault happens and the fault event is cleared at $t = 1.5$ s.

5.6.1 SLG fault

In this case study, the performance of the different controllers is analyzed assuming similar current limitations and fault conditions. In Fig. 5.15, the converter's response during the fault event is shown when the MMC is controlled using strategy C1 [72]. As it can be seen, such strategy cannot maintain the internal quantities of the converter within their design limits and imposes the undesired circulation of AC current in the DC side of the converter.

In Fig. 5.16, the MMC's behavior during and after the fault is shown when strategy C2 is employed. It is clear that strategy C2 has an improved performance in contrast to C1, as it avoids the AC oscillations in the DC network while maintaining all the converter's quantities

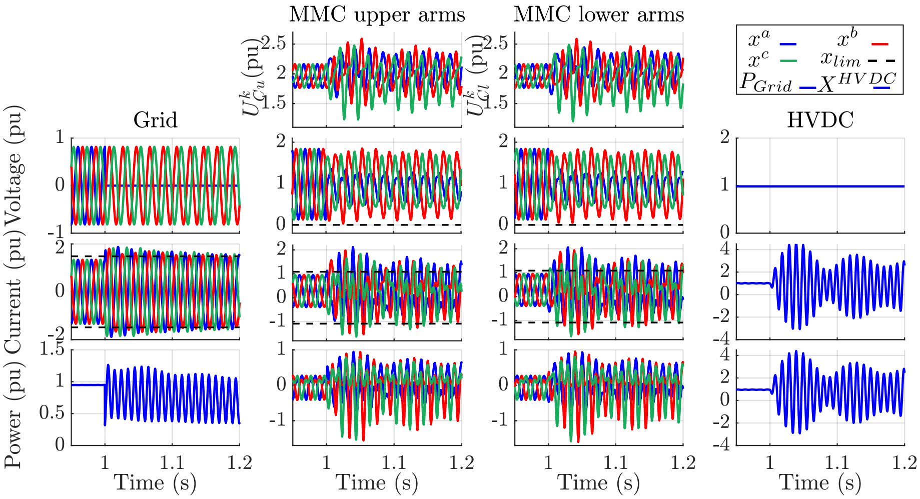

Fig. 5.15: Time-domain waveforms of the MMC during SLG fault using [72].

within their limits. Similar conclusions can be drawn when the proposed optimization-based reference calculation integrated control is employed, as it can be noted in Fig. 5.17. Under such conditions, both C2 and the optimization-based method present adequate performance and can be potentially employed in a real-application. However, strategy C2 would require less computational burden (as it does not require an optimization algorithm).

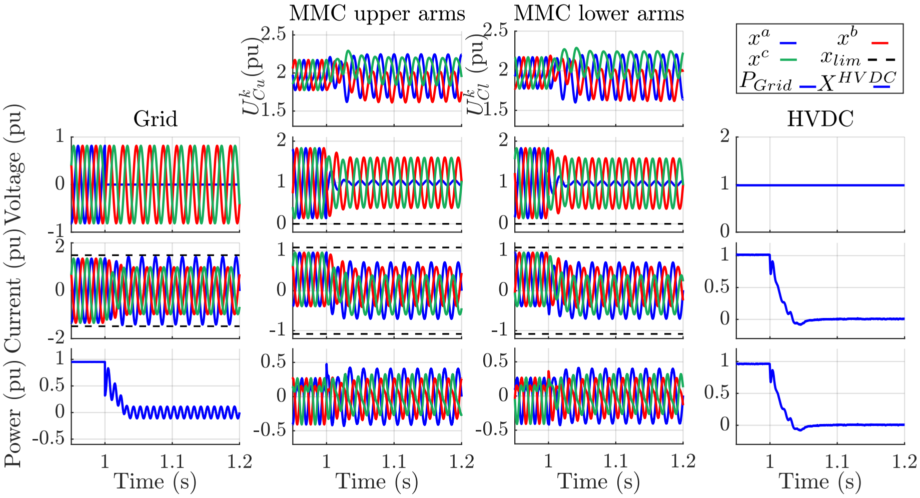

(a) Normal to fault.

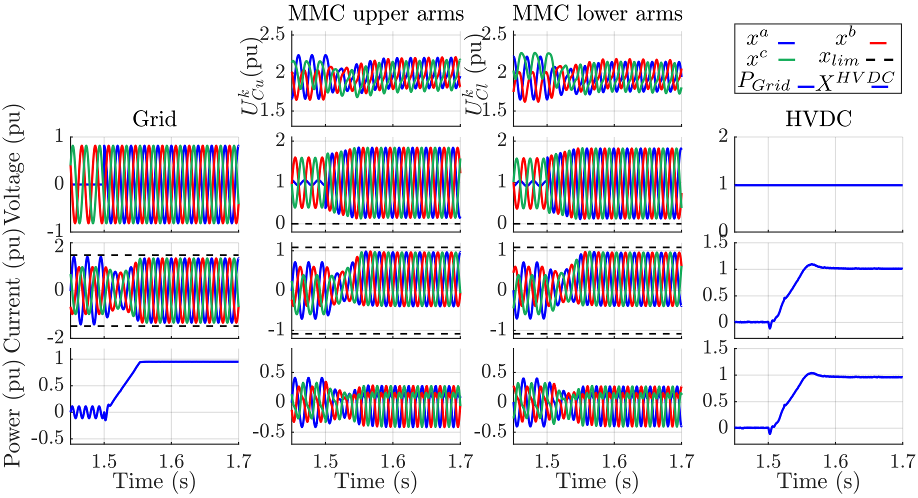

(b) Fault to normal.

Fig. 5.16: MMC waveforms for control strategy C2 [47] during SLG fault a) Fault is applied to the system and, b) Fault event is cleared.

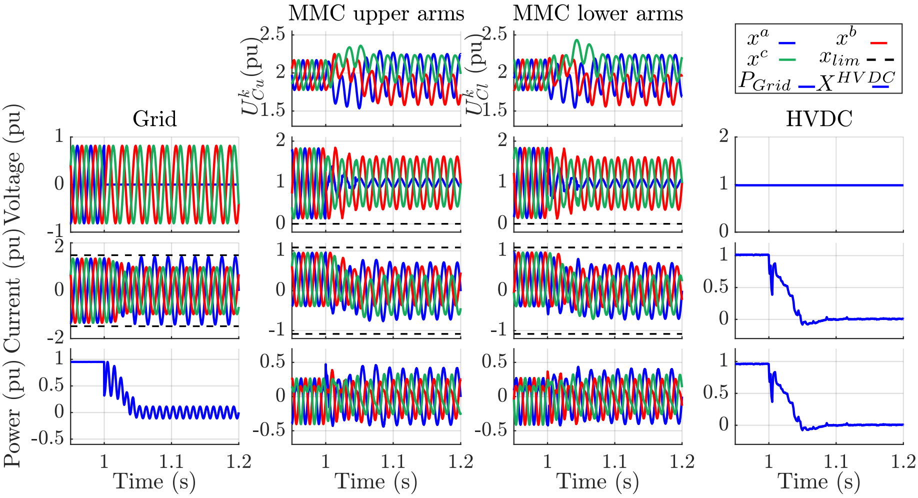

(a) Normal to fault.

5.6.2 Internal parameters deviations

For this study, the performance of the proposed optimization-based approach is analyzed and compared with C2 considering asymmetric MMC's arm impedances during a SLG fault. Strategy C1 has been disregarded, as it presented poor performance in the former analysis (see Section 5.6.1). The reference calculations, the design of the controllers gains and

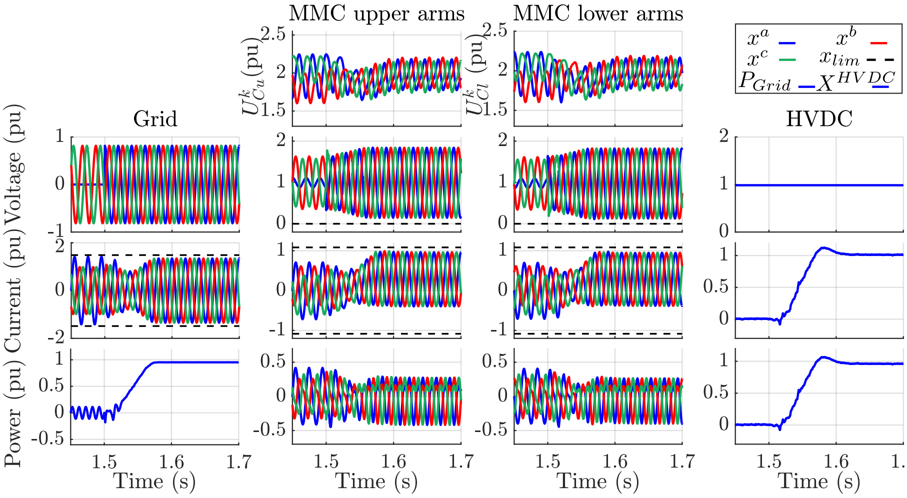

(b) Fault to normal.

Fig. 5.17: MMC waveforms for the proposed optimization-based control during SLG fault a) Fault is applied to the system and, b) Fault event is cleared.

the optimization parameters are maintained constant and they are obtained considering the parameters given in Table 5.1. The arm impedance values employed in this case are highlighted in Table 5.3. Finally, the comparison is done based on the time-domain waveforms of the main quantities of the converter before and after the fault events.

Table 5.3: Arm impedance values for Case study B.

Deviation of ±15%
$\underline{Z}^a_u = \underline{Z}_a - 0.15\underline{Z}_a$, $\underline{Z}^a_l = \underline{Z}_a + 0.05\underline{Z}_a$
$\underline{Z}^b_u = \underline{Z}_a - 0.10\underline{Z}_a$, $\underline{Z}^b_l = \underline{Z}_a + 0.10\underline{Z}_a$
$\underline{Z}^c_u = \underline{Z}_a + 0.13\underline{Z}_a$, $\underline{Z}^c_l = \underline{Z}_a - 0.08\underline{Z}_a$

where $\underline{Z}^k_{u,l}$ is the upper and lower arms impedances, with $k \in \{a, b, c\}$.

It can be noted from the top waveforms in Fig. 5.18a that strategy C2 is unable to maintain the MMC's capacitors with balanced voltage levels even prior to the fault event. Both upper and lower arms' capacitor voltages have different magnitudes, indicating that under asymmetric impedance conditions the control strategy has a poor performance regarding the internal energy of the converter, resulting in voltage unbalances in the SM capacitors. In addition, AC oscillations can be seen in the DC side of the converter. During the fault, the capacitor voltages, especially the lower arm ones, present a severe unbalance profile which may reach the maximum energy deviation allowed in the converter. Furthermore, the AC oscillation in the DC side are worsen during the fault transient. Once the fault is cleared, as it is shown in Fig. 5.18b, the aforementioned problems persist.

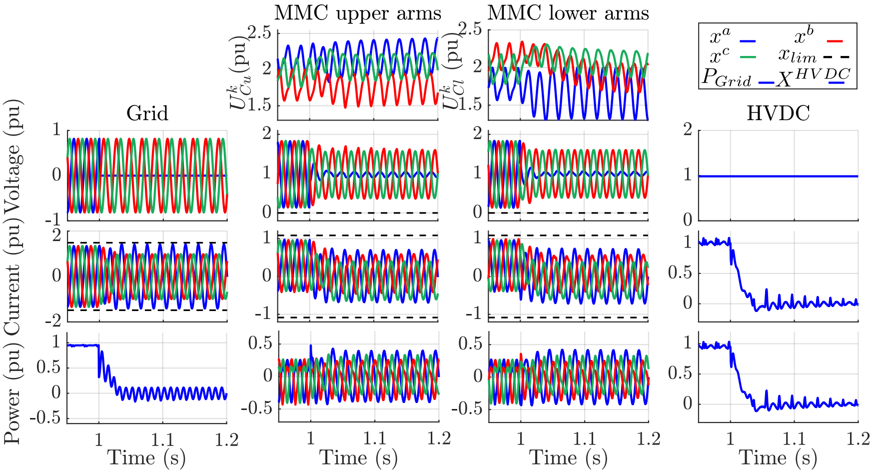

(a) Normal to fault.

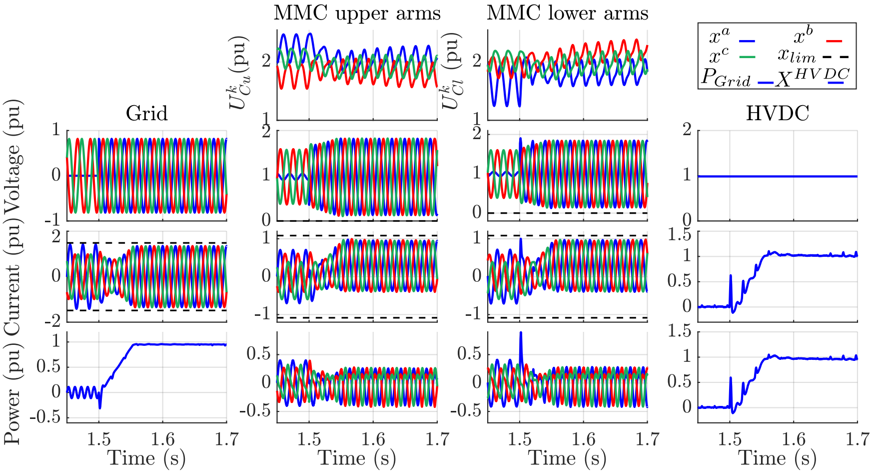

(b) Fault to normal.

Fig. 5.18: MMC waveforms for control strategy C2 [47] during SLG fault considering unbalanced arm impedances conditions within ±15% error. a) Fault is applied to the system and, b) Fault event is cleared.

Next, the same scenario is analyzed assuming that the proposed optimization-based reference calculation integrated control is employed. As it can observed from Fig. 5.19, the capacitors in the MMC's arms have a balanced voltage profile prior and after the fault. Although there is voltage deviation during the fault, such deviation is maintained constant throughout the fault, which would not lead to a potential trip of the converter. Moreover, the DC side oscillations are completely mitigated, as the optimization algorithm consider such issue in its formulations. Finally, it can be noted that even though C2 and the proposed method share the same controllers, the references provided by the optimization improved the MMC's performance. Allowing the controllers to mitigate the issues caused by asymmetric arm impedances during a severe unbalanced AC network voltage condition.

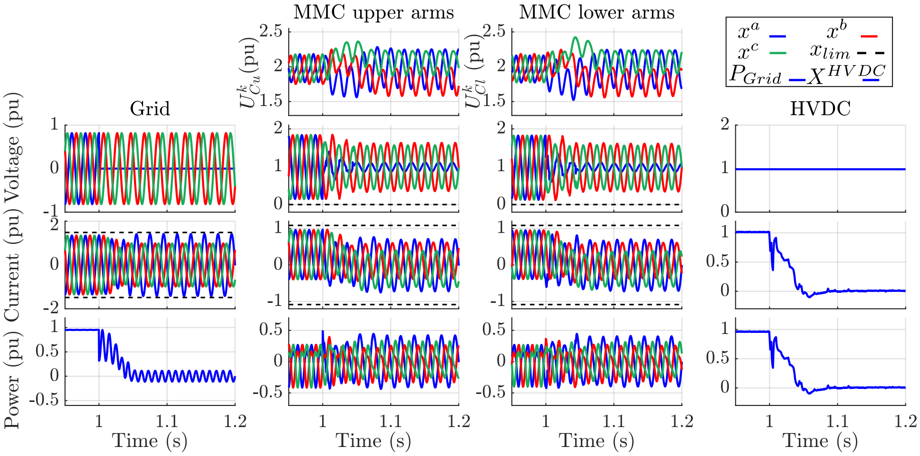

(a) Normal to fault.

5.6.3 Individual arm current limitation

In addition to the SLG fault, it is also considered the maximum allowed current for the upper arm in phase c is set to be equal to $I_{u_{max}}^c = 0.95$ pu, while for the remaining arms the maximum value is equal to 1.1 pu. Such reduction in the maximum allowed current may arise due to cooling or component aging issues. As it was shown in Section 5.6.1, during a SLG fault the strategy C1 [72] is unable to properly regulate the converter; thus, such approach is not included in this case study. Although strategy C2 [47] is capable of maintaining the converter operable during the fault, its formulation does not allow to saturate individual arm currents. This

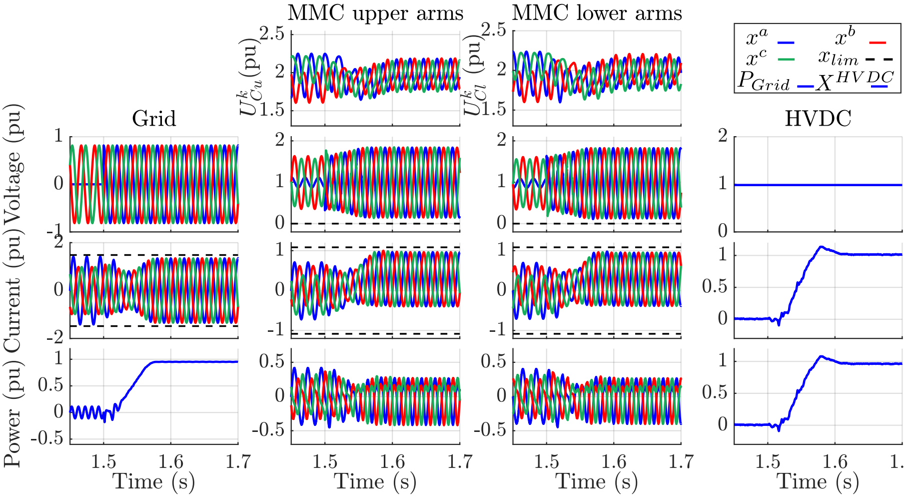

(b) Fault to normal.

Fig. 5.19: MMC waveforms for optimization-based control during SLG fault considering unbalanced arm impedances conditions within ±15% error. a) Fault is applied to the system and, b) Fault event is cleared.

happens due to the modelling formulation which uses differential and additive current components. Consequently, all the circulating currents must be reduced equally, leading to a potential converter's performance reduction. Contrarily, as the optimization problem is formulated considering the currents flowing through each individual arm, the proposed method is capable of specifying maximum allowed values for the currents circulating through the converter's arms. For comparison purposes, the saturations employed in the control strategy [47] have been modified. Now, the maximum allowed three-phase DC and AC additive currents are set to 0.95 pu. For the proposed method, the maximum allowed current is only reduced for phase c with $I^c_{u_{max}} = 0.95$ pu, whereas the for the remaining the maximum allowed current is set to be equal to 1.1 pu. In Figs. 5.20 and 5.21, the time-domain waveforms of the converter are presented during the fault event and its clearance.

Both strategies have similar grid support performance, with $I_q^+ = -1.1$ pu and $I_q^- = 0.3414$ pu. As it can be observed from Fig. 5.20a, the arm currents prior the fault using C2 are exceeding the imposed limitations and also present high-order frequency oscillations in the DC side of the converter due to the harmonic content in the AC additive currents. This control strategy is able to suppress these high order oscillations during

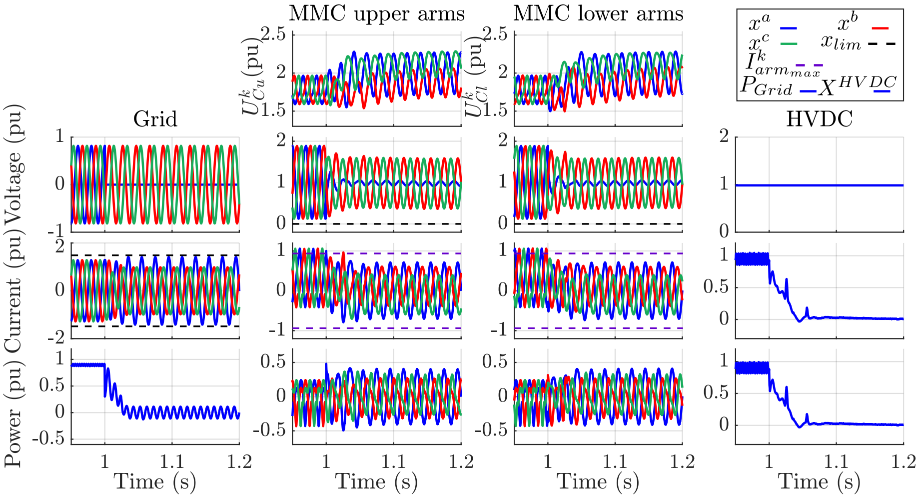

(a) Normal to fault.

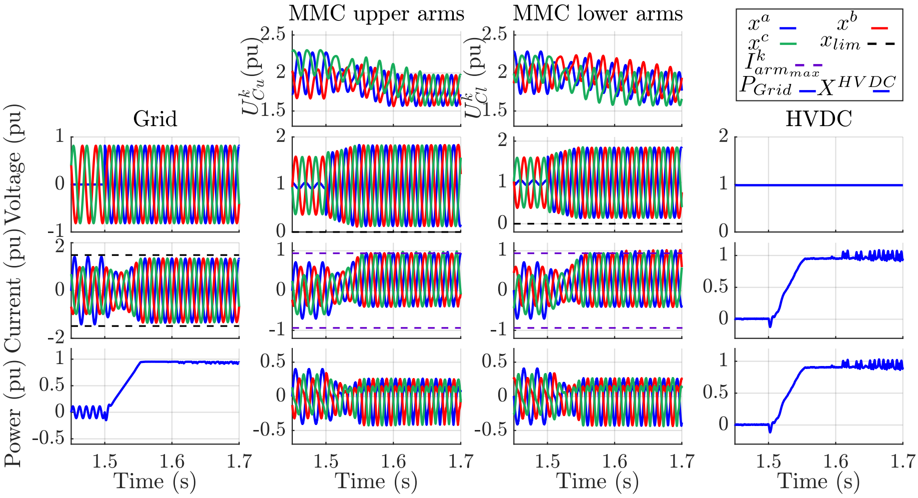

(b) Fault to normal.

Fig. 5.20: MMC waveforms for control strategy C2 [47] during SLG fault with $I^k_{arm_{max}} = 0.95$ pu . a) Fault is applied to the system and, b) Fault event is cleared.

the fault, but once the fault is cleared the oscillations can once more be observed in the DC side (see Fig. 5.20b). On the other hand, the proposed method is capable of avoiding the aforementioned issues throughout the whole operation, keeping the system within the desired limits (see Fig. 5.21). During normal operation conditions, the upper arm currents

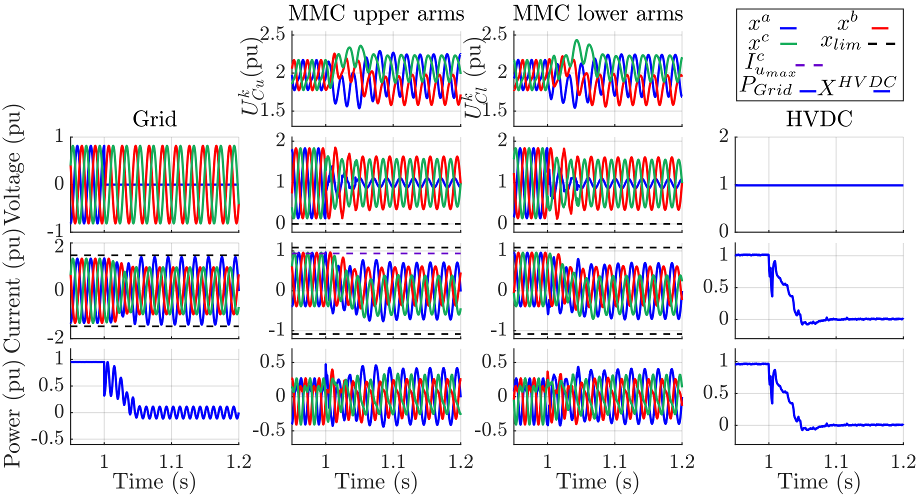

(a) Normal to fault.

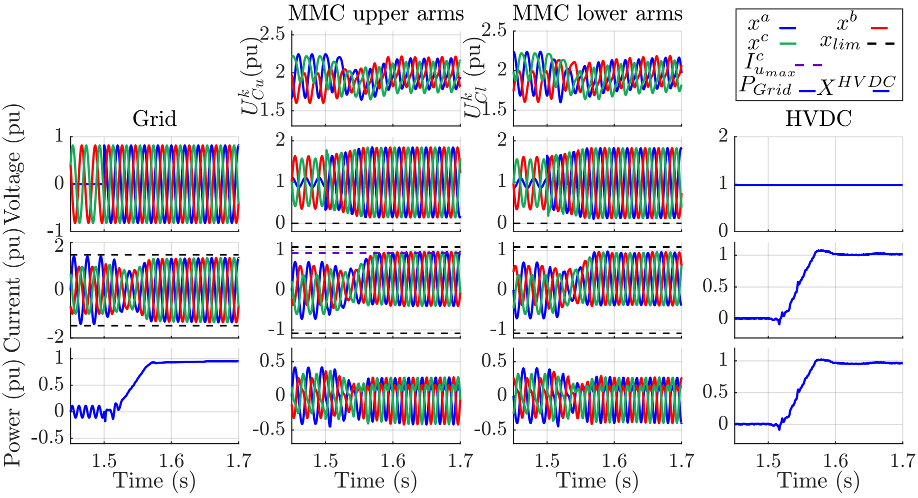

(b) Fault to normal.

Fig. 5.21: MMC waveforms for optimization-based control during SLG fault considering $I^c_{u_{max}} = 0.95$ pu. a) Fault is applied to the system and, b) Fault event is cleared.

present balanced profile and have lower maximum magnitudes compared to the lower arms. Such fact arises due two conditions; firstly, the optimization must maintain the power set-points imposed by the operator; secondly, the formulation of the optimization problem, which avoids zero sequence AC currents to flow into the DC side of the converter (observed when strategy C2 [47] was employed).

5.7 Conclusion

A real-time optimization-based reference calculation algorithm integrated with a control strategy for modular multilevel converter operating under balanced and unbalanced AC and DC network voltage conditions has been presented. The optimization algorithm has been formulated assuming on a multi-objective problem allowing the prioritization among the positive- and negative-sequence of the active and reactive current component, also considering the internal energy balance of the converter and the AC grid and arm current limitations. Due to the highly nonlinear characteristics of the model which would require nonlinear solver (high computational burden to be solved), the optimization algorithm has been linearized using time-varying approximation. Thus, the linearized optimization problem can be employed in real-time applications, as it can be solved at the same frequency as the control algorithm. The linearized algorithm has been validated through quantitative and time-domain simulations. For all case scenarios analyzed, it has been shown that optimization-based reference calculation integrated with the MMC controllers was capable of maintaining the proper operation of the converter, while attempting to fulfill the grid-code requirements and keeping the internal and AC currents within their design limitations. Furthermore, the computational viability of the proposed optimization reference generator for real-time implementations was further confirmed based on its convergence time for different network conditions. Finally, the suggested optimization method was compared with other conventional control strategies considering AC network faults and internal parameters deviations. It has been demonstrated that the proposed optimization-based reference calculation integrated control has an improved performance compared to the conventional strategies for all the different scenarios.

Chapter 6

Optimization-based methodology to design the MMC's SM capacitors

This chapter is based on the following work:

[**S-J7**] D. Westerman Spier, E. Prieto-Araujo, Huijie Lyu, Jiawei He, Bin Li and O. Gomis-Bellmunt, "Optimization-based methodology to design the MMC's SM capacitors", under review *IEEE Transactions on Power Delivery.*

6.1 Introduction

A desirable operation of the MMC can only be achieved when both its control strategy and its components are properly defined and designed. Compared to classical two- and three-level VSC, the MMC requires a large number of elements (e.g. active switches, arm inductors, SM capacitors, etc.). Such parts must be meticulously designed to minimize the installation costs and, along with the controllers, to maintain the converter properly operating under normal or faulted conditions [32,85]. Among the different components consisting the converter, the SM capacitors are responsible for more than 50% of its total size and 80% of the conversion station weight [86]. Therefore, reducing its size can have a great impact on the reduction of the installation cost of the converter, especially in Offshore applications [87].

Prior research has been developed in the attempt of improving the design method of the SM capacitors. Authors in [88–90] mainly focused on the energy effects in their design procedure. In [88], the SM capacitance is minimized based on the maximum and minimum energies in the SMs. The design procedure is improved in [89], where the internal AC voltage of the converter is used to obtain the SM capacitance. Reference [90] analyses the SM capacitors energy considering three distinct operating regions and depending on the region in which the converter will be operated, an energy fluctuation is obtained. Based on this energy variation the equation proposed in [89] is employed to define the SM capacitance.

The previous approaches are further enhanced by the authors in [91], where they also consider the maximum allowed voltage in the SM capacitors defined by either the operating point (OP) or by design constraints. Reference [85] develops analytic optimized equations to calculate the optimal number of SM to be installed and the size of the capacitor to be added to each SM. However, the optimization only considers the maximum SMs capacitor voltage as its main constraint; thus, constraints to avoid overmodulations are ill-defined in the method. Until now, the methods were only focused on the maximum levels of energy, voltage and ripple to ensure that the SM capacitor peak voltage do not exceed its limits. When the C_{SM} minimum voltage levels are considered, thus preventing overmodulations, additional constraints regarding the minimum value of sum of the SM capacitor voltages and the arm inductance effects are included in formulation proposed by [92]. Whereas, [93] expand the effects of the arm inductance by considering them in the arm applied voltages. Furthermore, the paper also includes third harmonic voltage injection to reduce the voltage ripple. However, it only considers the DC components of the circulating currents.

Nevertheless, all the previous designing proposals consider that the converter is operated under normal AC and DC network conditions. Under such circumstances, the normal practice is to assume that the control of the MMC is properly designed to keep the SM capacitor voltage ripple within its limits. In [48], the voltage ripple is reduced by imposing third order voltages in the arms of the converter. Whereas [94], implemented a machine learning-based method integrated with a CCSC control to extend the operating region of the converter during faults. However, as these methods are non-energy-based control approaches, they will lead to undesired AC currents to flow into the DC side of the converter. By assuming energy-based control strategies, the circulating currents of the converter can be enhanced leading to a potential decrease in the SM capacitor voltage fluctuation. In [95], the operating region of the converter is extended by controlling the circulating current to ensure that the peak voltage of the SM are the same as the maximum requested one. [96] controls the circulating current to minimize the SM energy ripple. More advanced methods have been proposed to improve the usage of these currents as the one proposed in [97], where a comprehensive analysis of the internal currents is carried in the attempt of optimizing their usage by the controllers.

To the best of the authors knowledge, a methodology to optimize the design of the SM capacitance for MMC stations taking into consideration all the internal quantities of the converter, while also considering the

TSO current requirements to support faulted networks and the MMC's limitations has not been proposed yet. To address such challenges, this paper proposes the following contributions:

- Derivation of the arm's energy expressions considering the internal DOFs and currents of the converter and their limitations.
- Formulation of an optimization-based methodology to minimize the SM capacitance assuming specific or several OPs which can be either in normal or unbalanced AC/DC network voltage conditions.
- The algorithm ensures that the obtained SM capacitance is sufficiently large to maintain the proper power transfer between the AC and DC networks and to keep the internal power balance of the converter and, to be small enough to avoid exceeding the SM capacitor maximum and minimum allowed voltages.
- The positive- and negative-sequence components of the AC grid current provided by the converter must be as close as possible to the ones required by the grid code.

In order to validate that the proposed optimization-based methodology to design the SM capacitor results in the minimum SM capacitor value for a proper operation of the converter, different OPs and network voltage conditions are analyzed analytically and through detailed time-domain simulations, where the converter is regulated assuming an energy-based control.

6.2 System assumptions

The mathematical models derived in this paper are based on the following assumptions:

- The SM capacitors are considered to be fully charged.
- The voltages in the SM capacitors within the same arm are balanced and under steady-state conditions. This can be achieved by different control methods (e.g. Nearest Level Control [47]).
- The applied voltages and currents flowing through the converter have zero and first-order frequency terms. The injection of third-order frequency components is disregarded as it might cause the circulation of AC currents in the DC-side of the converter.

- The effects of the modulation index are not considered.
- The topology, voltage and current ratings for each individual SM are the same in all SMs used in the converter.

6.3 Description of the methodology

This section describes the optimization-based methodology to minimize the SM capacitance value. The suggested tool considers the optimal values for the DC and AC quantities of the MMC to comply with the TSO active and reactive power set-point requirements and the converter design limits during balanced and unbalanced AC/DC network voltage conditions. The proposed method, its flowchart is displayed in Fig. 6.1, can be used in two manners. Either by assuming an specific OP ($ii_{max} = 1$), or by assuming different OPs ($ii_{max} > 1$). In which the user can input different AC/DC network voltages and/or different active and reactive power set-points and analyze the effect of such changes in the sizing of the C_{SM}. To ensure that the resultant SM capacitance comply with all the TSO's and MMC's requirements, the second option is recommended. Thus, the algorithm will run consecutive times considering the user's voltages and power settings inputs, resulting in several of minimal $C_{SM}(ii)$ capacitance values (one for each specific OP). Finally, these values are stored in the vector $\mathbf{C}_{SM}$, whereby the capacitance size C_{SM} to be selected should be $C_{SM} = \max(\mathbf{C}_{SM})$.

As it can be noted in Fig. 6.1, the suggested SM capacitance designing tool requires different inputs that can be imposed by the user (e.g. voltage and power set-points), obtained by design (e.g. number of SM in each arm $N^k_{u,l}$, U_{SM}, $I^k_{u,l_{max}}$, etc.), or by the grid code requirements (as ΔI_r, $\Delta U_{max_{1,2}}$, etc.). Next, each one of the three steps required to run the methodology are defined.

- Step 1 - Calculate the initial equilibrium points of the converter. In this step, no optimization algorithm is required. The equilibrium quantities are obtained based on a system of equations describing the MMC's steady-state profile, as the one presented in [66]. The voltages and currents resultant from this equation system are required as the initial conditions of the next step to speed up the convergence time and improve its accuracy.
- Step 2 - In this step, the optimal MMC steady-state values are obtained through an optimization method which is formulated to

maximize either the voltage or frequency support that the converter must provide during AC network voltage sags. The prioritization between the two types of support is defined in the objective function (OF) of this optimization problem according to the value of the weights $\lambda^{+-}_{I_{p,q}}$ given by the user, as presented in [49]. In order to meet the TSO's Fault Ride-Through (FRT) requirements, the algorithm requires as inputs the TSO's current and voltage levels during the fault (ΔI_r, $\Delta U_{max_{1,2}}$, $\Delta U_{min_{1,2}}$). Finally, to ensure that the MMC's currents are within design limitations, their maximum values ($I^k_{u,l_{max}}$, $I^k_{s_{max}}$) are also necessary inputs for this algorithm. Although the optimization method used in this step acknowledge potential power transferred among the phase-legs and upper and lower arms, it disregards the SM capacitance in the converter. The effect of such element in the MMC's operation will be included in the next step.

- Step 3 - This step employs the proposed optimization to design C_{SM} (see Section 6.3.1). Firstly, the algorithm requires as inputs, the internal and external voltages and currents of the converter, which are calculated in the previous two steps. Based on these values and the SM characteristics defined by design (e.g. $N, U_{C_{max}}, U_{SM}$), the suggested method attempts to minimize the value of C_{SM}. The algorithm is run for a full cycle of the AC grid (e.g. $T_s = 20$ ms for a 50 Hz grid); thus, the potential asymmetries in the SM capacitor voltages, which are related to the different OPs (see Section 6.4.2), can be fully considered in the formulation of optimization problem. This is necessary to ensure that throughout one operating cycle, the instantaneous arm applied voltages are smaller than the sum of the instantaneous SM capacitor voltages (overmodulation). This optimization method also considers the internal current limitations (defined by design), the maximum allowed voltage in the SM capacitor (defined by design), the minimum allowed voltage to be applied in each arm of the converter (defined according to the SM structure; 0 for half-bridge and $-u^k_C(t)$ for full-bridge) and the maximum and minimum allowed SM capacitance values (defined by design).

Although combining both optimizations from Step 2 and 3 is possible, the resultant algorithm problem would not ensure optimal values for the AC network currents or for C_{SM}. This is explained as different weights would be required in the OF for each specific component, leading to either a higher prioritization of the active and reactive currents injected or a higher prioritization to minimize the SM capacitance. By using two different optimization problems the prioritizations can be performed individually: TSO and converter current requirements (Step 2); minimum value of the SM capacitance C_{SM} respecting the MMC internal current and voltages limitations (Step 3). Therefore, the smallest value of C_{SM} can be guaranteed.

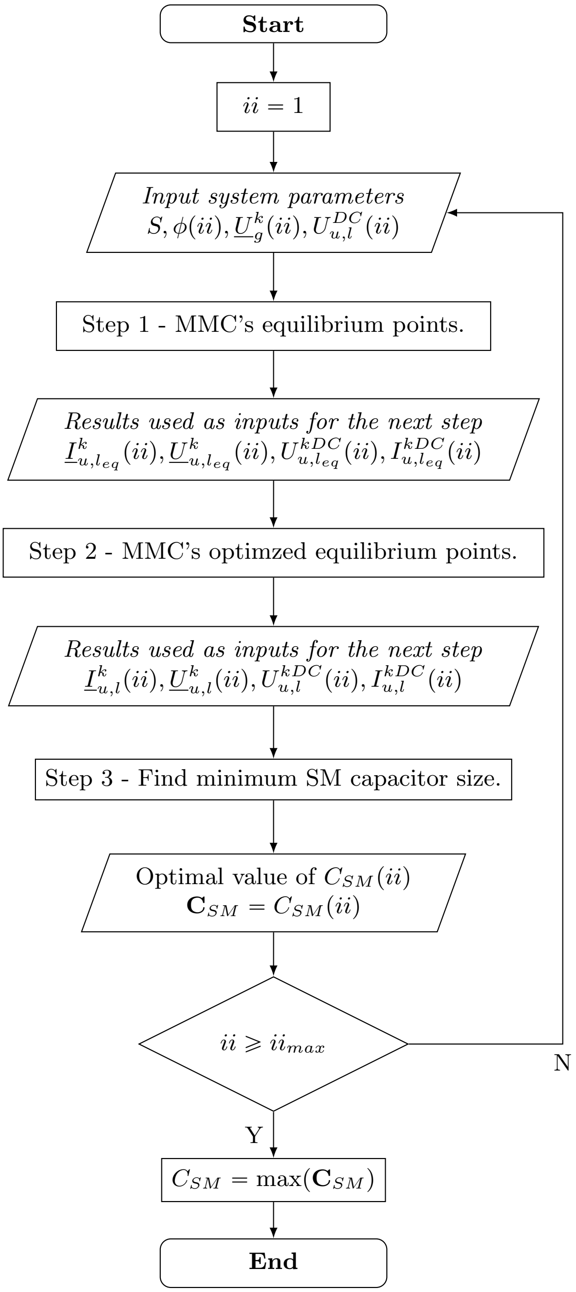

Fig. 6.1: Flowchart of the proposed methodology to optimize the SM capacitors considering different operating points, AC network voltages, TSO requirements and converter current limitations.

6.3.1 Proposed optimization algorithm to minimize the SM capacitances

Firstly, let us clarify that for problem formulation purposes, the phasor notation $\underline{X}^k = X_r^k + jX_i^k = X^k \underline{/\theta^k}$ will be adopted, with $x(t) = X^k \mathrm{Re}\{e^{j(\omega t+\theta^k)}\}$ $\forall k \in (a,b,c)$. The optimization problem that enables to minimize the size of the SM capacitors while ensuring that the MMC's currents and voltages are kept within their design limits is shown next

$$\underset{\underline{I}_{u,l}^k,\, I_{u,l}^{kDC},\, \underline{U}_{u,l}^k,\, U_{u,l}^{kDC},\, \underline{U}_{0n},\, C_{SM}}{\text{minimize}} \quad C_{SM} \tag{6.1a}$$

$$\text{subject to}$$

$$\underline{U}_{0n} = \underline{U}_g^k + \underline{Z}_s(\underline{I}_u^k - \underline{I}_l^k) + \underline{Z}_a\underline{I}_u^k + \underline{U}_u^k \tag{6.1b}$$

$$\underline{U}_{0n} = \underline{U}_g^k + \underline{Z}_s(\underline{I}_u^k - \underline{I}_l^k) - \underline{Z}_a\underline{I}_l^k - \underline{U}_l^k \tag{6.1c}$$

$$0 = \underline{I}_u^a + \underline{I}_u^b + \underline{I}_u^c \tag{6.1d}$$

$$\underline{I}_s^k = \underline{I}_u^k - \underline{I}_l^k \tag{6.1e}$$

$$0 = \sum_{k=a}^{c} \left[\mathrm{Re}\left\{ \underline{U}_u^k \underline{I}_u^k + \underline{U}_l^k \underline{I}_l^k \right\} + U_u^{kDC} I_u^{kDC} + U_l^{kDC} I_l^{kDC} \right] \tag{6.1f}$$

$$P_{u\to l}^k = \mathrm{Re}\left\{ \underline{U}_u^k \underline{I}_u^k - \underline{U}_l^k \underline{I}_l^k \right\} + \left(U_u^{kDC} I_u^{kDC} - U_l^{kDC} I_l^{kDC} \right) \tag{6.1g}$$

$$\begin{aligned} P_{a\to b} &= \mathrm{Re}\left\{ \left(\underline{U}_u^a \underline{I}_u^a + \underline{U}_l^a \underline{I}_l^a \right) \right\} + \left(U_u^{aDC} I_u^{aDC} + U_l^{aDC} I_l^{aDC} \right) \\ &- \left[\mathrm{Re}\left\{ \left(\underline{U}_u^b \underline{I}_u^b + \underline{U}_l^b \underline{I}_l^b \right) \right\} + U_u^{bDC} I_u^{bDC} + U_l^{bDC} I_l^{bDC} \right] \end{aligned} \tag{6.1h}$$

$$\begin{aligned} P_{a\to c} &= \mathrm{Re}\left\{ \left(\underline{U}_u^a \underline{I}_u^a + \underline{U}_l^a \underline{I}_l^a \right) \right\} + \left(U_u^{aDC} I_u^{aDC} + U_l^{aDC} I_l^{aDC} \right) \\ &- \left[\mathrm{Re}\left\{ \left(\underline{U}_u^c \underline{I}_u^c + \underline{U}_l^c \underline{I}_l^c \right) \right\} + U_u^{cDC} I_u^{cDC} + U_l^{cDC} I_l^{cDC} \right] \end{aligned} \tag{6.1i}$$

$$I_s^{kDC} = I_u^{kDC} - I_l^{kDC} \tag{6.1j}$$

$$I_{tot}^{DC} = I_u^{aDC} + I_u^{bDC} + I_u^{cDC} \tag{6.1k}$$

$$U_{tot}^{DC} = U_u^{kDC} + U_l^{kDC} + 2R_a \left(I_u^{kDC} + I_l^{kDC} \right) \tag{6.1l}$$

$$0 = 2\left(U_l^{aDC} - U_u^{aDC} \right) + \sum_{k=b}^{c} \left[U_u^{kDC} - U_l^{kDC} \right] \tag{6.1m}$$

$$0 = \left(U_u^{bDC} - U_l^{bDC} - U_u^{cDC} + U_l^{cDC} \right) \tag{6.1n}$$

$$I_{u,l}^k + I_{u,l}^{kDC} \leqslant I_{max}^{arm} \tag{6.1o}$$

$$u_{u,l_C}(t) \leqslant U_{C_{max}} \tag{6.1p}$$

$$0 \leqslant u_{u,l}^k(t) + U_{u,l}^{kDC}(t) \leqslant u_{u,l_C}^k(t) \tag{6.1q}$$

$$0 \leqslant C_{SM} \leqslant C_{SM_{max}} \tag{6.1r}$$

where U_{tot}^{DC} is the sum of the upper and lower DC poles' voltage. $\underline{U}_{0n}$

is the voltage between the AC grid neutral point n and the DC-poles common point 0. The active power transferred from the upper to the lower arms of the converter is set by $P_{u \to l}^{k}$, similarly $P_{a \to b}$ and $P_{a \to c}$ are the power transferred among the phase-legs of the converter. For the case studies presented in this chapter, it is assumed that there is no power difference between the halves and phase-legs of the converter ($P_{u \to l}^{k} = P_{a \to b} = P_{a \to c} = 0$). The inequality (6.1p) set the maximum allowed voltage of the SM capacitor's sum, while inequality (6.1q) set the maximum and minimum allowed voltage to be applied into the upper and lower arms of the converter (the derivation of the time-domain expressions $u_{u,l_C}(t)^k$ is given in details in Section 6.4.2). Finally, inequality (6.1r) limits the maximum SM capacitor $C_{SM_{max}}$. Note that the maximum voltage must be equal or smaller than the minimum value of the sum of the SM capacitor voltage to avoid overmodulation. The minimum allowed voltage to be applied into the SM is equal to zero, as the SM is assumed to be half-bridge topology. For full-bridge SMs, the minimum allowed voltage is set to $-u_C^k(t)$.

6.4 Analytic model of the SM capacitor voltages

This section focuses on describing the SM capacitors' energy and voltage analytical expressions that are required in the formulation of the optimization problem presented in Section 6.3. These terms are used to ensure that methodology keeps the SMs voltages within their respective maximum (set by the maximum allowed voltage of the component) and minimum (defined by the maximum applied voltages in the MMC's arms) levels. This is done by obtaining the oscillating instantaneous power and the AC and DC energy equations for each one of the six MMC's arms, which are later used to derive the instantaneous SM capacitor voltage model.

6.4.1 Instantaneous arm power and energy derivation

The instantaneous power for the upper and lower arms of the converter can be obtained by the product between its currents and voltages. Such quantities generally have DC and AC components which might be balanced or unbalanced, depending on the operating condition of the converter. Therefore, the generic expression describing the oscillating power for each individual arm unit can be described as

$$p^k_{u,l_{osc}}(t) = u^k_{u,l}(t) i^k_{u,l}(t) = \left(U^{kDC}_{u,l} + \hat{U}^k_{u,l}\cos(\omega t + \theta^k_{u,l})\right) \\ \left(I^{kDC}_{u,l} + \hat{I}^k_{u,l}\cos(\omega t + \phi^k_{u,l})\right) \quad (6.2)$$

where $\theta^k_{u,l}$ and $\psi^k_{u,l}$ are the upper and lower arms' currents and voltages phase-angles, $U^{kDC}_{u,l}$ and $I^{kDC}_{u,l}$ are the upper and lower arms' DC voltages and currents, respectively and $\hat{U}^k_{u,l}$ and $\hat{I}^k_{u,l}$ are the halves peak AC voltage and currents magnitudes. Expanding the previous equation results in

$$p^k_{u,l_{osc}}(t) = I^{kDC}_{u,l} U^{kDC}_{u,l} + U^k_{u,l} I^k_{u,l} \cos\left(\phi^k_{u,l} - \theta^k_{u,l}\right) + \\ U^{kDC}_{u,l} \hat{I}^k_{u,l} \cos(\omega t + \phi^k_{u,l}) + I^{kDC}_{u,l} \hat{U}^k_{u,l} \cos(\omega t + \theta^k_{u,l}) + \\ U^k_{u,l} I^k_{u,l} \cos(2\omega t + \theta^k_{u,l} + \phi^k_{u,l}) \quad (6.3)$$

Once the MMC has reached steady-state, it can be assumed that the sum of the non-oscillating AC and the DC active powers is equal to zero, considering that the internal losses of the converter are negligible. If such condition is not met, the SM capacitors' would be either in charge or discharge mode; thus, steady-state conditions are not held. Therefore, the instantaneous oscillating arms' power can be reduced to

$$p^k_{u,l_{osc}}(t) = U^{kDC}_{u,l} \hat{I}^k_{u,l} \cos(\omega t + \phi^k_{u,l}) + \\ I^{kDC}_{u,l} \hat{U}^k_{u,l} \cos(\omega t + \theta^k_{u,l}) + U^k_{u,l} I^k_{u,l} \cos(2\omega t + \theta^k_{u,l} + \phi^k_{u,l}) \quad (6.4)$$

Finally, the upper and lower arms' instantaneous steady-state oscillating energy is derived by integrating (6.4) over time; thus, resulting in

$$e^k_{u,l_{osc}}(t) = \frac{U^{kDC}_{u,l} \hat{I}^k_{u,l}}{\omega} \sin(\omega t + \phi^k_{u,l}) + \\ + \frac{I^{kDC}_{u,l} \hat{U}^k_{u,l}}{\omega} \sin(\omega t + \theta^k_{u,l}) + \frac{U^k_{u,l} I^k_{u,l}}{2\omega} \sin(2\omega t + \theta^k_{u,l} + \phi^k_{u,l}) \quad (6.5)$$

As it can be observed from (6.5), the oscillating energy expression has in total three terms, in which two are related to the first-order frequency and the other one is a second-order frequency term. In order to reduce such equation and ease the derivation of the expression describing the equivalent arm capacitor voltage, the principles presented in [98] are employed. By doing so, the first-order terms can be combined into a single one, consequently, the instantaneous energy expressions can be reduced to

$$e^{k}_{u,l_{osc}}(t) = \mathbf{E^{k}_{u,lmax_{\omega}}} \sin(\omega t + \psi^{\mathbf{k}}_{\mathbf{u,l}}) + \mathbf{E^{k}_{u,lmax_{2\omega}}} \sin(2\omega t + \gamma^{\mathbf{k}}_{\mathbf{u,l}}) \tag{6.6}$$

where $\mathbf{E^{k}_{u,lmax_{\omega}}}$ and $\psi^{\mathbf{k}}_{\mathbf{u,l}}$ are the magnitude and phase-angle resultant from the combination of the two first-order frequency terms, respectively. Similarly, $\mathbf{E^{k}_{u,lmax_{2\omega}}}$ and $\gamma^{\mathbf{k}}_{\mathbf{u,l}}$ are the magnitude and phase-angle for the second-order term. These terms have been defined in Chapter 4.

6.4.2 Analysis of energy ripple for the upper and lower arms'

Based on the energy expression derived in Section 6.4.1, the SM capacitor voltage equations can be obtained. However, it is important to notice that under distinct OPs, such energy expressions may present asymmetric behavior. This directly affects the maximum and minimum energy magnitudes, which must be considered while deriving the SM capacitance value. In order to provide further insights regarding these asymmetries, Fig. 6.2 depicts the waveforms of (6.6) during a full cycle of the grid (T_s = 20 ms), assuming that the sum of the first oscillating energies magnitudes and the first-order frequency phase-angle term are constant and equal to $\mathbf{E^{k}_{u,lmax_{\omega}}} = \mathbf{E^{k}_{u,lmax_{2\omega}}} = 1$ with $\psi^{\mathbf{k}}_{\mathbf{u,l}} = 0$, and that the phase-angle for the second-order frequency term $\gamma^{\mathbf{k}}_{\mathbf{u,l}}$ is variable.

As shown in Fig. 6.2, the amplitude of the maximum and minimum oscillating energies can present asymmetrical behavior depending on the operating point. However, the peak energy levels is only one of the requirements when designing the SM capacitor. The maximum and minimum energy magnitudes can be derived when $\sin(\omega t + \psi^{\mathbf{k}}_{\mathbf{u,l}}) + \sin(2\omega t + \gamma^{\mathbf{k}}_{\mathbf{u,l}}) = 1$, thus,

$$E^{k}_{u,l_{oscmax}} = \mathbf{E^{k}_{u,lmax_{\omega}}} + \mathbf{E^{k}_{u,lmax_{2\omega}}} \leftrightarrow \tag{6.7a}$$

$$\leftrightarrow \omega t + \psi^{\mathbf{k}}_{\mathbf{u,l}} = \pm\pi/2 + n_1\pi, \text{for } n_1 \in \mathbb{Z} \tag{6.7b}$$

$$\leftrightarrow 2\omega t + \gamma^{\mathbf{k}}_{\mathbf{u,l}} = \pm\pi/2 + n_2\pi, \text{for } n_2 \in \mathbb{Z} \tag{6.7c}$$

$$\leftrightarrow \pm\pi/2 + n_1\pi - \psi^{\mathbf{k}}_{\mathbf{u,l}} = \left(\pm\pi/2 + n_2\pi - \gamma^{\mathbf{k}}_{\mathbf{u,l}}\right)/2 \tag{6.7d}$$

$$\leftrightarrow \pi + 2n_1\pi - 2\psi^{\mathbf{k}}_{\mathbf{u,l}} = \pm\pi/2 + n_2\pi - \gamma^{\mathbf{k}}_{\mathbf{u,l}} \tag{6.7e}$$

$$\leftrightarrow \pm\pi/2 + (2n_1 - n_2)\pi = 2\psi^{\mathbf{k}}_{\mathbf{u,l}} - \gamma^{\mathbf{k}}_{\mathbf{u,l}} \tag{6.7f}$$

$$\leftrightarrow 2\psi^{\mathbf{k}}_{\mathbf{u,l}} - \gamma^{\mathbf{k}}_{\mathbf{u,l}} = \pm\pi/2 + n\pi \quad \forall k \in k = \{a, b, c\} \tag{6.7g}$$

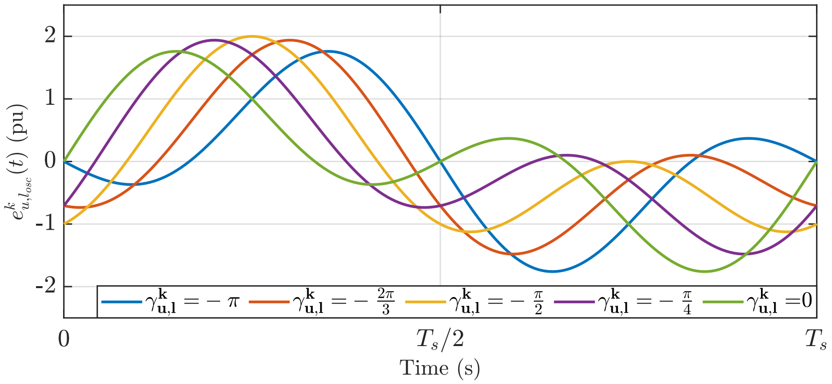

(a) $-\pi \leqslant \gamma^{\mathbf{k}}_{\mathbf{u,l}} \leqslant 0$.

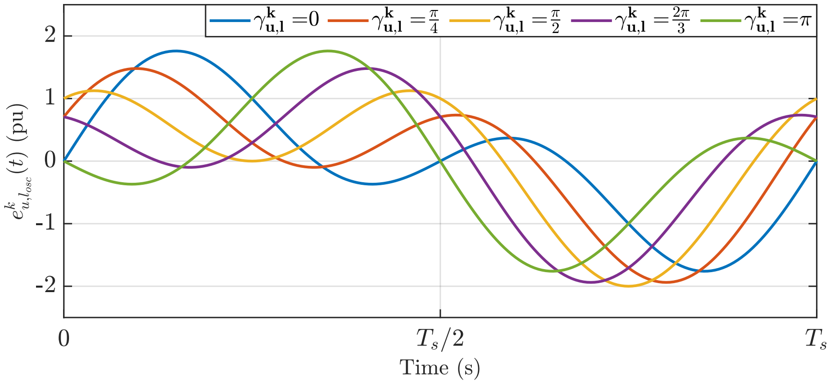

(b) $0 \leqslant \gamma^{\mathbf{k}}_{\mathbf{u,l}} \leqslant \pi$.

Fig. 6.2: Time-domain waveforms of $E^k_{u,l}(t)$ (6.6) under different operating points.

6.4.3 Final expression of the instantaneous arm energy and derivation of the SM capacitor voltage

Until now, the analysis focused on deriving a mathematical expression to describe the MMC's arms energy oscillation for any OP. However, such term alone cannot calculate the actual levels of SM capacitor voltages. Such fact arises as the analysis assumes that the converter already reached the steady-state, thus the SM capacitors, in addition to the oscillating energy term, will also have an average energy level. Such energy term can be calculated as

$$E^k_{u,l_{AVG}} = \frac{1}{2} C_{SM} U^2_{SM} N^k_{u,l} \tag{6.8}$$

where C_{SM} is the SM capacitance value, $N^k_{u,l}$ is the number of available

SM in each arm of the converter and U_{SM} is the SM rated voltage. Therefore, by adding the previous equation with the SM capacitors oscillating energy terms (6.5), the complete energy expression can be obtained and it is expressed as follows

$$\begin{gathered} e^k_{u,l}(t) = E^k_{u,l_{AVG}} + e^k_{u,l_{osc}}(t) = \frac{1}{2}C_{SM}U^2_{SM}N^k_{u,l} + \\ \mathbf{E^k_{u,lmax_{\omega}}}\sin(\omega t + \psi^{\mathbf{k}}_{\mathbf{u,l}}) + \mathbf{E^k_{u,lmax_{2\omega}}}\sin(2\omega t + \gamma^{\mathbf{k}}_{\mathbf{u,l}}) \end{gathered} \tag{6.9}$$

Finally, based on the energy expression (6.9), the sum of the instantaneous SM capacitor voltage used in the formulation of the optimization problem (see equations (6.1r) and (6.1q) in Section 6.3.1), can be expressed by employing

$$E = \frac{1}{2}CU^2 \tag{6.10a}$$

$$u^k_{u,l_C}(t) = \sqrt{\frac{2e^k_{u,l}(t)}{C_{SM}}} \tag{6.10b}$$

$$\begin{gathered} u^k_{u,l_C}(t) = \left(\frac{2}{C_{SM}}\right)^{\frac{1}{2}} \left[\frac{1}{2}C_{SM}U^2_{SM}N^k_{a_{u,l}} + \right. \\ \left. \mathbf{E^k_{u,lmax_{\omega}}}\sin(\omega t + \psi^{\mathbf{k}}_{\mathbf{u,l}}) + \mathbf{E^k_{u,lmax_{2\omega}}}\sin(2\omega t + \gamma^{\mathbf{k}}_{\mathbf{u,l}})\right]^{\frac{1}{2}} \end{gathered} \tag{6.10c}$$

6.5 Performance and comparison with other methods

In this section, the proposed optimization-based SM capacitance design is compared with distinct design methods assuming balanced AC and DC network voltage conditions and the worst SM capacitor ripple scenario. In which, for the optimization algorithm such scenario arises when $\gamma^{\mathbf{k}}_{\mathbf{u,l}} = \pi/2$ (see Section 6.4.2), whereas for the other methods the worst condition happens when the power factor angle is equal to $\phi = \frac{\pi}{2}$. All the different methods consider the same MMC parameters which are similar to the ones used in the HVDC link between Spain and France (INELFE), as shown in Table 6.1.

Table 6.1: System parameters.

Parameter	**Symbol**	**Value**	**Units**
Rated power	S	1000	MVA
Rated power factor	$\cos\phi$	0.95 (c)	-
AC-side rated voltage	$\underline{U}_g$	320	kV
HVDC link voltage	U^{DC}	±320	kV
Phase reactor impedance	$\underline{Z}_s$	0.004+j 0.15	pu
Arm reactor impedance	$\underline{Z}_a$	0.01+j 0.14	pu
Converter modules per arm	$N^k_{u,l}$	400	-
Optimal weighting factor 1	$\lambda_{I_p^+}$	10^{-6}	-
Optimal weighting factor 2	$\lambda_{I_q^+}$	1	-
Optimal weighting factor 3	$\lambda_{I_p^-}$	10^{-9}	-
Optimal weighting factor 4	$\lambda_{I_q^-}$	10^{-3}	-
Maximum MMC arm current	I^{arm}_{max}	1.0795	pu
Maximum AC grid current	I^{AC}_{max}	1.1	pu
Maximum SM capacitor voltage	$U_{C_{max}}$	1.15	pu

6.5.1 Case study A - Full active/reactive power injection/absorption $\gamma^{\mathbf{k}}_{\mathbf{u,l}} = \phi = [-\frac{\pi}{2}, 0, \frac{\pi}{2}]$

In this case study, the SM capacitance values obtained from the optimization-based algorithm are compared with other methods [89], [92] and [93] by assuming that the converter is either fully injecting/absorbing reactive power or fully injecting active power with balanced AC and DC network voltage conditions. As discussed in the Section 6.4.2, during reactive power injection/absorption, the SM capacitors are expected to experience maximum voltage ripple. For comparison purposes, the simulations are evaluated considering the same time-step and in the same software (Matlab/Simulink®). In Table 6.2, the capacitance values with each method are shown considering the three different OPs.

As it can be observed from Table II, all methods indicate similar results when the converter is injecting fully active power ($\phi = 0$). However, during the scenarios where it is either fully absorbing (e.g. STATCOM operation) or providing full reactive power (e.g. voltage support during AC network voltage sags), the methods presented contrasting SM capacitance values. To ensure that the values obtained with the different methods can be employed in the converter without leading to overmodulations, time-domain simulations are carried out. In Figs. 6.3 to 6.5, the waveforms of the applied voltages for the upper arms of the converter and the sum of the SM capacitor voltages are depicted assuming that the converter has achieved the steady-state. The simulations are performed employing an accelerated model of the MMC [61] using the NLC technique to calculate the number of active SMs in each arm [62] of the MMC. In addition, the converter is regulated by the energy based

Table 6.2: Capacitance design comparison.

ϕ	**Method**	**Capacitance** [mF]
$-\frac{\pi}{2}$	Proposed	9.8364
	Method I [89]	7.7443
	Method II [92]	12.7336
	Method III [93] (with 3^{rd} harmonics)	9.7821
	Method III [93] (without 3^{rd} harmonics)	9.6838
0	Proposed	6.3691
	Method I [89]	5.5581
	Method II [92]	9.0178
	Method III [93] (with 3^{rd} harmonics)	6.4531
	Method III [93] (without 3^{rd} harmonics)	6.5472
$\frac{\pi}{2}$	Proposed	9.0393
	Method I [89]	3.8389
	Method II [92]	11.9492
	Method III [93] (with 3^{rd} harmonics)	9.7821
	Method III [93] (without 3^{rd} harmonics)	9.6838

control proposed in [47].

Observing Fig. 6.3, it can be noted that the C_{SM} designed with Methods II, III-A, III-B and the proposed one is high enough to maintain the SM capacitor voltage level within the desired range. However, Method II leads to the oversizing such component, as the maximum SM capacitor voltage is far below its limit. On the other hand, Method I undersized the C_{SM}, resulting in high voltage ripples which are exceeding the design limitations of the component. Still, either Methods III-A, III-B or the proposed one can be used to design C_{SM}, as their voltage differences between the maximum allowed capacitor voltage and the capacitor voltage peak values are small, whereby Method-III-B is the smallest.

During the scenario where the converter is fully injecting active power ($\phi = 0$), as displayed in Fig. 6.4, similar conclusions as the previous case can be drawn. The main difference is that for this condition, the C_{SM} calculated with proposed method is the most suitable option as the peak magnitude for the sum of the SM capacitor voltages is the closest one to its maximum allowed value (without exceeding it).

The last scenario analyzed in this case study assumes that the converter is fully absorbing reactive current($\phi = \frac{\pi}{2}$), as depicted in Fig. 6.5. It can be noted that the C_{SM} resultant from Method I is too small, consequently, the converter is under overmodulation. In comparison to the remaining designing methods, the proposed approach can reduce the magnitude of C_{SM} up to 24% in comparison to Method II and up to 7.6% in relation to Method III without reaching overmodulation or exceeding the maximum SM capacitor voltage level.

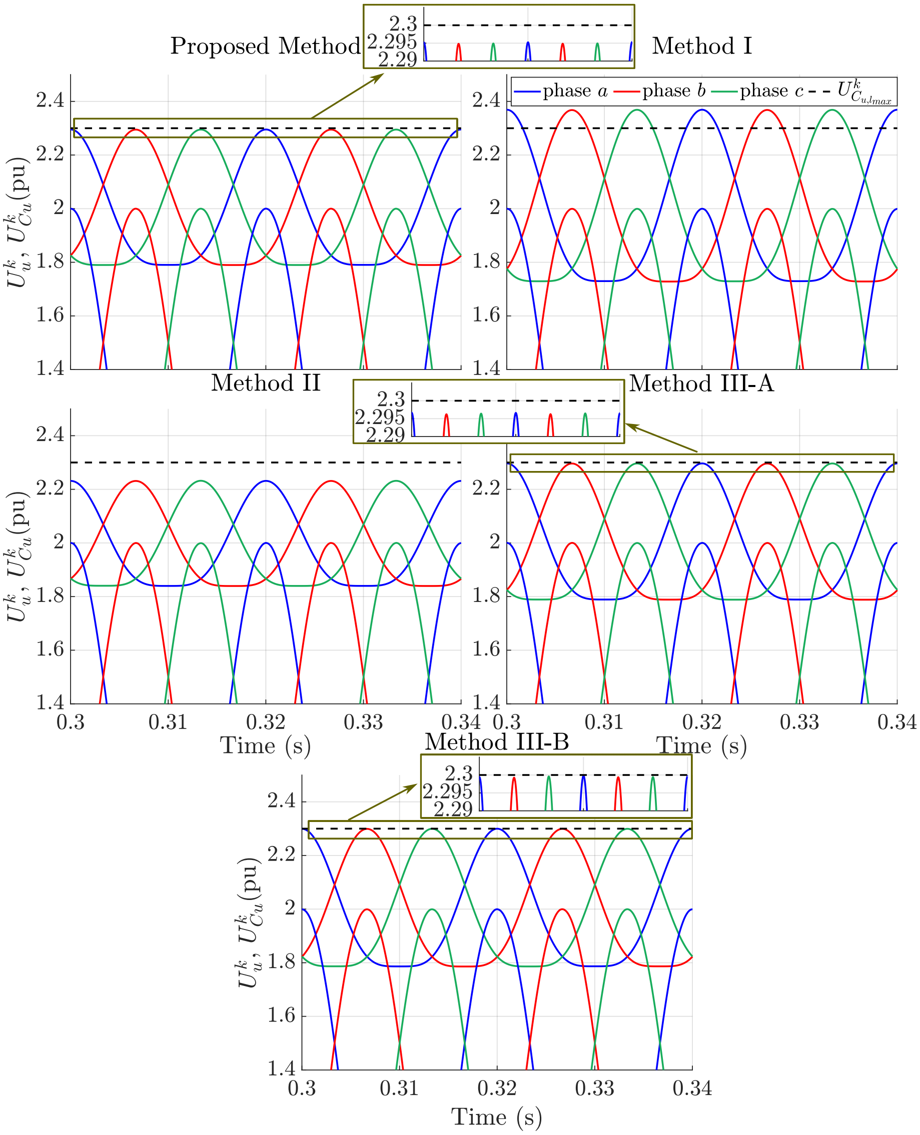

Fig. 6.3: Time-domain waveforms for the proposed method and Methods I to III-B of the upper arms applied voltages and the equivalent arm capacitor voltage $\phi = -\frac{\pi}{2}$.

6.5.2 Case study B: Effects of the variation in the number of SM

In this case study, the effects caused by the variation in the number of available sub-modules $N^k_{u,l}$ over the SM capacitance C_{SM} is analyzed. The analysis is conducted for different OPs and it compares the pro-

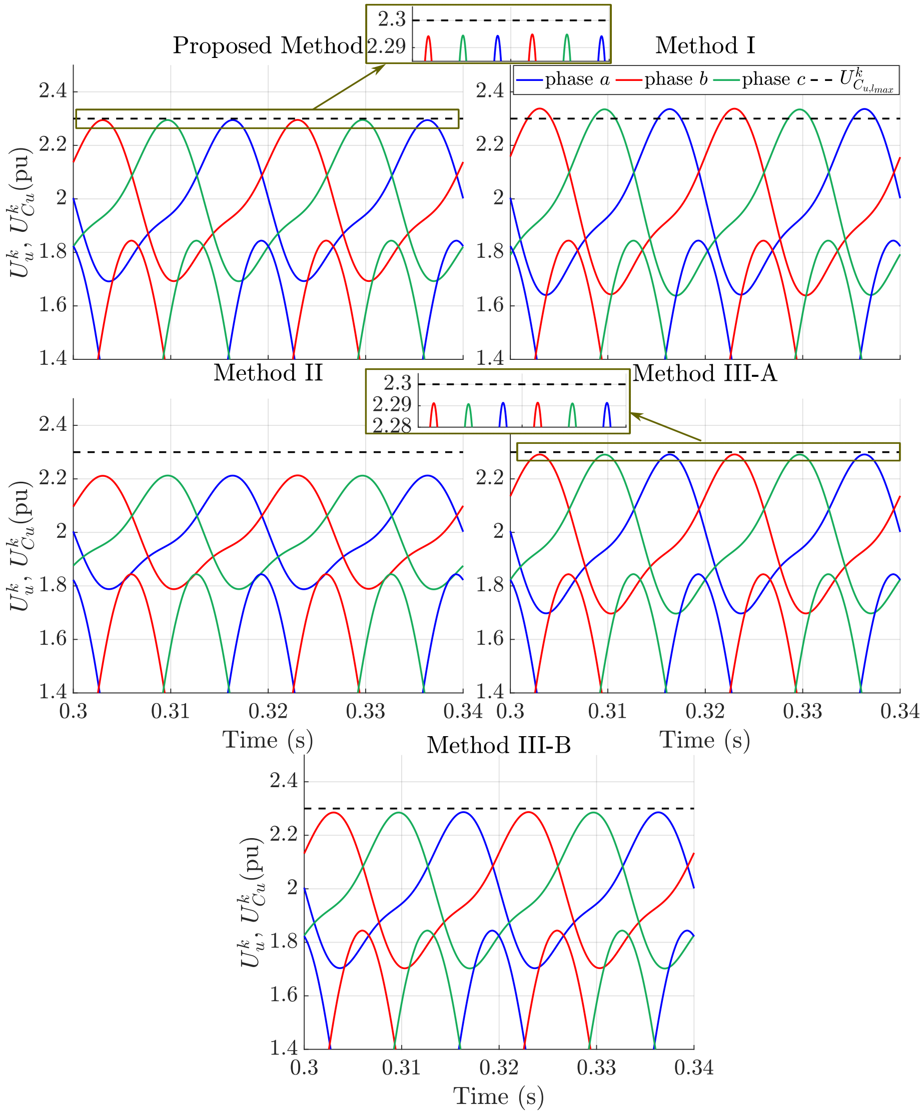

Fig. 6.4: Time-domain waveforms for the proposed method and Methods I to III-B of the upper arms applied voltages and the equivalent arm capacitor voltage for $\phi = 0$.

posed optimization-based design tool with the methods presented in the previous case study. The study considers that the average voltage in each SM capacitor U_{SM} varies based on $N^k_{a_{u,l}}$ to respect the relation ($U^{DC}_u + U^{DC}_l = U_{SM} N^k_{a_{u,l}}$). In Fig. 6.6, the relations among C_{SM}, $N^k_{a_{u,l}}$ and U_{SM} are displayed, whereby the $N^k_{a_{u,l}}$ is varied from 200 until 620 with incremental steps equal to 10.

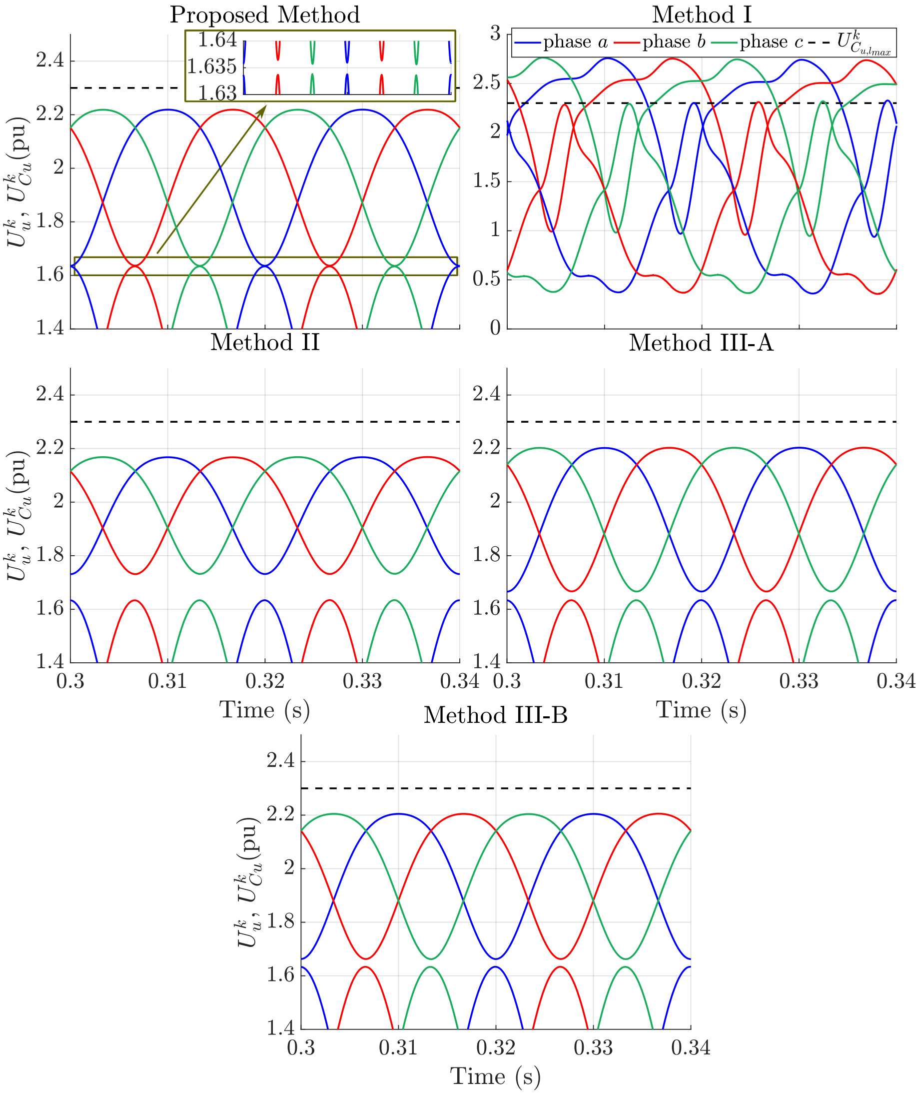

Fig. 6.5: Time-domain waveforms for the proposed method and Methods I to III-B of the upper arms applied voltages and the equivalent arm capacitor voltage $\phi = \frac{\pi}{2}$.

As it can be noted from Fig. 6.6, during full active power injection (top-left figure), all methods present similar profile. While $N^k_{a_{u,l}}$ raises, the value of the SM capacitance also increases linearly whereas the SM voltage U_{SM} has a nonlinear reduction. However, under full reactive power consumption or injection scenarios (see top-right and bottom figures), Methods III-A and III-B have convergence issues. Such issues

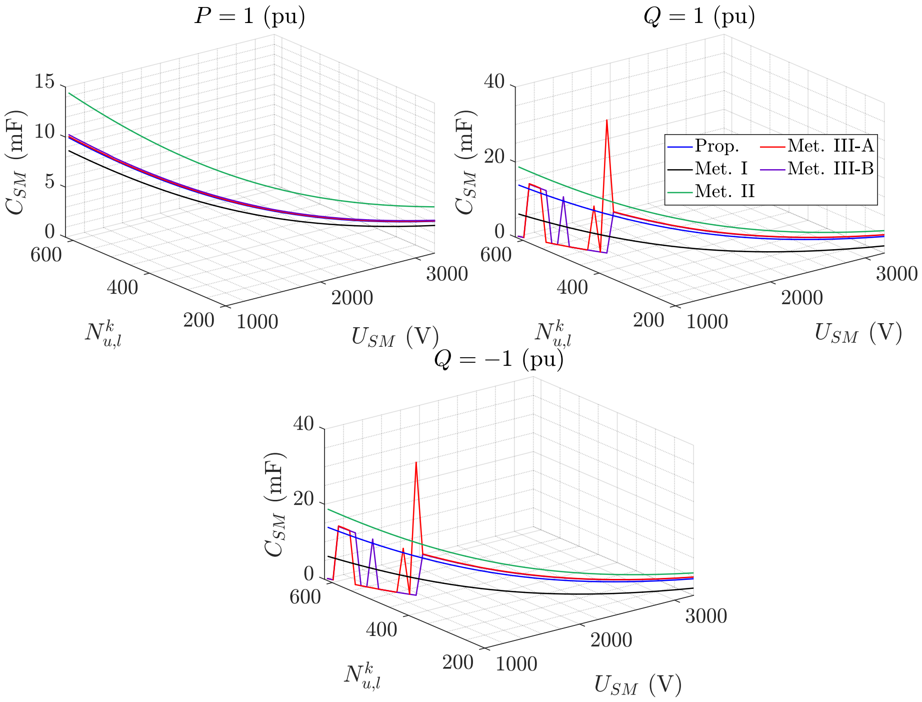

Fig. 6.6: Correlation between C_{SM} and number of installed SM assuming variable average SM capacitor voltage.

happen due to the formulation of the problem as their iteration requires the maximum allowed voltage and maximum ripple to respect certain conditions that can not be fully achieved after $N^k_{a_{u,l}} \geqslant 470$.

Methods I, II and the proposed one, on the other hand, are able to converge obtaining C_{SM} for all conditions analyzed. Method II leads to the oversizing C_{SM}, while Method I results in the smallest C_{SM} levels. As it was shown in Section V-A, when the SM capacitors obtained with Method I are used in the converter, it might lead to undesirable operations of the converter. Finally, the proposed approach is the most suitable one as it does not present any of the aforementioned drawbacks.

6.6 Full operation range of the converter

In this section, the proposed optimization-based SM capacitor design is run assuming that the converter is operated with nominal power, for several different active and reactive power set-points, as well as, AC network voltage scenarios. Under normal AC network voltage operation, the MMC must inject pure active power, however during voltage sag cases, the converter must inject/absorb reactive currents to provide voltage support (in accordance to the TSO's requirements [59]). Thus, the optimization algorithm will provide the minimal SM capacitance required to meet with those conditions, the converters constraints and, at the same time, respecting the SM capacitor maximum and minimum allowed voltages.

6.6.1 SM capacitance selection

The SM capacitor designed assuming the aforementioned conditions are shown in Fig. 6.7, where their optimal values are plotted for each active and reactive power set-points. As it can be noted, most SM capacitance magnitudes are obtained up to 10 mF. However, under few operating points analyzed, the device value can reach levels up to 18 mF. Although such value can ensure that the MMC is able to meet the TSO requirements while keeping the converter's quantities within their limitations for all analyzed cases, its implementation would lead to high installation costs due to its size and weight.

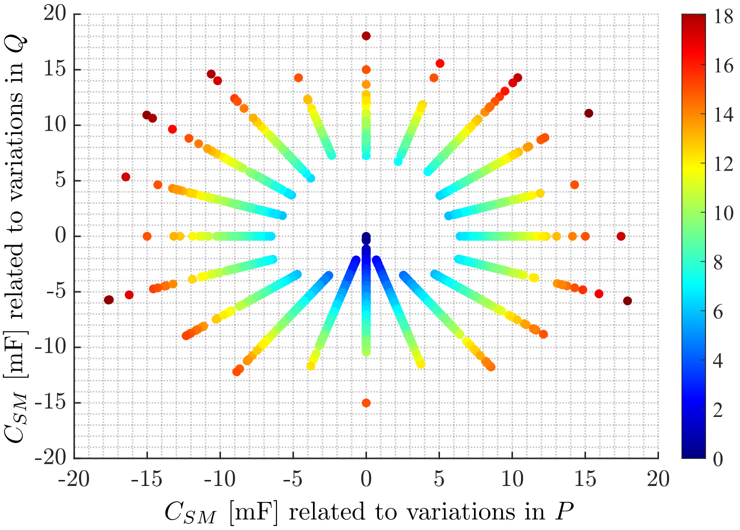

Fig. 6.7: Optimal C_{SM} for all the different OPs analyzed.

Further insights are observed in Fig. 6.8, in which the distribution of SM capacitance values is depicted related to different P and Q set-points (x-axis is related to the values of C_{SM} for different active power levels, while the y-axis is related to the reactive power). As it can be observed, the design value with highest occurrence is within the interval

$C_{SM} = (8, 9)$ mF. If $C_{SM} = 9$ mF is chosen, it can be ensured that during 86% of the different PQ and AC network voltage scenarios, the MMC is within its design limitations and the TSO's requirements are met. By increasing the SM capacitance, higher guaranteed rates can be obtained: for $C_{SM} = 9.5$ mF the rate is equal to 92% and $C_{SM} = 10$ mF results in rates equal to 94.3%. Once again, the trade-off between cost/weight and size plays a major role in the selection of the SM capacitor. Next, time-domain simulations are performed considering two different SM capacitance values $C_{SM} = 9$ mF and $C_{SM} = 9.5$ mF. The main waveforms of the converter are analyzed for different AC network fault scenarios assuming the converter is injecting full active power prior to the faults, and when during the occurrence of the fault, the converter must inject/absorb reactive current components in accordance to the TSO's requirements [47, 59].

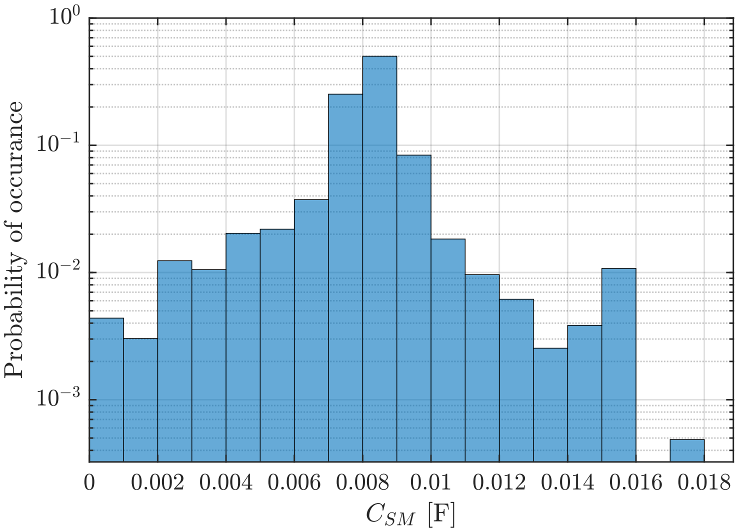

Fig. 6.8: C_{SM} histogram assuming different PQ and AC network voltage conditions.

6.6.2 Time-domain waveforms during AC voltage sags

For this case study, three different voltage sags are analyzed assuming the two values of SM capacitance mentioned earlier, $C_{SM} = 9$ mF and $C_{SM} = 9.5$ mF. First, the converter is operated under normal conditions, then at $t = 1$ s the faults are imposed in the AC network and they are cleared at $t = 1.5$ s. For all AC voltage sags studied, it is considered that $V = 0$ pu [51]. In Figs. 6.9 to 6.14, the upper and lower arms applied voltages $U^k_{u,l}$ and the sum of the SM capacitor voltages $U^k_{Cu,l}$ are depicted for a SLG fault, AC network singular voltage sag and internal voltage sag, respectively.

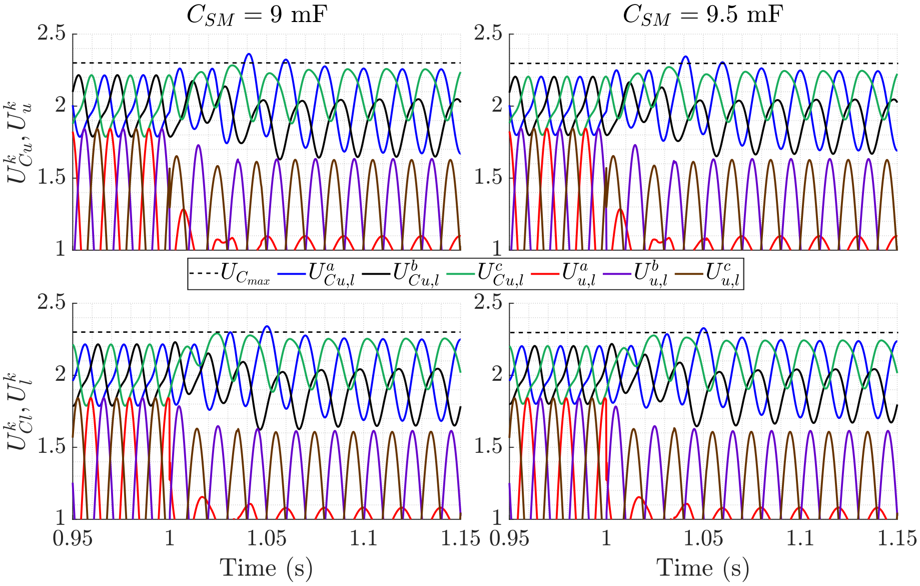

Fig. 6.9: Normal to fault during SLG fault.

It can be noted that prior the fault and once the fault achieved the steady-state, either SM capacitor magnitude can be selected as they are respecting the converter's limits and the TSO requirements. In addition, the converter's arm applied voltages and the sum of the SM capacitor voltage dynamics are similar for all faults analyzed for both values of C_{SM}. Although the results indicate that the maximum allowed sum of the SM capacitor voltage is exceeded when the fault occurs or that the arm applied voltages are higher than the sum of the SM capacitor voltages during recovery phase, they happen during short time instants and they won't influence the overall performance of the converter during FRT conditions.

By increasing the value the SM capacitor to $C_{SM} = 12$ mF, better dynamic response can be obtained. In Fig. 6.15, the waveforms of the converter are shown during the worst fault case presented earlier, AC network singular voltage sag, assuming $C_{SM} = 12$ mF. As it can be noted, throughout all the operation of the converter, the sum of the SM capacitor voltages are kept within limits and no overmodulation can be

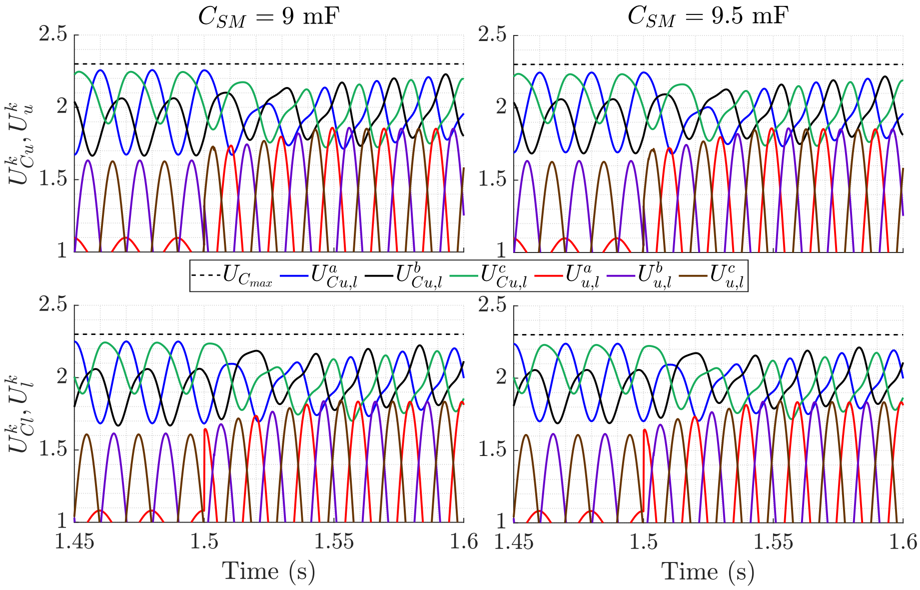

Fig. 6.10: Fault to normal during SLG fault.

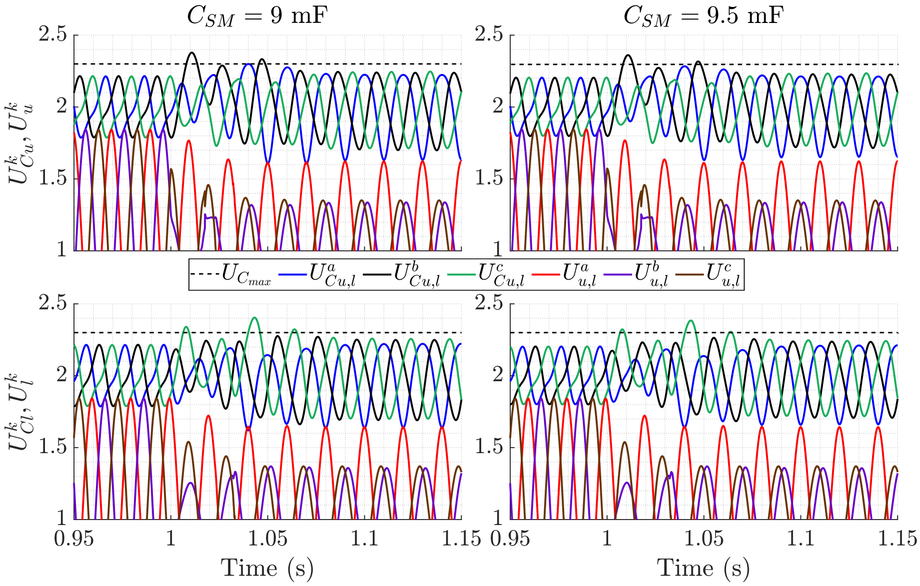

Fig. 6.11: Normal to fault during AC grid singular voltage sag type C.

observed.

In order to ensure that for all AC network faults and active and reactive set-points the converters' limitations are not exceed, the maximum value of SM capacitance obtained from the proposed methodology should be

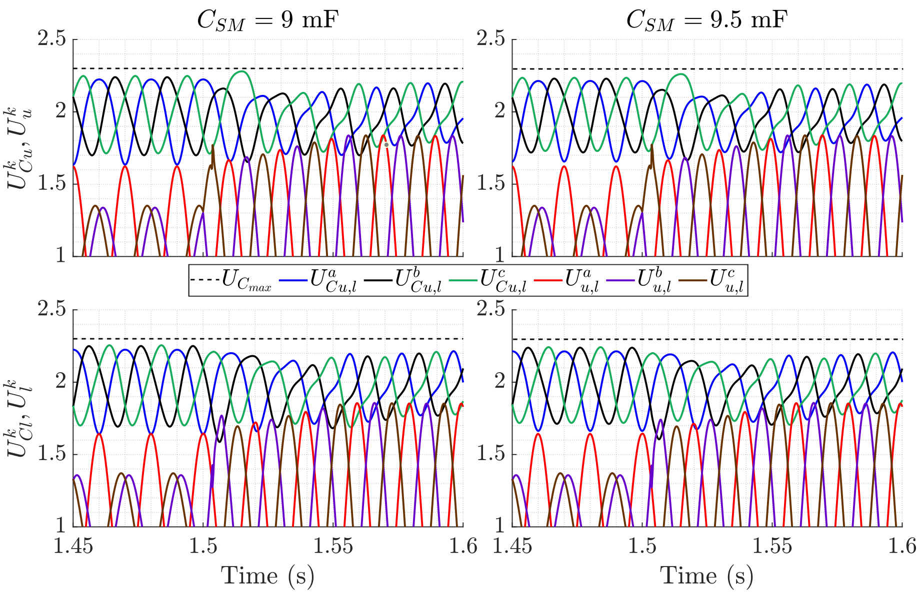

Fig. 6.12: Fault to normal during AC grid singular voltage sag type C.

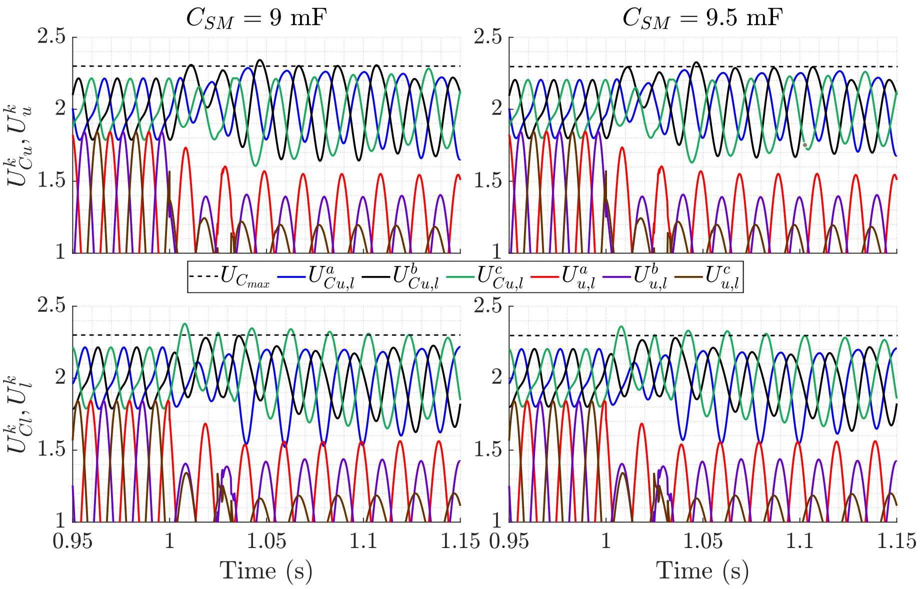

Fig. 6.13: Normal to fault during internal singular voltage sag type C.

employed, in this case $C_{SM} = 18$ mF. However, this highly conservative value would lead to a significant increase in volume, weight and costs of the converter station. Finally, for the converter configuration and control strategy used in the case studies, sub-module capacitors equal to

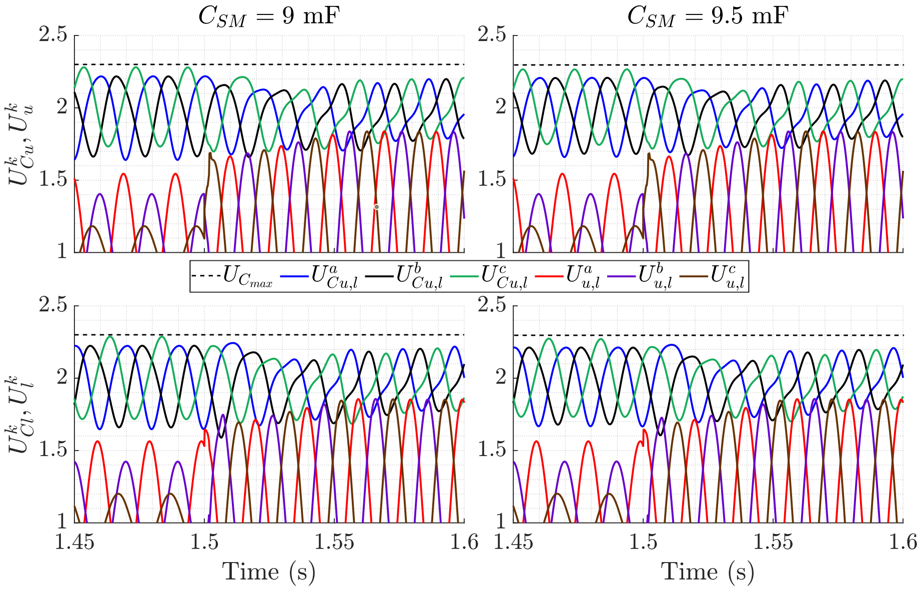
$C_{SM} = 9$ mF

$C_{SM} = 9.5$ mF

Fig. 6.14: Fault to normal during internal singular voltage sag type C.

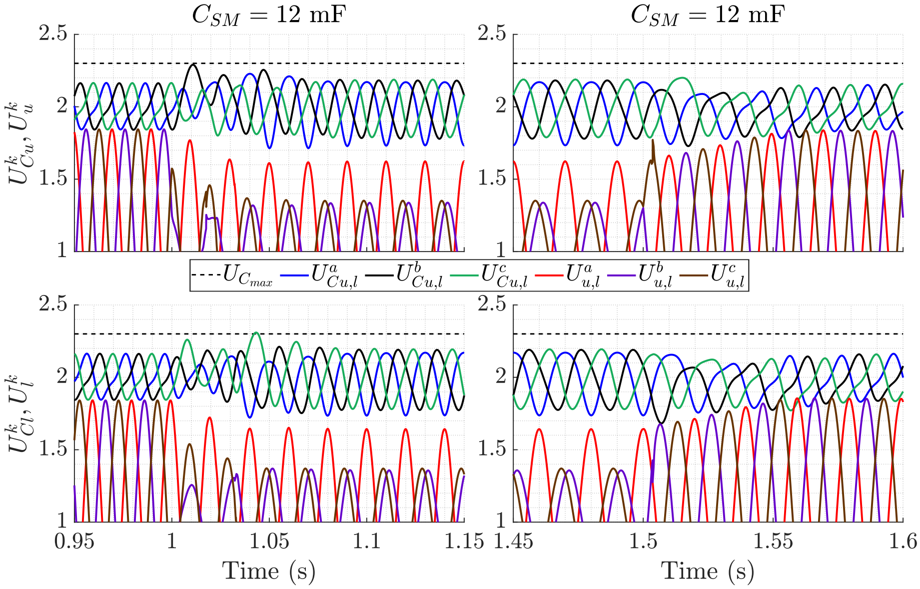
$C_{SM} = 12$ mF

$C_{SM} = 12$ mF

Fig. 6.15: Time-domain waveforms of the sum of the SM capacitor voltages and arm applied voltages for $C_{SM} = 12$ mF.

$C_{SM} = 9$ mF could be feasible. Even though they might exceed some limitations transiently during severe faults, the overall performance of the converter was not affected.

6.7 Conclusion

In this chapter, an optimization-based toolbox to design the SM capacitors of the MMC considering the converter's limitations and the TSO requirements during AC network voltage sags has been presented. Firstly, the instantaneous time-domain energy equations of the converter have been developed and their asymmetrical behavior during different OPs has been analyzed. Then, the suggested approach has been shown, whereby all its steps have been explained and validated by means of static and dynamic simulations. For the static validation, the suggested method is compared with different SM capacitor design approaches assuming different AC network active and reactive power set-points. It has been demonstrated that the optimization-based method can improve the SM capacitor design up to 24% in comparison to other methods. Finally, for the dynamic simulations, different values of C_{SM} capacitors have been used in time-domain simulations of the converter considering different voltage sag scenarios, whereas both values presented similar responses.

Chapter 7

Conclusions

With the increasing penetration of renewable energy based on power electronics into the power system, the MMC-HVDC will have a key role in the transmission of this energy to the consumption areas. This work has presented several studies to fully exploit the DOFs of the converter in order to improve its operation and design under normal or faulted operating conditions. To closure this thesis, this section gives an overall conclusion of this work, as well as, its specific contributions and future research lines.

7.1 General conclusions

Compared to classical two- and three-level VSC, the MMC requires more complex control strategies due to its increased number of DOFs. However, when properly regulated, they not only can improve the converter's operation especially under unbalanced network scenarios, but also can be used to enhance the design of the MMC components, such as the SM capacitors.

In the operational context, the DOFs play a crucial role in order to maintain the internal energy of the converter balanced. Although is well-known that the power transfer from the DC and AC networks and internally can be decoupled (when proper mathematical transformations are employed), it was presented that potential interactions among their respective quantities may occur.

If those interactions are not exploited, under different AC/DC network conditions or internal parameters mismatches, it was demonstrated a deteriorated performance of the converter's control. In order to overcome this issue, two potential solutions were proposed. One which is based on improving the AC circulating current reference calculation and another which consisted in calculating the optimized voltage and current references of the converter in real-time.

Finally, improvements in the sizing of the SM capacitors have been investigated. To do so, the DOFs are fully exploited by an optimization-based methodology to minimize the SM capacitor size. The methodology ensures that the SM capacitor size obtained meets the TSO's requirements under FRT conditions and, at the same time, respect the design limitations of the converter for distinct active and reactive power set-points and network voltage scenarios.

7.2 Contributions

The contributions of each chapter are detailed next.

- In **Chapter 2**, a comprehensive analysis of the MMC focusing on the DOFs to be considered in order to perform the internal energy balancing of the converter has been given. The analysis relies on the commonly used differential and additive reference frames. By means of a steady-state analysis, the different voltages components applied and currents components flowing through the converter are studied and an in-depth discussion of the roles of each DOF in the converter is presented. Furthermore, the mathematical expressions of the power exchanged between the AC/DC networks and within the converter, horizontally and vertically, are derived considering all the DOFs of the MMC, revealing potential interactions among the differential and additive quantities. Finally, the theoretical analysis is validated through comparisons between the values obtained with the mathematical expressions and the simulation results assuming different case scenarios.

- In **Chapter 3** an improved inner current reference calculation to be employed in the control of MMC operating during either balanced or unbalanced conditions has been addressed. The suggested reference calculation is derived based on the different DOFs of the converter. In addition, the impacts caused not only by the AC network's impedances but also by the MMC's arm impedances are also considered during the derivation of the AC additive current reference expressions. Another issue discussed is that singular voltage conditions, where the positive-sequence component is equal to the negative one, may occur not only in the AC network but also internally (within the converter's applied voltages). Several different inner current reference calculation methods are compared and their applicability during the former fault conditions is analyzed.

A detailed formulation of the inner current reference calculation is given and it is applied to different unbalanced AC grid faults.

- In **Chapter 4**, an optimization-based reference calculation method for MMCs operating in normal and constrained situations has been introduced. The optimization problem prioritizes to satisfy the external AC active and reactive current set-points demanded by the grid operator through the corresponding grid code. The optimization problem constraints are imposed based on the natural *abc* reference frame steady-state model. Then, the imposed limitations are the maximum allowed grid and arm currents, the maximum allowed arm voltages and the SM capacitor maximum voltages. A detailed formulation of the optimization problem is given and applied to several case studies.

- In **Chapter 5**, a real-time optimization-based reference calculation integrated with a control structure for MMCs has been proposed. In order to reduce the high computational burden, a Linear Time-Varying (LTV) approximation is applied, which permits to represent the nonlinear dynamics of the system as constant parameters, while a Linear Time-Invariant (LTI) system is used to formulate the optimization constraints. The converter's current references are determined in real-time by solving a constrained linearized optimization problem at each control time step, which considers the TSO's demands, the current MMC operating point and its physical limitations. Theoretical analyses comparing the responses of the linear and nonlinear optimization problems are performed to validate the accuracy of the LTV approximation. Finally, the linearized-optimization problem is integrated with the MMC controllers, evaluated under different AC and DC network conditions and compared with conventional control strategies.

- In **Chapter 6**, an optimization-based methodology to minimize the C_{SM} the MMC has been discussed. The analysis is performed considering both the converter's current and voltage limitations and the TSO FRT requirements. By means of a steady-state analysis, the time-domain expressions of the arm's energies of the converter are obtained and its behavior during numerous operating points is shown. Based on these expressions, the optimization-based problem is developed whereas its constraints are imposed focusing not only on the internal and external voltage and currents, but also the maximum and minimum allowed SM capacitor voltages. The suggested method is compared with different approaches for distinct active and reactive power set-points. Furthermore, time-domain simulations of the MMC considering several AC voltage sags are performed in order to show that the dynamics SM capacitor and the arm applied voltages are within acceptable margins.

7.3 Future work

The MMC is already the preferred choice of VSC in HVDC transmission systems and its usage is a growing trend. However, it still can be considered a relatively new technology in comparison to its predecessors. Thus, further research to improve the converter's design and FRT capabilities, to optimize its control's performance and to increase its robustness against network faulted scenario is needed. Based on the specific contributions presented in each chapter, potential research lines for future work arise. They are described next:

- Chapter 2:
    - Show the DOFs interactions in an experimental platform.
- Chapter 3:
    - Exploit further DOFs in the horizontal power balancing.
    - Validate the control strategy in an experimental platform.
- Chapter 4:
    - Validate the current and voltage results in an experimental prototype.
- Chapter 5:
    - Linearize the SM capacitor voltage ripple equations in order to add them in the formulation of the optimization problem.
    - Improve the calculation of the steady-state trajectories.
    - Validate the control strategy in an experimental platform.
    - Modify the control from traditional strategies to more advanced ones such as Model Predictive Control.
- Chapter 6:

- Modify the optimization formulation in order to design other components, such as the arm impedance.
- Include the DC breakers in its formulation to also consider DC fault scenarios.
- Validate the results in an experimental platform.

Appendix A

Publications

This section presents a list of the author's journal and conference papers. Some of them are directly related to the chapters of this thesis, whereas others correspond to other related works that have been done in collaboration with other universities.

Journal papers

Published - Included in the thesis

J1 D. Westerman Spier, E. Prieto-Araujo, J. López-Mestre and O. Gomis-Bellmunt, "Optimal Current Reference Calculation for MMCs Considering Converter Limitations", in *IEEE Transactions on Power Delivery*, vol. 36, no. 4, pp. 2097-2108, Aug. 2021.

J2 D. Westerman Spier, E. Prieto-Araujo, J. López-Mestre and O. Gomis-Bellmunt, "Improved current reference calculation for MMCs internal energy balancing control", in *IEEE Transactions on Power Delivery*, 2020.

J3 D. Westerman Spier, J. M. Rodriguez-Bernuz, E. Prieto-Araujo, J. López-Mestre, A. Junyent-Ferré and O. Gomis-Bellmunt, "Real-time optimization-based reference calculation integrated control for MMCs considering converter limitations", in *IEEE Transactions on Power Delivery*, 2021.

Published - Not included in the thesis

J4 D.Westerman Spier, G.G. Oggier, S.A.O. da Silva, "Dynamic modeling and analysis of the bidirectional DC-DC boost-buck converter for renewable energy applications", *Sustainable Energy Technologies and Assessments*, vol. 34, pp. 133-145, 2019.

J5 H. Lyu et al., "An Improved DC SSCB with Self-Adaptive Fault Current Limiting Capability", in *IEEE Transactions on Power Electronics*, 2021.

Submitted - Included in the thesis

S-J6 D. Westerman Spier, E. Prieto-Araujo, J. López-Mestre, H. Mehrjerdi and O. Gomis-Bellmunt, "On the roles and interactions of the MMC degrees of freedom in the internal energy balancing", under review *IEEE Transactions on Power Delivery.*

S-J7 D. Westerman Spier, E. Prieto-Araujo, Huijie Lyu, Jiawei He, Bin Li and O. Gomis-Bellmunt, "Optimization-based methodology to design the MMC's SM capacitors considering faulted scenarios and converter limitations", under review *IEEE Transactions on Power Delivery.*

Submitted - Not included in the thesis

S-J8 Qingquan Li et al.,"A Novel Design of Circulating Current Control Target to Minimize SM Capacitance in MMC", under review *International Journal of Electrical Power & Energy Systems.*

S-J9 Jiawei He et al., "A Passive Thyristor-based Hybrid DC Circuit Breaker", under review *IEEE Transactions on Power Electronics.*

Conferences

Published papers - Included in the thesis

C1 D. Westerman Spier, J. López-Mestre, E. Prieto-Araujo and O. Gomis-Bellmunt, "Steady-State Analysis of the Modular Multilevel Converter", *IECON 2019 - 45th Annual Conference of the IEEE Industrial Electronics Society*, 2019, pp. 4861-4866.

C2 D. Westerman Spier, J. López-Mestre, E. Prieto-Araujo and O. Gomis-Bellmunt, "Analytic estimation of the MMC sub-module capacitor voltage ripple for balanced and unbalanced AC grid conditions", 3^o *Simpósio Ibero-Americano em Microrredes Inteligentes com Integração de Energias Renováveis*, Oct. 2019, pp. 1-6.

- **C3** D. Westerman Spier, E. Prieto-Araujo, J. López-Mestre and O. Gomis-Bellmunt, "Optimization-based reference calculation for Modular Multilevel Converters in balanced and unbalanced network conditions", *2021 23rd European Conference on Power Electronics and Applications (EPE'21 ECCE Europe)*, 2021, pp. 1-6.

Bibliography

[1] U. Nations, “The paris agreement,” (accessed on 2021-11-26). [Online]. Available: https://www.un.org/en/climatechange/paris-agreement 1

[2] IRENA, “World energy transitions outlook: 1.5^{o}c pathway,” (accessed on 2021-11-26). [Online]. Available: https://www.irena.org/publications/2021/Jun/World-Energy-Transitions-Outlook xi, 1, 2

[3] D. Van Hertem and M. Ghandhari, “Multi-terminal VSC HVDC for the european supergrid: Obstacles,” *Renewable and Sustainable Energy Reviews*, vol. 14, no. 9, pp. 3156–3163, 2010. xi, 1, 2

[4] D. Van Hertem, O. Gomis-Bellmunt, and J. Liang, *HVDC Grids: For Offshore and Supergrid of the Future*, ser. IEEE Press Series on Power Engineering. Wiley, 2016. xi, 2, 7

[5] D. Tiku, “dc power transmission: Mercury-arc to thyristor HVdc valves [history],” *IEEE Power and Energy Magazine*, vol. 12, no. 2, pp. 76–96, 2014. 3

[6] H. Energy, “HVDC classic HVDC classic reference list thyristor valve projects,” 2021. xi, 3, 6, 7

[7] F. Nobre, “HVDC-systems applications and benefits,” in *X JORNADAS TÉCNICAS*, 2017. 3

[8] S. Energy, “HVDC classic - powerful and economical high-performance power transmission,” 2021. xi, 3, 6, 7

[9] O. E. Oni, I. E. Davidson, and K. N. Mbangula, “A review of LCC-HVDC and VSC-HVDC technologies and applications,” in *2016 IEEE 16th International Conference on Environment and Electrical Engineering (EEEIC)*, 2016, pp. 1–7. 3

[10] L. Han, L. Liang, Y. Kang, and Y. Qiu, “A review of SiC IGBT: Models, fabrications, characteristics, and applications,”

IEEE Transactions on Power Electronics, vol. 36, no. 2, pp. 2080–2093, 2021. 3

[11] K. Sheng, B. Williams, and S. Finney, "A review of IGBT models," *IEEE Transactions on Power Electronics*, vol. 15, no. 6, pp. 1250–1266, 2000. 3

[12] R. L. Sellick and M. Å kerberg, "Comparison of HVDC light (VSC) and HVDC classic (LCC) site aspects, for a 500mw 400kv HVDC transmission scheme," in *10th IET International Conference on AC and DC Power Transmission (ACDC 2012)*, 2012, pp. 1–6. 3

[13] N. Flourentzou, V. G. Agelidis, and G. D. Demetriades, "VSC-based HVDC power transmission systems: An overview," *IEEE Transactions on Power Electronics*, vol. 24, no. 3, pp. 592–602, 2009. 3

[14] S. Energy, "High voltage direct current transmission-proven technology for power exchange," 2011. 3

[15] F. Wang, L. Bertling, L. A. Tuan, M. Anders, and B. Jörgen, "An overview introduction of VSC-HVDC: State-of-art and potential applications in electric power systems," in *Cigrè International Symposium*, 2011, pp. 1–10. 4

[16] U. Axelsson, A. Holm, C. Liljegren, M. Aberg, K. Eriksson, and O. Tollerz, "The gotland HVDC light project-experiences from trial and commercial operation," in *16th International Conference and Exhibition on Electricity Distribution, 2001. Part 1: Contributions. CIRED. (IEE Conf. Publ No. 482)*, vol. 1, 2001, pp. 5 pp. vol.1–. 4

[17] G. Wolf. (2017) A short history: The voltage source converter. [Online]. Available: https://www.tdworld.com/digital-innovations/hvdc/article/20970224/a-short-history-the-voltage-source-converter 4

[18] WindPhotos. (1998). [Online]. Available: http://www.windpowerphotos.com/hvdcl.html xi, 4

[19] H. Energy. (2021) The eagle pass 36 MW back-to-back HVDC light installation is a voltage source converter (VSC) supported tie interconnecting transmission grids in texas and mexico. [Online]. Available: https://www.hitachienergy.com/latam/es/references/hvdc/eagle-pass 4

[20] T. Larsson, A. Petersson, A. Edris, D. Kidd, and F. Aboytes, "Eagle pass back-to-back tie: a dual purpose application of voltage source converter technology," in *2001 Power Engineering Society Summer Meeting. Conference Proceedings (Cat. No.01CH37262)*, vol. 3, 2001, pp. 1686–1691 vol.3. xi, 4, 5

[21] R. Marquardt, "Stromrichterschaltungen mit verteilten energiespeichern," *German Patent DE10103031*, vol. 28, no. 168, 2001. 5

[22] A. Lesnicar and R. Marquardt, "An innovative modular multilevel converter topology suitable for a wide power range," in *2003 IEEE Bologna Power Tech Conference Proceedings,*, vol. 3, 2003, pp. 6 pp. Vol.3–. 5, 8

[23] O. Gomis-Bellmunt, J. Sau-Bassols, E. Prieto-Araujo, and M. Cheah-Mane, "Flexible converters for meshed HVDC grids: From flexible AC transmission systems (FACTS) to flexible DC grids," *IEEE Transactions on Power Delivery*, vol. 35, no. 1, pp. 2–15, 2020. 5

[24] H. energy, "HVDC light it's time to connect," 2021. xi, 6

[25] H. Energy, "HVDC light projects worldwide," 2021. xi, 6, 7

[26] S. Energy, "HVDC - high-voltage direct current transmission- unrivaled practical experience," 2021. xi, 6, 7

[27] Tennet. (2021). [Online]. Available: https://www.tennet.eu/our-grid/offshore-projects-germany/dolwin1/ 6

[28] ——. (2021). [Online]. Available: https://www.tennet.eu/our-grid/offshore-projects-germany/dolwin2/ 6

[29] ——. (2021). [Online]. Available: https://www.tennet.eu/our-grid/offshore-projects-germany/sylwin1/ 6

[30] ——. (2021). [Online]. Available: https://www.tennet.eu/our-grid/offshore-projects-germany/borwin3/ 6

[31] S. W. . W. O. W. Industry. [Online]. Available: https://www.sunwindenergy.com/wind-energy/siemens-puts-converter-stations-hvdc-link-france-spain-operation xi, 7, 8

[32] K. Sharifabadi, L. Harnefors, H. Nee, S. Norrga, and R. Teodorescu, *Design, Control, and Application of Modular Multilevel Converters for HVDC Transmission Systems.* Wiley-IEEE Press, 2016, ch. 2, pp. 60–132. 8, 143

[33] E. Prieto-Araujo, A. Junyent-Ferré, G. Clariana-Colet, and O. Gomis-Bellmunt, “Control of modular multilevel converters under singular unbalanced voltage conditions with equal positive and negative sequence components,” *IEEE Transactions on Power Systems*, vol. 32, no. 3, pp. 2131–2141, 2017. xvi, 13, 18, 19, 48, 51, 52, 53, 54, 62, 65, 71

[34] S. Li, X. Wang, Z. Yao, T. Li, and Z. Peng, “Circulating current suppressing strategy for MMC-HVDC based on nonideal proportional resonant controllers under unbalanced grid conditions,” *IEEE Transactions on Power Electronics*, vol. 30, no. 1, pp. 387–397, 2015. 18

[35] J. Wang, J. Liang, C. Wang, and X. Dong, “Circulating current suppression for MMC-HVDC under unbalanced grid conditions,” *IEEE Transactions on Industry Applications*, vol. 53, no. 4, pp. 3250–3259, 2017. 18

[36] Y. Liang, J. Liu, T. Zhang, and Q. Yang, “Arm current control strategy for MMC-HVDC under unbalanced conditions,” *IEEE Transactions on Power Delivery*, vol. 32, pp. 125–134, 2017. 18, 47

[37] Z. Ou, G. Wang, and L. Zhang, “Modular multilevel converter control strategy based on arm current control under unbalanced grid condition,” *IEEE Transactions on Power Electronics*, vol. 33, no. 5, pp. 3826–3836, 2018. 18, 47

[38] G. Bergna-Diaz, J. A. Suul, E. Berne, J. Vannier, and M. Molinas, “Optimal shaping of the MMC circulating currents for preventing AC-side power oscillations from propagating into HVdc grids,” *IEEE Journal of Emerging and Selected Topics in Power Electronics*, vol. 7, no. 2, pp. 1015–1030, 2019. 18, 19, 47, 77, 107

[39] E. Prieto-Araujo, A. Junyent-Feré, C. Collados-Rodríguez, G. Clariana-Colet, and O. Gomis-Bellmunt, “Control design of modular multilevel converters in normal and AC fault conditions for HVDC grids,” *Electric Power Systems Research*, vol. 152, pp. 424 – 437, 2017. 18, 21, 23, 48, 49, 50, 53, 118

[40] S. Cui, H.-J. Lee, J.-J. Jung, Y. Lee, and S.-K. Sul, "A comprehensive AC-side single-line-to-ground fault ride through strategy of an MMC-based HVDC system," *IEEE Journal of Emerging and Selected Topics in Power Electronics*, vol. 6, no. 3, pp. 1021–1031, 2018. 18, 47

[41] J. Wang, Y. Tang, and X. Liu, "Arm current balancing control for modular multilevel converters under unbalanced grid conditions," *IEEE Transactions on Power Electronics*, vol. 35, no. 3, pp. 2467–2479, 2020. 18, 47

[42] S. Milovanović and D. Dujić, "Comprehensive comparison of modular multilevel converter internal energy balancing methods," *IEEE Transactions on Power Electronics*, vol. 36, no. 8, pp. 8962–8977, 2021. 18, 19

[43] J. Moon, J. Park, D. Kang, and J. Kim, "A control method of HVDC-modular multilevel converter based on arm current under the unbalanced voltage condition," *IEEE Transactions on Power Delivery*, vol. 30, no. 2, pp. 529–536, 2015. 19, 47

[44] H. Zhang, M. M. Belhaouane, F. Colas, R. Kadri, F. Gruson, and X. Guillaud, "On comprehensive description and analysis of MMC control design: Simulation and experimental study," *IEEE Transactions on Power Delivery*, vol. 36, no. 1, pp. 244–253, 2021. 19, 48

[45] M. M. Belhaouane, M. Ayari, X. Guillaud, and N. B. Braiek, "Robust control design of MMC-HVDC systems using multivariable optimal guaranteed cost approach," *IEEE Transactions on Industry Applications*, vol. 55, no. 3, pp. 2952–2963, 2019. 19, 48, 107

[46] A. E. Leon and S. J. Amodeo, "Energy balancing improvement of modular multilevel converters under unbalanced grid conditions," *IEEE Transactions on Power Electronics*, vol. 32, no. 8, pp. 6628–6637, 2017. 19, 47

[47] D. W. Spier, E. Prieto-Araujo, J. López-Mestre, and O. Gomis-Bellmunt, "Improved current reference calculation for MMCs internal energy balancing control," *IEEE Transactions on Power Delivery*, pp. 1–1, 2021. xiv, xv, 19, 23, 121, 132, 135, 137, 138, 139, 140, 141, 145, 157, 163

[48] J. Li, G. Konstantinou, H. R. Wickramasinghe, C. D. Townsend, and J. Pou, "Capacitor voltage reduction in modular multilevel converters under grid voltages unbalances," *IEEE Transactions on Power Delivery*, vol. 35, no. 1, pp. 160–170, 2020. 22, 144

[49] D. Westerman Spier, J. M. Rodriguez-Bernuz, E. Prieto-Araujo, J. López-Mestre, A. Junyent-Ferré, and O. Gomis-Bellmunt, "Real-time optimization-based reference calculation integrated control for MMCs considering converter limitations," *IEEE Transactions on Power Delivery*, pp. 1–1, 2021. 22, 147

[50] M. Tapia, "Use of superposition in writing state equations for networks with excess elements," *IEEE Transactions on Circuit Theory*, vol. 17, no. 4, pp. 624–626, 1970. 24

[51] M. Bollen and L. Zhang, "Different methods for classification of three-phase unbalanced voltage dips due to faults," *Electric Power Systems Research*, vol. 66, no. 1, pp. 59 – 69, 2003. 44, 88, 91, 96, 97, 116, 124, 164

[52] S. Wang, G. P. Adam, A. M. Massoud, D. Holliday, and B. W. Williams, "Analysis and assessment of modular multilevel converter internal control schemes," *IEEE Journal of Emerging and Selected Topics in Power Electronics*, vol. 8, pp. 697–719, 2020. 47

[53] J. Li, G. Konstantinou, H. R. Wickramasinghe, and J. Pou, "Operation and control methods of modular multilevel converters in unbalanced AC grids: A review," *IEEE Journal of Emerging and Selected Topics in Power Electronics*, vol. 7, no. 2, pp. 1258–1271, 2019. 47

[54] A. Junyent-Ferré, O. Gomis-Bellmunt, T. C. Green, and D. E. Soto-Sanchez, "Current control reference calculation issues for the operation of renewable source grid interface VSCs under unbalanced voltage sags," *IEEE Transactions on Power Electronics*, vol. 26, pp. 3744–3753, 2011. 48

[55] H. Akagi, E. H. Watanabe, and M. Aredes, "Instantaneous power theory and applications to power conditioning," 2007. 50, 121

[56] E. Sánchez-Sánchez, E. Prieto-Araujo, A. Junyent-Ferré, and O. Gomis-Bellmunt, "Analysis of MMC energy-based control structures for VSC-HVDC links," *IEEE Journal of Emerging and Se-*

lected Topics in Power Electronics, vol. 6, pp. 1065–1076, 2018. 51, 106

[57] L. Harnefors, A. Antonopoulos, S. Norrga, L. Ängquist, and H. Nee, "Dynamic analysis of modular multilevel converters," *IEEE Transactions on Industrial Electronics*, vol. 60, pp. 2526–2537, 2013. 55

[58] Elia, "Proposal for NC HVDC requirements of general application," April 2018, (accessed on 2020-12-03). [Online]. Available: https://www.febeg.be/sites/default/files/20180423_bga_comments_to_elia_proposal_for_general_requirements_nc_hvdc_sh.pdf 61, 78

[59] B. O. del Estado, "Orden TED/749/2020, de 16 de julio, por la que se establecen los requisitos técnicos para la conexión a la red necesarios para la implementación de los códigos de red de conexión," no. 208, pp. 62 406–62 458, Aug. 2020. 61, 78, 88, 112, 126, 133, 162, 163

[60] National Grid TSO, *The Grid Code*, Nov. 2020. [Online]. Available: https://www.nationalgrideso.com/document/162271/download 61, 78, 112

[61] J. Xu, C. Zhao, W. Liu, and C. Guo, "Accelerated model of modular multilevel converters in PSCAD/EMTDC," *IEEE Transactions on Power Delivery*, vol. 28, no. 1, pp. 129–136, 2013. 61, 122, 156

[62] Q. Tu and Z. Xu, "Impact of sampling frequency on harmonic distortion for modular multilevel converter," *IEEE Transactions on Power Delivery*, vol. 26, pp. 298–306, 2011. 61, 123, 156

[63] ENTSO-E, "ENTSO-E network code on requirements for grid connection of generators," (accessed on 2020-10-29). [Online]. Available: https://eur-lex.europa.eu/legal-content/EN/TXT/PDF/?uri=CELEX:32016R0631$&$from=EN 61, 122

[64] X. Shi, Z. Wang, B. Liu, Y. Li, L. M. Tolbert, and F. Wang, "Steady-state modeling of modular multilevel converter under unbalanced grid conditions," *IEEE Transactions on Power Electronics*, vol. 32, no. 9, pp. 7306–7324, 2017. 77

[65] X. Shi, Z. Wang, B. Liu, Y. Liu, L. M. Tolbert, and F. Wang, "Characteristic investigation and control of a modular multilevel converter-based HVDC system under Single-Line-to-Ground fault conditions," *IEEE Transactions on Power Electronics*, vol. 30, no. 1, pp. 408–421, 2015. 77

[66] D. W. Spier, J. López-Mestre, E. Prieto-Araujo, and O. Gomis-Bellmunt, "Steady-state analysis of the modular multilevel converter," in *IECON 2019 - 45th Annual Conference of the IEEE Industrial Electronics Society*, vol. 1, 2019, pp. 4861–4866. 79, 146

[67] H. Saad, S. Dennetiére, J. Mahseredjian, P. Delarue, X. Guillaud, J. Peralta, and S. Nguefeu, "Modular multilevel converter models for electromagnetic transients," *IEEE Transactions on Power Delivery*, vol. 29, no. 3, pp. 1481–1489, 2014. 82

[68] J. Wang, J. Liang, F. Gao, X. Dong, C. Wang, and B. Zhao, "A closed-loop time-domain analysis method for modular multilevel converter," *IEEE Transactions on Power Electronics*, vol. 32, no. 10, pp. 7494–7508, 2017. 84

[69] Z. Ali, N. Christofides, L. Hadjidemetriou, E. Kyriakides, Y. Yang, and F. Blaabjerg, "Three-phase phase-locked loop synchronization algorithms for grid-connected renewable energy systems: A review," *Renewable and Sustainable Energy Reviews*, vol. 90, pp. 434 – 452, 2018. 90

[70] S.-J. Kim, K. Koh, M. Lustig, S. Boyd, and D. Gorinevsky, "An interior-point method for large-scale ℓ_1-regularized least squares," *IEEE Journal of Selected Topics in Signal Processing*, vol. 1, no. 4, pp. 606–617, 2007. 95

[71] S. Dennetiere, P. Rault, and et. al., "Guide for electromagnetic transient studies involving VSC converters," Cigre, Tech. Rep. WG B4.70, 2021. 106, 132

[72] Q. Tu, Z. Xu, and L. Xu, "Reduced switching-frequency modulation and circulating current suppression for modular multilevel converters," *IEEE Transactions on Power Delivery*, vol. 26, no. 3, pp. 2009–2017, 2011. xiv, 106, 132, 133, 134, 138

[73] H. Fehr and A. Gensior, "Eigenvalue optimization of the energy-balancing feedback for modular multilevel converters," *IEEE Transactions on Power Electronics*, vol. 34, no. 11, pp. 11 482–11 495, 2019. 107

[74] Z. Gong, X. Wu, P. Dai, and R. Zhu, "Modulated model predictive control for MMC-based active front-end rectifiers under unbalanced grid conditions," *IEEE Transactions on Industrial Electronics*, vol. 66, no. 3, pp. 2398–2409, 2019. 107

[75] L. Qiu, X. Liu, J. Sun, J. Zhang, J. Ma, and Y. Fang, “Fast finite-set model predictive control for three-phase four-arm active front end modular multilevel converters under unbalanced and distorted network conditions,” *IEEE Access*, vol. 8, pp. 30 504–30 514, 2020. 107

[76] ENTSO-E, “Commission regulation (eu) 2016/1447 of 26 august 2016 establishing a network code on requirements for grid connection of high voltage direct current systems and direct current-connected power park modules,” p. 65, Aug. 2016. 107

[77] T. Huang, B. Wang, H. Xie, T. Wu, C. Li, S. Li, J. Hao, and J. Luo, “Research on reactive power control strategy of MMC HVDC converter,” in *2020 IEEE 4th Conference on Energy Internet and Energy System Integration (EI2)*, 2020, pp. 880–884. 107

[78] X. Chen, G. Irwin, D. Woodford, and A. Gole, “Reactive power control in MMC HVDC system during ac fault,” in *12th IET International Conference on AC and DC Power Transmission (ACDC 2016)*, 2016, pp. 1–5. 107

[79] M. I. Hossain and M. A. Abido, “Positive-negative sequence current controller for LVRT improvement of wind farms integrated MMC-HVDC network,” *IEEE Access*, vol. 8, pp. 193 314–193 339, 2020. 107

[80] D. W. Spier, E. Prieto-Araujo, J. López-Mestre, and O. Gomis-Bellmunt, “Optimal current reference calculation for MMCs considering converter limitations,” *IEEE Transactions on Power Delivery*, vol. 36, no. 4, pp. 2097–2108, 2021. 107, 110, 111

[81] J. M. Rodriguez-Bernuz, I. Mcinerney, A. Junyent-Ferré, and E. C. Kerrigan, “Design of a linear time-varying model predictive control energy regulator for grid-tied VSCs,” *IEEE Transactions on Energy Conversion*, pp. 1–1, 2021. 112

[82] J. Rodriguez-Bernuz and A. Junyent-Ferré, “Operating region extension of a modular multilevel converter using model predictive control: A single phase analysis,” *IEEE Transactions on Power Delivery*, vol. 35, no. 1, pp. 171–182, 2020. 113

[83] R. Fletcher, *Practical Methods of Optimization*, 2nd ed. New York, NY, USA: John Wiley & Sons, 1987. 115

[84] B. Stellato, G. Banjac, P. Goulart, A. Bemporad, and S. Boyd, "OSQP: an operator splitting solver for quadratic programs," *Mathematical Programming Computation*, vol. 12, no. 4, pp. 637–672, 2020. 115, 123

[85] C. Oates, "Modular multilevel converter design for VSC HVDC applications," *IEEE Journal of Emerging and Selected Topics in Power Electronics*, vol. 3, no. 2, pp. 505–515, 2015. 143, 144

[86] Y. Tang, M. Chen, and L. Ran, "A compact MMC submodule structure with reduced capacitor size using the stacked switched capacitor architecture," *IEEE Transactions on Power Electronics*, vol. 31, no. 10, pp. 6920–6936, 2016. 143

[87] H. Wang and F. Blaabjerg, "Reliability of capacitors for DC-link applications in power electronic convertersâan overview," *IEEE Transactions on Industry Applications*, vol. 50, no. 5, pp. 3569–3578, 2014. 143

[88] M. Merlin and T. Green, "Cell capacitor sizing in multilevel converters: Cases of the modular multilevel converter and alternate arm converter," *IET Power Electronics*, vol. 8, no. 3, pp. 350–360, Mar. 2015. 143

[89] K. Ilves, S. Norrga, L. Harnefors, and H.-P. Nee, "On energy storage requirements in modular multilevel converters," *IEEE Transactions on Power Electronics*, vol. 29, no. 1, pp. 77–88, 2014. 143, 156, 157

[90] L. Lin, Y. Lin, C. Xu, and Y. Chen, "Comprehensive analysis of capacitor voltage fluctuation and capacitance design for submodules in hybrid modular multilevel converter with boosted modulation index," *IEEE Journal of Emerging and Selected Topics in Power Electronics*, vol. 7, no. 4, pp. 2369–2383, 2019. 143

[91] H. Bärnklau, A. Gensior, and S. Bernet, "Submodule capacitor dimensioning for modular multilevel converters," *IEEE Transactions on Industry Applications*, vol. 50, no. 3, pp. 1915–1923, 2014. 144

[92] Y. Tang, L. Ran, O. Alatise, and P. Mawby, "Capacitor selection for modular multilevel converter," *IEEE Transactions on Industry Applications*, vol. 52, no. 4, pp. 3279–3293, 2016. 144, 156, 157

[93] Z. Liu, K.-J. Li, J. Wang, Z. Javid, M. Wang, and K. Sun, "Research on capacitance selection for modular multi-level converter," *IEEE*

Transactions on Power Electronics, vol. 34, no. 9, pp. 8417–8434, 2019. 144, 156, 157

[94] S. Wang, T. Dragicevic, Y. Gao, S. K. Chaudhary, and R. Teodorescu, “Machine learning based operating region extension of modular multilevel converters under unbalanced grid faults,” *IEEE Transactions on Industrial Electronics*, vol. 68, no. 5, pp. 4554–4560, 2021. 144

[95] K. Ilves, A. Antonopoulos, L. Harnefors, S. Norrga, L. Ängquist, and H.-P. Nee, “Capacitor voltage ripple shaping in modular multilevel converters allowing for operating region extension,” in *IECON 2011 - 37th Annual Conference of the IEEE Industrial Electronics Society*, 2011, pp. 4403–4408. 144

[96] M. Winkelnkemper, A. Korn, and P. Steimer, “A modular direct converter for transformerless rail interties,” in *2010 IEEE International Symposium on Industrial Electronics*, 2010, pp. 562–567. 144

[97] X. Li, Q. Song, W. Liu, S. Xu, Z. Zhu, and X. Li, “Performance analysis and optimization of circulating current control for modular multilevel converter,” *IEEE Transactions on Industrial Electronics*, vol. 63, no. 2, pp. 716–727, 2016. 144

[98] D. W. Spier, E. Prieto-Araujo, O. Gomis-Bellmunt, and J. L. Mestre, “Analytic estimation of the MMC sub-module capacitor voltage ripple for balanced and unbalanced AC grid conditions,” 2021. 152